A Dynamic Homogenization Method for Nuclear Reactor Core Calculations

Antonio Galia

université
PARIS-SACLAY

A Dynamic Homogenization Method for Nuclear Reactor Core Calculations

Thèse de doctorat de l'Université Paris-Saclay

École doctorale n° 576, PHENIICS
Spécialité de doctorat: énergie nucléaire
Unité de recherche: Université Paris-Saclay, CEA,
Service d'Études des Réacteurs et de Mathématiques Appliquées,
91191 Gif-sur-Yvette, France
Référent: Faculté des sciences d'Orsay

**Thèse présentée et soutenue à Saclay,
le 22 octobre 2020, par**

Antonio Galia

Composition du jury:

Prof. Pierre Désesquelles Université Paris-Saclay	Président
Prof. Jean C. Ragusa Texas A&M	Rapporteur & Examinateur
Prof. Piero Ravetto Politecnico di Torino	Rapporteur & Examinateur
Prof. Sandra Dulla Politecnico di Torino	Examinatrice
Prof. Olga Mula Université Paris Dauphine	Examinatrice
Dr. Richard Sanchez CEA Saclay	Directeur de thèse
Dr. Igor Zmijarevic CEA Saclay	Encadrant
Dr. Emiliano Masiello CEA Saclay	Invité

Thèse de doctorat

NNT: 2020UPASP042

Partenaire de la thèse

Acknowledgments

The author does not like to make private acknowledgements public. But few words to the professional entourage are due, right and proper.

I am grateful to CEA for the exciting and inspiring professional environment that I found and also for giving me the opportunity to run calculations on HPC machines. I believe these points are not necessarily evident.

I want to thank Piero Ravetto and Jean Ragusa for the time and the energy they spent in being reviewers of my PhD dissertation. Also, a special thanks to Sandra Dulla for doing the same work even though she was not officially in charge of it. Their remarks were precious to improve the quality of this work.

I am particularly thankful to Emiliano Masiello for the exciting conversations that last forever (thanks God CEA closes) and, of course, for all the help that he gave me with IDT and the HPC. Sharing his own experiences made me save a lot of time.

I don't know how to thank Richard Sanchez and Igor Zmijarevic. Incredible advisers. Their elegance has no limits. I am honored to have met them and to have worked with them. Hope to have lived up to them.

Thanks to them for making this experience a lot of **fun**!

Table of Contents

List of Figures

Figure **Page**

List of Tables

Table **Page**

Résumé en français

Un réacteur nucléaire est un système complexe dans lequel plusieurs phénomènes physiques de nature différente se produisent et s'influencent mutuellement. Les disciplines d'ingénierie impliquées dans le processus de production d'énergie nucléaire sont nombreuses, parmi lesquelles la physique des réacteurs joue le rôle central de fournir des taux de réaction aux autres. Un taux de réaction est une conséquence des interactions entre les particules et la matière. Ces interactions dépendent non seulement des propriétés physiques des matériaux dans lesquels les particules se déplacent, telles que la densité, la température, les informations géométriques, la composition isotopique, qui sont fournies par les autres disciplines, mais aussi de la population de particules qui, via des collisions, a une probabilité de générer un événement de la réaction d'intérêt. Ce dernier fait l'objet d'étude de la physique des réacteurs qui trouve ses racines dans la théorie du transport et décrit la nature statistique de ces interactions, introduisant le concept de distribution de probabilité de l'occurrence d'un événement dans l'espace des phases du système.

Cette approche a d'abord été adoptée par Ludwig Boltzmann et elle est bien connue sous le nom de mécanique statistique. Cependant, en raison des propriétés des neutrons, l'équation de transport de ces particules est en effet simplifiée par rapport à l'équation cinétique des gaz de Boltzmann. Cela est dû à l'hypothèse que les neutrons n'interagissent pas les uns avec les autres, ce qui est justifié par l'absence d'interactions de coulomb, car ils n'ont pas de charge, et la densité beaucoup plus faible du gaz neutron par rapport à la densité des autres matériaux dans un réacteur nucléaire [1]. Ainsi, les interactions neutron-neutron sont si rares qu'on peut les négliger et l'équation de Boltzmann se transforme en une équation linéaire. De plus, les photons sont également des particules neutres et ils interagissent à peine les uns avec les autres pour la même raison, ils obéissent donc à la même loi physique des neutrons même s'ils interagissent différemment avec la matière.

L'approche de la mécanique statistique permet de "relier" les grandeurs physiques macroscopiques d'un système à des grandeurs microscopiques qui fluctuent autour d'une moyenne. Par exemple, l'une des principales grandeurs macroscopiques d'intérêt technique est la puissance produite par les taux de fission, qui dépendent du nombre de neutrons qui heurtent un nucléide fissile et leur probabilité de produire une fission après collision, qui est fonction de l'énergie du neutron incident. Les neutrons sont les particules protagonistes qui participent au processus de production d'électricité dans

un réacteur nucléaire, qui est un processus de réaction en chaîne. En fait, chaque événement de fission produit non seulement deux ou plusieurs produits de fission qui sont des fragments instables du nucléide fissile initial, mais aussi peu de neutrons qui, à leur tour, génèrent d'autres événements de fission, si le système dans lequel ils se trouvent est propice. Lorsque la réaction en chaîne est auto-entretenue, le système est dit *critique*, et à des fins de sûreté et de conception une tâche de la physique des réacteurs consiste à résoudre une classe de problèmes appelés calculs de criticité. Une autre classe de problèmes d'intérêt technique est celle des calculs à source fixe où, contrairement à la source de fission en criticité, la source des particules injectées dans le système est connue et ne dépend pas des caractéristiques du système. La population de neutrons ou de photons, solution de l'équation de transport pour ce type de problème, est particulièrement recherchée dans le domaine de la radioprotection.

Bien que l'équation de transport des neutrons soit grandement simplifiée par rapport à l'équation de Boltzmann, sa solution dans un système complexe tel qu'un réacteur nucléaire est encore très difficile à trouver pour plusieurs raisons. Tout d'abord, un réacteur nucléaire est un très grand système hétérogène composé de différents éléments structurels contenant une grande variété de matériaux. Même si tous les composants avaient une géométrie simple, une solution analytique de l'équation de transport des neutrons ne serait pas possible en raison du changement rapide des propriétés nucléaires (sections efficaces) des matériaux contenus dans le système. Deuxièmement, la population de particules qui est solution de l'équation de transport est une distribution changeant dans le temps et définie sur tout l'espace des phases du problème qui inclut tous les états possibles du système, comprenant le domaine spatial tridimensionnel, le domaine angulaire bidimensionnel et le domaine énergétique. Avec les capacités actuelles des machines, nous sommes aujourd'hui en mesure d'effectuer un calcul en transport 3D de cœur entier en régime stationnaire à l'aide d'un calcul haute performance et d'obtenir une solution numérique très détaillée. Très souvent, cependant, cette information fine en espace, angle et énergie dans un système aussi grand n'est pas très utile pour les problèmes d'ingénierie, et elle est davantage utilisée comme calcul de référence pour valider des modèles numériques approximatifs qui sont beaucoup plus rapides et ne nécessitent pas une utilisation intensive de ressources informatiques. Ce qui ajoute des complications supplémentaires dans un modèle de réacteur est chaque phénomène physique qui provoque un changement dans l'espace et dans le temps des caractéristiques du système. Discutons les principales applications industrielles qui concernent ce type de phénomènes.

Les événements de fission épuisent le combustible contenu dans le système et les événements de capture le transmutent. Ainsi, les matériaux contenus dans le système avec lesquels les neutrons interagissent évoluent dans l'espace et dans le temps sous l'effet de la production d'énergie ou, plus généralement, de l'irradiation. Ce dernier génère les effets dits historiques qui sont irréversibles et peuvent influencer le comportement du système lui-même plus tard avec une échelle de temps caractéristique. Les effets de l'épuisement du combustible, par exemple, ont une échelle de temps de l'ordre d'heures ou de jours. Les neutrons retardés sont un autre phénomène qui permet le contrôle des réacteurs. Une petite partie des neutrons générés par la fission est émise par les fragments de fission appelés précurseurs qui se désintègrent en bêta en émettant un neutron quelques secondes plus tard. Ce phénomène a une échelle de

temps plus courte en ce qui concerne et il nécessite l'évaluation des sources de neutrons retardés dépendant de l'espace et du temps. De plus, les interactions des particules dépendent des propriétés physiques de la matière dans laquelle elles entrent en collision, telles que la densité et la température, qui sont des fonctions de distribution définies au sein du système et qui dépendent de la distribution de puissance produite par le système lui-même, résultant en un problème de multiphysique non linéaire. Ce type de problèmes permet de prendre en compte le contre-réactions en réactivité, dues à une modification des propriétés thermohydrauliques du système. De plus, un changement de température entraîne des dilatations de matière, qui peuvent être positives ou négatives, et, par conséquent, une modification des caractéristiques géométriques du système.

La prise en compte de l'ensemble de ces phénomènes augmente le nombre d'équations et de degrés de liberté d'un modèle de réacteur, ce qui rend impossible la détermination d'une solution numérique reproduisant exactement la situation réelle dans tout le cœur. Un tel calcul nécessiterait, en fait, une énorme quantité de ressources de calcul qui ne sont pas toujours disponibles, et un temps d'exécution de la simulation trop long pour des applications industrielles. Par conséquent, un ensemble d'approximations est généralement introduit dans la modélisation des réacteurs qui ont un régime de validité et donc d'applicabilité.
Une séquence de calculs intermédiaires avec leurs propres approximations qui permet de parvenir à la solution finale du problème du réacteur dans le cadre de la physique du réacteur est appelée schéma de calcul. Un schéma de calcul est une arme à double tranchant car d'une part, si les approximations utilisées sont petites et ont une validité physique, le calcul est à la fois rapide et précis, ce que nous pouvons demander de mieux. En revanche, il nécessite souvent une validation par rapport à un calcul de référence coûteux car il peut être appliqué au-delà de son régime de validité. De plus, la séquence de calculs intermédiaires introduit un bon nombre d'options de calcul, aboutissant à de nombreuses solutions comme le nombre de toutes les combinaisons d'options possibles. Il s'ensuit que parfois le bon réglage d'option doit être choisi par un œil expert. D'autre part, le besoin d'un schéma de calcul aujourd'hui n'est pas évitable et il semble être quelque chose *intrinsèque* de l'approche déterministe, même pour un calcul de transport direct 3D comme nous le verrons plus loin.

L'approche déterministe nécessite la discrétisation de tout l'espace des phases du problème pour lequel l'équation de transport discrétisée est résolue. Cela signifie qu'une solution déterministe est trouvée la plupart du temps également dans des " régions " de l'espace des phases qui ne sont pas utiles pour les applications d'ingénierie, comme dit précédemment, ou qui ont une faible importance sur les quantités d'intérêt. Par contre, en analyse numérique, il est indispensable que la discrétisation du domaine soit suffisamment fine pour garantir à la fois la stabilité d'une méthode et la précision de la solution, qui ne doivent pas être affectées par des erreurs de troncature. En particulier, lorsqu'il s'agit de la discrétisation du domaine énergétique, le formalisme dit multigroupe, un code déterministe doit, tout d'abord, traiter et condenser les sections efficaces dépendant de l'énergie continue pour produire un ensemble de valeurs multigroupes. L'inconvénient de cette approche est que si l'on adopte des valeurs moyennes de groupe pour les sections efficaces multigroupes, alors le nombre de groupes d'énergie à utiliser pour représenter correctement les fonctions d'énergie de section efficace est

de l'ordre de plusieurs dizaines de milliers [2], et cela rendrait la démarche déterministe chevaleresque. Ceci est dû à deux raisons: le domaine énergétique à résoudre est très grand (une dizaine de décades en échelle logarithmique) et les sections efficaces des nucléides lourds sont généralement des fonctions piquées en énergie en raison de leur comportement résonnant à certaines énergies, ce qui nécessiterait groupes d'énergie très fins. En pratique, des valeurs de groupe efficaces au lieu de la moyenne sont utilisées pour résoudre l'équation de transport multigroupe, dont l'évaluation nécessite des calculs intermédiaires et l'introduction d'approximations constituant un modèle d'auto-protection, sans lequel la solution du modèle global du réacteur ne peut être précise.

L'autre approche utilisée pour résoudre un problème de transport est la voie stochastique, qui utilise l'intégration Monte Carlo pour simuler l'évolution de la population de particules dans un système et déterminer les quantités d'intérêt intégrées dans une partie de l'espace des phases. Cette approche est capable de trouver une solution dans le domaine de l'énergie continue sans approximations et pour toutes géométries compliquées. Ainsi, un code Monte Carlo est un outil puissant, également appliqué dans d'autres domaines que la physique des réacteurs, et il est considéré comme un code de référence pour les calculs de transport déterministes. Contrairement à ce dernier, il ne donne une solution que pour les quantités qu'il est demandé d'observer, et il peut appliquer des techniques qui obligent les particules à explorer des régions de l'espace des phases qui apportent plus de contribution à la solution, par exemple par un échantillonnage d'importance pendant la simulation, laissant d'autres régions largement inexplorées. Cependant, le taux de convergence de l'incertitude statistique sur la solution est en $1/\sqrt{N}$, où N est le nombre d'histoires simulées, ce qui fait de Monte Carlo une méthode chronophage avec des temps d'exécution qui ne sont pas pratiques à des fins de design industriel. De plus, développer des schémas de calcul qui utilisent des calculs stochastiques et emploient des approximations pour simplifier le problème global n'est pas dans l'esprit de Monte Carlo et ne sont jamais appliqués, sauf lorsque les calculs déterministes et stochastiques sont couplés dans un schéma de calcul hybride.

D'un autre côté, une solution de base entièrement déterministe peut être obtenue grâce à différents chemins basés soit sur une approche en deux étapes, soit sur une approche directe.
Les schémas de calcul classiques et largement utilisés pour l'analyse du cœur sont basés sur une approche en deux étapes, qui utilise la théorie de l'homogénéisation pour simplifier et réduire la taille du problème du réacteur complet. Il s'agit de la construction de bibliothèques pré-calculées contenant des sections efficaces homogénéisées, voire des matrices de réponse, qui sont déterminées avec des calculs de transport hors ligne séparés des motifs géométriques qui se trouvent dans un réacteur, comme les assemblages de combustible. L'idée fondamentale est de séparer l'échelle microscopique des phénomènes de transport locaux qui nécessitent des calculs détaillés, de celle macroscopique à l'échelle centrale. Les données homogénéisées sont stockées dans les bibliothèques pour différents paramètres physiques, tels que la température du combustible, la densité du modérateur, le burnup, etc., puis interpolées à l'état réel dans le cœur. La deuxième étape consiste en un calcul de cœur qui est effectué sur des maillages énergétiques et spatiales grossiers, en appliquant un opérateur d'ordre inférieur qui est

généralement un opérateur de diffusion 3D. Ce dernier est l'opérateur le plus simple qui puisse être dérivé par la théorie de transport en introduisant des approximations fortes qui rendent le calcul incroyablement plus rapide, mais aussi imprécis dans certaines conditions. Cette approche permet de prendre en compte des phénomènes physiques évoqués précédemment avec des temps d'exécution raisonnables, et elle ne donne qu'une information "condensée" de la solution, en fonction de la géométrie d'homogénéisation et du maillage énergétique grossier. Le prix à payer pour cette approche est une plage d'applicabilité limitée dictée par les approximations introduites au cours du schéma de calcul.

Par opposition à un calcul en deux étapes, l'autre approche est dite "directe" car elle permet de trouver une solution au problème du cœur complet en utilisant une information détaillée, comme pour la géométrie et les distributions isotopiques et de température, afin de reproduire les conditions réelles dans chaque crayon de combustible dans le cœur. Cependant, cette approche nécessite encore des calculs hors ligne pour l'auto-protection des sections efficaces qui sont généralement effectués sur des géométries 2D simplifiées au niveau de l'assemblage ou même sur des plans radiaux du cœur.
Supposons maintenant que les sections efficaces multigroupes soient données, un calcul direct peut également être effectué de différentes manières, et simplifié si nécessaire. Les calculs directs du cœur en régime stationnaire ont été réalisés par un opérateur de transport 3D, la méthode de fusion 2D/1D et, plus récemment, via la méthode d'homogénéisation dynamique.

La méthode d'homogénéisation dynamique est une nouvelle approche et fait l'objet de ce travail, qui vise à développer un schéma de calcul qui, d'une part, tire parti des avantages d'un schéma de calcul direct et, d'autre part, utilise certains des idées classiques qui sont particulières à une approche en deux étapes, afin de simplifier encore plus le problème du réacteur complet par rapport à la méthode de fusion. Le concept le plus important inspiré de l'approche classique est de séparer l'échelle microscopique des phénomènes de transport locaux de l'échelle macroscopique au niveau central, mais en introduisant un retour d'informations entre les deux échelles. Par conséquent, ici l'opérateur de transport fin n'a pas le rôle de solveur du problème, mais plutôt de générateur de paramètres d'homogénéisation pour l'opérateur grossier, qui peut avantageusement être la diffusion. D'autre part, l'homogénéisation dynamique diffère d'une approche classique par la manière dont les sections efficaces sont homogénéisées. Dans un schéma de calcul en deux étapes, le modèle d'homogénéisation d'un motif séparé ne peut pas avoir l'information sur l'environnement, qui n'est connue que dans la deuxième étape au niveau du cœur. Par conséquent, certaines hypothèses sur les fuites de neutrons sont nécessaires. Une approche directe, au contraire, a toujours ce type d'informations qui peuvent être utilisées en faveur d'un meilleur modèle d'homogénéisation qui tient compte de l'environnement réel. Le résultat est l'élimination de certaines approximations et une plus grande plage de validité par rapport à un calcul en deux étapes. La qualité de la solution d'homogénéisation dynamique dépend toujours de l'opérateur d'ordre inférieur appliqué au problème du cœur complet, à la différence qu'elle est construite en utilisant des sections efficaces homogénéisées améliorées ou, plus généralement, des paramètres d'homogénéisation. Ainsi, la méthode est un compromis qui peut se situer entre les calculs de transport

classique et direct en termes de précision et de performance, mais pour être faisable, comme nous le verrons plus loin, elle a encore besoin d'un cadre parallèle. Ces propriétés pourraient faire de la méthode un bon candidat capable de fonctionner dans les futures machines de bureau.

Organisation du document

Ce document est organisé en deux parties. La première décrit l'état de l'art des méthodes numériques et des schémas de calcul utilisés en théorie du transport neutronique dans le cadre de l'approche déterministe, tandis que la seconde partie concerne la méthode d'homogénéisation dynamique dans tous ses aspects: théorie, développement et application. La seconde partie constitue la contribution de ce travail.

La Partie I est divisé en trois chapitres.

Le Chapitre 1 présente les équations de transport et de diffusion et les grandeurs physiques nécessaires pour fournir les vitesses de réaction. Les principales méthodes numériques utilisées pour résoudre les équations de transport et de diffusion multigroupes dans les applications industrielles sont décrites dans le Chapitre 2. Quelques détails sont également donnés pour l'accélération de la convergence d'un calcul de transport. Ces méthodes constituent les outils et les briques d'un schéma de calcul. Certains d'entre eux, en fait, sont ensuite utilisés dans la Partie II pour le développement et les applications de la méthode d'homogénéisation dynamique. Par conséquent, ce chapitre définit la notation qui sera utilisée dans le reste du document.

Le Chapitre 3 introduit les techniques d'homogénéisation les plus courantes qui permettent de construire un opérateur d'ordre inférieur qui préserve les taux de réaction d'un problème d'homogénéisation de référence. Le schéma de calcul classique en deux étapes, qui est basé sur la théorie de l'homogénéisation, est illustré dans la deuxième partie de ce chapitre, mettant en évidence où les approximations sont employées et les limites de l'approche. Chaque brique qui compose la séquence de calculs pour cette approche est discutée: auto-protection, calcul réseau, modèle de fuites critiques, homogénéisation d'assemblage, équivalence et calcul cœur.
Aussi, la seconde partie du Chapitre 3 est consacrée aux schémas de calcul direct plus récents qui reposent sur le calcul haute performance: les calculs de transport 3D résolus par la méthode de décomposition de domaine, et la méthode de fusion 2D/1D basée sur intégration nodale transversale. Les approximations et les propriétés de stabilité de l'approche 2D/1D sont discutées à la fin du chapitre.

La Partie II est organisé en trois chapitres.

Le Chapitre 4 présente la méthode d'homogénéisation dynamique et décrit comment la méthode recherche un meilleur problème d'homogénéisation de référence pour produire les sections efficaces homogénéisées. Le processus itératif du schéma de calcul est décrit pour un cadre parallèle MPI. De plus, les techniques d'homogénéisation les plus populaires appliquées en physique des réacteurs sont révisées et adaptées pour les problèmes d'homogénéisation de référence avec fuites surfaciques non nulle, et nous montrons comment la méthode peut devenir une accélération non linéaire pour la convergence du problème de transport complet.

La théorie présentée dans ce chapitre sera utilisée à la fois dans les Chapitres **??**.

Le Chapitre 5 concerne l'application de la méthode d'homogénéisation dynamique dans une configuration de cœur 2D, et représente une étape préliminaire pour l'objectif réel de ce travail, qui est le calcul du cœur 3D.
Cette étape d'analyse vise à étudier certaines propriétés de la méthode, telles que la précision, le taux de convergence et les temps d'exécution dans le cas plus simple où les effets de transport axiaux ne sont pas présents. Nous avons exploré différentes options d'homogénéisation, telles que l'homogénéisation pin-by-pin ou sur maillage grossier, à travers des techniques de flux-volume, de théorie d'équivalence et de facteurs de discontinuité du flux.

Dans le Chapitre 6 nous redéfinissons le problème d'homogénéisation de référence pour une configuration de coeur 3D, en introduisant un modèle approché pour les fuites axiales. Ce modèle permet les points suivants: 1) de coupler les problèmes transport 2D avec ses voisins axiaux, afin de prendre en compte l'environnement axial; 2) de produire une source fictive qui alimente le calcul de transport pour le réflecteur axial; 3) de garder la cohérence entre les opérateurs de transport 2D et de diffusion 3D. Différentes configurations et options d'homogénéisation sont analysées pour le calcul du cœur 3D en termes de précision et de performances. En particulier, nous avons testé la méthode pour deux types de problèmes de cœur 3D: le cœur axialement uniforme et le cœur partiellement barré.

Le Chapitre 7 résume les problèmes rencontrés dans ce travail et les meilleures options dans un cadre d'homogénéisation dynamique pour les calculs de cœur 3D. Il conclut avec tous les avantages de la nouvelle méthodologie en termes de précision, de performances et de nouvelles possibilités de calcul pour des calculs de cœur plus précis, rapides et fiables. Une petite section est donnée pour les travaux futurs.

Introduction

General Context

A nuclear reactor is a complex system in which many physical phenomena of different nature take place and mutually influence each other. The engineering disciplines involved in the process of nuclear power production are numerous, among which reactor physics plays the core role of providing reaction rates to the other ones. A reaction rate is a consequence of the interactions between particles and matter. These interactions not only depend on the physical properties of the materials where the particles travel, such as density, temperature, geometrical information, isotopic composition, that are provided by the other disciplines, but also on the particle population that, via collisions, has a probability to generate an event of the reaction of interest. The latter is the object of study of reactor physics that has its roots in transport theory and describes the statistical nature of these interactions, introducing the concept of probability distribution of the occurrence of an event in the phase space of the system.

This approach was firstly adopted by Ludwig Boltzmann and it is well known as the statistical mechanics approach. However, because of neutron properties, the transport equation of these particles is indeed simplified with respect to the Boltzmann's kinetic equation of gases. This is due to the assumption that neutrons do not interact with each other, that is justified by the absence of coulomb interactions, since they do not have charge, and the much lesser density of the neutron gas with respect to the density of other materials in a nuclear reactor [1]. Thus, the neutron-neutron interactions are so rare that can be neglected and the Boltzmann equation turns into a linear equation. Moreover, photons are also neutral particles and they barely interact with each other for the same reason, so they obey the same physical law of neutrons even if they interact with matter differently.

The statistical mechanics approach allows to "bridge" macroscopic physical quantities of a system to microscopic ones that fluctuate around an average. For instance, one of the main macroscopic quantities of engineering interest is the power produced by the fission rates, that depend on the number of neutrons that collide a fissile nuclide and their probability to produce fission after collision, which is a function of the incident neutron energy. Neutrons are the protagonist particles taking part to the process of power generation in a nuclear reactor which is a self-sustained chain reaction process. Each fission event, in fact, not only produces two or more fission products

that are unstable fragments of the initial fissile nuclide, but also few neutrons which in turn generate other fission events, if the system they are traveling in is propitious. When the chain reaction is self-sustained the system is said *critical*, and for safety and design purposes a task of reactor physics is to solve a class of problems that are called criticality calculations. Another class of problems of engineering interest is the fixed source calculations where, unlike in criticality, the source of particles injected in the system is known and, as opposed to the fission source, does not depend on the system characteristics. The population of either neutrons or photons, solution of the transport equation for this type of problem, are especially required in the field of radiation shielding and protection.

Although the neutron transport equation is greatly simplified with respect to the Boltzmann equation, its solution in a complex system such a nuclear reactor is still very difficult to find for several reasons. First of all, a nuclear reactor is a very large heterogeneous system composed of different structural elements that contain a large variety of materials. Even if all components had a simple geometry, an analytical solution of the neutron transport equation would not be possible because of the fast change in the nuclear properties (cross sections) of the materials contained in the system. Secondly, the population of particles that is solution of the transport equation is a distribution changing in time and defined over the whole phase space of the problem that includes all possible states of the system, comprising the three-dimensional space domain, the two-dimensional angular domain and the energy domain. With the current machine capabilities, today we are able to perform a steady-state full core 3D transport calculation with the aid of high-performance computing and obtain a very detailed numerical solution. Very often, however, this fine information in space, angle and energy in such a large system is not very useful for engineering problems, and it is more used as reference calculation to validate approximate numerical models that are much faster and do not require extensive use of computational resources. What adds additional complications in a calculation of a reactor model is every physical phenomenon that causes a change in space and time of the characteristics of the system. Let us discuss the main industrial applications and purposes that concern this type of phenomena.

The fission events deplete the fuel contained in the system and the capture events transmute it. Thus, the materials contained in the system with which neutrons interact change in space and time as a consequence of power production or, more generally, irradiation. The latter generates the so called history effects that are irreversible and may later influence the behavior of the system itself with a characteristic time scale. The effects of fuel depletion, for instance, have a time scale of the order of hours or days. Another phenomenon that allows reactor controls is the delayed neutrons. A small part of neutrons generated by fission is emitted by the fission fragments called precursors which beta decay emitting a neutron some seconds later. This phenomenon has a shorter time scale with respect to depletion and it requires the evaluation of the space and time dependent sources of delayed neutrons. Moreover, the interactions of particles depend on the physical properties of the matter in which they collide, such as density and temperature, that are distribution functions defined within the system which depend on the power distribution produced by the system itself, resulting in a nonlinear multi-physics problem. This type of problems allows to take into account the reactivity feedback due to a change in the thermal-hydraulics properties of the system.

Also, a change in the temperature results in material expansions, that can be positive or negative, and, therefore, a change in the geometrical characteristics of the system.

Taking into account all of these phenomena increases the number of equations and degrees of freedom of a reactor model, which makes infeasible the determination of a numerical solution that exactly reproduces the actual situation in the whole core. Such a calculation would require, in fact, an enormous amount of computational resources that are not always available, and a simulation run-time too long for industrial applications and purposes. Therefore, an ensemble of approximations is typically introduced in reactor modeling that have a regime of validity and therefore of applicability.
A sequence of intermediary calculations with their own approximations that allows to achieve the final solution for the reactor problem in the framework of reactor physics is called calculation scheme. A calculation scheme is a double-edged sword because in one hand, if the approximations that are employed are small and have physical insight, the computation is fast and accurate at the same time, which is the best that we can ask. On the other hand, it often requires a validation against an expensive reference calculation because it might have been applied beyond its regime of validity. Moreover, the sequence of intermediary calculations introduces a good number of calculation options, resulting in many solutions as the number of all possible combinations of options. It follows that sometimes the good option setting should be chosen by an expert eye. On the other hand, the need of a calculation scheme today is not avoidable and it seems to be something *intrinsic* of the deterministic approach, even for a 3D direct transport calculation as we shall discuss later.

The deterministic approach requires the discretization of the whole problem phase space for which the discretized transport equation is solved. This means that a deterministic solution is found most of the time also in "regions" of the phase space that are not useful for engineering applications, as said earlier, or that have low importance on the quantities of interest. On the other hand, in numerical analysis it is indispensable that the domain discretization is fine enough to guarantee both the stability of a method and the precision of the solution, that should not be affected by truncation errors. In particular, when dealing with the discretization of the energy domain, the so called multigroup formalism, a deterministic code has, first of all, to process and condense the continuous energy dependent cross sections to produce a set of multigroup values. The inconvenient of this approach is that if one adopts group averaged values for the multigroup cross sections, then the number of energy groups that should be used in order to properly represent the cross section energy functions is of the order of many tens of thousands [2], that would make the deterministic approach quixotic. This is caused by two reasons: the energy domain that has to be resolved is very large (around ten decades in logarithmic scale) and the heavy nuclides cross sections are typically sharp functions in energy due to their resonant behavior at certain energies, that would require very thin energy groups. In practice, effective group values instead of average are used to solve the multigroup transport equation, whose evaluation requires intermediary calculations and the introduction of approximations constituting a resonance self-shielding model, without which the solution of the overall reactor model cannot be accurate.

The other approach used to solve a transport problem is the stochastic way, that uses Monte Carlo integration to simulate the evolution of the population of particles

in a system and determine the quantities of interest integrated in a part of the phase space. This approach is capable to find a solution in the continuous energy domain with no approximations and for any complicated geometry. Thus, a Monte Carlo code is a powerful tool, also applied in other fields than reactor physics, and it is considered as reference code for deterministic transport calculations. As opposed to the latter, it gives a solution only for those quantities it is asked to observe, and it can apply techniques that force particles to explore regions of the phase space that give more contribution to the solution by, for instance, importance sampling during the simulation, possibly leaving other regions largely unexplored. However, the convergence rate of the statistical uncertainty on the solution is in $1/\sqrt{N}$, where N is the number of simulated histories, which makes Monte Carlo a time-consuming method with run-times that are not practical for industrial design purposes. Moreover, developing calculation schemes that use stochastic calculations and employ approximations to simplify the full core problem is not in the spirit of Monte Carlo and are never applied, except when deterministic and stochastic calculations are coupled together in a hybrid calculation scheme that takes advantage from both approaches.

On the other hand, a fully deterministic core solution can be achieved through different paths that are based either on a two-step approach or a direct approach.
The classical and widely used calculation schemes for core analysis are based on a two-step approach, which makes use of homogenization theory to simplify and reduce the size of the full reactor problem. It involves the construction of pre-calculated libraries containing homogenized cross sections, or even response matrices, that are determined with separate offline transport calculations of the geometrical motifs that are found in a reactor, such as the fuel assemblies of cluster of assemblies. The ground idea is to separate the microscopic scale of local transport phenomena that require detailed calculations, from the macroscopic ones at the core scale. The homogenized data are stored in the libraries for different physical parameters, such as fuel temperature, moderator density, burnup, etc, and then interpolated to the actual state in the core. The second step consists in a core calculation that is performed on coarse energy and spatial meshes, applying a low-order operator that is typically a 3D diffusion operator. The latter is the simplest operator that can be derived by transport theory introducing some strong approximations that make the computation incredibly faster, but also inaccurate under certain conditions. This approach allows to account for the physical phenomena earlier discussed with reasonable run-times, and it gives only a "condensed" information of the solution, depending on the geometry of homogenization and the coarse energy mesh. The price to pay for this approach is a limited range of applicability dictated by the approximations that are introduced during the course of the calculation scheme.

As opposed to a two-step calculation, the other approach is said "direct" because it founds a solution for the full core problem using a detailed information, such as for the geometry and the isotopic and temperature distributions, in order to reproduce the actual conditions in each fuel pin in the core. However, this approach still requires some offline calculations for cross-section self-shielding that are typically performed on simplified 2D geometries at the assembly level or even on core radial planes.
Suppose now that the multigroup cross sections are given by a self-shielding model, a direct calculation can also be performed in different manners, and simplified where

necessary. Steady-state direct core calculations have been achieved by a 3D transport operator, the 2D/1D fusion method and, more recently, via the method of Dynamic Homogenization.

The results of 3D transport calculations have shown that this type of calculation scheme can be applied even in the most severe configurations without losing in accuracy, suggesting that a classical self-shielding model might be sufficient. A severe configuration arises when the system experiences strong gradients of the neutron flux that are not well predicted by a diffusion operator. These gradients can be generated by a non-uniform source distribution, or by the boundary conditions with vacuum, or by the presence of material heterogeneities that have very different nuclear properties, such as in presence of control rods, or different types of fuels that deplete differently, or at the periphery of the core next to the reflector. Most of the time, this approach relies on domain decomposition methods that can be massively parallelized [3], otherwise it would be impossible to perform. The 3D transport calculations are mainly penalized, in terms of computational cost, by the large number of regions contained in the spatial domain and the non-negligible number of operations that are needed to compute one single region.
Recently the 2D/1D fusion method has been applied [4] aiming to reduce the two factors aforementioned (number of regions and number of operations per regions). This approach takes advantage of the axially extruded geometries that are characteristic in water reactors, in order to achieve a solution with a "nearly transport accuracy". It applies a transverse integration to the 3D transport equation over a set of axial layers composing the 3D geometry, so as to obtain two equations: the first one is a 2D equation that is solved over the core radial plane per each axial layer, while the second one is a 1D equation that allows to determine approximate axial leakage and to couple the radial solutions. The method can be, then, naturally parallelized, where each 2D problem is a different task, as well as each 1D problem.
Both 3D transport calculations and the 2D/1D fusion method show excellent agreement with reference Monte Carlo calculations, but still remaining computationally impractical in the framework of multi-physics applications, core depletion calculations and time dependent problems.

Finally, the Dynamic Homogenization method is a novel approach and is the subject of this work, which aims to develop a calculation scheme that, in one hand, takes the advantages of a direct calculation scheme and, on the other hand, utilizes some of the classical ideas that are peculiar of a two-step approach, in order to simplify even further the full reactor problem with respect to the fusion method. The most important concept inspired by the classical approach is to separate the microscopic scale of local transport phenomena from the macroscopic scale at the core level, but introducing a feedback between the two scales. Therefore, here the fine transport operator has not the role of the problem solver, but rather of the generator of homogenization parameters for the coarse core operator, that advantageously can be the very fast diffusion. On the other hand, the dynamic homogenization differs from a classical approach in the way cross sections are homogenized. In a two-step calculation scheme the homogenization model of a separate motif cannot have the information on the environment, which is only known in the second step at the core level, therefore some assumptions on the neutron leakage are necessary. A direct approach, instead, always has this type of

information that can be used in favor of a better homogenization model that accounts for the actual environment. The result is the elimination of some approximations and a larger range of validity with respect to a two-step calculation. The quality of the solution of Dynamic Homogenization still depends on the low-order operator applied to the full core problem, with the difference that it is constructed using improved homogenized cross sections or, more generally, homogenization parameters. Thus, the method is a compromise that can lie between the classical and the direct transport calculations in terms of accuracy and performance, but to be feasible, as we shall see later, it still needs a parallel framework. These properties might make the method a good candidate capable to run in future desktop machines.

Organization of the document

This document is organized in two parts. The first one describes the state-of-the-art of numerical methods and calculation schemes used in neutron transport theory in the framework of the deterministic approach, while the second part the method of Dynamic Homogenization in all of its aspects: theory, development and application. The second part constitutes the contribution of this work.

Part I is divided in three chapters.

Chapter 1 presents the transport and diffusion equations and the physical quantities required to provide the reaction rates. The main numerical methods used to solve the multigroup transport and diffusion equations in industrial applications are described in Chapter 2. Some details are also given for the acceleration of the convergence of a transport calculation. These methods constitute the tools and the bricks of a calculation scheme. Some of them, in fact, are later used in Part II for the development and the applications of the method of Dynamic Homogenization. Therefore, this chapter fixes the notation that will be used in the rest of the document.

Chapter 3 introduces the most popular homogenization techniques that allow to construct a low-order operator that preserves the reaction rates of a reference homogenization problem. The classical two-step calculation scheme, which is based on homogenization theory, is illustrated in the second part of this chapter, highlighting where the approximations are employed and the limitations of the approach. Every single brick that composes the sequence of calculations for this approach is discussed: self-shielding, lattice calculation, critical leakage model, assembly homogenization, equivalence and core calculation.
Also, the second part of Chapter 3 is devoted to the more recent direct calculation schemes that rely on high-performance computing: the 3D transport calculations solved by the domain decomposition method, and the 2D/1D Fusion method based on transverse nodal integration. The approximations and the stability properties of the 2D/1D approach are discussed at the end of the chapter.

Part II is organized in three chapters.

Chapter 4 presents the method of Dynamic Homogenization and describes how the method seeks for a better reference homogenization problem for cross-section homogenization. The iterative process of the calculation scheme is described for an MPI

framework. Moreover, the most popular homogenization techniques applied in reactor physics are revised and adapted for reference homogenization problems that have non-zero surface leakage, and we show how the method can become a nonlinear acceleration for the convergence of the full transport problem.
The theory presented in this chapter will be used in both Chapters 5 and 6.

Chapter 5 concerns the application of the method of Dynamic Homogenization in a 2D core configuration, and it represents a preliminary step for the actual objective of this work, which is the 3D core calculation.
This analysis step aims to investigate on some properties of the method, such as accuracy, convergence rate and run-times in the simpler case where the axial transport effects are not present. We explored different homogenization options, such as the pin-by-pin or the coarse mesh homogenization, through flux-volume, equivalence theory and flux discontinuity factors techniques.

In Chapter 6 we redefine the reference homogenization problem for a 3D core configuration, by introducing an approximate model for the axial leakage. This model allows the following points: 1) to couple the 2D transport problems with its axial neighbors, in order to take into account the axial environment; 2) to produce a fictive source that feeds the transport calculation for the axial reflector; 3) to keep the consistency between 2D transport and 3D diffusion operators. Different configurations and homogenization options are analyzed for the 3D core calculation in terms of accuracy and performance. In particular, we tested the method for two types of 3D core problems: the axially uniform core and the partially rodded core.

Chapter 7 summarizes the problems encountered in this work and the best options in a dynamic homogenization framework for 3D core calculations. It concludes with all the advantages of the new methodology in terms of accuracy, performances and new computational possibilities for more accurate, fast and reliable core calculations. A small section is given for future work.

List of published material

- Antonio Galia, Richard Sanchez and Igor Zmijarevic, *A dynamic homogenization method for 3D core calculations*, Annals of Nuclear Energy, (Submitted October 2020).

- Antonio Galia, Richard Sanchez and Igor Zmijarevic, *A method of dynamic homogenization: application to 2D core calculation*, Annals of Nuclear Energy, Volume 151, 2021, 107774, ISSN 0306-4549, `https://doi.org/10.1016/j.anucene.2020.107774`.

- Antonio Galia, Igor Zmijarevic and Richard Sanchez, *3D core calculation based on the method of dynamic homogenization*, Proceedings of PHYSOR 2020, Cambridge, United Kingdom, April 2020.

- Antonio Galia, Igor Zmijarevic and Richard Sanchez, *2D core calculation based on the method of dynamic homogenization*, Proceedings of M&C 2019, Portland, OR, USA, August 2019.

Part I

State-of-the-Art of Deterministic Core Calculation

Chapter 1

Transport of Particles in Matter

This chapter presents the transport and diffusion equations and the physical quantities required to provide the reaction rates.

1.1 Cross sections

A cross section is defined as the probability that a specific event occurs when two particles interact. It is classically introduced supposing a beam of n particles per unit volume that travels at fixed relative velocity v_r with respect to a target surface that has small width ds and a number of nuclides per unit volume N of the same isotope. The number of reactions of type x per unit surface and unit time is observed to be proportional to the number of incident particles per unit surface and unit time (nv_r) and the number of nuclides per unit surface (Nds):

$$d\tau_x = \sigma_x \, N \, nv_r \, ds,$$

where $d\tau_x$ is the surface reaction rate of type x, and the proportionality constant σ_x is called microscopic cross section of a reaction x between two particles. The dimension of σ_x is an area and it is often interpreted as the quantity that expresses, figuratively speaking, "how large the target is seen by the incident particle". The bigger, the more chances they will interact to produce a reaction x.

The microscopic cross sections are functions of the relative velocity of the incident beam with respect to the target. Their values are tabulated in the reference situation where the target is at rest at 0 K. This is the situation where the relative velocity of the incident particles coincides with their actual velocity v. Suppose now that the absolute temperature T defines a velocity distribution of the target particles $p^T(v_t)$, where t stands for target and:

$$v_r = |v - v_t|.$$

In order to account for the effects of the thermal agitation, the cross sections values at 0 K $\sigma_x^0(v_r)$ can be replaced by average values $\sigma_x^T(v)$ in such a way that:

$$d\tau_x = \sigma_x^T(v) \, N \, nv \, ds, \tag{1.1}$$

where the average values are obtained by a convolution of the type:

$$\sigma_x^T(v) = \frac{1}{v} \int_\infty dv_t \; p^T(v_t) \, |v - v_t| \, \sigma_x^0(|v - v_t|).$$

It follows that the probability of a nuclear reaction is tabulated for the energy E of the incident particle ($E = \frac{1}{2}mv^2$) and for the temperature T of the target particle, due to the effect of the thermal agitation that is called Doppler effect. The latter has an important aspect in the stability analysis of a nuclear reactor, since it is responsible of a part of the thermal feedback, object of the study in multi-physics applications.

When a target material is a mixture of different isotopes i, it is practical to use a quantity that includes all of them, that is called macroscopic cross section Σ_x and it is

defined as:

$$\Sigma_x = \sum_i \Sigma_{x,i} = \sum_i \sigma_{x,i}^T N_i. \tag{1.2}$$

The dimension of the macroscopic cross section is $\frac{1}{cm}$ and it represents the probability per unit path for a particle to undergo reaction x in a material.

We now call *medium* a region in the space where the particle travels, that is characterized by a geometry, an isotopic distribution and a temperature profile. Then, a unique macroscopic cross section is associated to each medium in a system and it is a function of the position due to the varying composition and temperature. Very often in numerical simulations, it is assumed that each medium has uniform nuclear properties, resulting in a spatially constant macroscopic cross section.

The types of nuclear reactions are numerous and can be divided in absorption cross sections σ_a and scattering cross sections σ_s. The former include the types of reactions that make the particles disappear from the system, while the latter change the characteristics of the particle by, for instance, slowing it down or deviating the direction of its motion. The absorption typically includes the fission reaction (σ_f), that generates power, fission fragments and other neutrons, and the capture (σ_c), where other particles can be emitted, for instance in case of photons it is said radiative capture (σ_γ), due to the excited state of the nuclide after the capture. The scattering, instead, often includes the collision events that can be elastic or inelastic, and also spallation reaction ($\sigma_{\mathrm{n},x\mathrm{n}}$), that produces x secondary particles as a result of hitting a heavy nuclide with high-energy particles.

All the possible scattering events for an incident particle are described by a differential scattering cross section or transfer function $\Sigma_\mathrm{s}(E \to E', \mathbf{\Omega} \to \mathbf{\Omega}')$, that indicates the probability density function per unit path that a particle traveling around energy E and direction $\mathbf{\Omega}$ incurs into a collision event with the target particle and subsequently has an energy between E' and $E' + dE'$ and direction within $\mathbf{\Omega}'$ and $\mathbf{\Omega}' + d\mathbf{\Omega}'$.

The materials treated in reactor physics are typically isotropic for neutrons, which means that cross sections are independent of the incident direction of a particle and depends only on the angle of deviation of the incident particle whose cosine is $\mu_0 = \mathbf{\Omega} \cdot \mathbf{\Omega}'$. It follows that:

$$\Sigma_\mathrm{s}(E \to E', \mathbf{\Omega} \to \mathbf{\Omega}') = \frac{1}{2\pi}\Sigma_\mathrm{s}(E \to E', \mathbf{\Omega} \cdot \mathbf{\Omega}'), \tag{1.3}$$

where 2π takes into account all equally probable directions defined in a unit sphere that form an angle $\cos^{-1}(\mu_0)$ with $\mathbf{\Omega}$. At this point, the differential scattering cross section is generally expanded over a Legendre polynomial basis P_ℓ up to the scattering order L, in order to separate the energy and angular variables, such that:

$$\Sigma_\mathrm{s}(E \to E', \mu_0) \approx \sum_{\ell=0}^{L} \frac{2\ell+1}{2}\Sigma_{\mathrm{s}\ell}(E' \to E)P_\ell(\mu_0), \tag{1.4}$$

with

$$\Sigma_{s\ell}(E \to E') = \int_{-1}^{1} d\mu_0 \Sigma_s(E \to E', \mu_0) P_\ell(\mu_0). \tag{1.5}$$

For $L = 0$, the collision events are isotropic so the incident particle has a uniform probability to scatter in all directions, while for $L = 1$ the scattering is said linearly anisotropic, where $\frac{\Sigma_{s1}(E \to E')}{\Sigma_{s0}(E \to E')}$ is the average deviation cosine $\overline{\mu}_0$ of a particle scattering from E to an interval dE' around E'. For detailed transport calculations, in reactor physics the scattering order is generally up to five. The Legendre polynomials are defined by the relations:

$$P_0(\mu_0) = 1, \quad P_1(\mu_0) = \mu,$$
$$P_{\ell+1}(\mu_0) = \frac{1}{\ell+1}[(2\ell+1)\mu_0 P_\ell(\mu_0) - \ell P_{\ell-1}(\mu_0)], \ell > 0.$$

The total scattering macroscopic cross section $\Sigma_s(E)$ is the probability per unit path that a particle will scatter in any direction and energy after the collision, and it is obtained integrating Equation (1.4) in all the possible E' and μ_0:

$$\Sigma_s(E) = \int_0^\infty dE' \sum_{\ell=0}^{L} \Sigma_{s\ell}(E \to E') \int_{-1}^{1} d\mu_0 \frac{2\ell+1}{2} P_\ell(\mu_0) = \int_0^\infty dE' \Sigma_{s0}(E \to E').$$

In the last equation, the integration in $d\mu_0$ of the Legendre polynomials equals 0 except for P_0. From now on if not specified, we will refer to $\Sigma_s(E \to E', \mu_0)$ as transfer function if we consider it in terms of probability distribution defined in all energies and deviation cosines, and to $\Sigma_s(E)$ as scattering cross section.

The *total* macroscopic cross section is here indicated as Σ and it is equal to the sum of absorption and the scattering macroscopic cross sections:

$$\Sigma(E) = \Sigma_c(E) + \Sigma_f(E) + \Sigma_s(E),$$

thus it represents the probability per unit path that two particles collide, no matter which type of reaction. The inverse of this quantity is dimensionally a length corresponding to the average distance traveled by the particle in a medium without colliding, and it is called mean free path $l = \frac{1}{\Sigma}$.

It is often useful in reactor physics, especially in multigroup diffusion theory, to define a removal macroscopic cross section Σ_r that equals:

$$\Sigma_r = \Sigma - \Sigma_{s0}, \tag{1.6}$$

that represents the probability per unit path that the incident particle is "removed" from an energy group, which explains the omission of the energy dependency. This

cross section includes all the possible events except for the probability that a particle is deviated without changing its energy group. This event arises in case of elastic shock where the target nuclide keeps its average velocity unchanged, and it is said *self*-scattering, indicated here as Σ_{s0}. Moreover, the scattering event $E \to E'$ is said *down*-scattering if $E > E'$, and it is responsible of the neutron slowing down process, while it is said *up*-scattering if $E < E'$, that typically arises at low energies (thermal energy domain) where neutrons and nuclides are at the equilibrium and mutually exchange energy.

1.2 The Phase Space

Using a statistical mechanics approach, the transport equation describes how neutrons move in the phase space of the system. The phase space contains all possible states that a particle can have in the system, and it is generally the product of the position space V, containing the position vectors $\mathbf{r}$ with respect to a reference frame, and the momentum space containing the momentum vectors $\mathbf{p} = m\mathbf{v}$. Both of these spaces have three dimensions for a Cartesian reference frame, resulting in a six-dimensional phase space. However, in reactor physics the nuclear data are tabulated in energy, so it is advantageous to split the momentum space in an angular space such that $\mathbf{\Omega}$ is defined in the unit sphere, where $\mathbf{\Omega} = \frac{\mathbf{p}}{p}$ is the solid angle for a given direction, and the energy space such that $E \in [0, \infty[$, where $E = \frac{p^2}{2m}$.

We define here the position and the solid angle vectors as:

$$\mathbf{r} = x\mathbf{i} + y\mathbf{j} + z\mathbf{k}, \quad \mathbf{\Omega} = \Omega_x\mathbf{i} + \Omega_y\mathbf{j} + \Omega_z\mathbf{k},$$

where $\mathbf{i}$, $\mathbf{j}$, $\mathbf{k}$ are the Cartesian unit vectors, (x, y, z) is the coordinates vector and $(\Omega_x, \Omega_y, \Omega_z) = (\mu, \eta, \zeta)$ are the direction cosines with respect to the Cartesian axes such that:

$$\mu^2 + \eta^2 + \zeta^2 = 1.$$

The angle $\mathbf{\Omega}$ is defined in a unit sphere, and it is common to use two quantities to define it: the cosine of the polar angle $\mu \in [-1, 1]$ with respect to the x-axis, and the azimuth angle $\varphi \in [0, 2\pi]$ for all the directions in a radial plane yz, such that:

$$\mathbf{\Omega} = \begin{bmatrix} \mu \\ \sqrt{1-\mu^2}\cos\varphi \\ \sqrt{1-\mu^2}\sin\varphi \end{bmatrix}. \tag{1.7}$$

It is possible to show that:

$$\int_{4\pi} d\mathbf{\Omega}\Omega_i^n = \begin{cases} 0 & \text{if } n \text{ odd} \\ \frac{4\pi}{n+1} & \text{if } n \text{ even} \end{cases}, \quad \forall i \tag{1.8}$$

1.3 Neutron Flux and Current

The population density $n(\mathbf{r}, \mathbf{\Omega}, E, t)$ is a distribution of the number of particles in the phase space and a function of time, such that $n(\mathbf{r}, \mathbf{\Omega}, E, t)d\mathbf{r}d\mathbf{\Omega}dE$ is the total number of particles at time t, in the volume element $d\mathbf{r}$ around $\mathbf{r}$, in the solid angle element $d\mathbf{\Omega}$ with direction $\mathbf{\Omega}$ traveling with energy between E and $E + dE$. The characteristics of a medium are given in terms of probability per unit path (macroscopic cross sections), so it is useful to know the total distance traveled in one second by all of the particles contained in an element of the phase space $d\mathbf{r}d\mathbf{\Omega}dE$. This quantity is called *angular flux* and it is equal to the product of the population density and the module of their average velocity:

$$\psi(\mathbf{r}, \mathbf{\Omega}, E, t) = v(\mathbf{r}, E)n(\mathbf{r}, \mathbf{\Omega}, E, t), \tag{1.9}$$

and, for physical constraints, it is non-negative in any point $(\mathbf{r}, \mathbf{\Omega}, E)$ of the phase space. The number of reactions per unit time, unit volume and energy interval occurring around point $\mathbf{r}$ and energy E, is the result of the contributions of all the particles coming from any direction, and the quantity used to determine it, is the *scalar flux* defined as:

$$\phi(\mathbf{r}, E, t) = \int_{4\pi} d\mathbf{\Omega}\psi(\mathbf{r}, \mathbf{\Omega}, E, t). \tag{1.10}$$

Equation (1.1) can be rearranged for the volumetric distribution of the expected reaction rate occurring around energy E, using the definitions of Equations (1.2) and (1.9) and integrating in all directions:

$$\tau_x(\mathbf{r}, E, t) = \Sigma_x(\mathbf{r}, E)\phi(\mathbf{r}, E, t). \tag{1.11}$$

However, the actual information of engineering interest is rather the *total reaction rate* occurring in a volume V:

$$\tau_{x,V}(t) = \int_0^\infty dE \int_V d\mathbf{r}\, \Sigma_x(\mathbf{r}, E)\phi(\mathbf{r}, E, t) \tag{1.12}$$

It is important, also, to quantify the number of particles exiting and entering a control volume enclosed by its control surface. For a given surface element dS around $\mathbf{r}$ with

normal vector $\mathbf{n}$, the only particles crossing dS at the instant $t + dt$ are those that at the instant t were contained in the volume element $dS\mathbf{v}dt$, where $\mathbf{v}dt = \mathbf{\Omega}vdt$ is the displacement vector traced by the particles traveling with velocity v in the direction $\mathbf{\Omega}$ during the time interval dt:

$$\mathbf{\Omega}vn(\mathbf{r}, \mathbf{\Omega}, E, t)dt \cdot dS\mathbf{n}.$$

The quantity $\mathbf{j}(\mathbf{r}, \mathbf{\Omega}, E, t) = \mathbf{\Omega}\psi(\mathbf{r}, \mathbf{\Omega}, E, t)$ is called *angular current* and it is typically integrated in all the directions resulting in the net current vector:

$$\mathbf{J}(\mathbf{r}, E, t) = \int_{4\pi} d\mathbf{\Omega}\mathbf{\Omega}\psi(\mathbf{r}, \mathbf{\Omega}, E, t). \tag{1.13}$$

This vector has components that, in average, represent the preferential direction of the motion of particles, and a module that is equal to the net number of particles moving in that direction. Therefore, the scalar quantity $\mathbf{J}(\mathbf{r}, E, t) \cdot \mathbf{n}$ is simply called *net current* that indicates the net number of particles per unit time crossing a surface element with normal vector $\mathbf{n}$ around $\mathbf{r}$ with energy E at the instant t.

Very often we will refer to *partial currents* as the components of the net current that have *outgoing* (J^+) and *incoming* (J^-) directions with respect to the normal vector of a surface, such that:

$$J^+(\mathbf{r}, E, t) = \int_{2\pi} d\mathbf{\Omega}(\mathbf{\Omega} \cdot \mathbf{n})\psi(\mathbf{r}, \mathbf{\Omega}, E, t), \quad \mathbf{\Omega} \cdot \mathbf{n} > 0, \tag{1.14}$$

$$J^-(\mathbf{r}, E, t) = -\int_{2\pi} d\mathbf{\Omega}(\mathbf{\Omega} \cdot \mathbf{n})\psi(\mathbf{r}, \mathbf{\Omega}, E, t), \quad \mathbf{\Omega} \cdot \mathbf{n} < 0, \tag{1.15}$$

and

$$\mathbf{J}(\mathbf{r}, E, t) \cdot \mathbf{n} = J(\mathbf{r}, E, t) = J^+(\mathbf{r}, E, t) - J^-(\mathbf{r}, E, t). \tag{1.16}$$

Note that, as for the angular flux, the scalar flux and the partial currents are always non-negative quantities in any point $(\mathbf{r}, E)$, while the net current can assume any value.

1.4 Transport Equation for Neutrons

The transport equation describes how the balance of particles in each point of the phase space $(\mathbf{r}, \mathbf{\Omega}, E)$ changes in time. In reactor physics, the main assumptions that are generally adopted are the following:

- Neutrons do not interact with each other, justified by the nearly absence of force fields and the much lesser density of the neutron gas with respect to that of the materials, making the probability per unit path to interact with other neutrons so small that the event is rare and can be neglected;
- The neutrons are modeled as points moving along straight lines called free paths,

that are defined as the distance between two collision points and are much larger than the neutron size;

- The materials are isotropic in space;

- The nuclides are in thermal equilibrium with their neighbors.

To construct the neutron transport equation, we generally adopt an Eulerian approach, so we observe an element $d\mathbf{r}d\mathbf{\Omega}dE$ of the phase space, centered in the position $\mathbf{r}$, solid angle $\mathbf{\Omega}$ and energy E, we call it $A(\mathbf{r}, \mathbf{\Omega}, E)$, and see how the number of particles changes in it during a time interval dt between the instants t and $t+dt$. This variation is expressed as:

$$[n(\mathbf{r}, \mathbf{\Omega}, E, t+dt) - n(\mathbf{r}, \mathbf{\Omega}, E, t)]d\mathbf{r}\mathbf{\Omega}dE.$$

We now consider all the events for which the particles are emitted in $A(\mathbf{r}, \mathbf{\Omega}, E)$. We define $S(\mathbf{r}, \mathbf{\Omega}, E, t)$ an *external source* density that provides the number of particles emitted in $A(\mathbf{r}, \mathbf{\Omega}, E)$ per unit volume, unit solid angle and unit energy element at time t. The total number of emitted particles in the time interval dt is then:

$$S(\mathbf{r}, \mathbf{\Omega}, E, t)d\mathbf{r}d\mathbf{\Omega}dEdt.$$

Neutrons can also be emitted in $A(\mathbf{r}, \mathbf{\Omega}, E)$ through scattering events, for which any particle traveling with all possible energies and directions around $\mathbf{r}$ may have a probability to scatter into $A(\mathbf{r}, \mathbf{\Omega}, E)$. The contribution of *the scattering source* in the variation of the number of particles is given by the number of scattering events:

$$\int_{4\pi} d\mathbf{\Omega}' \int_0^\infty dE'\, \Sigma_\mathrm{s}(\mathbf{r}, E' \to E, \mathbf{\Omega} \cdot \mathbf{\Omega}')\psi(\mathbf{r}, \mathbf{\Omega}', E', t)\, d\mathbf{r}d\mathbf{\Omega}dEdt,$$

where we have used the isotropic material assumption. The *fission source* is the other responsible, of major interest, involved in the neutron production process. Its contribution to $A(\mathbf{r}, \mathbf{\Omega}, E)$ is the following:

$$\sum_i \frac{\chi_i(\mathbf{r}, E)}{4\pi} \int_{4\pi} d\mathbf{\Omega}' \int_0^\infty dE'\, \nu\Sigma_{\mathrm{f},i}(\mathbf{r}, E')\psi(\mathbf{r}, \mathbf{\Omega}', E', t)\, d\mathbf{r}d\mathbf{\Omega}dEdt.$$

In the last equation, $\nu_i(E')$ is the average number of neutrons produced by the fission of an isotope i and it depends on the incident particle energy. Very often in numerical simulation it is stored together with the fission macroscopic cross section as a unique cross section $\nu\Sigma_\mathrm{f}$. The neutrons produced by fission are typically modeled isotropically, resulting in a uniform probability of emission in angle equal to $\frac{1}{4\pi}$, and distributed in energy according to a fission spectrum $\chi_i(E)$, that is characteristic of each fissionable isotope and supposed independent of the energy of the incident particles, except for very high energies. As for the energy distribution, the fission spectrum is normalized to one.

On the other hand, the events for which particles disappear from the element $A(\mathbf{r}, \mathbf{\Omega}, E)$ are the absorption, any type of scattering to another element of the phase space, and the spatial leakage from the volume element $d\mathbf{r}$. The first two can be summarized by the probability to have a collision of any type, thus the number of collisions contributing to the variation of particles is:

$$\Sigma(\mathbf{r}, E)\psi(\mathbf{r}, \mathbf{\Omega}, E, t)\, d\mathbf{r}d\mathbf{\Omega}dEdt.$$

The loss due to the leakage is expressed by the angular current crossing all the surfaces of the volume of $A(\mathbf{r}, \mathbf{\Omega}, E)$:

$$\mathbf{\Omega}\psi(\mathbf{r}, \mathbf{\Omega}, E, t)d\mathbf{\Omega}dEdt \cdot dS\mathbf{n},$$

which can be advantageously expressed as:

$$\nabla \cdot \mathbf{\Omega}\psi(\mathbf{r}, \mathbf{\Omega}, E, t)d\mathbf{r}d\mathbf{\Omega}dEdt,$$

applying the divergence theorem to the element $d\mathbf{r}$. Because the angular variable does not depend on space, it is possible to substitute $\nabla \cdot \mathbf{\Omega}\psi = \mathbf{\Omega} \cdot \nabla\psi$, such that the leakage from the element $A(\mathbf{r}, \mathbf{\Omega}, E)$ is:

$$\mathbf{\Omega} \cdot \nabla\psi(\mathbf{r}, \mathbf{\Omega}, E, t)d\mathbf{r}d\mathbf{\Omega}dEdt.$$

In order to preserve the balance of neutrons in $A(\mathbf{r}, \mathbf{\Omega}, E)$ at each instant t, the variation of the population in the interval dt must equal:

$$\text{Population Variation} = -\,\textbf{Loss} + \textbf{Emission}.$$

Putting together all the previous contributions for the losses and the emissions in the last equation, dividing by $d\mathbf{r}d\mathbf{\Omega}dEdt$ both sides of the equation and taking the limit as $dt \to 0$, the neutron transport equation reads:

$$\begin{aligned}\frac{1}{v(\mathbf{r}, E)}\frac{\partial\psi(\mathbf{r}, \mathbf{\Omega}, E, t)}{\partial t} = &-\mathbf{\Omega} \cdot \nabla\psi(\mathbf{r}, \mathbf{\Omega}, E, t) - \Sigma(\mathbf{r}, E)\psi(\mathbf{r}, \mathbf{\Omega}, E, t) \\ &+ \int_{4\pi} d\mathbf{\Omega}' \int_0^\infty dE'\, \Sigma_{\mathrm{s}}(\mathbf{r}, E' \to E, \mathbf{\Omega} \cdot \mathbf{\Omega}')\psi(\mathbf{r}, \mathbf{\Omega}', E', t) \\ &+ \sum_i \frac{\chi_i(\mathbf{r}, E)}{4\pi} \int_0^\infty dE'\, \nu\Sigma_{\mathrm{f},i}(\mathbf{r}, E')\phi(\mathbf{r}, E', t) \\ &+ S(\mathbf{r}, \mathbf{\Omega}, E, t),\end{aligned} \tag{1.17}$$

where we have substituted $n(\mathbf{r}, \mathbf{\Omega}, E, t) = \frac{1}{v(\mathbf{r},E)}\psi(\mathbf{r}, \mathbf{\Omega}, E, t)$.

Equation (1.17) is the integrodifferential form of the neutron transport equation, which is a first-order differential equation with respect to space and time. It requires one initial condition such that:

$$\psi(\mathbf{r}, \mathbf{\Omega}, E, t = 0) = \psi_0(\mathbf{r}, \mathbf{\Omega}, E), \tag{1.18}$$

and one boundary condition such that:

$$\psi^-(\mathbf{r_b}, \mathbf{\Omega}_{\text{in}}, E, t) = \beta(\mathbf{r_b}' \to \mathbf{r_b}, \mathbf{\Omega}_{\text{out}} \to \mathbf{\Omega}_{\text{in}})\psi^+(\mathbf{r_b}', \mathbf{\Omega}_{\text{out}}, E, t) + \psi_{\text{in}}(\mathbf{r_b}, \mathbf{\Omega}_{\text{in}}, E, t), \tag{1.19}$$

where $\mathbf{b}$ stands for boundaries of the spatial domain or control surface, $\mathbf{\Omega}_{\text{in}}$ and $\mathbf{\Omega}_{\text{out}}$ are respectively any incoming direction such that $\mathbf{\Omega} \cdot \mathbf{n}(\mathbf{r_b}) < 0$ and any outgoing direction such that $\mathbf{\Omega} \cdot \mathbf{n}(\mathbf{r_b}) > 0$, and β is the albedo parameter that accounts for any albedo boundary condition. In the latter, the incoming angular flux is a function of the outgoing angular flux at position $\mathbf{r_b}'$, like in the case of periodic boundary condition. For the particular case of vacuum boundary condition, the parameter β equals zero, and one can impose ψ_{in} as an incoming boundary source which does not depend on the angular flux of the system, so it is considered as an external source.

In reactor physics, most of the time any problem can be simplified so as to solve, once or several times, the steady-state transport equation, because in time-dependent problems the angular flux of the previous time step can be seen as a term of emission source for the following step. We rewrite here the steady-state transport problem using a compact form:

$$\begin{cases} L\psi = H\psi + F\psi + S \\ \\ \psi^- = \beta\psi^+ + \psi_{\text{in}}, \quad \mathbf{r_b} \in \partial V \end{cases} \tag{1.20}$$

where the loss operator includes the leakage and collision terms as $L = (\mathbf{\Omega} \cdot \nabla + \Sigma)$, H and F are respectively the scattering and fission source operators, S is the external source and V is the control volume of the system.

Equation (1.20) is employed to solve a class of problems with an external source, where external means that it does not depend on the system properties, and they are called *fixed source problems*. If the system is not multiplicative, typical of shielding calculations, the equation reduces to $(L - H)\psi = S$.
In *criticality problems*, instead, the fission is the only type of source that injects neutrons in the system, thus the transport equation turns into a homogeneous equation: $(L-H-F)\psi = 0$. Aside the trivial solution $\psi = 0$, we seek for the non-trivial solution solving the eigenvalue problem $B\psi = k\psi$, with k the largest eigenvalue of the operator $B = (L - H)^{-1}F$, which is a real number and it is associated to the fundamental solution that is the only eigensolution with a physical meaning (real non-negative). This value is called effective multiplication constant k_{eff} and it represents the quantity that

should divide to the fission source in order to obtain a steady-state solution:

$$\begin{cases} (L-H)\psi = \frac{1}{k_{\text{eff}}} F\psi \\ \psi^- = \beta\psi^+ + \psi_{\text{in}}, \quad \mathbf{r_b} \in \partial V \end{cases} \tag{1.21}$$

We now define the operator $\langle w, \cdot \rangle$ the integration over the whole phase space of a distribution, weighted by a function w, such that:

$$\langle w, f \rangle = \int_V d\mathbf{r} \int_{4\pi} d\mathbf{\Omega} \int_0^\infty dE\, w(\mathbf{r}, \mathbf{\Omega}, E) \cdot f(\mathbf{r}, \mathbf{\Omega}, E), \tag{1.22}$$

where f is the given distribution. We now apply this operator to Equation (1.21) with constant $w = 1$, even if one is free to choose other types of functions, so that the multiplication constant can be defined as:

$$k_{\text{eff}} = \frac{\mathbf{F}}{\mathbf{A} + \mathbf{J}^+ - \mathbf{J}^-}, \tag{1.23}$$

where $\mathbf{F} = \langle 1, \nu\Sigma_{\text{f}}\psi \rangle$ is the total number of neutrons produced by the fission source in the whole domain, $\mathbf{A} = \langle 1, \Sigma_{\text{a}}\psi \rangle$ is the total number of absorptions and $\mathbf{J}^+ - \mathbf{J}^- = \langle 1, \mathbf{\Omega} \cdot \nabla\psi \rangle$ is the total leakage of neutrons from the domain. Note that scattering has an impact to particle distribution in the phase space, but it does not contribute to particle balance, since neutrons are not produced or lost by collision events. It ensues, that k_{eff} is the ratio between the total number of emitted particles and the total number of lost particles, and it is constant everywhere in the phase space of the system.

The problem in Equation (1.21) is solved using the power iteration method, that consists in an iterative process between right and left sides of the equation, in order to find the solution associated to the greatest eigenvalue. The right side is calculated with the solution ψ^n of the previous iteration n, and then used as fixed source to solve the transport problem at the iteration $n+1$:

$$(L-H)\psi^{n+1} = \frac{1}{k_{\text{eff}}^n} F\psi^n, \tag{1.24}$$

where the eigenvalue is $k_{\text{eff}}^{n+1} = \frac{\langle w, F\psi^{n+1} \rangle}{\langle w, (L-H)\psi^{n+1} \rangle}$, but it is rather updated according to the following equation:

$$k_{\text{eff}}^{n+1} = k_{\text{eff}}^n \frac{\langle w, F\psi^{n+1} \rangle}{\langle w, F\psi^n \rangle}, \tag{1.25}$$

where we have used Equation (1.24).

The norm of the solution is generally dictated by a design parameter, like the total

power P produced by the system such that:

$$P = \langle 1, E_{\mathrm{f}} \Sigma_{\mathrm{f}} \psi \rangle, \tag{1.26}$$

where E_{f} is the energy released by one fission event, and for U^{235} has an average value of $200MeV$. Another design parameter could be a limit for the highest peak of fission rates such that:

$$\tau_{\mathrm{f}}(\mathbf{r}) < \tau_{\mathrm{f}}^{\max}, \quad \forall \mathbf{r} \in V. \tag{1.27}$$

1.5 Treatment of the Scattering Source

The assumption of isotropic materials, and the representation of the differential scattering cross section with an expansion of Legendre polynomials for the scattering cross sections, presented in Equation (1.5), leads to a scattering source of the following form:

$$(H\psi)(\mathbf{r}, \mathbf{\Omega}, E) = \int_0^\infty dE' \sum_{\ell=0}^{L} \frac{2\ell+1}{4\pi} \Sigma_{\mathrm{s}\ell}(E' \to E) \int_{4\pi} d\mathbf{\Omega}' P_\ell(\mathbf{\Omega}' \cdot \mathbf{\Omega}) \psi(\mathbf{r}, \mathbf{\Omega}', E'). \tag{1.28}$$

In order to compute the integral in $d\mathbf{\Omega}'$ of the last equation, we take advantage of the spherical harmonics properties, and in particular of the Legendre addition theorem which states that:

$$P_\ell(\mathbf{\Omega}' \cdot \mathbf{\Omega}) = \sum_{m=-\ell}^{\ell} Y_{\ell,m}(\mathbf{\Omega}) Y_{\ell,m}(\mathbf{\Omega}'), \tag{1.29}$$

where $Y_{\ell,m}$ are the real spherical harmonics, obtained with the Ferrer definition as follows:

$$Y_{\ell,m}(\mathbf{\Omega}) = N_\ell^m P_\ell^{|m|}(\mu) T_m(\varphi), \tag{1.30}$$

where N_ℓ^m is a normalization constant:

$$N_\ell^m = \sqrt{\frac{(\ell - |m|)!}{(\ell + |m|)!}}, \tag{1.31}$$

$P_\ell^{|m|}$ are the associated Legendre functions defined in terms of Legendre polynomials:

$$P_\ell^{|m|}(\mu) = (1-\mu^2)^{m/2} \frac{d^m}{d\mu^m} P_\ell(\mu), \quad m \geq 0 \tag{1.32}$$

and

$$T_m(\varphi) = \begin{cases} \sqrt{2}\cos(m\varphi), & m > 0 \\ 1, & m = 0 \\ \sqrt{2}\sin(-m\varphi), & m < 0 \end{cases} \tag{1.33}$$

. The orthogonal functions earlier defined are normalized as follows:

$$\int_{2\pi} d\varphi T_m(\varphi) T_{m'}(\varphi) = 2\pi\delta_{mm'}, \tag{1.34}$$

$$\int_{-1}^{1} d\mu P_\ell^m(\mu) P_{\ell'}^m(\mu) = \frac{2(\ell+m)!}{(2\ell+1)(\ell-m)!}\delta_{\ell\ell'}, \tag{1.35}$$

which produces the following real spherical harmonics normalization:

$$\int_{4\pi} d\mathbf{\Omega} Y_{\ell,m}(\mathbf{\Omega}) Y_{\ell',m'}(\mathbf{\Omega}) = \frac{4\pi}{2\ell+1}\delta_{\ell\ell'}\delta_{mm'}. \tag{1.36}$$

There exists several definitions for the spherical harmonics, but the one that we presented has the advantage to deal with only real functions and to simplify the low-order angular expansions yielding:

$$Y_{0,0} = 1, \quad Y_{1,0} = \Omega_x, \quad Y_{1,1} = \Omega_y, \quad Y_{1,-1} = \Omega_z. \tag{1.37}$$

We can then represent the angular distribution of the flux, defined over a unit sphere, with an expansion of spherical harmonics approximated to the L-order:

$$\psi(\mathbf{r}, \mathbf{\Omega}, E) = \sum_{\ell=0}^{L} \frac{2\ell+1}{4\pi} \sum_{m=-\ell}^{\ell} \phi_{\ell,m}(\mathbf{r}, E) Y_{\ell,m}(\mathbf{\Omega}), \tag{1.38}$$

where $\phi_{\ell,m}$ are the *angular moments* of the neutron flux such that:

$$\phi_{\ell,m}(\mathbf{r}, E) = \int_{4\pi} d\mathbf{\Omega} Y_{\ell,m}(\mathbf{\Omega}) \psi(\mathbf{r}, \mathbf{\Omega}, E). \tag{1.39}$$

Using Equation (1.39) and according to Equation (1.36), the first angular moments associated to $\ell = 0$ and $\ell = 1$ correspond respectively to the scalar flux and the net current:

$$\phi(\mathbf{r}, E) = \phi_{0,0}(\mathbf{r}, E), \quad \mathbf{J}(\mathbf{r}, E) = \phi_{1,0}(\mathbf{r}, E)\mathbf{i} + \phi_{1,1}(\mathbf{r}, E)\mathbf{j} + \phi_{1,-1}(\mathbf{r}, E)\mathbf{k} \tag{1.40}$$

Finally, the scattering source is indeed simplified substituting Equations (1.29) and (1.39) into Equation (1.28), such that:

$$(H\psi)(\mathbf{r},\mathbf{\Omega},E) = \int_0^\infty dE' \sum_{\ell=0}^{L} \frac{2\ell+1}{4\pi}\Sigma_{\mathrm{s}\ell}(E'\to E)\sum_{m=-\ell}^{\ell} Y_{\ell,m}(\mathbf{\Omega})\phi_{\ell,m}(\mathbf{r},E'). \tag{1.41}$$

1.6 Transport Correction

In reactor physics the computation of high-order moments of the scattering source may have a non-negligible extra-cost. It is then common to introduce an approximation for the effects of anisotropic scattering, by correcting the self-scattering macroscopic cross sections, so as to minimize the error due to the absence of the higher-order moments of the scattering source. As consequence the total cross section is also corrected. We express the corrected cross sections as:

$$\Sigma^*(E) = \Sigma(E) - \Delta(E), \quad \Sigma^*_{\mathrm{s}\ell}(E'\to E) = \Sigma_{\mathrm{s}\ell}(E'\to E) - \Delta(E)\delta(E'-E), \tag{1.42}$$

where both cross sections have the same correction $\Delta(E)$, due to the definition of the total cross section $\Sigma = \Sigma_{\mathrm{a}} + \Sigma_{\mathrm{s}}$, which leads to $\Sigma^* = \Sigma_{\mathrm{a}} + \Sigma^*_{\mathrm{s}}$. In order to determine $\Delta(E)$, we follow the approach adopted by S. Choi *et al* in [5], and we write the steady-state one-dimensional transport equation with scattering order $L+1$, omitting the variable x:

$$\begin{aligned}\mu\frac{d\psi(\mu,E)}{dx} + \Sigma(E)\psi(\mu,E) &= S(\mu,E) \\ &+ \sum_{\ell=0}^{L+1}\frac{2\ell+1}{2}P_\ell(\mu)\int_0^\infty dE'\Sigma_{\mathrm{s}\ell}(E'\to E)\phi_\ell(E'),\end{aligned} \tag{1.43}$$

where S contains all the other types of sources, and the 1D equation has been obtained integrating over the azimuth angle the 3D equation and assuming planar symmetry, thus applying the operator $\int_{2\pi} d\varphi\cdot$. We now use the spherical harmonics expansion for the flux, presented in Equation (1.38), to rewrite the collision term using the definition of Dirac delta as follows:

$$\begin{aligned}\Sigma(E)\psi(\mu,E) &= \sum_{\ell}^{L+1}\frac{2\ell+1}{2}P_\ell(\mu)\Sigma(E)\phi_\ell(E) = \\ &= \int_0^\infty dE'\sum_{\ell}^{L+1}\frac{2\ell+1}{2}P_\ell(\mu)\Sigma(E')\phi_\ell(E')\delta(E'-E)\end{aligned}$$

and then we move the collision term in the last form into the scattering kernel of the right side of Equation (1.43) :

$$\mu\frac{d\psi(\mu,E)}{dx} = S(\mu,E) + \sum_{\ell=0}^{L+1}\frac{2\ell+1}{2}P_\ell(\mu)\int_0^\infty dE'[\Sigma_{s\ell}(E'\to E) - \Sigma(E)\delta(E'-E)]\phi_\ell(E'),$$

and, then we add the term $\Sigma^*(E)\psi(\mu,E)$ to both sides of the equation:

$$\mu\frac{d\psi(\mu,E)}{dx} + \Sigma^*(E)\psi(\mu,E) = S(\mu,E)$$
$$+\sum_{\ell=0}^{L+1}\frac{2\ell+1}{2}P_\ell(\mu)\int_0^\infty dE'[\Sigma_{s\ell}(E'\to E) - (\Sigma(E)-\Sigma^*(E))\delta(E'-E)]\phi_\ell(E'),$$

where, because of the $\delta(E'-E)$, only the moments of the self-scattering are concerned by the manipulation. The last equation is equivalent to Equation (1.43) and preserves the same particle balance. This can be seen by simply imposing $\Sigma = \Sigma^*$. We now truncate the expansion for the scattering source to the order L to obtain the corrected P_L^* equation:

$$\mu\frac{d\psi(\mu,E)}{dx} + \Sigma^*(E)\psi(\mu,E) = S(\mu,E) + \sum_{\ell=0}^{L}\frac{2\ell+1}{2}P_\ell(\mu)\int_0^\infty dE'\Sigma^*_{s\ell}(E'\to E)\phi_\ell(E'),$$

and we look for a definition of the transport correction that minimizes the error:

$$\frac{2L+3}{2}P_{L+1}(\mu)\int_0^\infty dE'[\Sigma_{s(L+1)}(E'\to E) - \Delta(E)\delta(E'-E)]\phi_{L+1}(E'),$$

which can be reduced to zero if:

$$\Delta(E) = \frac{\int_0^\infty dE'\Sigma_{s(L+1)}(E'\to E)\phi_{L+1}(E')}{\phi_{L+1}(E)}. \tag{1.44}$$

The inconvenient of Equation (1.44) is that one has to know a priori the angular moment of order $L+1$, which is never the case, except if a finer transport calculation is performed previously. At this point, the most common approximations that are introduced in order to compute the transport correction are the inflow [5], the diagonal and the outflow [6] corrections. The former [5] supposes a flux shape of the form

$\phi_\ell(x,E) = \phi_\ell(E)e^{iBx}$, so as to obtain a relation for the angular moments using the P_N equations. The moments of order $L+1$ are determined iteratively as a function of lower-order moments, and then used to compute the inflow transport correction with Equation (1.44).

The diagonal correction is the simplest and the most inaccurate because it neglects all the in-scatter contributions in Equation (1.44) as if the problem was monokinetic, resulting in:

$$\Delta(E) \approx \Sigma_{\mathrm{ss}(L+1)}(E). \tag{1.45}$$

The outflow transport correction, instead, assumes that:

$$\int_0^\infty dE'\Sigma_{\mathrm{s}(L+1)}(E' \to E)\phi_{L+1}(E') \approx \phi_{L+1}(E)\int_0^\infty dE'\Sigma_{\mathrm{s}(L+1)}(E \to E'),$$

which has shown to be a good approximation [2] for $L = 0$, and offers the advantage of simplifying Equation (1.44) into:

$$\Delta(E) \approx \int_0^\infty dE'\Sigma_{\mathrm{s}(L+1)}(E \to E'), \tag{1.46}$$

therefore, it does not require the knowledge of the angular moments and it is the most popular correction used in reactor physics.
In the particular case of $L = 0$, the transport corrected total macroscopic cross section Σ^* is simply called *transport cross section* and it equals:

$$\Sigma_{tr}(E) = \Sigma(E) - \int_0^\infty dE'\Sigma_{\mathrm{s1}}(E \to E'). \tag{1.47}$$

1.7 Diffusion Equation

The diffusion equation can be obtained by transport theory in different ways. This equation is also a balance of particles but some approximations are introduced. In diffusion theory it is assumed that the neutron flux is *linearly anisotropic* and the media have up to linearly anisotropic scattering law. However, especially in multigroup diffusion calculations it is practical use to suppose *isotropic scattering* source. Because of the neutron flux assumption, the expansion of Equation (1.38) is truncated to $\ell = 1$ such that:

$$\psi(\mathbf{r},\mathbf{\Omega},E) = \frac{1}{4\pi}[\phi_{0,0}(\mathbf{r},E) + 3\sum_{m=-1}^{1}\phi_{1,m}(\mathbf{r},E)Y_{1,m}(\mathbf{\Omega})],$$

that, using Equations 1.40, can be written as:

$$\psi(\mathbf{r},\mathbf{\Omega},E) = \frac{1}{4\pi}[\phi(\mathbf{r},E) + 3\mathbf{\Omega}\cdot\mathbf{J}(\mathbf{r},E)]. \tag{1.48}$$

We now substitute the last definition into the left side of the steady-state transport equation in (1.21), omitting the dependency $(\mathbf{r}, E)$ of ϕ and $\mathbf{J}$:

$$\frac{1}{4\pi}\mathbf{\Omega}\cdot\nabla(\phi+3\mathbf{\Omega}\cdot\mathbf{J})+\frac{\Sigma}{4\pi}(\phi+3\mathbf{\Omega}\cdot\mathbf{J}) = \frac{1}{4\pi}\left[\sum_i \Omega_i[\frac{\partial\phi}{\partial x_i}+3\Omega_i\frac{\partial J_i}{\partial x_i}]\right]+\frac{\Sigma}{4\pi}(\phi+3\sum_i \Omega_i J_i)$$

where the sum over i means in all axes. The scattering source is by assumption isotropic, resulting in:

$$(H_0\psi)(\mathbf{r},\mathbf{\Omega},E) = \frac{1}{4\pi}\int_0^\infty dE'\Sigma_{s0}(E'\to E)\phi(\mathbf{r},E'), \tag{1.49}$$

where the expansion has been truncated to $\ell = 0$. The equation can now be rewritten as follows:

$$\frac{1}{4\pi}\left[\sum_i[\Omega_i\frac{\partial\phi}{\partial x_i}+3\Omega_i^2\frac{\partial J_i}{\partial x_i}]\right]+\frac{\Sigma}{4\pi}(\phi+3\sum_i\Omega_i J_i) = H_0\psi+F\psi+S, \tag{1.50}$$

In order to eliminate the angular dependency in favor of an equation for the scalar flux, we integrate Equation (1.50) in angle applying the operator $\int_{4\pi} d\mathbf{\Omega}\cdot$, so as to obtain the so called P_0 equation:

$$\nabla\cdot\mathbf{J}(\mathbf{r},E)+\Sigma\phi(\mathbf{r},E) = \mathrm{H}_0\phi(\mathbf{r},E)+\mathrm{F}\phi(\mathbf{r},E)+\mathrm{S}(\mathbf{r},E), \tag{1.51}$$

where the integrals of Ω_i^n, as presented in Equation (1.8), equal zero if the exponent n is odd, otherwise they are equal to $\frac{4\pi}{3}$ if $n = 2$, the sum of the derivative over the axes has been replaced by the divergence $(\sum_i \frac{\partial}{\partial x_i} = \nabla\cdot)$, and the isotropic sources are simply $\mathrm{H}_0\phi(\mathbf{r},E) = 4\pi H_0\psi(\mathbf{r},\mathbf{\Omega},E)$, $\mathrm{F}_0\phi(\mathbf{r},E) = 4\pi F_0\psi(\mathbf{r},\mathbf{\Omega},E)$ and $\mathrm{S}(\mathbf{r},E) = 4\pi S(\mathbf{r},\mathbf{\Omega},E)$. We now need another equation to couple the scalar flux and the net current. The latter is obtained by projecting Equation (1.50) to the spherical harmonics for $\ell = 1$, thus applying the operator $\int_{4\pi} d\mathbf{\Omega}\Omega_j\cdot$ such that:

$$\frac{1}{4\pi}\left[\frac{4\pi}{3}\frac{\partial\phi}{\partial x_j}+0\right]+\frac{\Sigma}{4\pi}[0+3\frac{4\pi}{3}J_j] = 0+0,$$

where all the integrals involving $\int_{4\pi} d\mathbf{\Omega}\Omega_j\Omega_i^n\cdot$ are equal to zero except when $n = 1$ and $i = j$, thus one obtains the popular Fick's law as closure equation:

$$\mathbf{J}(\mathbf{r},E) = -D(\mathbf{r},E)\nabla\phi(\mathbf{r},E), \tag{1.52}$$

with D the diffusion coefficient such that $D(\mathbf{r}, E) = \frac{1}{3\Sigma(\mathbf{r},E)}$. Very often, however, the P_0 equation (1.51) and the Fick's law are rather constructed with the transport corrected P_0^* cross sections, thus for a better estimation of the flux:

$$D(\mathbf{r}, E) = \frac{1}{3\Sigma_{tr}(\mathbf{r}, E)}. \tag{1.53}$$

Combining Equations (1.51) and (1.52), the steady-state diffusion equation can be rewritten in its complete form as follows:

$$\begin{aligned} -\nabla \cdot (D(\mathbf{r}, E)\nabla\phi(\mathbf{r}, E)) + \Sigma(\mathbf{r}, E)\phi(\mathbf{r}, E) = \\ + \int_0^\infty dE' \Sigma_{\mathrm{s0}}(\mathbf{r}, E' \to E)\phi(\mathbf{r}, E') \\ + \frac{1}{k_{\mathrm{eff}}} \sum_i \chi_i(\mathbf{r}, E) \int_0^\infty dE'\, \nu\Sigma_{\mathrm{f},i}(\mathbf{r}, E')\phi(\mathbf{r}, E') \\ + S(\mathbf{r}, E), \end{aligned} \tag{1.54}$$

and it is a second-order differential equation in space.

In diffusion theory it is possible to find an expression for the partial currents thanks to the assumption that the flux is linearly isotropic. According to Equation (1.14) and substituting Equation (1.48), it follows that:

$$\begin{aligned} J_x^{\pm} &= \frac{1}{4\pi} \int_{2\pi^{\pm}} d\mathbf{\Omega}(\mathbf{\Omega} \cdot \mathbf{i})[\phi + 3\mathbf{\Omega} \cdot \mathbf{J}] = \\ &= \frac{1}{4\pi} \int_0^{\pm 1} d\mu \int_{2\pi} d\varphi\mu[\phi + 3\mu J_x + 3\sqrt{1-\mu^2}\cos\varphi J_y + 3\sqrt{1-\mu^2}\sin\varphi J_z] = \\ &= \frac{1}{2} \int_0^{\pm 1} d\mu\mu[\phi + 3\mu J_x] + 0 + 0 = \\ &= \frac{1}{4}\phi\mu^2\big|_0^{\pm 1} + \frac{1}{2}J_x\mu^3\big|_0^{\pm 1} = \\ &= \frac{1}{4}\phi \pm \frac{1}{2}J_x \end{aligned}$$

where we have considered a surface perpendicular to the x axis. The result is that the partial currents depend only on the scalar flux and on the net current in every point of the system, according to the following equations:

$$J^{\pm}(\mathbf{r}, E) = \frac{1}{4}\phi(\mathbf{r}, E) \pm \frac{1}{2}\mathbf{J} \cdot \mathbf{n}, \tag{1.55}$$

and knowing that $\mathbf{J} \cdot \mathbf{n} = J^+ - J^-$, it reads:

$$\phi(\mathbf{r}, E) = 2[J^+(\mathbf{r}, E) + J^-(\mathbf{r}, E)]. \tag{1.56}$$

This has the interesting consequence that Equations (1.52), (1.54) and (1.55) constitute a system of four equations where the four unknowns ϕ, J, J^+ and J^- are linearly dependent. This means that the diffusion equation can be solved for any of the four unknowns and requires only one boundary condition. It follows that it is possible to impose a boundary condition such that:

$$\Upsilon(\mathbf{r_b}, E) = \Upsilon_b(E), \tag{1.57}$$

where Υ can be any of the four variables (ϕ, J, J^+, J^-) at the boundaries of V.

Clearly, the boundary conditions that have more physical insight are those where Υ is the flux or the incoming current. The net current is also widely used and acquires a physical meaning in case of reflective boundary condition ($J = 0$) or, in the more rare case, when the leakage of the system is known in every point of the boundaries. Finally, a condition for the outgoing current ($\Upsilon = J^+$) is not intuitive, because one should know a priori how the system behaves under certain conditions. However, if one has experimental measures of the outgoing current crossing a surface contained in a more complicated system, then the diffusion equation can be used to "reconstruct" the flux in the region beyond the surface, since the imposed value takes into account the information of the environment.

Diffusion theory eliminates the angular dependence and the higher-order moments of the scattering source. This reduces considerably the number of operations in the computation of the flux, but what makes diffusion incredibly fast with respect to transport, is the assumption on the shape of the angular flux (linearly anisotropic). By contrast, this is the reason why the diffusion approximation is valid only in those regions of the systems where the leakage term is small with respect to the collision term or the sources. What makes the leakage dominant is any situation where the flux or the total cross section change fast within a mean free path $\frac{1}{\Sigma}$. Typically, this arises at the interfaces between materials with very different properties.

Chapter 2

Deterministic Numerical Methods

This chapter gives a summary of the main numerical methods used to solve the multigroup transport and diffusion equations in industrial applications. Some details are also given for the acceleration of the convergence of a transport calculation. These methods constitute the tools and the bricks of a calculation scheme. Some of them, in fact, are later used in Part II for the development and the applications of the method of Dynamic Homogenization. Therefore, this chapter fixes the notation that will be used in the rest of the document.

2.1 Multigroup Energy Formalism

The energy domain is the first domain in the phase space to be treated by a deterministic method, since it is directly associated to the discretization of the energy-dependent cross sections of the materials in the system. The energy range must be primarily defined between the maximum ($E_{\max}$) and the minimum ($E_{\min}$) energies that a particle can have in the system, and divided into a finite number of energy groups N_g inside which the neutrons are considered uniformly distributed and interact with matter with constant probability within the group. The multigroup cross sections are then to be precomputed per each energy group as follows:

$$\Sigma_{x,i}^{g}(\mathbf{r}) = \frac{\int\limits_{E\in\Delta E_g} dE\Sigma_{x,i}(\mathbf{r},E)w(\mathbf{r},E)}{\int\limits_{E\in\Delta E_g} dEw(\mathbf{r},E)}, \tag{2.1}$$

where ΔE_g is the energy interval associated to group g, x and i are respectively the reaction type and the isotope, and w is a weighting function. The latter could be equal to one if the energy mesh was fine enough to suppose constant cross section within the group. However, in doing so the number of energy groups would increase infeasibly for a transport calculation, because some isotopes have a resonant behavior for which their cross sections are sharp functions. Therefore, w is generally replaced by a weighting spectrum in order to determine the effective values that preserve the reaction rates in each group. This process is also called cross section condensation and a rigorous treatment would require the angular flux as weighting function or the angular moments. Nevertheless, this would produce angle-dependent multigroup cross sections, resulting in a large amount of data to process, and requiring a more detailed information that is hard to find if one does not perform a very fine transport calculation.

The issue that comes up, in fact, is that the weighting flux has to be known in advance to generate the multigroup cross sections but it is actually what we aim to compute. The only way is to apply a representative flux in the system and we typically choose to use a scalar flux $\phi_w(\mathbf{r},E)$ as weighting function. For non-resonant isotopes or in the energy domain where cross sections are smooth functions, such as in the fast and thermal energy domains, the distribution of the neutrons can be obtained from statistical mechanics models, thus the multigroup cross sections can be directly calculated. In the epithermal region instead, the neutron flux experiences a depression in correspondence of the resonance peaks, known as the energy self-shielding phenomenon, making more difficult the determination of the integral $\int_{\Delta E_g} dE\Sigma(\mathbf{r},E)\phi(\mathbf{r},E)$. This depression, in fact, depends on the resonant behavior of the isotope itself as well as the other isotopes contained in the medium and the spatial variations of the flux. In order to determine the weighting flux and account for these phenomena, some assumptions are introduced constituting a model of self-shielding, that allows to estimate the effective values of multigroup cross sections. More details on self-shielded cross sections will be given in Chapter 3 and here they are assumed as given to show the resolution of the multigroup transport equation.

As for the multigroup cross sections, the multigroup angular flux is also a step function in the energy domain, and it generally represents the integrated flux in the energy group, as follows:

$$\psi^g(\mathbf{r}, \mathbf{\Omega}) = \int_{\Delta E_g} dE \psi(\mathbf{r}, \mathbf{\Omega}, E), \tag{2.2}$$

which naturally leads to the definition of multigroup scalar flux and net current:

$$\phi^g(\mathbf{r}) = \int_{4\pi} d\mathbf{\Omega} \psi^g(\mathbf{r}, \mathbf{\Omega}), \quad \mathbf{J}^g(\mathbf{r}) = \int_{4\pi} d\mathbf{\Omega}\mathbf{\Omega} \psi^g(\mathbf{r}, \mathbf{\Omega}) \tag{2.3}$$

and that of the multigroup reaction rate:

$$\tau_x^g(\mathbf{r}) = \Sigma_x^g(\mathbf{r})\phi^g(\mathbf{r}). \tag{2.4}$$

At this point, in order to obtain the multigroup transport equation, we apply the operator $\int_{\Delta E_g} dE$ to each term of the transport equation for an eigenvalue problem:

- Loss operator:

$$\begin{aligned} L^g\psi(\mathbf{r}, \mathbf{\Omega}) &= \int_{\Delta E_g} dE[\mathbf{\Omega} \cdot \nabla\psi(\mathbf{r}, \mathbf{\Omega}, E) + \Sigma(\mathbf{r}, E)\psi(\mathbf{r}, \mathbf{\Omega}, E)] \\ &\approx \mathbf{\Omega} \cdot \nabla\psi^g(\mathbf{r}, \mathbf{\Omega}) + \Sigma^g(\mathbf{r})\psi^g(\mathbf{r}, \mathbf{\Omega}), \end{aligned}$$

  where we used the symbol "$\approx$" because in a rigorous treatment the multigroup total cross section should be angle dependent;

- Scattering source:
  the integral over the whole energy domain appearing in the scattering source is expressed as a sum of integrals over all the energy groups [7], such that:

$$\int_0^\infty dE' = \sum_{g'}^{N_g} \int_{\Delta E_{g'}} dE'.$$

  Starting from Equation (1.41), where we already separated the angular variable using the spherical harmonic expansion, and using the last expression, the multi-

group scattering source can be written as follows:

$$H^g\psi(\mathbf{r},\mathbf{\Omega}) = \sum_{\ell=0}^{L}\frac{2\ell+1}{4\pi}\sum_{m=-\ell}^{\ell}Y_{\ell,m}(\mathbf{\Omega})\int_{\Delta E_g}dE\int_0^{\infty}dE'\Sigma_{\mathrm{s}\ell}(E'\rightarrow E)\phi_{\ell,m}(\mathbf{r},E')$$
$$\approx \sum_{g'}^{N_g}\sum_{\ell=0}^{L}\frac{2\ell+1}{4\pi}\Sigma_{\mathrm{s}\ell}^{g'\rightarrow g}(\mathbf{r})\sum_{m=-\ell}^{\ell}Y_{\ell,m}(\mathbf{\Omega})\phi_{\ell,m}^{g'}(\mathbf{r}),$$

where we defined:

$$\Sigma_{\mathrm{s}\ell}^{g'\rightarrow g}(\mathbf{r})\phi_{\ell,m}^{g'}(\mathbf{r}) = \int_{\Delta E_{g'}}\phi_{\ell,m}(\mathbf{r},E')\int_{\Delta E_g}\Sigma_{\mathrm{s}\ell}(E'\rightarrow E)dEdE'.$$

However, we used again the symbol "≈" in the multigroup scattering source definition, because the moments of the multigroup differential scattering cross section are often weighted, as for the other cross sections, by the scalar flux as follows:

$$\Sigma_{\mathrm{s}\ell}^{g'\rightarrow g}(\mathbf{r}) = \frac{\int_{\Delta E_g'}\phi_w(\mathbf{r},E')\int_{\Delta E_g}\Sigma_{\mathrm{s}\ell}(\mathbf{r},E'\rightarrow E)dEdE'}{\int_{\Delta E_{g'}}\phi_w(\mathbf{r},E')dE'},$$

instead of using the angular moments of the flux. This approach is widely used in reactor physics because applying the flux angular moments as weighting function in the last equation involves at least two issues. The first one concerns the knowledge of these quantities, since very often the model used to compute them contains internal symmetries (such as in 2D geometries) that result in some angular moments exactly equal to zero. Secondly, the higher moments can be close to zero, making the condensation more difficult to compute because of numerical instabilities.

- Fission source

$$F^g\psi(\mathbf{r},\mathbf{\Omega}) = \sum_i\int_{\Delta E_g}dE\frac{\chi_i(\mathbf{r},E)}{4\pi}\int_{4\pi}d\mathbf{\Omega}'\int_0^{\infty}dE'\nu\Sigma_{\mathrm{f},i}(\mathbf{r},E')\psi(\mathbf{r},\mathbf{\Omega},E')$$
$$= \sum_i\frac{\chi_i^g(\mathbf{r})}{4\pi}\sum_{g'}^{N_g}\int_{4\pi}d\mathbf{\Omega}'\nu\Sigma_{\mathrm{f},i}^{g'}(\mathbf{r})\psi^{g'}(\mathbf{r},\mathbf{\Omega}')$$
$$= \sum_i\frac{\chi_i^g(\mathbf{r})}{4\pi}\sum_{g'}^{N_g}\nu\Sigma_{\mathrm{f},i}^{g'}(\mathbf{r})\phi^{g'}(\mathbf{r}),$$

where we have integrated the angular flux since the fission cross section does not depend on $\mathbf{\Omega}$.

By rearranging all the terms so as to describe the particle balance for each energy group, the transport equation turns into a system of N_g mono-kinetic equations coupled by

the terms of scattering and fission sources:

$$\boldsymbol{\Omega}\cdot\nabla\psi^g(\mathbf{r},\boldsymbol{\Omega})+\Sigma^g(\mathbf{r})\psi^g(\mathbf{r},\boldsymbol{\Omega})=\sum_{g'}^{N_g}\sum_{\ell=0}^{L}\frac{2\ell+1}{4\pi}\Sigma_{\mathrm{s}\ell}^{g'\to g}(\mathbf{r})\sum_{m=-\ell}^{\ell}Y_{\ell,m}(\boldsymbol{\Omega})\phi_{\ell,m}^{g'}(\mathbf{r})$$
$$+\frac{1}{k}\sum_{i}\frac{\chi_i^g(\mathbf{r})}{4\pi}\sum_{g'}^{N_g}\nu\Sigma_{\mathrm{f},i}^{g'}(\mathbf{r})\phi^{g'}(\mathbf{r}),\quad\forall g\in[1,...,N_g] \tag{2.5}$$

The scattering matrix $\Sigma_{\mathrm{s}\ell}^{g'\to g}$ of a generic order ℓ is a square matrix and it is generally constructed so as to arrange the incident group g' per column and the exiting group g per row. It follows that it is composed of a lower triangular matrix until the last fast group, since the thermal neutrons cannot scatter toward fast energy groups, and a rectangular matrix for the thermal zone, due to the thermal equilibrium between neutrons and nuclides that exchange energy between each other.
For a simpler notation, we divide the scattering matrix in a diagonal *self*-scattering matrix, a lower triangular *down*-scattering matrix and an upper triangular *up*-scattering matrix as follows:

$$H_{\mathrm{ss}}^g\psi(\mathbf{r},\boldsymbol{\Omega})=\sum_{\ell=0}^{L}\frac{2\ell+1}{4\pi}\Sigma_{\mathrm{s}\ell}^{g\to g}(\mathbf{r})\sum_{m=-\ell}^{\ell}Y_{\ell,m}(\boldsymbol{\Omega})\phi_{\ell,m}^{g}(\mathbf{r}), \tag{2.6}$$

$$H_{\mathrm{dw}}^g\psi(\mathbf{r},\boldsymbol{\Omega})=\sum_{g'<g}^{N_g}\sum_{\ell=0}^{L}\frac{2\ell+1}{4\pi}\Sigma_{\mathrm{s}\ell}^{g'\to g}(\mathbf{r})\sum_{m=-\ell}^{\ell}Y_{\ell,m}(\boldsymbol{\Omega})\phi_{\ell,m}^{g'}(\mathbf{r}), \tag{2.7}$$

$$H_{\mathrm{up}}^g\psi(\mathbf{r},\boldsymbol{\Omega})=\sum_{g'>g}^{N_g}\sum_{\ell=0}^{L}\frac{2\ell+1}{4\pi}\Sigma_{\mathrm{s}\ell}^{g'\to g}(\mathbf{r})\sum_{m=-\ell}^{\ell}Y_{\ell,m}(\boldsymbol{\Omega})\phi_{\ell,m}^{g'}(\mathbf{r}). \tag{2.8}$$

so that the mono-kinetic equation in compact form for a generic group g is:

$$L^g\psi=H_{\mathrm{ss}}^g\psi+H_{\mathrm{dw}}^g\psi+H_{\mathrm{up}}^g\psi+\frac{1}{k}F^g\psi. \tag{2.9}$$

For the fast groups it reads $H_{\mathrm{up}}^g\psi=0$ and for the first fast group $H_{\mathrm{dw}}^{g=1}\psi=0$.

In order to solve the system of N_g equations, a direct inversion of the operator $L-H$ is never employed, because the number of unknowns is too large. Therefore, the solution is obtained through an iterative process that is composed of three nested iteration loops as described in Algorithm 1. The iteration loops are the following:

Outers The outermost loop consists in the power iterations, as discussed in Section 1.4, where the fission source and the eigenvalue are fixed for all the other loops, and

are updated only at the end of each outer iteration using the new neutron flux:

$$L^g\psi^{n+1} = H^g_{\text{ss}}\psi^{n+1} + H^g_{\text{dw}}\psi^{n+1} + H^g_{\text{up}}\psi^{n+1} + \frac{1}{k^n}F^g\psi^n, \tag{2.10}$$

where n is the index for the outer iteration and the updates are the following:

$$F^g\psi^{n+1} = \sum_i \frac{\chi^g_i(\mathbf{r})}{4\pi}\sum_{g'}^{N_g}\nu\Sigma^{g'}_{\text{f},i}(\mathbf{r})\phi^{g',n+1}(\mathbf{r}), \tag{2.11}$$

and

$$k^{n+1} = k^n\frac{\langle w, F\psi^{n+1}\rangle}{\langle w, F\psi^n\rangle}, \tag{2.12}$$

where the weighting function is typically $w = F\psi^n$.
At this point, because of the nature of the scattering matrix, the transport equations for the N_{fg} fast groups are solved recursively by forward substitution of the precedent fluxes in the down-scattering source.

Thermals In the thermal zone instead, not all the terms of the scattering source are known, because it contains up-scattering which depends on the fluxes of higher energy group, that have not been computed yet. The system of thermal groups is solved using a Gauss-Seidel iterative method, adding an additional loop called thermal iterations:

$$L^g\psi^{t+1} = H^g_{\text{ss}}\psi^{t+1} + H^g_{\text{dw}}\psi^{t+1} + H^g_{\text{up}}\psi^{t} + \frac{1}{k^n}F^g\psi^n, \tag{2.13}$$

with t the thermal iteration index, and the up-scattering source is updated at the end of each iteration according to Equation (2.8) and using $\phi^{g',t+1}_{\ell,m}$. At the convergence of the up-scattering source, we indicate the end of thermal loop as t_∞, and it yields $\psi^{n+1} = \psi^{t_\infty}$.

Inners The convergence of the self-scattering source, instead, is achieved in the inner iteration loop, as follows:

$$L^g\psi^{i+1} = H^g_{\text{ss}}\psi^{i} + H^g_{\text{dw}}\psi^{t+1} + H^g_{\text{up}}\psi^{t} + \frac{1}{k^n}F^g\psi^n, \tag{2.14}$$

with i the inner iteration index, the self-scattering source is updated using Equation (2.6), and at the convergence of the inners it yields $\psi^{t+1} = \psi^{i_\infty}$.

In order to update the scattering sources, it is required the knowledge of the angular moments of the flux $\phi^g_{\ell,m}$ up to the order L. These are obtained solving the transport equation in space and angle with a fixed source for a given group that equals the sum of all the sources:

$$[\mathbf{\Omega}\cdot\nabla + \Sigma^g(\mathbf{r})]\psi^g(\mathbf{r},\mathbf{\Omega}) = Q^g(\mathbf{r},\mathbf{\Omega}) \tag{2.15}$$

Algorithm 1: Multigroup Formalism

```
Initialization of ψ and λ;
while k, Fψ have not converged do
    for g ∈ [1, N_fg] do
        while H^g_ss ψ has not converged do
            solve inner iteration (Equation (2.14));
            update H^g_ss ψ (Equation (2.6));
        end
    end
    while H_up ψ has not converged do
        for g ∈ [N_fg + 1, N_g] do
            while H^g_ss ψ has not converged do
                solve inner iteration (Equation (2.14));
                update H^g_ss ψ (Equation (2.6));
            end
        end
        update H_up ψ (Equation (2.8));
    end
    update Fψ (Equation (2.11)) ;
    update k (Equation (2.12));
end
```

where $Q^g(\mathbf{r}, \mathbf{\Omega})$ is called *emission density* that depends on the neutron flux, therefore, it is also expanded on spherical harmonics as follows:

$$Q^g(\mathbf{r}, \mathbf{\Omega}) = \sum_{\ell=0}^{L} \frac{2\ell+1}{4\pi} \sum_{m=-\ell}^{\ell} Y_{\ell,m}(\mathbf{\Omega}) Q^g_{\ell,m}(\mathbf{r}), \tag{2.16}$$

with

$$Q^g_{\ell,m}(\mathbf{r}) = \sum_{g'}^{N_g} \Sigma_{\mathrm{s}\ell}^{g' \to g}(\mathbf{r}) \phi^{g'}_{\ell,m}(\mathbf{r}) + \frac{1}{k} \sum_i \chi^g_i(\mathbf{r}) \sum_{g'}^{N_g} \nu \Sigma^{g'}_{\mathrm{f},i}(\mathbf{r}) \phi^{g'}_{\ell,m}(\mathbf{r}) \delta_{\ell 0}, \tag{2.17}$$

where fission is supposed to be an isotropic source.

The computational cost of the resolution of a multigroup problem can be expressed in terms of the total number of inner iterations and the cost of one inner iteration, since the solution is found solving N_{inn} times Equation (2.15). Generally, the number of inners per group and the number of thermals per outer are limited to a maximum value, because it has been shown that an incomplete convergence of the scattering source does not compromise the stability of the nested iterative process, and that it can be time consuming to "push" the inner iterations if the fission source is not close to convergence.

The convergence criteria used to stop the iteration process typically involve the evaluation of the L_∞ or L_2 norms of a quantity computed at two consecutive iterations, that is compared with a tolerance value defined by the user. Each iteration loop has then a convergence criterion and a tolerance, below which a solver stops iterating. For the inner iterations, the quantities that are checked are the angular moments of the flux in each computational region as follows:

$$\left\| \frac{\phi_{\ell,m}^{i+1} - \phi_{\ell,m}^{i}}{\max\left[\phi_{\ell,m}^{i+1}, \phi_{0,0}^{i+1}\right]} \right\|_\infty < \varepsilon_{\mathrm{i}}, \quad \forall \ell, m. \tag{2.18}$$

This criterion assures that the self-scattering source is converged as well, and the denominator has been adapted to the cases where the higher angular moments are very small and may produce numerical instabilities when computing the relative error.
For the thermal iteration loop, one should check punctually the flux moments of each thermal energy group, in order to guarantee the convergence of the up-scattering source. However, this can be a very severe criterion. Moreover, the convergence of the angular moments is already tested at the inner level, and the spatial convergence is also partially checked, with partially meaning with constant up-scattering source in the same iteration loop. Therefore, it is very common to test only the scalar flux integrated in the whole domain for each thermal energy group as follows:

$$\frac{\int_V d\mathbf{r}\phi^{t+1}(\mathbf{r}) - \int_V d\mathbf{r}\phi^{t}(\mathbf{r})}{\int_V d\mathbf{r}\phi^{t+1}(\mathbf{r})} < \varepsilon_{\mathrm{t}}, \quad \forall g \,\text{thermal}. \tag{2.19}$$

This test is specially adopted when the calculation also has to iterate on the fission source, since this loop involves again a spatial region-wise convergence. If this is not the case and the system is not multiplicative, then a punctual spatial convergence for the thermal iteration is mandatory.
The outermost iteration loop checks for the fission integral in each computational region and the eigenvalue as follows:

$$\left\| \frac{\left(\sum_g^{N_g} \nu\Sigma_{\mathrm{f},i}^g \phi^g\right)^{n+1} - \left(\sum_g^{N_g} \nu\Sigma_{\mathrm{f},i}^g \phi^g)\right)^{n}}{\left(\sum_g^{N_g} \nu\Sigma_{\mathrm{f},i}^g \phi^g\right)^{n+1}} \right\|_\infty < \varepsilon_{\mathrm{f}}, \quad \forall i \tag{2.20}$$

$$\left| k^{n+1} - k^n \right| < \varepsilon_{\mathrm{k}}\,. \tag{2.21}$$

We can observe that between two consecutive outer iterations there is no test on the multigroup flux for each energy group, although one could employ it instead of the fission integral test. This is justified by the fact that reaction rates integrated in energy are generally the quantities of interest and for which a narrow criterion is adopted. The same tolerance applied to the multigroup flux, however, is generally of little use and time-consuming. Experience has shown, though, that the error on the multigroup flux

is less than $\sim N_g \varepsilon_{\mathrm{f}}$, where typically $\varepsilon_{\mathrm{f}} = 10^{-4}$ and the order of magnitude of N_g is not higher than 10^2.

2.2 Forms of the Transport Equation

Before starting the presentation of the main numerical methods employed in reactor physics to solve Equation (2.15), we introduce here the most popular forms of the transport equation: the integrodifferential and the integral forms. From both equations, several numerical methods can be derived that have different properties and, therefore, numerical advantages or disadvantages depending on the situation and the problem to solve. The integral equation [8] can be directly derived from the integrodifferential equation, which is also known as first-order transport equation because it involves only first derivatives in space. However, the second-order form or even-parity form of the transport equation has also been applied, and it primarily differs from the other ones because second derivatives in space appear in the equation and the solution is found for one half of the angular domain. The methods obtained by this form of the transport equation are generally not found in industrial codes. They will not be discussed in this section, but the reader is directed to the reference [9] for a detailed description and bibliography.

The integrodifferential form has already been introduced and it presents a differential operator for the streaming term and an integral operator for the source. We rewrite it here omitting the group index:

$$[\mathbf{\Omega} \cdot \nabla + \Sigma(\mathbf{r})]\psi(\mathbf{r}, \mathbf{\Omega}) = Q(\mathbf{r}, \mathbf{\Omega}) \tag{2.22}$$

The integral form of the transport equation presents instead only integral operators and describes the balance in a particle trajectory, or characteristic, of its motion, which is a straight line with direction $\mathbf{\Omega}$. The parametric form of a trajectory can be written as:

$$\mathbf{r}'(s) = \mathbf{r} - s\mathbf{\Omega}, \quad s = |\mathbf{r} - \mathbf{r}'| \geq 0, \tag{2.23}$$

where $\mathbf{r}'$ and $\mathbf{r}$ are two points of a straight line with distance s, that represent an event for which a particle is transferred so as $\mathbf{r}' \rightarrow \mathbf{r}$. Knowing that $\frac{d\mathbf{r}'}{ds} = -\mathbf{\Omega}$ and

$$-\frac{d\mathbf{r}'}{ds} \cdot \nabla = -\sum_i \frac{dx_i'}{ds}\frac{\partial}{\partial x_i'} = -\frac{d}{ds},$$

with i the axis index, we can change the streaming operator in favor of the material derivative in ds, and write the balance for a generic point $\mathbf{r}'$:

$$[-\frac{d}{ds} + \Sigma(\mathbf{r} - s\mathbf{\Omega})]\psi(\mathbf{r} - s\mathbf{\Omega}, \mathbf{\Omega}) = Q(\mathbf{r} - s\mathbf{\Omega}, \mathbf{\Omega}). \tag{2.24}$$

Equation (2.24) is a first order heterogeneous differential equation and its solution can

be found using the method of variation of constants. The homogeneous solution ψ_{h} is determined using the method of separation of variables with $Q = 0$:

$$\psi_{\mathrm{h}}(\mathbf{r} - s\mathbf{\Omega}, \mathbf{\Omega}) = Ce^{\int_0^s dt\Sigma(\mathbf{r}-t\mathbf{\Omega})}, \tag{2.25}$$

where the integral in the exponent of e is called optical length, that is here indicated as a function of two points in a characteristic $\mathbf{r}'$ and $\mathbf{r}$, as follows:

$$\tau(\mathbf{r}', \mathbf{r}) = \int_0^s dt\Sigma(\mathbf{r} - t\mathbf{\Omega}_s), \quad s = |\mathbf{r} - \mathbf{r}'|, \mathbf{\Omega}_s = \frac{\mathbf{r} - \mathbf{r}'}{|\mathbf{r} - \mathbf{r}'|}. \tag{2.26}$$

The general solution is obtained with the constant variation $C = f(s)$:

$$\psi(\mathbf{r} - s\mathbf{\Omega}, \mathbf{\Omega}) = f(s)e^{\tau(\mathbf{r}-s\mathbf{\Omega},\mathbf{r})}, \tag{2.27}$$

where f is a function to be determined. We combine the last equation with Equation (2.24) so that:

$$\begin{aligned}
&-\frac{df(s)}{ds}e^{\tau(\mathbf{r}-s\mathbf{\Omega},\mathbf{r})} - f(s)e^{\tau(\mathbf{r}-s\mathbf{\Omega},\mathbf{r})}\Sigma(\mathbf{r} - s\mathbf{\Omega}) + \Sigma(\mathbf{r} - s\mathbf{\Omega})f(s)e^{\tau(\mathbf{r}-s\mathbf{\Omega},\mathbf{r})} = Q(\mathbf{r} - s\mathbf{\Omega}, \mathbf{\Omega}) \\
&\frac{df(s)}{ds} = -Q(\mathbf{r} - s\mathbf{\Omega}, \mathbf{\Omega})e^{-\tau(\mathbf{r}-s\mathbf{\Omega},\mathbf{r})} \\
&f(s) = f(0) - \int_0^s dtQ(\mathbf{r} - t\mathbf{\Omega}, \mathbf{\Omega})e^{-\tau(\mathbf{r}-t\mathbf{\Omega},\mathbf{r})}.
\end{aligned}$$

We now invert Equation (2.27) to express $f(s)$ as:

$$f(s) = \psi(\mathbf{r} - s\mathbf{\Omega}, \mathbf{\Omega})e^{-\tau(\mathbf{r}-s\mathbf{\Omega},\mathbf{r})} \quad \text{and} \quad f(0) = \psi(\mathbf{r} - 0\mathbf{\Omega}, \mathbf{\Omega})e^{-\tau(\mathbf{r},\mathbf{r})} = \psi(\mathbf{r}, \mathbf{\Omega}),$$

and rearranging the terms it reads:

$$\psi(\mathbf{r}, \mathbf{\Omega}) = \psi(\mathbf{r} - s\mathbf{\Omega}, \mathbf{\Omega})e^{-\tau(\mathbf{r}-s\mathbf{\Omega},\mathbf{r})} + \int_0^s dtQ(\mathbf{r} - t\mathbf{\Omega}, \mathbf{\Omega})e^{-\tau(\mathbf{r}-t\mathbf{\Omega},\mathbf{r})}, \tag{2.28}$$

that is called the integral form of the transport equation. If the domain is infinite, the first term goes to zero and the solution equals only the integral of the source. If the domain is finite, the maximum length corresponds to the distance s_b between the point $\mathbf{r}$ and the point $\mathbf{r}_b$ located at the boundary. The equations can be rewritten as follows:

$$\psi(\mathbf{r}, \mathbf{\Omega}) = \psi(\mathbf{r}_b, \mathbf{\Omega})e^{-\tau(\mathbf{r}_b,\mathbf{r}_b+s_b\mathbf{\Omega})} + \int_0^{s_b} dtQ(\mathbf{r}_b + t\mathbf{\Omega}, \mathbf{\Omega})e^{-\tau(\mathbf{r}_b+t\mathbf{\Omega},\mathbf{r}_b+s_b\mathbf{\Omega})}.$$

In a more general way, knowing that the incoming flux ψ^- can be considered as a source for the system, using $d^3\mathbf{r}' = s^2 ds d\mathbf{\Omega}$ and $d^2\mathbf{r}' = s^2 d\mathbf{\Omega}$, Equation (2.28) can be formally rewritten as:

$$\psi(\mathbf{r}, \mathbf{\Omega}) = \int_{4\pi} d\mathbf{\Omega}' \int_V d\mathbf{r}' [\psi^-(\mathbf{r}', \mathbf{\Omega}')\delta_b + Q(\mathbf{r}', \mathbf{\Omega}')]\delta_{\mathbf{\Omega}_s} \frac{e^{-\tau(\mathbf{r}', \mathbf{r})}}{|\mathbf{r} - \mathbf{r}'|^2}, \tag{2.29}$$

where

$$\delta_b = \begin{cases} -(\mathbf{n} \cdot \mathbf{\Omega}'), \ \mathbf{r}' \in \partial V \\ 0, \ \text{otherwise} \end{cases}, \quad \delta_{\mathbf{\Omega}_s} = \begin{cases} 1, \ \text{if} \quad \frac{\mathbf{r}-\mathbf{r}'}{|\mathbf{r}-\mathbf{r}'|} = \mathbf{\Omega} = \mathbf{\Omega}' \\ 0, \ \text{otherwise} \end{cases}$$

and $\delta_{\mathbf{\Omega}_s}$ is the product of two Placzek's delta functions as follows:

$$\delta_{\mathbf{\Omega}_s} = \delta_2(\mathbf{\Omega}_s \cdot \mathbf{\Omega}') \cdot \delta_2(\mathbf{\Omega}_s \cdot \mathbf{\Omega}), \quad \text{with} \quad \mathbf{\Omega}_s = \frac{\mathbf{r} - \mathbf{r}'}{|\mathbf{r} - \mathbf{r}'|}. \tag{2.30}$$

We can present, therefore, a compact form of the integral transport equation as follows:

$$\psi = G(Q + \psi^- \delta_b), \tag{2.31}$$

where ψ^- is defined only on the hemisphere with negative $(\mathbf{n} \cdot \mathbf{\Omega})$, and G the integral transport operator that is the inverse of the loss operator $L = \mathbf{\Omega} \cdot \nabla + \Sigma$ such that:

$$Gf(\mathbf{r}, \mathbf{\Omega}) = \int_{4\pi} d\mathbf{\Omega}' \int_V d\mathbf{r}' g(\mathbf{r}' \to \mathbf{r}, \mathbf{\Omega}' \to \mathbf{\Omega}) f(\mathbf{r}', \mathbf{\Omega}'), \tag{2.32}$$

where g can be seen as the Green function of the operator L and it is defined as:

$$g(\mathbf{r}' \to \mathbf{r}, \mathbf{\Omega}' \to \mathbf{\Omega}) = \delta_{\mathbf{\Omega}_s} \frac{e^{-\tau(\mathbf{r}', \mathbf{r})}}{|\mathbf{r} - \mathbf{r}'|^2}, \tag{2.33}$$

where the term $e^{-\tau(\mathbf{r}', \mathbf{r})}$ indicates the "probability to survive" for a particle emitted in $\mathbf{r}'$ and moving along its trajectory with destination $\mathbf{r}$.

The two forms of the transport equation describe the same physical phenomenon of motion of particles, but with two different approaches: the integrodifferential form utilizes an Eulerian approach while the integral form a Lagrangian approach. The former is based on local neutron balance and leads to sparse matrices, while the latter on a global neutron balance, resulting in a strongly coupled system of equations. However, because of the $\delta_{\mathbf{\Omega}_s}$, the coupling is limited to only those regions crossed by a trajectory. The deterministic methods based on the integrodifferential form typically use a regular spatial mesh to represent the geometry of the problem and, sometimes, they require a

large number of regions for a good description in complicated geometries. The integral methods, instead, treat the geometrical representation in an exact way, and are based on tracking techniques for numerical integration in space. The number of regions required is generally lower than for the integrodifferential methods, but the number of operations per regions is higher, depending on the number of trajectories crossing the region. When the system is large, the integral form of the transport equation is generally not convenient, because of the coupling of the angular fluxes from one boundary to the opposite boundary, therefore the integrodifferential equation is generally preferred. On the other hand, for small systems with a certain amount of geometrical details, the integral methods are the best choice.

In order to take advantage from both approaches, an effort has been put into "hybrid" methods, also called nodal methods, to improve the computational cost of integral methods in calculations of large systems. The idea of the nodal method is to divide the domain into regions called nodes, and to introduce an approximation for the transmission of the angular fluxes between nodes [10]. It follows that, on one hand, the integral equation can be used to determine the coupling matrices between interior, entering and exiting fluxes for a node, treating exactly the geometrical details inside the node and saving in number of regions. On the other hand, each node is connected with its neighboring nodes imposing the continuity condition of the interface angular fluxes, leading to sparse matrices that can be solved by node sweeping, where the outgoing angular flux of a node is used as incoming angular flux for the adjacent ones. The equations that describe the behavior of a node are two, one for the interior flux and one for the outgoing flux, that are expressed as a function of the incoming flux and the volumetric sources. This form of the transport equation is called for historical reasons Interface-Current formalism, and the coupled equations have generally the following compact form:

$$\begin{cases} \psi = I\psi^- + CQ \\ \psi^+ = T\psi^- + EQ \end{cases} \tag{2.34}$$

where I, C, T, E are respectively the Incoming, Collision, Transmission and Escape matrices. The incoming matrix associates each surface element of a node to each region inside the node ($s' \to r$), the collision matrix all the regions of a node between each other ($r' \to r$), the transmission matrix the surface elements of the node with each other ($s' \to s$) and the escape matrix all the emitting regions with each surface element ($r' \to s$). More details will be given in the next sections, with a particular focus on the Method of Short Characteristics that has been used as transport operator for our analysis and applications in Part II of this document.

2.3 Angular Representation of the Flux

At this point, in order to solve the mono-kinetic transport equation, either in the integrodifferential form (Equation (2.22)) or the integral form (Equation (2.28)), several methods have been developed that are mainly based on two types of numerical techniques for the representation of the neutron flux: the projection or expansion methods

and the quadrature methods. These techniques can be applied for the discretization in both spatial and angular domains, but we focus here the attention to the angular domain. Both approaches consist in *i*) approximating the flux with a set of a finite number N of values that represent the angular distribution, and *ii*) replacing the transport equation with a system of N equations to determine it. Generally, the higher N, the closer the approximate flux to the true flux. On the other hand, the difference between the two techniques resides in the way the flux is represented, that can be mediated with a set of functions or points.
The projection methods approximate the angular flux with a set of functions as follows:

$$\psi(\mathbf{\Omega}) \approx \widetilde{\psi}(\mathbf{\Omega}) = \sum_{m=1}^{N} \phi_m f_m(\mathbf{\Omega}), \tag{2.35}$$

where f_m are chosen so as they constitute a complete orthogonal basis such that:

$$\int_{4\pi} d\mathbf{\Omega} f_n(\mathbf{\Omega}) f_m(\mathbf{\Omega}) = c\delta_{nm}, \tag{2.36}$$

where δ_{nm} is the Kronecker delta that is always zero except for $n = m$ where it equals one, and c is a normalization constant, and

$$\psi = \lim_{N\to\infty} \widetilde{\psi}.$$

Equation (2.35) can be obtained applying a projector P to the unknown variable that is defined such that:

$$P\psi(\mathbf{\Omega}) = \sum_{m=1}^{N} P_m \psi(\mathbf{\Omega}) f_m(\mathbf{\Omega}) = \sum_{m=1}^{N} \langle f_m(\mathbf{\Omega}), \psi(\mathbf{\Omega})\rangle f_m(\mathbf{\Omega}) = \widetilde{\psi}(\mathbf{\Omega}) \tag{2.37}$$

where $P_m = \langle f_m, \cdot \rangle$ is the projection operator on a basis function and the flux moments read:

$$\phi_m = \langle f_m(\mathbf{\Omega}), \psi(\mathbf{\Omega})\rangle = \int_{4\pi} d\mathbf{\Omega} f_m(\mathbf{\Omega}) \psi(\mathbf{\Omega}).$$

Thanks to the orthogonality property, an expansion method always relies on the projection of the original equation to each basis function, so as to obtain the projected equations that usually are easier to solve. For the integrodifferential transport equation, it reads:

$$L\widetilde{\psi} = Q \quad \rightarrow \quad P_n L\widetilde{\psi} = P_n Q, \quad n = 1 \text{ to } N$$

We can take advantage from the orthogonality such that the terms of the projected equation read:

$$P_n L\widetilde{\psi} = \langle f_n, \sum_{m=1}^{N} L f_m \phi_m \rangle = \sum_{m=1}^{N} \langle f_n, L f_m \rangle \phi_m = \sum_{m=1}^{N} L_{nm} \phi_m,$$

and

$$P_n Q = \langle f_n, Q \rangle = Q_n.$$

The system of N equations to be solved for a projection method has, finally, the following form:

$$\sum_{m=1}^{N} L_{nm} \phi_m = Q_n, \quad n = 1 \text{ to } N. \tag{2.38}$$

Quadrature methods instead, represent an angular function with a set of N points associated to discrete directions $\mathbf{\Omega}_n$ of the angular domain. Each direction is associated to a weight that is used for integration in angle as follows:

$$\int_{4\pi} d\mathbf{\Omega} g(\mathbf{\Omega}) \approx \sum_{n}^{N} w_n g(\mathbf{\Omega}_n). \tag{2.39}$$

The functions that have to be integrated are generally approximated with polynomials, therefore the set of directions and weights depends on the quadrature formula, that is built so as to integrate exactly the polynomial with the highest possible degree. Because the integrodifferential transport equation has integral terms only on the right side for sources, an angular quadrature method leads to a system of equations of the following form:

$$L_n \psi_n = \sum_{m=1}^{N} w_m Q_{nm}, \quad n = 1 \text{ to } N. \tag{2.40}$$

A comparison of Equations (2.38) and (2.40) shows that a projection method is said to diagonalize the scattering kernel, because the equations are coupled by the streaming term. By contrast, the quadrature method diagonalizes the streaming operator producing a system of equations coupled by the scattering source. Depending on configuration, one method can be computationally more advantageous than the other one. Typically projection methods of the integrodifferential form are the most efficient for optically large systems and nearly diffusive systems. For optically small systems that are strongly heterogeneous and the flux can be highly anisotropic, the quadrature methods are instead the best option.

In a similar way, it is also possible to apply the two techniques to the integral transport equation, producing a system of equations of the following form:

$$\phi_n = G_n Q, \quad n = 1 \text{ to } N, \tag{2.41}$$

for the projection technique where $G_nQ = \langle f_n, GQ \rangle$, and:

$$\psi_n = G \sum_{m=1}^{N} w_m Q_{nm}, \quad n = 1 \text{ to } N, \tag{2.42}$$

for the quadrature technique. For the last equations, the integral operator G is defined in Equation (2.32). Both systems of equations are coupled by the emission density and, unlike in the integrodifferential form (Equation (2.38)), in Equation (2.41) the source cannot be directly projected. On the other hand, Equation (2.42) is simply the inverse of Equation (2.40). The main difference of the two systems of integral equations (2.41,2.42) is that the projection technique leads to a full coupling in space, produced by the integration in angle of the operator G which in turn integrates along a trajectory, as shown in the last section. On the other hand, in the quadrature form of integral equation the coupling in space is limited to those regions that are crossed by a trajectory. Equation (2.41) can have an advantage only if the number of regions is small and if the source shape is known in advance or approximated. This advantage is given by the elimination of the angular variable that is often not necessary for reaction rate calculation. Moreover, an interesting difference between the two systems of projected equations in Equations (2.38) and (2.41) resides in the fact that in the integrodifferential system the N equations approximate the angular distribution of both flux and source, while in the case of the system of integral equations only the source is affected by the approximation to the order N.

2.4 Numerical Transport Methods

The combination of these two numerical techniques with different forms of the transport equations produces different classes of transport methods. For each class several variations of the method can be found in literature, and we limit here the description of those methods that are the most relevant for their class.
The integrodifferential form of the transport equation leads to the spherical harmonics method (P_N) and the discrete ordinates method (S_N) respectively for the projection and quadrature techniques. From the integral form instead, the collision probability method (CP) and the method of characteristics (MOC) can be derived respectively applying the projection and the quadrature techniques. Finally, for a symmetry a bit forced by the author, some methods based on the interface-current formalism can also be distinguished with the same approach adopted for the other methods. We present here the interface-current method IC, which is based on CP, and the method of short characteristics (MOSC), which is based on MOC, as the most popular methods that belong to the class of, respectively, projection and quadrature hybrid methods.

This classification is summarized in Table 2.1, and it concerns only the techniques used to represent the angular flux and the forms of the transport equation to which they are applied. This means that numerical methods used for the spatial representation are not classified in this section, since they can be applied to more the one class of Table 2.1. For instance, transverse nodal and finite element methods have been applied

to both P_N and S_N methods.

Method	Integrodifferential Form	Integral Form	Hybrid
Projection	P_N	CP	IC
Quadrature	S_N	MOC	MOSC

Table 2.1. Classification of transport methods, based on projection and quadrature techniques for the angular representation of the neutron flux that are applied to different forms of the transport equation. In the table, P_N=Spherical Harmonics Method, S_N=Discrete Ordinates Method, CP=Collision Probability Method, MOC=Method Of Characteristics, IC=Interface Current Method, MOSC=Method Of Short Characteristics.

2.4.1 The Spherical Harmonics Method

The P_N method [1, 7, 11] employs the spherical harmonics as basis functions for the projection of the integrodifferential equation. The choice of this basis is explained by the fact that the scattering source is already expanded in spherical harmonics, thus the projection technique simplifies the initial equation. Following the approach shown in Section 2.3, the P_N equations are given by expanding and projecting Equation (2.15), yielding:

$$\nabla \cdot \left[\sum_{\ell'}^{N} \frac{2\ell'+1}{4\pi} \sum_{m'=-\ell'}^{\ell'} \phi_{\ell',m'}(\mathbf{r}) \int_{4\pi} d\mathbf{\Omega} \mathbf{\Omega} Y_{\ell,m}(\mathbf{\Omega}) Y_{\ell',m'}(\mathbf{\Omega}) \right] + \Sigma(\mathbf{r}) \phi_{\ell,m}(\mathbf{r}) = Q_{\ell,m}(\mathbf{r}), \tag{2.43}$$

where the group index has been omitted, the indexes ℓ' and m' are those for the flux expansion while ℓ and m for the projected equation, and N is the order of the flux approximation, and we have used the orthogonality condition in the collision term and the source. Note that N must be greater than or equal to the order of anisotropy for the scattering source ($N \geq L$), but it is generally higher in order to better represent the anisotropy of the flux.

At this point we need to rearrange the term $\mathbf{\Omega} Y_{\ell,m}$ in Equation (A.1) so as to obtain the dependence among the angular moments and the system of P_N equations. To do that, a demonstration is given in Appendix A.

The recursive equation for the P_N method is:

$$\begin{aligned}
&\frac{\ell-|m|+1}{2\ell+1}\frac{N_\ell^m}{N_{\ell+1}^m}\frac{\partial\phi_{\ell+1,m}(\mathbf{r})}{\partial x}+\frac{\ell+|m|}{2\ell+1}\frac{N_\ell^m}{N_{\ell-1}^m}\frac{\partial\phi_{\ell-1,m}(\mathbf{r})}{\partial x}\\
&+\frac{1}{2(2\ell+1)}\frac{N_\ell^m}{N_{\ell-1}^{m+1}}\left[\frac{\partial\phi_{\ell-1,m+1}(\mathbf{r})}{\partial y}-\frac{\partial\phi_{\ell-1,-(m+1)}(\mathbf{r})}{\partial z}\right]\\
&-\frac{1}{2(2\ell+1)}\frac{N_\ell^m}{N_{\ell+1}^{m+1}}\left[\frac{\partial\phi_{\ell+1,m+1}(\mathbf{r})}{\partial y}-\frac{\partial\phi_{\ell+1,-(m-1)}(\mathbf{r})}{\partial z}\right]\\
&+\frac{(\ell-|m|+1)(\ell-|m|+2)}{2(2\ell+1)}\frac{N_\ell^m}{N_{\ell+1}^{m-1}}\left[\frac{\partial\phi_{\ell+1,m-1}(\mathbf{r})}{\partial y}+\frac{\partial\phi_{\ell+1,-(m-1)}(\mathbf{r})}{\partial z}\right]\\
&-\frac{(\ell+|m|)(\ell+|m|-1)}{2(2\ell+1)}\frac{N_\ell^m}{N_{\ell-1}^{m-1}}\left[\frac{\partial\phi_{\ell-1,m-1}(\mathbf{r})}{\partial y}+\frac{\partial\phi_{\ell-1,-(m-1)}(\mathbf{r})}{\partial z}\right]\\
&+\Sigma(\mathbf{r})\phi_{\ell,m}(\mathbf{r})=Q_{\ell,m}(\mathbf{r}),\qquad \ell\in[0,N],\quad m\in[-\ell,\ell],
\end{aligned}\tag{2.44}$$

which is used to produce as many equations as desired that approximate the angular flux up to the order N. The system to be solved is composed of $(N+1)^2$ first order differential equations in a 3D problem. The space-dependent solution is generally found using the finite difference or the finite element methods.

For reflective conditions the odd moments are typically set equal to zero at the boundaries, which leads to an exact treatment of the boundary condition. The vacuum boundary conditions are commonly treated using the Marshak boundary condition [12] or the Mark boundary condition, which are both approximate. The former is based on setting the odd moments equal to zero projected to the hemisphere of incoming directions, which leads to the weaker condition of zero incoming current instead of zero incoming angular fluxes. The Mark condition sets the angular flux of the incoming directions equal to zero, and these directions are the positive roots of the $(N+1)$-th Legendre polynomials in plane geometry.

As anticipated in Section 2.3, the system of equations is coupled by the streaming operator, where each angular moment is dependent on ten other moments in a 3D geometry. If on one hand the source term results to be simple to treat, on the other hand, the streaming term causes a strong coupling that makes the method difficult to solve in an efficient manner. For this reason, the P_N method is rather used with a low-order approximation or in simplified geometries such as in 1D, where most of the angular moments are null because of the geometrical symmetries. In this case, the system of equations can be directly obtained by considering only the streaming operator in Equation (A.10) along x and the moments with $m=0$:

$$\frac{\ell+1}{2\ell+1}\frac{d\phi_{\ell+1}(x)}{dx}+\frac{\ell}{2\ell+1}\frac{d\phi_{\ell-1}(x)}{dx}+\Sigma(x)\phi_\ell(x)=Q_\ell(x),\quad \ell\in[0,N],\tag{2.45}$$

that is equivalent to the 1D diffusion equation for a flux approximation order $N=1$ and scattering anisotropy order $L=0$.
Because of the simplified structure of the Equation (2.45), in 1960 Gelbard [13] pro-

posed a heuristic approach to use it in 2D and 3D problems, and named the new equations as the SP_N method, where S stands for simplified. This approach is based on the following replacements: $\frac{d}{dx} \to \nabla\cdot$ for the even ℓ equations, and $\frac{d}{dx} \to \nabla$ for the odd ℓ equations, yielding:

$$\begin{cases} \frac{\ell+1}{2\ell+1}\nabla\cdot\mathbf{\Phi}_{\ell+1} + \frac{\ell}{2\ell+1}\nabla\cdot\mathbf{\Phi}_{\ell-1} + \Sigma\phi_\ell = Q_\ell, & \ell \in [0, N-1],\ \ell \text{ even} \\ \frac{\ell+1}{2\ell+1}\nabla\phi_{\ell+1} + \frac{\ell}{2\ell+1}\nabla\phi_{\ell-1} + \Sigma\mathbf{\Phi}_\ell = Q_\ell, & \ell \in [1, N],\ \ell \text{ odd} \end{cases} \tag{2.46}$$

where ϕ_ℓ are the scalar even angular moments, $\mathbf{\Phi}_\ell$ are the vector odd angular moments and the $\mathbf{r}$-dependence has been omitted. These equations are indeed simplified with respect to the P_N method, so they can be solved more efficiently. It has been shown [14] that in some configurations using a higher order expansion than $N = 1$, the simplified P_N equations produce a more accurate solution than diffusion, when the latter is defined as SP_1. This can be explained by the fact that more angular moments are taken into accounts, and the transport effects, even if approximated, are better modeled especially if they can be well represented by a mono-dimensional problem. However, the fact of employing an incomplete basis of orthogonal functions does not guarantee the convergence of the numerical solution as ℓ increases [2]. Moreover, it has been shown that using the leakage coefficient as diffusion coefficient, obtained in B_1 leakage theory (presented in Chapter 3), a PWR core solution in diffusion theory shows to be more accurate than SP_5 [15], especially for a small number of energy groups, despite being more rapid to compute.

2.4.2 The Discrete Ordinates Method

The S_N approximation [16] is one of the most widely used methods developed in transport codes for high fidelity simulations due to its computational efficiency. As said in Section 2.3, in this technique the angular flux is computed for a finite number of directions $\mathbf{\Omega}_d$, so that the mono-kinetic transport equation becomes a system of N_d first order differential equations, with N_d the number of directions. These equations are coupled by the angular dependent source term, which becomes a linear combination of the angular fluxes ψ_d with directions $\mathbf{\Omega}_d$, and, omitting the group index, they have the following form:

$$[\mathbf{\Omega}_d\cdot\nabla + \Sigma(\mathbf{r})]\psi_d(\mathbf{r}) = Q_d(\mathbf{r}), \quad d = 1 \text{ to } N_d \tag{2.47}$$

with

$$Q_d(\mathbf{r}) = \sum_{\ell=0}^{L}\frac{2\ell+1}{4\pi}\sum_{m=-\ell}^{\ell} Y_{\ell,m}(\mathbf{\Omega}_d)Q_{\ell,m}(\mathbf{r}). \tag{2.48}$$

In the last equations, $\mathbf{\Omega}_d$ is the directional vector containing the cosines with respect to the three axes ($\mathbf{\Omega}_d = [\mu_d, \eta_d, \zeta_d]$) and the source moments are given by Equation (2.17). These moments depend on the flux moments, and the closure equation is given by the

quadrature formula as follows:

$$\phi_{\ell,m}(\mathbf{r}) = \int_{4\pi} d\mathbf{\Omega} Y_{\ell,m}(\mathbf{\Omega})\psi(\mathbf{r},\mathbf{\Omega}) \approx \sum_{d}^{N_d} w_d Y_{\ell,m}(\mathbf{\Omega}_d)\psi_d(\mathbf{r}). \tag{2.49}$$

In the particular case of the moments for $\ell = 1$, the net currents, or similarly the partial currents, are determined with the following expression:

$$\mathbf{J}(\mathbf{r}) \cdot \mathbf{n}_i \approx \sum_{d}^{N_d} w_d \mu_{i,d} \psi_d(\mathbf{r}), \tag{2.50}$$

with $\mu_{i,d}$ the direction cosine with respect to the axis i. The boundary conditions for the discrete ordinates method are naturally defined as:

$$\psi_d(\mathbf{r_b}) = \psi^-(\mathbf{r_b}, \mathbf{\Omega}_d), \quad \mathbf{n} \cdot \mathbf{\Omega}_d < 0.$$

The quadrature rule is generally built so as to integrate exactly the highest number of spherical harmonics in Equation (2.49) by minimizing the number of quadrature points. The most popular types of quadrature rules are the triangular and the product ones. The former are constructed so as to preserve planar symmetries and rotations between the axes, thus they are also called level-symmetric quadratures and the discrete direction form a triangular pattern with respect to a plane. Because of their construction, these quadrature rules may lead to negative weights when increasing in the number of quadrature points [2]. In triangular rules the approximation order N of the S_N method indicates the number of distinct direction cosines for each axis associated to (μ, η, ζ). For instance, an S_{16} triangular formula has 16 distinct cosines for each axis, resulting in a total number of directions $N_d = N(N+2) = 288$.
The product quadratures, instead, combine two one-dimensional quadratures with positive weights that are typically a Gauss-Legendre quadrature for the cosine of the polar angle, and a Chebyshev-Gauss quadrature for the azimuthal angle, which is used to approximate integrals of the form:

$$\int_{-1}^{1} \frac{f(x)}{\sqrt{1-x^2}}\, dx\,.$$

An inner iteration consists of solving Equation (2.47) for all the directions, and eventually the self-scattering source is updated with the new angular fluxes. At this point Equation (2.47) is discretized in space defining a computational mesh that is composed of homogeneous cells. The angular flux ψ_d exiting a computational cell is then used as incoming angular flux for the downstream adjacent ones. The advantage of this approach is the possibility to avoid a direct inversion of the complete matrix containing coefficients for all the spatial regions in the domain.

For a given incoming flux, in order to compute the interior and the exiting fluxes of a cell, it is necessary not only the balance equation (2.47), but also an auxiliary equation that relates volume-averaged quantities, required for the source terms, with surface-averaged ones. Generally, the interior flux is eliminated such that Equation (2.47) is solved in favor of the outgoing flux, that is then directly available for the neighboring cells.
The auxiliary equations are given by the spatial representation for the flux that is assumed by the numerical method adopted for the approximation of the spatial derivative. The simplest method is the Diamond Difference (DD) scheme, used for Cartesian meshes, which assumes the interior flux as the average of the surface fluxes. Other popular numerical approximation in Cartesian geometries are the characteristics and the transverse nodal schemes [17, 18].
The characteristics scheme uses the integral form of the transport equation in order to introduce an auxiliary transmission equation for the surface fluxes, while the interior flux is deduced by local balance. The transverse nodal scheme is based on a transverse integration procedure which consists in a projection of the flux over each Cartesian axis, and it introduces a polynomial expansion for the spatial representation of the projected flux. It can be shown that this leads to a representation of 3D flux as an expansion in products of polynomials. The mono-kinetic mono-directional equation becomes then a system of three mono-dimensional equations (one for each spatial dimension), coupled by a term of transverse leakage expressed as an additional volumetric source.

Finally, the Discontinuous Finite Element Method (DFEM) is employed for both Cartesian and unstructured meshes and are typically based on the Galerkin projection of the transport equation so as to obtain a system of equations for the volumetric flux. Unlike in transverse nodal methods, where the expansion concerns the projected flux, the DFEM directly expands the 3D flux in polynomial functions that are defined over the computational cell or element, and the exiting flux is simply evaluated as the volumetric flux at the border of the element.

The main disadvantage of the S_N approximation is the ray effect, which typically arises in problems described by at least two angular coordinates (1D cylinder, 2D and 3D Cartesian) when the sources are localized in the domain and the media have low scattering. It is caused by the insufficient quadrature points for the angular flux used to represent a continuous distribution. The method exhibits then oscillations of flux that are generally limited employing ad hoc methods, or simply increasing the approximation order of the angular quadrature.

The S_N approach is suitable for parallel algorithms, mainly due to the low coupling of the angular fluxes. In one inner iteration, in fact, the angular source is fixed and therefore the unknowns $\psi_d(\mathbf{r})$ are independent of each other. The domain can then be swept for different directions at the same time using several processors, and the information is exchanged only at the end of the sweep so as to update the source.

2.4.3 The Collision Probability Method

The collision probability method results from the projection on spherical harmonics of the integral form of the transport equation, that produces a system of equations of

the form presented in Equation (2.41) as follows:

$$\phi_{\ell,m}(\mathbf{r}) = \int_V d^3\mathbf{r}' \frac{e^{-\tau(\mathbf{r}',\mathbf{r})}}{|\mathbf{r}-\mathbf{r}'|^2} Y_{\ell,m}(\mathbf{\Omega}_s) Q(\mathbf{r}', \mathbf{\Omega}_s) + \int_{\partial V} d^2\mathbf{r}' Y_{\ell,m}(\mathbf{\Omega}_s) \psi^-(\mathbf{r}', \mathbf{\Omega}_s) \frac{e^{-\tau(\mathbf{r}',\mathbf{r})}}{|\mathbf{r}-\mathbf{r}'|^2}, \quad \forall \ell, m. \tag{2.51}$$

We remind the reader that $\mathbf{\Omega}_s = \frac{\mathbf{r}-\mathbf{r}'}{|\mathbf{r}-\mathbf{r}'|}$, which comes up from the $\delta_{\mathbf{\Omega}_s}$, and that ψ^- is defined only on the hemisphere with negative $(\mathbf{n} \cdot \mathbf{\Omega}_s)$.
Because of the full coupling in space that can easily lead to expensive calculations, historically these equations have been solved introducing some approximations on the scattering source. A truncation of the source expansion is typically applied up to the order of anisotropy $L = 1$. However, the most widely used assumption is to consider only isotropic sources, for which $Y_{0,0} = 1$. It follows that both volumetric and boundary sources are isotropic, and the former is generally calculated with transport corrected P_0^* scattering. This assumption greatly simplifies the computation because it eliminates the angular variable, resulting in only one equation for the scalar flux that reads:

$$\phi(\mathbf{r}) = \int_V d^3\mathbf{r}' \frac{e^{-\tau(\mathbf{r}',\mathbf{r})}}{|\mathbf{r}-\mathbf{r}'|^2} Q^{0^*}(\mathbf{r}') + \int_{\partial V} d^2\mathbf{r}' \frac{J^-(\mathbf{r}')}{\pi} \frac{e^{-\tau(\mathbf{r}',\mathbf{r})}}{|\mathbf{r}-\mathbf{r}'|^2}, \tag{2.52}$$

where Q^{0^*} is the total in-group source with P_0^* scattering, and $\frac{J^-}{\pi}$ is the isotropic component of the incoming boundary flux, that introduces further approximations to the equation.
In order to numerically solve the last equation in multidimensional geometries, the domain is divided into a finite number of homogeneous regions N_r, and for simplicity both scalar flux and the cross sections are supposed constant within a region, although not necessary. The volume integral in the whole domain becomes then a sum over all regions j of volume V_j and the surface integral on the boundaries becomes a sum over the N_s boundary surfaces S_b with area A_b. The equation is then integrated over the volume of a region i as follows:

$$V_i \phi_i = \sum_j^{N_r} Q_j^{0^*} \int_{V_i} d^3\mathbf{r} \int_{V_j} d^3\mathbf{r}' \frac{e^{-\tau(\mathbf{r}',\mathbf{r})}}{|\mathbf{r}-\mathbf{r}'|^2} + \sum_b^{N_s} \frac{J_b^-}{\pi} \int_{V_i} d^3\mathbf{r} \int_{S_b} d^2\mathbf{r}' \frac{e^{-\tau(\mathbf{r}',\mathbf{r})}}{|\mathbf{r}-\mathbf{r}'|^2}.$$

The last equation can be compacted in the following form:

$$V_i \phi_i = \sum_j^{N_r} Q_j^{0^*} V_j P_{ij} + \sum_b^{N_s} J_b^- A_b P_{ib}, \tag{2.53}$$

with

$$P_{ij} = \frac{1}{V_j} \int_{V_i} d^3\mathbf{r} \int_{V_j} d^3\mathbf{r}' \frac{e^{-\tau(\mathbf{r}',\mathbf{r})}}{|\mathbf{r}-\mathbf{r}'|^2}, \tag{2.54}$$

and

$$P_{ib} = \frac{1}{\pi A_b} \int_{V_i} d^3\mathbf{r} \int_{S_b} d^2\mathbf{r}' \frac{e^{-\tau(\mathbf{r}',\mathbf{r})}}{|\mathbf{r}-\mathbf{r}'|^2}, \tag{2.55}$$

where we have applied the reciprocity property of the P_{ij} matrix. This property comes from the fact that $\tau(\mathbf{r}',\mathbf{r}) = \tau(\mathbf{r},\mathbf{r}')$, for which $P_{ji}V_i = P_{ij}V_j$ and $P_{bi} = \frac{A_b}{4}P_{ib}$, which entails that the P_{ij} matrix is symmetric and, therefore, the number of coefficients to be computed is $N_r(N_r+1)/2$. Each element of this matrix P_{ij} corresponds to the probability that a neutron emitted uniformly and isotropically in region j can be transmitted to the region i. The product of this probability times the total macroscopic cross section $\Sigma_i P_{ij}$ is called the "first-flight collision probability" in zone i for a neutron uniformly and isotropically emitted in j, from which the method takes the name [10]. The matrix P_{ib}, instead, represents the uncollided flux at i produced by one neutron entering the body in b uniformly and isotropically, and $\frac{P_{bi}}{V_i}$ is the first-flight escape probability from i across b. We can also define a transmission probability $P_{bb'}$ that represents the probability that a particle entering isotropically across a surface b exits across surface b':

$$P_{b'b} = \frac{1}{\pi A_b} \int_{S_{b'}} d^2\mathbf{r} \int_{S_b} d^2\mathbf{r}' \frac{e^{-\tau(\mathbf{r}',\mathbf{r})}}{|\mathbf{r}-\mathbf{r}'|^2}, \tag{2.56}$$

that can be used to write an equation for the outgoing flux as follows:

$$A_{b'} \frac{J_{b'}^+}{\pi} = \sum_j^{N_r} Q_j^{0^*} V_j P_{b'j} + \sum_b^{N_s} J_b^- A_b P_{b'b}. \tag{2.57}$$

The elements of the CP matrix are determined with a numerical integration using the information of a tracking technique and the knowledge of the total macroscopic cross section in a computational region. Moreover, in order to determine the contribution in the collision probability matrix of the reflective condition at the boundaries, the trajectories are generally reflected to the specular directions and the integration is also performed "outside" the computational domain. This is possible because the information is available "inside" the geometrical motif that is repeated infinite number of times. When the contribution of the boundary conditions to a region of the domain becomes negligible because of the distance traveled along a trajectory, the integration is interrupted.

The CP method is mainly applied to small geometries where the number of regions is relatively small, due to their full coupling. Another limitation of the method is the approximation of the isotropic angular source, that otherwise would involve the computation of higher angular moments with similar full matrices. On the other hand, the method offers the advantage of eliminating the angular variable with no approximations on the flux representation and, additionally, the possibility to group several regions with similar properties and environment, under the assumption that they ex-

perience a similar neutron flux.

2.4.4 The Method of Characteristics

The Method of Characteristics overcomes the limitations of CP by employing a quadrature method for the representation of the angular flux, instead of expanding and projecting. Because of this, the MOC is often considered a discrete ordinate method but, similarly to CP, it involves the resolution of the integral form of the transport equation. The method that was firstly proposed in the seventies [19], partitions a general unstructured geometry into regions where the cross sections are typically supposed constant (homogeneous region). For each discrete direction $\mathbf{\Omega}_d$ of the quadrature formula, a set of parallel trajectories is traced in the whole geometry from boundary to boundary, for which the method is also known as method of long characteristics. Each characteristic line has a cross-sectional area that is also called transverse weight w_t because it is used for space integration. Depending on trajectory density and their cross-sectional area, a certain number of trajectories will cross a region as shown in Figure 2.1. In particular, the trajectories of this figure have constant transverse weight, resulting in a rectangular tracking that is the simplest and most widely used tracking technique for the long characteristics. The information required by a trajectory t for a given direction $\mathbf{\Omega}_d$ and transverse weight w_t, is the ensemble of intersections k with the regions in the domain, that are represented by the region index r and the cord length l across the region: $t = \{r_k, l_k, k = 1, N_k\}$. The volume of a region V_r^d results to be angular dependent, and it equals the sum of the volumes traced by the trajectories as follows:

$$V_r^d = \sum_{\substack{t \| \mathbf{\Omega}_d \\ t \cap r}} w_t l_t. \tag{2.58}$$

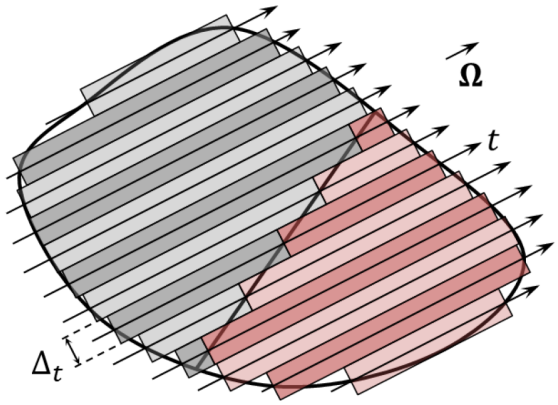

Figure 2.1. Space discretization based on trajectory tracking. Figure modified from [20].

The most common representation of the flux is the Step Characteristic scheme, where the emission density is supposed flat inside a region. The flux follows the same representation of the source as usual. The methods of characteristics typically utilize the integral transport equation as transmission equation to compute the angular flux

exiting a region along a trajectory as follows:

$$\begin{aligned}\psi^{+}_{t,r,d} =& \psi^{-}_{t,r,d} e^{-\int_0^{l_t} ds \Sigma_r} + \int_0^{l_t} ds Q_{r,d} e^{-\int_s^{l_t} dt' \Sigma_r} \\ =& \psi^{-}_{t,r,d} e^{-\Sigma_r l_t} + \frac{1 - e^{-\Sigma_r l_t}}{\Sigma_r} Q_{r,d},\end{aligned} \tag{2.59}$$

where $\psi^{\pm}_{t,r,d}$ are the angular fluxes respectively exiting and entering a region r along an intersecting trajectory t with direction d and the total macroscopic cross section Σ_r and the angular source $Q_{r,d}$ are supposed constant within the region r. The inner iterations are carried out by a region-to-region sweep along all the trajectories. At the end of an inner iteration, the source moments have to be updated, and this involves the computation of the average angular flux in each region and direction $\psi_{r,d}$. In the step approximation, it is determined by simply averaging the fluxes of all trajectories crossing a region:

$$\psi^{i+1}_{r,d} = \frac{1}{V_r} \int_{V_r} d\mathbf{r} \psi^{i+1}(\mathbf{r}, \mathbf{\Omega}) = \frac{1}{V_r} \int_{S_r} d\mathbf{r}_\perp \int_0^l ds \psi^{i+1}(\mathbf{r}_\perp + s\mathbf{\Omega}) \approx \frac{\sum_{\substack{t \| \mathbf{\Omega}_d \\ t \cap r}} w_t l_t \overline{\psi}^{i+1}_{t,r,d}}{\sum_{\substack{t \| \mathbf{\Omega}_d \\ t \cap r}} w_t l_t},$$

where i is the inner iteration index and $\overline{\psi}_{t,r,d}$ is the average volumetric angular flux in a cord. In order to compute the latter, a balance equation is applied to the cord, that is obtained by averaging along the cord length either the integral or the integrodifferential transport equation:

$$\begin{aligned}&\frac{d}{ds}\psi_{t,r,d}(s) + \Sigma_r \psi_{t,r,d}(s) = Q_{r,d} \\ &\psi^{+}_{t,r,d} - \psi^{-}_{t,r,d} + \Sigma_r l_t \overline{\psi}_{t,r,d} = Q_{r,d} l_t, \\ &\overline{\psi}_{t,r,d} = \frac{1}{\Sigma_r}[Q_{r,d} - \frac{\psi^{+}_{t,r,d} - \psi^{-}_{t,r,d}}{l_t}].\end{aligned}$$

However, for the step approximation it is more convenient to apply the balance equation directly to the region rather than each trajectory, resulting in a lesser number of operations. It follows that:

$$\psi^{i+1}_{r,d} = \frac{Q^{i}_{r,d}}{\Sigma_r} - \frac{1}{\Sigma_r V^d_r} \sum_{\substack{t \| \mathbf{\Omega}_d \\ t \cap r}} w_t [\psi^{+,i+1}_{t,r,d} - \psi^{-,i+1}_{t,r,d}], \tag{2.60}$$

where the net angular current is directly computed manipulating the transmission

equation as follows:

$$[\psi^+_{t,r,d} - \psi^-_{t,r,d}] = (\frac{Q_{r,d}}{\Sigma_r} - \psi^-_{t,r,d})(1 - e^{\Sigma_r l_t}). \tag{2.61}$$

Finally, the angular moments of the flux required for the computation of the emission density are determined as for any S_N method with an angular quadrature formula:

$$\phi_{r,\ell,m} \approx \sum_d^{N_d} w_d Y_{\ell,m}(\mathbf{\Omega}_d)\psi_{r,d}. \tag{2.62}$$

Several schemes for the approximation of the angular flux in a region or along a trajectory have been implemented, by assuming for instance a polynomial representation such as $\psi(\mathbf{r}, \mathbf{\Omega}) = \psi(\mathbf{\Omega}) \cdot f(\mathbf{r})$. The most popular higher order schemes are the linear characteristic [21] and the linear surface characteristic schemes [22], where the latter uses linear interpolation on surface values for the angular source. High order schemes allow to decrease the number of regions to be computed obtaining the same precision of the step characteristics. On the other hand, the step scheme is intrinsically conservative and leads to positive values for the source and the angular fluxes.

The boundary conditions for the MOC can easily be included in the transmission equation when the incoming flux at the boundaries is a known quantity. Nevertheless, for those boundary conditions where an entering flux is a function of an exiting flux, such as specular reflection, periodic and translation boundary conditions, a set of cyclic trajectories is generally applied, because it is a strategy capable to treat exactly the fluxes at the boundaries. The cyclic trajectories are reintroduced inside the domain when they reach a boundary, generally reflected in the specular direction. Depending on the geometry to be treated, they are constructed so as they can return back to the exact point where they have been introduced at first. This allows to express the period L of a trajectory as the distance traveled to reach the starting point, such that:

$$\psi_t(s + L) = \psi_t(s). \tag{2.63}$$

Using the last property in Equation (2.59), the incoming angular flux can be determined after one cycle as follows:

$$\psi^-_t = \frac{\int_0^L ds Q(s) e^{-\int_s^L dt' \Sigma(t')}}{1 - e^{-\int_0^L ds \Sigma(s)}} \tag{2.64}$$

where the integral values are cumulated and stored during the first sweep. The last equation can be seen as an acceleration for the convergence of the boundary conditions that, otherwise, would require more inner iterations to reach the converged values.

The method of characteristic is a powerful tool because it allows to treat exactly any unstructured geometry with the only approximation of the multigroup formalism

if the spatial integration is fine enough. Its solution is often considered as the closest to Monte Carlo and also as numerical reference for other deterministic methods. The numerical reference differs from the physical reference (Monte Carlo), because it involves only validation of the flux solver for a given set of self-shielded multigroup cross sections. Another advantage of the method is the minimization of the memory requirement, because it does not involve the storage of matrix coefficients for the sweep, since the integral operators are pre-tabulated in terms of optical paths $\tau = \Sigma l$, and computed "on-the-fly" using a linear interpolation. This peculiarity becomes considerably advantageous when the domain is composed of a large number of different types of media, for which other numerical methods generally require evaluation of matrices that are specific of each medium. For instance, this can easily arise in case of depleting media whose isotopic composition depends on local reaction rates. Moreover, as for any S_N method, the MOC can be easily parallelized in terms of sweep, where each process task involves integration along a single trajectory.

On the other hand, the method presents some limitations in terms of computational cost for large systems. The problem is mainly due to the tracking strategy that can drastically affect the precision of MOC if trajectories are not dense enough. In order to precisely integrate in space, in fact, it is necessary to trace in such a way that several trajectories cross the same computational region for a given direction. In the case of a rectangular tracking strategy where the transverse weight is constant for all parallel trajectories, it is often necessary that this weight is many times smaller than the transverse projection of the smallest region in the domain. If this condition is not satisfied and the cross-sectional area is too large, it may happen that a rectangle of volume $w_t l_t$ used for integration, intersects more than one region. However, the intersections are generally determined with a center line that may not cross all the regions in the rectangle. It ensues that the contribution of the sources of the "non-contemplated" regions in the tube is not accounted, resulting in region numerical dispersion. This problem is represented in Figure 7-I of [23]. One is then obliged to trace finely enough in order to have a precise and stable computation. Consequently, the higher the number of trajectories, the higher the computational cost. Sometimes even only one small region located in a zone of the domain can compromise the performance of the method, since the transverse weight is constant everywhere, also for regions where it is not necessary. In case of domain decomposition, the cost of the operations can be highly reduced thanks to the parallelization, because a trajectory is swept only locally from boundary to boundary of a subdomain, instead of sweeping the whole domain. On the other hand, one has to store the interface fluxes that are transmitted to the neighboring subdomains for each trajectory crossing the boundaries in each exiting direction and for each energy group, resulting in a large amount of data to be exchanged.

Another tracking strategy has been proposed in order to reduce the region numerical dispersion while minimizing the number of trajectories. The idea is to project all discontinuities on the transverse plane for a given direction, and use a Gaussian quadrature, generally a three-point formula, in each macro segment to integrate in volume. This technique allows to integrate exactly with no region numerical dispersion, but it is not effective for large domains where there are a lot of media and discontinuities, because the number of segments projected on the transverse plane can be too many and the segment itself too small. It ensues that the number of trajectories can be even

higher than the rectangular tracking. Some other tracking strategies such as the macro band technique [24] have been developed as compromise of the discontinuity projection and the rectangular strategies.
However, the Gaussian quadrature technique is a strategy suitable for hybrid methods, where the domain is partitioned into a finite number of nodes, and the discontinuities can be locally, and not globally, projected in order to integrate the motif efficiently, as we shall see in the next sections for IC and MOSC.

2.4.5 The Interface Current Method

The idea of the Interface Current method is to divide the domain into a finite number of nodes, that generally corresponds to a pin cell for a fuel assembly. Then the CP method is applied independently to each node in order to compute the incoming, collision, transmission and escape matrices presented in Equation (2.34). Any method can be applied to produce these matrices, but the choice of CP is justified on one hand by the fact that it is an integral method, so it can treat exactly any unstructured geometry inside the node and, on the other hand, by historical reasons since CP was more popular than MOC for assembly calculations, where the number of regions was still relatively small and the transport corrected P_0^* source was a common approximation.

The result of this approach is a drastic reduction of the coupling between regions of the domain, which entails that the cost of computing the IC matrices is much lower than the full CP matrices. Moreover, one generally subdivides the domain so as to obtain an ensemble of nodes with same geometrical and isotopic characteristics, which is a common feature in fresh fuel assemblies and cores. It follows that the IC matrices are stored only for each node type and not for each node, decreasing the memory requirements with respect to a full CP calculation.
Because of the aforementioned points, the IC method offers much higher performances than CP, but it requires the introduction of an approximation for the representation in space and angle of the interface fluxes transmitted to the neighboring nodes. The interface fluxes, in fact, are expanded on polynomial functions that are projected to the external surfaces of the node. Although not necessary, however, the fluxes in IC are typically constant in both regions and surfaces of the node. Because IC belongs to the class of projection methods, the surface angular flux is generally represented with a double expansion $\mathrm{DP_N}$ as follows:

$$\psi^{\pm}(\mathbf{r}_s, \mathbf{\Omega}) = \sum_n J_n^{\pm}(\mathbf{r}_s) f_n(\mathbf{\Omega}), \tag{2.65}$$

where $\mathbf{r}_s$ is a point in the external surface of the node, $J_n^{\pm}$ the angular moments and f_n the polynomial basis defined on a node surface for $\pm(\mathbf{n}\cdot\mathbf{\Omega}) > 0$ such that:

$$\int_{2\pi} d\mathbf{\Omega}(\mathbf{n}\cdot\mathbf{\Omega}) f_n(\mathbf{\Omega}) f_m(\mathbf{\Omega}) = \pm\frac{\delta_{nm}}{\pi}. \tag{2.66}$$

The system of equations for a node is then obtained by substituting the new definition

of the surface flux to Equations (2.53) and (2.57):

$$\begin{cases} \phi_i V_i = \sum_j^{N_r} Q_j V_j P_{ij} + \sum_b^{N_s} \sum_n J_n^- P_{ib}^n A_b \\ J_{n',b'}^+ A_{b'} = \sum_j^{N_r} Q_j V_j P_{jb'}^n + \sum_b^{N_s} \sum_n J_n^- P_{b'b}^{n'n} A_b \end{cases} \tag{2.67}$$

where the matrices P_{ib}^n and $P_{b'b}^n$ are obtained by projection on the polynomial function of the matrices respectively P_{ib} and $P_{b'b}$. The outgoing flux is then used as incoming flux for the adjacent nodes, allowing an iterative strategy with a cell-to-cell sweep. The angular expansion for the surface flux is generally truncated up to the second order, also justified by the coarse projection in space. A detailed angular representation, in fact, typically requires a fine discretization in space in order to be properly taken into account. Some variations of the method, instead of applying the CP method in the node, utilize a 2D model in cylindrical coordinates to compute the IC matrices analytically, sometimes with an intermediary projections on interior surfaces, resulting in a faster computation.
The IC method can easily fail in case of strong gradients where the approximation at the node interfaces is not sufficient to represent the actual situation. This problem is caused by the fact that the neutron flux is no more continuous along trajectories, and a loss of information arises at the interfaces due to the spatial and angular projections. This phenomenon is also known as interface numerical dispersion [23].

2.4.6 The Method of Short Characteristics

The method of short characteristic is based on the same approach of the interface current method, so it relies on domain partition into a finite number of nodes, on the spatial projection technique for the surface fluxes at the node interfaces, but, unlike the IC method, it avoids the angular projection. The similitudes between integral and hybrid methods discussed so far can be summarized by the following mathematical proportion [25]:

$$\textbf{IC} \ : \ \textbf{CP} \ = \ \textbf{MOSC} \ : \ \textbf{MOC}$$

The four interface-current matrices in MOSC are determined applying independently the MOC to each node type. These matrices are defined for each discrete direction and an S_N quadrature is used for angular integration.
The angular information at the node interfaces results to be much finer with respect to the IC method, amounting to one value per direction and surface instead of two values per surface (one for each hemisphere in the DP_0 expansion). In the IC method, this is justified by the fact that the projection surfaces are quite coarse, and a higher order angular representation would not improve considerably the quality of the solution if the spatial representation is not refined as well. By contrast, for MOSC in terms of gain in accuracy versus degree of discretization, it is advantageous to have a finer spatial representation for the surface fluxes with respect to the IC method, that is achieved by subdividing each external surface of a node into few subsurfaces, and by

introducing a higher order polynomial expansion for the surface flux. The volumetric fluxes and the internal sources are also expanded on a polynomial basis, giving the advantage to decrease the number of computational regions in the node. However, the polynomial expansion increases the number of floating operations per region, so it can offer improved performances than a step approximation if the number of regions is reduced enough in order to compensate this extra-cost.

The MOSC is then more expensive but more accurate than IC and, on the other hand, more performant than MOC especially for large systems, where trajectory sweeping from boundary to boundary results in much more floating operations than cell-to-cell sweeping from boundary to boundary. This is mainly due to the higher number of angular fluxes to be swept in MOC because of a large number of trajectories, for which, otherwise, the calculation would be affected by region numerical dispersion.
The method of short characteristic is presented here as it has been developed in the IDT solver [17, 26, 27]. In these works the surface expansion is applied to a 2D or 3D rectangular cell called Heterogeneous Cartesian Cell (HCC), and the interior regions are defined using concentric circles or cylinders (respectively in 2D and 3D configurations). These two geometrical simplifications are not necessary to apply the method, but they allow fast tracking and computation of the matrices and an efficient sweep. Moreover, this type of geometry is characteristic in water reactors.
The volumetric angular flux of a node is represented with the polynomial expansion as follows:

$$\psi(\mathbf{r}, \mathbf{\Omega}_d) \approx \sum_{r}^{N_r} \sum_{n=0}^{N_n} f_{r,n}(\mathbf{r}) \psi_{r,n}(\mathbf{\Omega}_d), \tag{2.68}$$

which entails that the source follows the same expansion:

$$Q(\mathbf{r}, \mathbf{\Omega}_d) \approx \sum_{r}^{N_r} \sum_{n=0}^{N_i} f_{r,n}(\mathbf{r}) Q_{r,n}(\mathbf{\Omega}_d), \tag{2.69}$$

and similarly for the surface fluxes that are expanded on a different basis:

$$\psi^{\pm}(\mathbf{r}, \mathbf{\Omega}_d) \approx \sum_{s}^{N_s^{\pm}} \sum_{b=0}^{N_b} f_{s,b}(\mathbf{r}) \psi_{s,b}^{\pm}(\mathbf{\Omega}_d). \tag{2.70}$$

In the last equations, N_r and N_i are respectively the number of interior regions and the degree of freedom of the volumetric expansion, while $N_s^{\pm}$ and N_b are respectively the number of external surfaces in a node in the upstream directions $(-)$ and downstream directions $(+)$, and the degree of freedom of the surface expansion. The polynomial functions are orthonomalized as follows:

$$\langle f_{r,n}, f_{r,n'} \rangle_r = V_r \delta_{nn'} \tag{2.71}$$

and

$$\langle f_{s,b}, f_{s,b'} \rangle_s = A_s \gamma_s(\mathbf{\Omega}) \delta_{bb'}, \quad \text{with} \quad \gamma_s(\mathbf{\Omega}) = |\mathbf{n}_s \cdot \mathbf{\Omega}|. \tag{2.72}$$

where V_r is the volume of region r and A_s the area of surface element s. The spatial coordinate $\mathbf{r}$ is defined with respect to the center of mass of the node and the polynomial basis for a linear expansion have the following forms:

$$\mathbf{f}_r = \begin{bmatrix} 1 \\ \mathbf{r} - \mathbf{r}_r \end{bmatrix}, \quad \mathbf{f}_s = \begin{bmatrix} 1 \\ \mathbf{r} - \mathbf{r}_s \end{bmatrix}$$

where $\mathbf{r}_r$ and $\mathbf{r}_s$ are the centers of mass respectively for region r and surface s.
The linear moments are orthogonal to the constant moment but not necessarily to each other, therefore, we define the mass matrices of a region r and a surface s as follows:

$$\mathbf{M_r} = \langle \mathbf{f}_r, \mathbf{f}_r \rangle = \begin{bmatrix} V_r & \mathbf{0} \\ \mathbf{0} & \langle \mathbf{r} - \mathbf{r}_r, \mathbf{r} - \mathbf{r}_r \rangle \end{bmatrix}, \quad \mathbf{M_s} = \langle \mathbf{f}_s, \mathbf{f}_s \rangle = \begin{bmatrix} A_s & \mathbf{0} \\ \mathbf{0} & \langle \mathbf{r} - \mathbf{r}_s, \mathbf{r} - \mathbf{r}_s \rangle \end{bmatrix}.$$

The volumetric and surface moments of the angular flux are then defined such that:

$$\mathbf{\Psi}_r^d = [\mathbf{M_r}]^{-1} \langle \mathbf{f}_r(\mathbf{r}), \psi(\mathbf{r}, \mathbf{\Omega}_d) \rangle = [\mathbf{M_r}]^{-1} \int_{V_r} d\mathbf{r}\, \mathbf{f}_r(\mathbf{r}) \psi(\mathbf{r}, \mathbf{\Omega}_d) \tag{2.73}$$

$$\mathbf{\Psi}_s^{\pm\, d} = [\mathbf{M_s}]^{-1} \langle \mathbf{f}_s(\mathbf{r}), \psi^{\pm}(\mathbf{r}, \mathbf{\Omega}_d) \rangle = [\mathbf{M_s}]^{-1} |\mathbf{n}_s \cdot \mathbf{\Omega}_d| \int_{A_s} d\mathbf{r}\, \mathbf{f}_s(\mathbf{r}) \psi^{\pm}(\mathbf{r}, \mathbf{\Omega}_d), \tag{2.74}$$

The zeroth spatial moments $\psi_{r,0}$ and $\psi^{\pm}_{s,0}$ correspond respectively to the average angular flux in region r and the average angular currents exiting $(+)$ and entering $(-)$ the surface element s.
In order to compute the interface current matrices, we trace a set of trajectories within the node, and rewrite the MOC equation along a trajectory (Equation (2.59)) in the following form:

$$\begin{aligned} \psi_t(\mathbf{r}_t^- + s\mathbf{\Omega}_d, \mathbf{\Omega}_d) = {} & \psi_t^-(\mathbf{r}_t^-, \mathbf{\Omega}_d) e^{-\tau_t(0,s)} \\ & + \sum_{j \in t}^{i} \int_{s_{j-1}}^{\min(s, s_j)} dt\, Q(\mathbf{r}_t^- + t\mathbf{\Omega}_d, \mathbf{\Omega}_d) e^{-\tau_t(t,s)} \end{aligned} \tag{2.75}$$

where ψ_t is the angular flux along a trajectory t, j is the index for the intersections between the trajectory and all the regions and surfaces in the node, i is the first intersection downstream the point s, s_j is the distance of the intersection point j from the point $\mathbf{r}_t^-$, that is the intersection of the trajectory with the upstream external

surface of the node ($s_0 = 0$). Moreover, for a simpler notation we have used the following definition:

$$\tau_t(x, y) = \tau(\mathbf{r}_t^- + x\mathbf{\Omega}_d, \mathbf{r}_t^- + y\mathbf{\Omega}_d) = \int_x^y ds\Sigma(\mathbf{r}_t^- + s\mathbf{\Omega}_d).$$

We now substitute the definitions in Equations (2.69) and (2.70) into the right side of Equation (2.75):

$$\begin{aligned}\psi_t(\mathbf{r}_t^- + s\mathbf{\Omega}_d, \mathbf{\Omega}_d) = &\sum_{s'}^{N_s^-} \mathbf{f}_{s'}^{\mathbf{T}}(\mathbf{r}_t^-) \cdot \mathbf{\Psi}_{s'}^{-\,d} e^{-\tau_t(0,s)} \\ &+ \sum_{r'}^{N_r} \sum_{j \in t \cap r'}^{i} \int_{s_{j-1}}^{\min(s,s_j)} dt\, \mathbf{f}_{r'}^{\mathbf{T}}(\mathbf{r}_t^- + t\mathbf{\Omega}_d) \cdot \mathbf{Q}_{r'}^d e^{-\tau_t(t,s)}\end{aligned} \tag{2.76}$$

where we have written the sum over the moments as scalar product between the basis vector and the moments vector, and $\mathbf{T}$ stands for transpose. The flux moments in region r are obtained projecting Equation (2.76) on the polynomial basis. To do that, we need to apply Equation (2.73) integrating with trajectories as follows:

$$\begin{aligned}\mathbf{\Psi}_r^d &= [\mathbf{M_r}]^{-1} \int_{V_r} d\mathbf{r}\, \mathbf{f}_r(\mathbf{r}) \psi(\mathbf{r}, \mathbf{\Omega}_d) \\ &\approx [\mathbf{M_r}]^{-1} \sum_{\substack{t \| \mathbf{\Omega}_d \\ t \cap r}} w_t \sum_{i \in t \cap r} \int_{s_{i-1}}^{s_i} ds\, \mathbf{f}_r(\mathbf{r}_t^- + s\mathbf{\Omega}_d) \psi_t(\mathbf{r}_t^- + s\mathbf{\Omega}_d, \mathbf{\Omega}_d),\end{aligned} \tag{2.77}$$

where w_t is the transverse weight of trajectory t and the integration in the region volume becomes a sum of integrals over the cords length traced by the trajectory. We now substitute Equation (2.76) in (2.77) so as to obtain the first equation for the volumetric moments of angular flux in region r:

$$\mathbf{\Psi}_r^d = \sum_{s'}^{N_s^-} \mathbf{I}_{s' \to r}^d \cdot \mathbf{\Psi}_{s'}^{-\,d} + \sum_{r'}^{N_r} \mathbf{C}_{r' \to r}^d \cdot \mathbf{Q}_{r'}^d \tag{2.78}$$

where the incoming and collision matrices are respectively:

$$\mathbf{I}_{s' \to r}^d = [\mathbf{M_r}]^{-1} \sum_{\substack{t \| \mathbf{\Omega}_d \\ t \cap r}} w_t \sum_{i \in r} e^{-\tau_t(0, s_{i-1})} \left(\int_{s_{i-1}}^{s_i} ds e^{-\tau_t(s_{i-1}, s)} \mathbf{f}_r(\mathbf{r}_t^- + s\mathbf{\Omega}_d) \cdot \mathbf{f}_{s'}^{\mathbf{T}}(\mathbf{r}_t^-) \right) \tag{2.79}$$

$$\mathbf{C}^{d}_{r'\to r} = [\mathbf{M_r}]^{-1} \sum_{\substack{t \| \mathbf{\Omega}_d \\ t\cap r}} w_t \sum_{i\in t\cap r} \sum_{j\in t\cap r'}^{i}$$
$$\left(\int_{s_{i-1}}^{s_i} ds\, \mathbf{f}_r(\mathbf{r}_t^- + s\mathbf{\Omega}_d) e^{-\tau_t\left(\min(s,s_j),s\right)} \cdot \int_{s_{j-1}}^{\min(s,s_j)} dt\, \mathbf{f}^{\mathbf{T}}_{r'}(\mathbf{r}_t^- + t\mathbf{\Omega}_d) e^{-\tau_t\left(s_{j-1},\min(s,s_j)\right)} \right). \tag{2.80}$$

In order to obtain the second equation for the moments of the outgoing angular flux, we firstly express it in terms of transverse integrals of trajectories as follows:

$$\begin{aligned} \mathbf{\Psi}^{+\,d}_s &= [\mathbf{M_s}]^{-1} |\mathbf{n}_s \cdot \mathbf{\Omega}_d| \int_{A_s} d\mathbf{r}\, \mathbf{f}_r(\mathbf{r}) \psi^+(\mathbf{r}, \mathbf{\Omega}_d) \\ &\approx [\mathbf{M_s}]^{-1} |\mathbf{n}_s \cdot \mathbf{\Omega}_d| \sum_{\substack{t \| \mathbf{\Omega}_d \\ t\cap r}} w_t \mathbf{f}_s(\mathbf{r}_t^+) \psi_t(\mathbf{r}_t^+, \mathbf{\Omega}_d), \end{aligned} \tag{2.81}$$

where $\mathbf{r}_t^+$ is the point of intersection of a trajectory t with the downstream external surface of the node, such that $\mathbf{r}_t^+ = \mathbf{r}_t^- + s^+\mathbf{\Omega}_d$. This time, we project the transmission equation to a surface element s by substituting Equation (2.76) in (2.81), that yields:

$$\mathbf{\Psi}^{+\,d}_s = \sum_{s'}^{N_s^-} \mathbf{T}^{d}_{s'\to s} \cdot \mathbf{\Psi}^{-\,d}_{s'} + \sum_{r'}^{N_r} \mathbf{E}^{d}_{r'\to s} \cdot \mathbf{Q}^{d}_{r'}, \tag{2.82}$$

where the transmission and escape matrices are respectively:

$$\mathbf{T}^{d}_{s'\to s} = [\mathbf{M_s}]^{-1} |\mathbf{n}_s \cdot \mathbf{\Omega}_d| \sum_{\substack{t \| \mathbf{\Omega}_d \\ t\cap s}} w_t e^{-\tau(0,s^+)} \left(\mathbf{f}_s(\mathbf{r}_t^+) \cdot \mathbf{f}^{\mathbf{T}}_{s'}(\mathbf{r}_t^-) \right), \tag{2.83}$$

$$\mathbf{E}^{d}_{r'\to s} = [\mathbf{M_s}]^{-1} |\mathbf{n}_s \cdot \mathbf{\Omega}_d| \sum_{\substack{t \| \mathbf{\Omega}_d \\ t\cap s}} w_t \sum_{j\in t\cap r'} \left(\mathbf{f}_s(\mathbf{r}_t^+) e^{-\tau(s_j,s^+)} \cdot \int_{s_{j-1}}^{s_j} ds \mathbf{f}^{\mathbf{T}}_{r'}(\mathbf{r}_t^- + s\mathbf{\Omega}_d) e^{-\tau(s,s_j)} \right). \tag{2.84}$$

Equations (2.78) and (2.82) are solved simultaneously for given internal and boundary sources, which come from the adjacent cell during the sweep of the domain in a direction. At the end of each inner iteration, the internal source moments are updated with the new angular moments of the neutron flux, where the latter are determined according to the S_N quadrature formula as follows:

$$\mathbf{\Phi}^{\ell,m}_r = [\mathbf{M_r}]^{-1} \int_{4\pi} d\mathbf{\Omega} Y_{\ell,m}(\mathbf{\Omega}) \int_{V_r} d\mathbf{r}\, \mathbf{f}_r(\mathbf{r}) \psi(\mathbf{r}, \mathbf{\Omega}) \approx \sum_d w_d Y_{\ell,m}(\mathbf{\Omega}_d) \mathbf{\Psi}^d_r.$$

The method of short characteristic has a lot of advantages. Firstly, it performs an accurate and robust numerical integration in each node. This is mediated by projecting all the region discontinuities on the transverse plane for trajectory tracking, as shown in Figure 2.2. Each transverse segment is then integrated using a Gaussian quadrature with generally three points. As said before, this technique eliminates the region numerical dispersion while minimizing the number of trajectories required for an exact integration. It is particularly advantageous in MOSC rather than in MOC because in the latter the number of discontinuities would be too large, producing too many trajectories.

Another numerical method that could be used for an even more precise node integration is Monte Carlo. However, if on one hand the latter can allow to have the exact interface current matrices with a correct integration in energy and with no need for a cross-section self-shielding model, on the other hand, it would be too much time consuming to achieve good statistics for each energy group, discrete direction, region and surface.

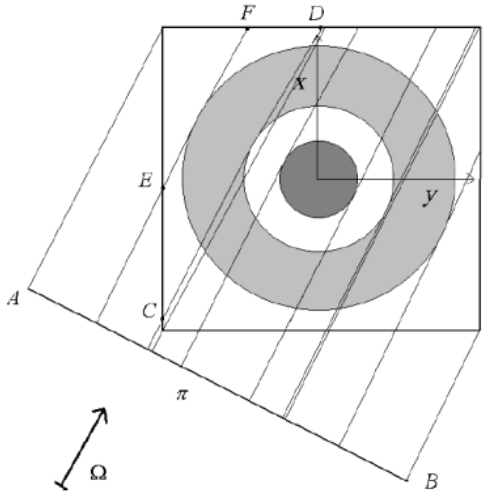

Figure 2.2. Projection of region discontinuities for a Heterogeneous Cartesian Cell.

The Cartesian mesh is also another advantage for two reasons. Firstly, it allows an efficient sweep of the domain thanks to the simple geometry. Secondly, it is suitable for domain decomposition algorithms, since each subdomain can have at most six interfaces with its neighbors, and the surface fluxes to be exchanged are directly available from sweep. Moreover, the number of surface values that are exchanged between subdomains is appreciably reduced with respect to MOC, since the number of surface elements at the boundaries of a subdomain is generally smaller than the number of trajectories crossing the boundaries. To recapitulate, thanks to the domain decomposition the computation can be advantageously parallelized in space, and because of the S_N approach, the sweeps can be easily parallelized per each direction. This makes the method of short characteristic suitable for high-performance computing in 3D LWR core calculations.

On the other hand, the MOSC has some disadvantages related to the memory requirements that are not present in MOC. The interface current matrices are generally

computed once for all, such that they are directly available during the sweep. These matrices are stored for each energy group, each direction and each cell type, and their dimension is proportional to the number of regions and/or external surfaces in the node and the number of spatial moments. It follows that for a detailed calculation the matrix coefficients occupy a lot of memory and their computation may require a lot of time. This is especially true when the nodes are all different from each other, for instance in case of depletion calculation. In order to partially overcome this problem, the matrices are stored only for some energy groups and are recomputed "on-the-fly" when necessary. However, this results in a loss of performance.

2.5 Acceleration

The interest of developing acceleration methods for the inner iterations solved by an S_N method comes from two main issues that may arise in the source iteration scheme for highly diffusive media: slow convergence and false convergence.
First of all, it must be said that the scattering source iteration scheme could be avoided if one inverted directly the operator $L - H_{ss}$, solving the equation $L - H_{ss}\psi = Q$. However, this situation is always avoided because the scattering kernel is an integral operator and it is hard to invert. On the other hand, inverting the loss operator is much easier and it is then preferred to solve the equation by source iteration as follows:

$$L\psi^{i+1} = H_{ss}\psi^i + Q. \tag{2.85}$$

The physical interpretation for the number of self-scattering source iterations is the average number of collisions that particles must undergo to be removed from an energy group. Formally, the neutron flux at the iteration $i+1$ has collided at most i times if the initial flux $\psi^0 = 0$.
It follows that for short neutron histories, due for instance to strong absorbers or leakage, the source iteration scheme is effective and converges in few iterations. On the other hand, when particle histories are long and neutrons need several collisions in order to be captured, the algorithm becomes time-consuming caused by low convergence rate.
Equation (2.85) can be rewritten as:

$$\psi^{i+1} = B\psi^i + S, \tag{2.86}$$

with $B = L^{-1}H_{ss}$ and $S = L^{-1}Q$. The last equation can be subtracted from the converged equation $\psi^\infty = B\psi^\infty + S$, and applied recursively for each iteration such that:

$$\psi^\infty - \psi^{i+1} = B(\psi^\infty - \psi^i) = B^2(\psi^\infty - \psi^{i-1}) = B^{i+1}(\psi^\infty - \psi^0). \tag{2.87}$$

If we take the norm of Equation (2.87), it yields:

$$||\psi^{\infty} - \psi^{i+1}|| = ||B^{i+1}||\,||\psi^{\infty} - \psi^{0}|| \approx \rho^{i+1}||\psi^{\infty} - \psi^{0}||, \tag{2.88}$$

where the spectral radius ρ is the largest eigenvalue of B. The rate of convergence does not depend on the source, but rather on the magnitude of ρ that must be $\rho < 1$, a necessary condition but not sufficient, so that for $i \to \infty$ the error $||\psi^{\infty} - \psi^{i+1}||$ approaches zero. It can be shown that for an infinite slab the spectral radius equals the scattering ratio $c = \frac{\Sigma_{s0}}{\Sigma}$, that is close to one for highly diffusive media. For finite systems the spectral radius depends on the optical thickness of the system, since it is representative of the spatial dependence of the solution. Typically, optically thick domains with scattering ratio close to one are the most difficult to converge because in weakly coupled systems the solution in a spatial region is more affected by the internal (scattering) source rather than the transmission of the incoming source. By contrast, if the finite system is optically thin and albedo conditions are imposed at the boundaries, the spectral radius can also be higher than that of an infinite slab because the solution is affected by the convergence rate of the boundary conditions, which depend on the outgoing fluxes.

From Equation (2.87) it can be obtained an expression for the decay rate of the error between two consecutive iterations, as follows:

$$\psi^{\infty} - \psi^{i+1} = B(\psi^{\infty} - \psi^{i}) = B(\psi^{\infty} - \psi^{i}) + B\psi^{i+1} - B\psi^{i+1} = (I - B)^{-1}B(\psi^{i+1} - \psi^{i}), \tag{2.89}$$

which yields the following estimation:

$$||\psi^{\infty} - \psi^{i+1}|| \approx \frac{\rho}{1-\rho}||\psi^{i+1} - \psi^{i}|| \approx \frac{\rho\varepsilon}{1-\rho}, \tag{2.90}$$

where we have substituted the tolerance ε for the convergence criterion, as the error between the angular fluxes at two consecutive iterations has got the same order of magnitude. However, when $\rho \to 1$, the error with respect to the actual converged solution could be much higher than the desired tolerance. In this case, the computation would terminate with a wrong solution, resulting in *false convergence*.

The introduction of an acceleration in the iterative scheme is then necessary in order to reduce the number of iterations, and therefore the computational time, and to ensure a good convergence in most of the calculations. Both objectives are achieved by reducing the spectral radius of the iterative operator.
The first popular methods that were adopted in reactor physics are the Chebychev extrapolation [28] and the Coarse-Mesh Rebalance (CMR) [29]. However, both methods do not show particular improvement especially for scattering ratios close to one [29], and CMR can also diverge for large spatial meshes [30].
Today the most widely used methods are the synthetic and the nonlinear accelerations, since they are the most effective of the state-of-the-art. We shall present the basic concepts of these techniques, which both rely on an iterative scheme where each transport sweep is followed by a calculation performed with a low-order operator. The idea is

that all the iterative effort required for the convergence of the source is deployed by the acceleration operator rather than the transport operator, where the former must be less time-consuming than the latter in order to gain in performance. The two methods differ in the way the low-order operator is used and how the transport solution is accelerated. Both types of methods can be applied to accelerate the inner iterations or the outer iterations. In the next sections, the equations are written for the inner loop, but the same approach can be used to find the equations for the outer loop.

2.5.1 Synthetic Acceleration

The synthetic acceleration is based on an additive correction that is applied to the transport solution to approach it to the converged solution as follows:

$$\psi^{i+1} = \psi^{i+\frac{1}{2}} + \delta\psi^{i+1}, \tag{2.91}$$

where ψ^{i+1} is the accelerated angular flux at the end of the inner iteration, $\psi^{i+\frac{1}{2}}$ is the non-accelerated angular flux given by the transport sweep, and $\delta\psi^{i+1}$ is the correction computed by the acceleration. Note that the correction is applied to the angular moments of the flux, rather than the angular flux itself, but it depends on the method and for simplicity we use ψ as a general representation of the angular flux.
In order to obtain an equation for the correction $\delta\psi$ we write the transport equation at iteration $i+1$ supposing that we can invert the scattering operator, and the equation for the transport sweep at iteration $i+\frac{1}{2}$, as follows:

$$(L - H_{\text{ss}})\psi^{i+1} = Q, \tag{2.92}$$

$$L\psi^{i+\frac{1}{2}} = H_{\text{ss}}\psi^{i} + Q. \tag{2.93}$$

Note that a direct inversion of Equation (2.92) gives the exact solution such that $\psi^{i+1} = \psi^{\infty}$. If we explicit for Q Equations (2.92) and (2.93), and then add and subtract the term $H_{\text{ss}}\psi^{i+\frac{1}{2}}$ on the right side, it yields:

$$Q = (L - H_{\text{ss}})\psi^{i+1} = L\psi^{i+\frac{1}{2}} - H_{\text{ss}}\psi^{i} + H_{\text{ss}}\psi^{i+\frac{1}{2}} - H_{\text{ss}}\psi^{i+\frac{1}{2}}.$$

Rearranging the terms of the last equation and applying (2.91), we obtain an equation for the correction of the transport flux:

$$(L - H_{\text{ss}})\delta\psi^{i+1} = H_{\text{ss}}(\psi^{i+\frac{1}{2}} - \psi^{i}). \tag{2.94}$$

The solution of Equation (2.94) gives the exact correction that should be applied to the flux $\psi^{i+\frac{1}{2}}$ in order to obtain the exact solution of Equation (2.92). However, inverting the operator $(L - H_{\text{ss}})$ is the operation the one wants to avoid, and if the inversion

was straightforward enough, then it can be directly applied to the exact angular flux in Equation (2.92). At this point, the operator on the left side of Equation (2.94) is substituted with a low-order operator that is much easier to invert, yielding:

$$(\widehat{L} - \widehat{H}_{\mathrm{ss}})\delta\psi^{i+1} = H_{\mathrm{ss}}\delta\psi^{i+\frac{1}{2}}, \tag{2.95}$$

where the symbol $\widehat{.}$ means low-order and we have defined $\delta\psi^{i+\frac{1}{2}} = (\psi^{i+\frac{1}{2}} - \psi^{i})$. We must note that now if $\delta\psi^{i+1} \neq 0$, then it is not the correction that gives the converged solution ($\psi^{i+1} \neq \psi^{\infty}$), but it approaches to it. The source on the right side of Equation (2.95) requires the knowledge of the necessary angular moments of two consecutive iterations. When the source equals zero, the correction is null as well, which entails that either the iteration process has converged, or the acceleration is no more effective. This can arise when the accelerated lower moments have reached the asymptotic values, while the higher moments, that are computed only in the transport sweep, require more iterations to converge.
The iterative operator of the accelerated problem can be obtained combining Equations (2.91), (2.93) and (2.95) as follows:

$$\begin{aligned}
\psi^{i+1} &= \psi^{i+\frac{1}{2}} + (\widehat{L} - \widehat{H}_{\mathrm{ss}})^{-1} H_{\mathrm{ss}}(\psi^{i+\frac{1}{2}} - \psi^{i}) \\
&= L^{-1}H_{\mathrm{ss}}\psi^{i} + L^{-1}Q + (\widehat{L} - \widehat{H}_{\mathrm{ss}})^{-1}(H_{\mathrm{ss}}L^{-1}H_{\mathrm{ss}}\psi^{i} + H_{\mathrm{ss}}L^{-1}Q - LL^{-1}H_{\mathrm{ss}}\psi^{i}) \\
&= [I - (\widehat{L} - \widehat{H}_{\mathrm{ss}})^{-1}(L - H_{\mathrm{ss}})]L^{-1}H_{\mathrm{ss}}\psi^{i} + [I + (\widehat{L} - \widehat{H}_{\mathrm{ss}})^{-1}H_{\mathrm{ss}}]L^{-1}Q.
\end{aligned}$$

The last equation shows that the accelerated iterative process has a spectral radius which goes to zero as the low-order operator $(\widehat{L} - \widehat{H}_{\mathrm{ss}})$ gets closer to $(L - H_{\mathrm{ss}})$. It follows that if the low-order operator is a good approximation for the configuration to be computed, the iterative scheme will converge in few iterations. By contrast, if it is not sufficient to describe the physics of the problem, one can choose a higher order operator to improve the convergence rate. However, this requires extra computational time for each matrix inversion, thus it is convenient only if the gain given by the reduction of the number of iterations is larger.

Gelbard and Hageman [31] were the first to use the synthetic acceleration for the S_N equations. Few years later Reed [32] showed that the method may diverge for spatial meshes larger than one mean free path, and it is effective if the meshes are fine enough. Alcouffe [33] found that the synthetic method is unconditionally stable if the equations of the acceleration are discretized consistently with the transport equations. It follows that the advantage is that the source iteration scheme can be accelerated in an effective and robust manner. On the other hand, the constraint of a fine spatial mesh may require considerable computational and memory resources.

The synthetic acceleration method takes the name from the low-order operator. Because of simplicity and rapidity, one of the first operators that was explored is diffusion, producing the Diffusion Synthetic Acceleration (DSA) [33]. A lower order S_N operator has been used as well resulting in Transport Synthetic Acceleration (TSA)

[29], and also other operators that employ approximations only at the mesh interfaces, giving a system of equations similar to the interface current method. These operators belong to the family of Boundary Projection Accelerations (BPA), where the projection of the angular flux can be performed using polynomial functions such as in the DP_N [34, 35], or using a lower order S_N space [18, 36].

2.5.2 Nonlinear Acceleration

A nonlinear acceleration does not employ the low-order operator to find an additive correction, but rather to directly estimate the solution on a projected space, which is typically coarser than in transport. The projector operator is based on homogenization theory (presented in Chapter 3) and it has the following form:

$$\mathbf{P}_R^G = \sum_{g\in G}\sum_{r\in R}\frac{V_r}{V_R}\sum_d w_d, \quad \forall R, G, \tag{2.96}$$

where r and g are respectively the region and energy group for the discretization of the transport operator, while R and G are respectively the coarse region and the coarse energy group (or macro-region and macro-group) for which the low-order operator solves the homogenized problem. Note that if the acceleration is used for the inner iteration loop, there is no energy homogenization since the equations to be solved are mono-kinetics. Here we generalize the formalism for both inner and outer iterations.

Because of the projection on a coarser space, in order to accelerate the transport solution, it is required a sort of reconstruction on the fine transport space. This is mediated by using the last available transport flux and the *prolongation* equation:

$$\psi_{h,r,g}^{i+1} = \psi_{h,r,g}^{i+\frac{1}{2}} \times \frac{\Phi_{R,G}^{i+1}}{\mathbf{P}_R^G \cdot \psi_{0,r,g}^{i+\frac{1}{2}}}, \tag{2.97}$$

where $h = (\ell + m)$ is the index for the angular moments, $\psi^{i+\frac{1}{2}}$ is the non-accelerated flux given by the transport sweep, ψ^{i+1} is the accelerated transport flux, and $\Phi_{R,G}^{i+1}$ is the scalar flux that is solution of the homogenized problem and defined in the coarse space. Note that we adopted the index $i+1$ for the coarse flux in order to express that the accelerated transport flux is normalized to the coarse solution.
While in the synthetic acceleration the additive correction equals zero at convergence, in a nonlinear acceleration the iterative scheme can converge only if the normalization factor $\frac{\Phi}{\mathbf{P}\psi_0}$ goes to one for each macro-region and macro-group, such that:

$$\Phi_{R,G}^{\infty} = \mathbf{P}_R^G \cdot \psi_{0,r,g}^{\infty}, \quad \forall R, G. \tag{2.98}$$

At this point it is worth to point out that because of the nonlinear prolongation equation, it is hard to use the higher-order moments of the low-order operator to accelerate the transport solution, because they can be very close to zero or negative values, that

make the iterative process unstable. This is why a nonlinear acceleration generally utilizes diffusion as low-order operator whose solution is only a coarse scalar flux, that is used to accelerate all the transport angular moments. This is not possible in the synthetic acceleration, where only the angular moments computed by the low-order operator are used to accelerate their counterpart in transport.

To recapitulate, an iteration is composed of a transport sweep, an acceleration sweep and the prolongation of the transport solution according to Equation (2.97). As for the synthetic method, the transport sweep is given by the equation:

$$L\psi^{i+\frac{1}{2}} = H_{\text{ss}}\psi^{i} + Q. \tag{2.99}$$

while the acceleration equation is solved on the projected space:

$$\mathbf{P}(L - H_{\text{ss}})\psi^{i+1} = \mathbf{P}Q. \tag{2.100}$$

However, the last equation is of little use in order to find a solution in the coarse space in an efficient way. One would rather solve a modified low-order equation as follows:

$$(\widehat{L} - \widehat{H}_{\text{ss}})\Phi^{i+1} = \mathbf{P}Q, \tag{2.101}$$

such that the transport balance from Equation (2.99) is preserved in each element of the coarse space. To do that, the construction of the "equivalent" coarse operators $\widehat{L}$ and $\widehat{H}_{\text{ss}}$ is typically based on homogenization theory, that relies on preservation of average transport reaction rates and leakage on coarse spatial and energy meshes.

It follows that the coarse operators are dependent of the transport solution itself, that characterizes the non-linearity of the iterative scheme. This is the main difference with respect to the synthetic method, where the transport solution is used to construct the source of the low-order problem.

A physical interpretation of this mathematical feature is that homogenization produces a loss of information that avoids going back to the fine space. This entails that an exact dehomogenization is possible only if the fine solution is known.

The transport flux that is used to construct $(\widehat{L} - \widehat{H}_{\text{ss}})$ is clearly the last available (with index $i + \frac{1}{2}$) since it is the closest to the converged solution. The acceleration equation can be finally written as follows:

$$(\widehat{L}^{i+\frac{1}{2}} - \widehat{H}_{\text{ss}}^{i+\frac{1}{2}})\Phi^{i+1} = \mathbf{P}Q, \tag{2.102}$$

which entails that the low-order operator keeps changing during the iterative process as long as the convergence is attained, and therefore it must be recomputed at each iteration.

As said earlier, diffusion is the most popular low-order operator used in a nonlinear acceleration, and in particular with a finite difference representation for the spatial derivative of the flux, resulting in the so called Coarse Mesh Finite Difference (CMFD)

acceleration. However, the Fick's law in the diffusion equation cannot reproduce the average transport solution, therefore a transport correction term is introduced to the definition of the diffusion current in order to construct the coarse operator $\widehat{L}\Phi$ that equals $\mathbf{P}L\psi$. Generally, this correction forces a relation between coarse currents and scalar fluxes, that has not necessarily a physical meaning, but a mathematical constraint to the diffusion equation so as to reproduce the transport balance.

The correction that is employed to construct $\widehat{L}$ determines the type of method. The most popular CMFD accelerations are MCNH (by Moon, Cho, Noh and Hong) [37], the pCMFD (partial current CMFD) [38] and the AAF (Aragones and Ahnert Formulation) [39].

Later in this document, it will be shown that a Nodal Expansion representation can also be used as nonlinear acceleration, which, according to our knowledge, has never been proposed in literature because of the higher computational cost with respect to CMFD.

Recently, a nonlinear transport acceleration has been proposed called Response Matrix Acceleration (RMA) [40, 41], where the low-order operator is directly obtained combining the balance and the transmission equations of the interface current formalism, resulting in a response matrix equation for the partial currents exiting the regions. The scalar flux is then deduced by the balance equation with the new currents or by a mathematical expression the relates partial currents with scalar flux. As in CMFD, the latter is used to accelerate all the transport angular moments and, in addition to that, the partial currents are used to accelerate the incoming and outgoing angular fluxes at the interfaces.

2.5.3 Synthetic vs Nonlinear

The two types of acceleration can be considered mirrors of each other in terms of advantages and disadvantages.

First of all, in the synthetic acceleration (SA) the low-order operator does not depend on the transport solution, so the iterative scheme is linear. This has the advantage of a straightforward application of the spectral radius analysis and of the Fourier analysis, so the stability and performance properties of the method can be exactly determined. A nonlinear iterative scheme (NL), instead, must be firstly linearized in order to perform the aforementioned analysis, thus the convergence and stability properties are studied only when the solution is near convergence.

Secondly, the low-order operator is constructed once for all in the synthetic acceleration and it might be a time-consuming operation because of the large number of meshes. Then it is simply applied for a different source term that changes at each iteration. By contrast, in a nonlinear scheme the matrix coefficients are fast to determine, but they must be recomputed at each iteration, requiring, as the most expensive operation, a 3D homogenization.

Thirdly, if on one hand the NL acceleration requires more operations to construct the operator, on the other hand, the SA requires more memory resources. This is due to the fact that the SA coefficients are stored for each fine region and energy group, since the low-order operator must be discretized consistently with the transport operator, while in the NL they are stored for each macro-region and macro-group. Clearly, the

number of macro-regions can be advantageously lesser than that of transport regions. The memory requirements concern also the storage of the necessary information from the transport solution. In SA it is the transport angular moments to be accelerated, that are used to compute the source term, while in NL it is the transport currents and scalar fluxes for each coarse region.

Fourthly, because of the larger number of regions in SA, and therefore, of unknowns, the solution of the NL low-order operator is much faster to obtain than in SA. This is particularly true for the outer iteration loop, where the energy condensation can drastically reduce the size of the problem phase space. Furthermore, the low-order operator in SA does not need to provide an exact numerical solution in order to guarantee the stability of the iterative scheme. This means, for instance, that in some configurations where the problem contains media that are not very different, the coefficients of the SA low-order operator could be computed for some regions and then interpolated, saving computational time and memory. It has been shown that one can clearly get some advantages from this procedure [42]. On the other hand, the NL low-order operator must reproduce exactly the average transport solution, otherwise the prolongation equation makes the iterative scheme unstable.

Another advantage of nonlinear accelerations that is given by homogenization is the possibility, as said earlier, to use a computational mesh different from the transport problem. This does not concern only the number of coarse regions, but also the convenience of using a Cartesian geometry for the homogenized problem, even if not necessary, since it can be solved more efficiently.

Finally, the synthetic acceleration has shown very good stability properties that make the method robust even for the most difficult configurations. The NL acceleration, instead, needs some techniques in order to stabilize the iterative process and avoid divergence, sometimes at the cost of modifying the low-order operators making the acceleration ineffective.

A combination of the two approaches is, probably, the best option to accelerate the convergence of a transport solution, so as to take advantages from both. For instance, the strategy that we adopted for our calculations in Part II is to use a synthetic method for the inner iterations and a nonlinear method of the outer iterations.

2.6 Numerical Diffusion Methods

Diffusion theory is widely used in reactor physics either as an acceleration, as said in the last sections, or as an operator to compute large systems such as the reactor core. The diffusion equation is very fast to solve with respect to the transport equation, thanks to the elimination of the angular variable and the Fick's law that provides a relation between scalar flux and current. However, there is another reason that makes diffusion even faster, which concerns the discretization of the spatial and energy domains.

As said in Section 1.7, diffusion is a good approximation of a high-order transport solution in large and highly scattering media, where the solution is very smooth and, therefore, the flux gradients are not dominant in the local balance. In 1D geometries diffusion is equivalent to the P_1 equations with isotropic scattering. We write here the

complete system of equations up to the order 1 omitting the group index:

$$\begin{cases} \frac{d\phi_1}{dx} + \Sigma\phi_0 = \Sigma_{s0}\phi_0 + Q_0 \\ \cancelto{\approx 0}{\frac{2}{3}\frac{d\phi_2}{dx}} + \frac{1}{3}\frac{d\phi_0}{dx} + \Sigma\phi_1 = \cancelto{\approx 0}{Q_1} \end{cases} \tag{2.103}$$

where Q_n are the angular moments of the source, that includes down- and up- scattering, and fission if the system is multiplicative. In order to obtain the diffusion equation, the equation of order 1 is firstly truncated by eliminating the term of the moment ϕ_2. This procedure is equivalent to suppose the neutron flux linearly anisotropic. Next, the first moment of the angular source is also neglected because of the hypothesis of isotropic sources ($Q_1 \approx 0$), producing the Fick's law. Part of this approximation is mitigated by the transport correction of cross sections. Finally, substituting the Fick's law in the first equation of (2.103), one obtains the well-known second order differential equation of diffusion theory.

The assumption of linearly anisotropic flux easily fails in highly heterogeneous systems, while that of isotropic source supposes that the group transfer due to the first moment is negligible. Both of the assumptions are not valid for most of realistic systems, but it is possible to define a problem that at the same time has these features and is representative of the actual transport problem. Thus, the fine details of a heterogeneous geometry are substituted by large geometries containing "fictitious" media with average nuclear properties. Moreover, in order to minimize the group-to-group scattering source, the energy domain is discretized very coarsely using few macrogroups (generally 2), so as to reduce the probability for a neutron to be scattered in another energy group. A fine multigroup discretization for diffusion would increase the contribution of Q_1, making the second equation of (2.103) no more valid.

It follows that such a reduction of the spatial and energy information surprisingly allows to obtain more precise results at lesser computational cost. The only drawback is that of producing the good few-group cross sections of these fictitious media that must be representative of the actual problem. These data are provided by homogenization theory that avails of the detailed information of the transport solution in the corresponding heterogeneous problem. One more thing that speeds up the diffusion calculation in reactor physics is the possibility to define the homogenized problem in a Cartesian geometry, in order to numerically find a solution in a more efficient manner.

In multigroup formalism, the P_0^* corrected self-scattering cross section is moved to the left side of the diffusion equation 1.54, and one uses the removal cross section instead of the total for the collision term which, according to Equation (1.6), it is not affected by the transport correction: $\Sigma_r = \Sigma - \Sigma_{ss} = \Sigma^* - \Sigma_{ss}^*$. It follows that the

multigroup steady-state diffusion equation for the core eigenvalue problem reads:

$$-\nabla\cdot(D^g(\mathbf{r})\nabla\phi^g(\mathbf{r}))+\Sigma_{\mathrm{r}}^g(\mathbf{r})\phi^g(\mathbf{r})=\sum_{g'\neq g}\Sigma_{\mathrm{s0}}^{g'\to g}(\mathbf{r})\phi^{g'}(\mathbf{r})+\frac{1}{k_{\mathrm{eff}}}\sum_i\chi_i^g(\mathbf{r})\sum_{g'}\nu\Sigma_{\mathrm{f},i}^{g'}(\mathbf{r})\phi^{g'}(\mathbf{r}),$$

In this section we present the most popular methods used in industry and research fields for diffusion core calculations on Cartesian geometries: the finite difference method (FD) and the nodal expansion method (NEM). The Finite Element Method (FEM) is also applied to this type of problems, but it is less popular than the other two. However, when the geometry is not Cartesian, the FEM way is the preferred alternative.

The FD method assumes a linear spatial representation for the flux, while NEM utilizes a higher order expansion (generally up to order 4). The advantage of using one method rather than the other depends, then, on the geometrical dimension of the homogenized media. If the latter are large, like for a quarter of assembly that is around 10 cm, the finite difference method would require submeshing to minimize numerical diffusion, so NEM is generally preferred. On the contrary, if the homogenized media are defined at the fuel pin level, NEM with a quartic expansion is definitely too expensive, and FD is typically employed. However, sometimes FD requires submeshing even for the pin size, or intermediary size, so the parabolic expansion in NEM is presented as well, as compromise of the two possibilities.

2.6.1 The Finite Difference Method

The Finite Difference method presented in this section relies on the mesh-centered scheme. This scheme gives a direct solution for the average flux in each region, while in other schemes, such as the mesh-corner, the unknowns are the fluxes at the mesh interfaces. The mesh-centered scheme is the most applied and it is also used for the discretization of the CMFD acceleration, as we shall discuss in Chapter 3.

Suppose a 1D geometry divided into a finite number of nodes with constant cross sections, where the average flux is defined as:

$$\phi_k=\frac{1}{\Delta x_k}\int_{x_{k-\frac{1}{2}}}^{x_{k+\frac{1}{2}}}dx\phi(x), \tag{2.104}$$

with k the node index and Δx_k the node size along the x-axis. The mesh-centered equation is obtained by integrating over the node the diffusion equation (1.54) as follows:

$$\Big[-D_k\frac{d\phi}{dx}\Big|_{k+\frac{1}{2}}+D_k\frac{d\phi}{dx}\Big|_{k-\frac{1}{2}}\Big]+\Sigma_{\mathrm{r},k}\phi_k\Delta x_k=Q_k\Delta x_k. \tag{2.105}$$

The spatial derivative is then substituted with the finite difference approximation,

knowing that because of the linear representation, the average flux can be considered located in the middle point of the node:

$$-D_k \frac{d\phi}{dx}\Big|_{k+\frac{1}{2}} \approx -\frac{2D_k}{\Delta x_k}(\phi_{k+\frac{1}{2}} - \phi_k) \tag{2.106}$$

and similarly for the interface at $x_{k-\frac{1}{2}}$. In order to eliminate the dependence of the surface flux at the node interface, we use the continuity condition of the net current:

$$J_{k+\frac{1}{2}} = -\frac{2D_k}{\Delta x_k}(\phi_{k+\frac{1}{2}} - \phi_k) = -\frac{2D_{k+1}}{\Delta x_{k+1}}(\phi_{k+1} - \phi_{k+\frac{1}{2}}), \tag{2.107}$$

so as to obtain an expression for the surface fluxes as a function of the volumetric ones:

$$\phi_{k+\frac{1}{2}} = \frac{D_k \Delta x_{k+1}\phi_k + D_{k+1}\Delta x_k \phi_{k+1}}{D_k \Delta x_{k+1} + D_{k+1}\Delta x_k}. \tag{2.108}$$

Substituting Equation (2.108) in Equation (2.106), and then Equation (2.106) in Equation (2.105), one obtains the FD system of equations that have the following form:

$$-a\phi_{k-1} + b\phi_k - c\phi_{k+1} = Q_k \Delta x_k, \quad \forall k \tag{2.109}$$

with

$$a = \frac{2D_k D_{k-1}}{D_k \Delta_{k-1} + D_{k-1}\Delta_k}, \quad c = \frac{2D_k D_{k+1}}{D_k \Delta_{k+1} + D_{k+1}\Delta_k}, \quad b = a + c + \Sigma_{\mathrm{r},k}\Delta x_k. \tag{2.110}$$

Similarly for the 3D equation, the leakage term is function of the seven fluxes, where six are for neighboring nodes. The matrix associated to the system of equations has then an epta-diagonal structure. Because of the definition in Equation (2.110), b (the diagonal coefficient) is larger than the sum of the other terms of the same row, which entails that the FD matrix is diagonally dominant, allowing the application of efficient numerical techniques for inversion. As diffusion operator, the method can admit any boundary condition discussed in Section 1.7, that is accounted directly modifying the FD matrix. In case of domain decomposition, in order to construct the boundary condition for a subdomain, the mesh-centered scheme needs both the flux of neighbors and the corresponding matrix coefficient containing the geometrical and material information of the neighboring subdomains.

2.6.2 The Nodal Expansion Method

The Nodal Expansion Method (NEM) that we present here has been implemented by Sanchez et al. in [43], and it is the diffusion numerical method employed in our

analysis of Dynamic Homogenization in Part II.

NEM is a class of methods that takes advantage of the Cartesian geometry by applying a transverse operator of the form $\frac{1}{\Delta y \Delta z}\int_{\Delta y}\int_{\Delta z} dydz\cdot$ to the 3D diffusion Equation (1.54) (called transverse integration procedure) in order to obtain a system of three one-dimensional equations coupled by the transverse leakage source term. Each one-dimensional equation has the following form defined for a general axis x:

$$\frac{d}{dx}J_x(x) + \Sigma_{\mathrm{r}}(x)\Phi_x(x) = q_x(x) - L_x(x), \tag{2.111}$$

with:

$$\begin{aligned}
&\Phi_x(x) = \frac{1}{\Delta y \Delta z}\int_{\Delta y}\int_{\Delta z} dydz\Phi(x,y,z),\\
&L_x(x) = L_{xy}(x) + L_{xz}(x) = \frac{1}{\Delta y \Delta z}\int_{\Delta y}\int_{\Delta z} dydz(\frac{d}{dy}J_y(x,y,z) + \frac{d}{dz}J_z(x,y,z)),\\
&q_x(x) = H\Phi_x(x) + \frac{1}{\lambda}F\Phi_x(x),
\end{aligned}$$

where Σ_{r} is the removal cross section, H and F are the operators respectively for the scattering and the fission sources and λ the eigenvalue. Note that the group index has been omitted. The one-dimensional flux $\Phi_x(x)$ is then approximated using an expansion of Legendre polynomials truncated at the N-th order and defined on a node k of size Δx:

$$\Phi_x(x) = \overline{\Phi} + \sum_{n=1}^{N}\phi_{x,n}P_n(\mu), \tag{2.112}$$

where

$$x \in [-\frac{\Delta x}{2}, \quad \frac{\Delta x}{2}], \quad \mu = \frac{2x}{\Delta x}, \quad \mu \in [-1,1].$$

From the Lengendre polynomials properties, we have:

$$P_n(\pm 1) = (\pm)^n,$$

so the expression of the flux at the interfaces $x_\pm$ of a node k, where $+$ and $-$ stand respectively for right and left, is:

$$\Phi_{x_\pm} = \overline{\Phi} + \sum_{n=1}^{N}(\pm)^n\phi_{x,n}, \tag{2.113}$$

while knowing that:

$$J_x(x) = -D\partial_x\phi(x), \quad \partial_x P(\mu) = \frac{2}{\Delta x}P'(\mu), \quad P'_n(\pm 1) = (\pm)^{n+1}\frac{n(n+1)}{2},$$

we can derive an expression for the current at the node interfaces:

$$J_{x_\pm} = -\frac{2D}{\Delta x}\sum_{n=1}^{N}(\pm)^{n+1}n(n+1)\phi_{x,n}, \tag{2.114}$$

2.6.2 Parabolic Expansion

The lowest possible expansion is nodal diffusion is of second order (NEM2), otherwise a linear expansion would correspond to the FD method. We now want to eliminate the dependency of the flux moments for $N = 2$ in favor of the response matrix formulation for the partial currents exiting (J^{out}) and entering (J^{in}) a node. Substituting the following equations

$$\Phi_{x_\pm} = 2(J^{out}_{x_\pm} + J^{in}_{x_\pm}), \tag{2.115}$$

into Equation (2.113), we obtain an expression for the flux moments as a function of the partial currents:

$$\begin{aligned}\phi_{x,1} &= \frac{1}{2}(\Phi_{x_+} - \Phi_{x_-}) = (J^{out}_{x_+} + J^{in}_{x_+}) - (J^{out}_{x_-} + J^{in}_{x_-}),\\ \phi_{x,2} &= \frac{1}{2}(\Phi_{x_+} + \Phi_{x_-}) - \overline{\Phi} = (J^{out}_{x_+} + J^{in}_{x_+}) + (J^{out}_{x_-} + J^{in}_{x_-}) - \overline{\Phi}.\end{aligned}$$

Replacing these expressions in Equation (2.114), it follows:

$$J_{x_+} = J^{out}_{x_+} - J^{in}_{x_+} = -\frac{D}{\Delta x}[8(J^{out}_{x_+} + J^{in}_{x_+}) + 4(J^{out}_{x_-} + J^{in}_{x_-}) - 6\overline{\Phi}], \tag{2.116a}$$

$$J_{x_-} = -J^{out}_{x_-} + J^{in}_{x_-} = \frac{D}{\Delta x}[4(J^{out}_{x_+} + J^{in}_{x_+}) + 8(J^{out}_{x_-} + J^{in}_{x_-}) - 6\overline{\Phi}]. \tag{2.116b}$$

Now, by averaging Equation (2.111) over a node k, the discretized balance equation becomes:

$$\frac{1}{\Delta x}[J_{x_+} - J_{x_-}] + \Sigma_{\mathrm{r}}\overline{\Phi} = Q_x, \tag{2.117}$$

with

$$Q_x = \frac{1}{\Delta x}\int_{\Delta x} dx[q_x(x) - L_x(x)] = \overline{q} - \overline{L}_x,$$

and

$$\overline{L}_x = \overline{L}_{xy} + \overline{L}_{xz} = \frac{1}{\Delta y}[J_{y_+} - J_{y_-}] + \frac{1}{\Delta z}[J_{z_+} - J_{z_-}].$$

Finally, from the balance Equation (2.117) we explicit the average scalar flux in a node:

$$\overline{\Phi} = \frac{1}{\Sigma_{\mathrm{r}}}[Q_x - \frac{1}{\Delta x}(J^{out}_{x_+} - J^{in}_{x_+} + J^{out}_{x_-} - J^{in}_{x_-})], \tag{2.118}$$

and substitute it into the definitions of the interface net currents (Equation (2.116)) to obtain:

$$\mathbf{A}_x \mathbf{J}^{out}_x = \mathbf{B}_x \mathbf{J}^{in}_x + \mathbf{Q}_x, \quad \forall k \in [1, N_x], \tag{2.119}$$

where

$$\mathbf{J}^{out}_x = \begin{bmatrix} J^{out}_{x_-} \\ J^{out}_{x_+} \end{bmatrix}, \quad \mathbf{J}^{in}_x = \begin{bmatrix} J^{in}_{x_-} \\ J^{in}_{x_+} \end{bmatrix}, \quad \mathbf{Q}_x = \begin{bmatrix} \gamma Q_x \\ \gamma Q_x \end{bmatrix},$$

$$\mathbf{A}_x = \begin{bmatrix} 1+8\alpha+6\beta & 4\alpha+6\beta \\ 4\alpha+6\beta & 1+8\alpha+6\beta \end{bmatrix}, \quad \mathbf{B}_x = \begin{bmatrix} 1-8\alpha+6\beta & -4\alpha+6\beta \\ -4\alpha+6\beta & 1-8\alpha+6\beta \end{bmatrix},$$

$$\alpha = \frac{D}{\Delta x}, \quad \beta = \frac{D}{\Sigma_{\mathrm{r}}(\Delta x)^2}, \quad \gamma = \frac{6D}{\Sigma_{\mathrm{r}}\Delta x}.$$

Equation (2.119) is a system of $2N_x$ equations, with N_x the number of nodes for an axis x, that is solved for the outgoing currents by inverting a tridiagonal matrix. Note that for the continuity condition of the partial current, the incoming current is equal to the current exiting the neighboring nodes, therefore:

$$\mathbf{J}^{in}_x = \mathbf{J}^{out}_{x^{\mathrm{nk}}} \quad \text{and} \quad \mathbf{J}^{out}_{x^{\mathrm{nk}}} = \begin{bmatrix} J^{out}_{x^{k-1}_+} \\ J^{out}_{x^{k+1}_-} \end{bmatrix}, \tag{2.120}$$

where nk stands for neighbors of node k. The 3D solution is achieved by sweeping along the three axes and iterating on the transverse leakage sources L_x, L_y, L_z, that are updated at the end of each sweep (inner iterations loop). When L_x, L_y, L_z converge, the new average flux is determined with Equation (2.118) using the last scattering and fission sources that are fixed for the whole inner iterations loop. The diffusion NEM2 operator can admit boundary conditions either for the net currents, or for the incoming partial currents, or also for the boundary flux. For specular boundary conditions, clearly, zero net current has to be imposed, while for vacuum boundary conditions typically the incoming current is set equal to zero. When the NEM2 operator is spatially decomposed, the only information required by each subdomain to perform the sweep is the partial currents exiting the neighbors according to Equation (2.119), somehow similarly to transport that involves only the boundary angular fluxes and no

information of the neighboring geometry is needed.

2.6.2 Quartic Expansion

The interest of a higher order flux expansion arises when the geometry contains large coarse meshes, because it avoids the increase in the number of computational meshes used to solve the discretized problem. The most common expansion in industrial application is of fourth order (NEM4). In this case the two conditions of Equation (2.115) are not sufficient to eliminate the dependency of the four flux moments in favor of the partial currents. In order to find the two additional constraints, we can take advantage of the Legendre polynomials properties. We substitute Equations (2.112) and (2.114) into Equation (2.111) and we write the balance equation for a node k:

$$-\frac{4D}{(\Delta x)^2}\sum_{n=1}^{N}\phi_{x,n}P_n''(\mu)+\Sigma_{\mathrm{r}}(\overline{\Phi}+\sum_{n=1}^{N}\phi_{x,n}P_n(\mu))=\overline{q}_x+\sum_{n=1}^{N}q_{x,n}P_n(\mu)-L_x, \quad (2.121)$$

where we have assumed that the scattering and fission sources have same expansion of the flux, and the diffusion coefficient is constant within the node. We recall here that the orthogonality of the Legendre polynomials yields:

$$< P_m, P_n >= \frac{1}{\Delta x}\int_{-\Delta x/2}^{\Delta x/2} P_m(\mu)P_n(\mu)dx = \frac{1}{2}\int_{-1}^{1} P_m(\mu)P_n(\mu)d\mu = \frac{1}{2m+1}\delta_{m,n},$$

where $\delta_{m,n}$ is the Kronecker function, and we observed that:

$$\langle P_m, P_n''\rangle = (2m+3)\delta_{m+2,n}.$$

By projecting Equation (2.121) on P_m and using the last properties, we obtain:

$$-\frac{4D}{(\Delta x)^2}(2m+3)\phi_{x,m+2}+\Sigma_{\mathrm{r}}\frac{1}{2m+1}\phi_{x,m}=\frac{1}{2m+1}q_{x,m}-< P_m, L_x >,$$

which allows to have an expression for the higher moments as a function of the lower order moments of the flux and the source :

$$\phi_{x,m+2}=\alpha_m\Sigma_{\mathrm{r}}\phi_m-Q_{x,m}, \quad (2.122)$$

where

$$\alpha_m=\frac{1}{4(2m+1)(2m+3)}\frac{(\Delta x)^2}{D}$$

and

$$Q_{x,m}=\alpha_m(q_{x,m}-L_{x,m}), \quad L_{x,m}=(2m+1)< P_m, L_x >, \quad m>0.$$

We now substitute the expressions for the moments of order 3 and 4 given by Equation (2.122) into Equations (2.113) and (2.114):

$$\Phi_{x_\pm} = \overline{\Phi} \pm (1 + \alpha_1 \Sigma_\mathrm{r} \phi_{x,1}) + (1 + \alpha_2 \Sigma_\mathrm{r} \phi_{x,2}) \mp Q_{x,1} - Q_{x,2}, \tag{2.123}$$

$$J_{x_\pm} = -\frac{2D}{\Delta x}[(1 + 6\alpha_1 \Sigma_\mathrm{r} \phi_{x,1}) \pm (3 + 10\alpha_2 \Sigma_\mathrm{r} \phi_{x,2}) - 6Q_{x,1} \mp 10Q_{x,2}, \tag{2.124}$$

and by combining Equations (2.115) and (2.123) we obtain the expressions for the first two flux moments as a function of the partial currents:

$$\phi^k_{x,1} = \frac{1}{1 + \alpha_1 \Sigma_\mathrm{r}}[(J^{out}_{x_+} + J^{in}_{x_+}) - (J^{out}_{x_-} + J^{in}_{x_-}) + Q_{x,1}],$$

$$\phi_{x,2} = \frac{1}{1 + \alpha_2 \Sigma_\mathrm{r}}[(J^{out}_{x_+} + J^{in}_{x_+}) + (J^{out}_{x_-} + J^{in}_{x_-}) + Q_{x,2} - \overline{\Phi}].$$

We then substitute the last expressions and Equation (2.118) into Equation (2.124) to obtain:

$$\begin{aligned} J_{x_\pm} = \pm(J^{out}_{x_\pm} - J^{in}_{x_\pm}) = -\frac{D}{\Delta x}\{&c_1[(J^{out}_{x_+} + J^{in}_{x_+}) - (J^{out}_{x_-} + J^{in}_{x_-})] \pm c_2[(J^{out}_{x_+} + J^{in}_{x_+}) + (J^{out}_{x_-} + J^{in}_{x_-})] \\ &\pm \frac{c_2}{\Sigma_\mathrm{r}\Delta x}[(J^{out}_{x_+} - J^{in}_{x_+}) + (J^{out}_{x_-} - J^{in}_{x_-})] \mp \frac{c_2}{\Sigma_\mathrm{r}}\overline{Q}_x - (12 - c_1)Q_{x,1} \mp (20 - c_2)Q_{x,2}\}, \end{aligned}$$

where

$$c_1 = 2\frac{1 + 6\alpha_1 \Sigma_\mathrm{r}}{1 + \alpha_1 \Sigma_\mathrm{r}}, \quad c_2 = 2\frac{3 + 10\alpha_2 \Sigma_\mathrm{r}}{1 + \alpha_2 \Sigma_\mathrm{r}}, \quad \overline{Q}_x = (\overline{q} - \overline{L}_x).$$

The response matrix formulation for one node k is then:

$$\mathbf{A}_x \mathbf{J}^{out}_x = \mathbf{B}_x \mathbf{J}^{in}_x + \mathbf{Q}_x, \quad \forall k \in [1, N_x], \tag{2.125}$$

where

$$\mathbf{J}^{out}_x = \begin{bmatrix} J^{out}_{x_-} \\ J^{out}_{x_+} \end{bmatrix}, \quad \mathbf{J}^{in}_x = \begin{bmatrix} J^{in}_{x_-} \\ J^{in}_{x_+} \end{bmatrix}, \quad \mathbf{Q}_x = \begin{bmatrix} Q_{x,-} \\ Q_{x,+} \end{bmatrix},$$

where the source terms are:

$$Q_{x,\pm} = \frac{D}{\Delta x}[\frac{c_2}{\Sigma_\mathrm{r}}\overline{Q}_x \pm (12 - c_1)Q_{x,1} + (20 - c_2)Q_{x,2}],$$

and the matrix coefficients are:

$$\mathbf{A}_x = \begin{bmatrix} 1+a+e & -b+e \\ -b+e & 1+a+e \end{bmatrix}, \quad \mathbf{B}_x = \begin{bmatrix} 1-a+e & b+e \\ b+e & 1-a+e \end{bmatrix},$$

with

$$a = \frac{D}{\Delta x}(c_1 + c_2), \quad b = \frac{D}{\Delta x}(c_1 - c_2), \quad e = \frac{Dc_2}{\Sigma_{\mathrm{r}}(\Delta x)^2}.$$

At this point we need to find the closure equation that allows to determine the moments of the transverse leakage source. We recall that the latter has two components corresponding to each transverse axis: $L_x(x) = L_{xy}(x) + L_{xz}(x)$, and both are functions of x. The projection on the polynomial basis can be determined if the shape of the functions is known. We introduce then a model that approximates the leakage shape assuming: *i*) a quadratic expansion over a node k of the following form:

$$L^k_{xy}(x) \approx \overline{L}^k_{xy} + \sum_{n=1}^{2} L^k_{xy,n} P_n(\mu),$$

with

$$\overline{L}^k_{xy} = \frac{J^k_{y_+} - J^k_{y_-}}{\Delta y^k},$$

in order to take advantage of the orthogonality of the Legendre polynomials in the projected equation; it ensues that in order to define the parabolic function, two additional conditions are needed, that are given by the assumption that *ii*) the average of this function over the adjacent nodes results in the average transverse leakage:

$$\overline{L}^{k\pm1}_{xy} = \pm\frac{1}{\Delta x^{k\pm1}} \int_{\pm\frac{\Delta x^k}{2}}^{\pm(\frac{\Delta x^k}{2}+\Delta x^{k\pm1})} dx L^k_{xy}(x) = \overline{L}^k_{xy} + \sum_{n=1}^{2} \gamma^{k\pm1}_{x,n} L^k_{xy,n},$$

where, by adopting the change of variable $x = \frac{\pm\Delta x}{2}\mu'$, which implies the change $\mu \to \pm\mu'$, the expansion coefficients are:

$$\gamma^{k\pm1}_{x,n} = \pm\frac{1}{\Delta x^{k\pm1}} \int_{\pm\frac{\Delta x^k}{2}}^{\pm(\frac{\Delta x^k}{2}+\Delta x^{k\pm1})} dx P_n(\mu) = \frac{(\pm)^n}{\alpha^{k\pm1}} \int_1^{1+\alpha^{k\pm1}} d\mu' P_n(\mu'),$$

with

$$\alpha^{k\pm1} = 2\frac{\Delta x^{k\pm1}}{\Delta x^k}.$$

It follows that the moments of the transverse leakage source can be determined using:

$$\begin{bmatrix} L_{xy,1} \\ L_{xy,2} \end{bmatrix} = \begin{bmatrix} \gamma_{x,1}^{k+1} & \gamma_{x,2}^{k+1} \\ \gamma_{x,1}^{k-1} & \gamma_{x,2}^{k-1} \end{bmatrix}^{-1} \begin{bmatrix} \overline{L}_{xy}^{k+1} - \overline{L}_{xy}^{k} \\ L_{xy}^{k-1} - \overline{L}_{xy}^{k} \end{bmatrix}, \tag{2.126}$$

where

$$\gamma_{x,1}^{k\pm1} = \pm\frac{2+\alpha^{k\pm1}}{2}, \quad \gamma_{x,2}^{k\pm1} = \frac{(\alpha^{k\pm1})^2 + 3\alpha^{k\pm1} + 2}{2}.$$

Despite the boundary conditions either for the net currents, or for the incoming partial currents, or for the boundary flux, the NEM4 operator requires an additional condition for the transverse leakage source at the boundary nodes, since it depends on the leakage of the adjacent nodes. For specular boundary conditions one has to impose $\overline{L}_{xy}^{\text{bbd}} = \overline{L}_{xy}^{k_{\text{bd}}}$, where bbd stands for beyond the boundaries and k_{bd} for boundary node. For vacuum boundary conditions, the leakage bbd is typically imposed equal to zero. When the NEM4 operator is spatially decomposed, each subdomain requires the exchange with its neighbors of the incoming partial currents, the average leakage at the boundary nodes for each transverse axis and its spatial mesh size according to Equations (2.125) and (2.126).

Chapter 3

Homogenization Theory & Core Calculation Schemes

In nuclear reactor physics, homogenization techniques play a fundamental role in core modeling because they allow to simplify such complicated systems, for which direct transport (DT) calculations are time demanding and require considerable computational resources. Moreover, the highly detailed information that DT can provide is generally not used for routine industrial applications. The objective of homogenization theory is then:

1 to reduce the problem size, either substituting detailed heterogeneous geometries with homogeneous ones, and/or averaging the energy dependencies;

2 to construct a low-order operator that reproduces average transport quantities (typically the reaction rates) of the original system.

Since we do not know the fine-transport reference solution in the core, the most delicate part of point 1 is to define a Reference Homogenization Problem (RHP) that typically corresponds to an assembly calculation, whose solution is used as weighting function for cross-section homogenization. In order to obtain accurate results, the solution of the RHP must then be representative of the actual conditions in the core.

The two features discussed earlier have led homogenization theory to two opposite applications. Both of them rely on the construction of a simplified problem with fictitious properties that emulates the actual configuration, but they differ in the manner the coarse solution is used. In one hand, the coarse solution corresponds to the core solution that can be achieved by a model, and therefore homogenization theory is used to compose calculation schemes based on a two-step approach. On the other hand, the coarse solution is used to accelerate the convergence of the source iteration scheme for the full DT problem, and therefore the level of details and accuracy achieved is that of a reference calculation. This application appeared later in literature because of the evolution of computational resources.

An issue with the homogenization process is the loss of the detailed information on the cross sections. Thus, the coarse operator resulting from the homogenization can at most reproduce the RHP macroscopic reaction rates in macro-regions and macro-groups when provided with a concurrent macroscopic description of references sources and boundary conditions. Moreover, with the exception of very limited cases, flux homogenized cross sections fail to reproduce reference reaction rates and it is then necessary to recur to special techniques, such as equivalence theory or the use of flux discontinuity ratios to reproduce the reference reaction rates in the RHP. These techniques have been developed in the framework of the classical two-step calculation scheme, and have become popular thanks to the improvement in the core solution with a negligible cost.

The operator of the Coarse Mesh Finite Difference acceleration (CMFD) is also constructed using flux homogenized cross sections, and requires special modification in the streaming term in order to reproduce macro reaction rates. In this case, the RHP corresponds to the full DT problem, and it is redefined at each iteration as long as the source iteration scheme has not converged. This acceleration has become popular in direct calculation schemes because of its efficacy at reducing the number of source iterations, with negligible computational cost and memory requirements.

The first part of this chapter presents the aforementioned homogenization techniques, while the second part is devoted to the most popular calculation schemes for 3D core calculations.

3.1 Homogenization Techniques

3.1.1 Cross-section Homogenization

A homogenization process requires, above all, the definition of a reference homogenization problem that provides the macroscopic quantities to be used in the construction of the low-order operator. As mentioned in the introduction, the objective of a homogenization technique is to construct a coarse operator that reproduces the average reaction rates and, therefore, the particle balance for the RHP, under the assumption that these quantities are close to those extant in the core. Regarding this last condition, a natural framework for the construction of the RHP is supplied by the exact solution for the flux in the RHP considering the RHP in its actual situation in the reactor core [44]. This flux is the solution of a source transport problem with fixed eigenvalue, where the eigenvalue is the core eigenvalue and the source is the angular flux entering the assembly. For the calculation of reactor cores in normal operation conditions, a good approximation for the former is $k_{\text{eff}} = 1$, however the exact incoming angular flux can only be provided by a full exact solution of the entire core. Hence, a determining factor in the construction of the RHP for assembly homogenization will be to construct a realistic entering angular flux.

The RHP is typically solved with a fine-transport operator that can treat all the heterogeneities of the geometry, such as the Method of Characteristics (MOC) or Monte Carlo [45]. The most common types of homogenization are full assembly or pin-by-pin. The former can be seen as infinite medium homogenization, while the latter is a particular case of the more general piecewise homogenization. In this case the coarse geometry upon which the homogenization relies contains more than one output medium. However, when all the output media of a piecewise homogenization have same average nuclear properties, then it is equivalent to the infinite medium homogenization.

The flux-weighted homogenized cross sections associated to each coarse region are defined as:

$$\Sigma^{h,G}_{x,i,R} = \frac{\sum_{g\in G}\sum_{r\in R}\Sigma^{g}_{x,i,r}\Phi^{g}_{r}V_r}{\Phi^{G}_{R}V_R} = \frac{\tau^{G}_{x,i,R}}{\Phi^{G}_{R}V_R}, \tag{3.1}$$

$$\Phi^{G}_{R} = \frac{\sum_{g\in G}\sum_{r\in R}\Phi^{g}_{r}V_r}{V_R}, \tag{3.2}$$

where $\Sigma^{h,G}_{x,i,R}$ is the homogenized macroscopic cross section for reaction x and isotope i in the coarse region R and coarse energy group G, while $\Sigma^{g}_{x,i,r}$ is the macroscopic cross section in region r and group g of the fine discretization for the RHP calculation. The τ^{G}_{R} and the Φ^{G}_{R} defined in Equation (3.2) are respectively the reference reaction rate and average scalar flux for R and G. A rigorous treatment would require the angular flux as weighting function but it would result in angular-dependent homogenized cross sections, so generally it is not applied. If required, anisotropic transfer cross sections are typically homogenized with the scalar flux instead of using the angular moments.

A remark is necessary at this point. We note that the homogenized cross sections

are obtained by dividing the reference reaction rate by the volume of the macro-region times the averaged flux in the macro-region. For the flux-weighted cross sections defined in Equation (3.1) this flux is the reference flux but, as we will discuss soon, it is often necessary to use a different flux, such as the flux computed with the low order operator. What is important to note is that, regardless of the flux used to obtain the homogenized cross sections for all reactions and isotopes, all these cross sections can be obtained from the set of total cross sections $\Sigma_R^{h,G}$. Indeed, for any reaction and isotope we have

$$\Sigma_{x,i,R}^{h,G} = \frac{\tau_{x,i,R}^G}{\tau_R^G} \Sigma_R^{h,G}, \tag{3.3}$$

where τ_R^G is the total reference reaction rate and the ratio of the reference reaction rates is provided by the reference transport solution.

It follows from relations (3.3) that the only unknown coarse cross sections to be determined are the total cross sections $\Sigma_R^{\mathrm{C},G}$ for all macro-regions and macro-groups. These cross sections are conditioned by the associated reaction rate conservation equations

$$\Sigma_R^{\mathrm{C},G} V_R \Phi_R^{\mathrm{C},G}(\overrightarrow{\Sigma}^{\mathrm{C}}) = \tau_R^G, \forall R, G, \tag{3.4}$$

where the fluxes $\Phi_R^{\mathrm{C},G}$ are obtained from the solution of the coarse RHP and are therefore functions of all the total coarse cross sections $\overrightarrow{\Sigma}^{\mathrm{C}} = \{\Sigma_R^{\mathrm{C},G}, \forall R, G\}$. Moreover, coarse boundary conditions are also defined so as to reproduce the macroscopic boundary values of the fine reference problem. Finally, if the RHP is an eigenvalue problem we will also request the preservation of the eigenvalue. However, the latter can be superfluous, albeit numerically advantageous, because, when the coarse operator is constructed so as to preserve net global leakage, then global neutron balance ensures that the eigenvalue is automatically preserved.

The starting point for our discussion is the global neutron balance equations in the entire geometrical domain D of the RHP. For a given macro-group G these equations for the fine and the coarse RHP problems read:

$$\sum_{S \in \partial D} A_S J_S^{+,G} - \sum_{S \in \partial D} A_S J_S^{-,G} + \sum_{R \in D} \Sigma_R^{h,G} V_R \Phi_R^G = \sum_{R \in D} V_R Q_R^G, \tag{3.5}$$

$$\sum_{S \in \partial D} A_S J_S^{+,\mathrm{C},G} - \sum_{S \in \partial D} A_S J_S^{-,\mathrm{C},G} + \sum_{R \in D} \Sigma_R^{\mathrm{C},G} V_R \Phi_R^{\mathrm{C},G} = \sum_{R \in D} V_R Q_R^{\mathrm{C},G}, \tag{3.6}$$

$$Q = H_0 \Phi + \frac{1}{\lambda} F \Phi, \tag{3.7}$$

$$Q^{\mathrm{C}} = H_0^{\mathrm{C}} \Phi^{\mathrm{C}} + \frac{1}{\lambda^{\mathrm{C}}} F^{\mathrm{C}} \Phi^{\mathrm{C}}. \tag{3.8}$$

In these equations, the boundary ∂D of D has been partitioned into a set of macro-surfaces noted S, C stands for coarse, Q and Q^{C} are the isotropic sources comprising scattering (H_0) and fission (F) as in Equations (3.7) and (3.8) and $J_S^{\pm}$ are the outgoing

(+) and incoming (−) average partial currents crossing surface S of area A_S:

$$J_S^{\pm} = \frac{1}{A_S} \sum_{s \in S} A_s J_s^{\pm}, \tag{3.9}$$

where s denotes a boundary surface of the fine transport mesh. We also note that the balance equations have been obtained by direct integration over the entire geometric domain of the original equations (transport, diffusion, etc.) and express a relation between the cross sections and the solution (fluxes, currents) of the equations constructed with those cross sections. Therefore, these equations are satisfied for any regular set of cross sections for which the equations have a solution. This means that the conservation relations are valid *regardless* of the constraints (3.3) and/or (3.4) or any other constraint that one might impose between the cross sections, as long as the equations admit a solution.

In the following, we shall use total leakage and local leakage to refer to the leakage of the whole domain D or to the leakage associated to a coarse region R, respectively.

We discuss now the construction of the coarse operator whose cross sections satisfy constraints (3.3) or (3.4), for which the only independent cross sections are the total ones. Consider first the case when the coarse operator has the same total net leakage as the fine operator. Then, macro-region reaction rates conservation ensures that the eigenvalue is also preserved. Furthermore, it is also possible to show that the constraints in (3.4) are linearly dependent. We follow here an argument given in the reference [43], whereupon the nonlinear problem defined by Equation (3.4) is replaced by an equivalent homogenization problem where the detailed sources $Q^{\mathrm{C},G}(\mathbf{r})$ are those obtained from the solution of the original problem. Hence, the modified problem split into a set of one-group source problems each of which satisfies balance Equation (3.6). It follows that the sum of the macro-region reactions rates is conserved for each macro-group,

$$\sum_{R \in D} \Sigma_R^{\mathrm{C},G} V_R \Phi_R^{\mathrm{C},G} = \sum_{R \in D} \tau_R^G, \forall G, \tag{3.10}$$

as a comparison of Equations (3.5) and (3.6) shows, and this conservation is satisfied *regardless* of the values adopted for the total homogenized cross sections. This is true because the fine and coarse operators have the same global balance equation, which is the case for all operators used in reactor physics: transport, diffusion, simplified $\mathrm{P_N}$, etc. The implication is that the homogenization problem has one degeneracy per macro-group.

Conservation of total net leakage is always true for the traditional infinite lattice model, for which the leakage contributions vanish for both the reference and the coarse calculations. However, if the RHP has non-conservative boundary conditions the preservation of the total net leakage cannot be always incorporated in the definition of the coarse RHP problem and, ultimately, it all depends on the type of boundary condition that the coarse operator can support. Transport-like operators require incoming fluxes and therefore the coarse boundary condition can preserve only the incoming reference currents in Equation (3.5). For these operators it is the sum of the total leakage

and of the total reaction rate per macro-group that is unconditionally preserved and, therefore, constraints Equation (3.4) are not degenerated. Note that the implication is that the solution of the homogenization problem will preserve the total exiting current but not the detailed exiting current over each surface. By imposing that the eigenvalue is preserved as well as the reaction rates, we ensure the existence of a single coarse operator. On the other hand, for elliptic operators such as diffusion it is possible to use the total reference currents as boundary conditions and achieve then net leakage conservation. Here, the eigenvalue is automatically preserved but we have again a degeneracy per macro-group and the homogenization problem accepts an infinite number of solutions, with multiplicity equal to the number of macro-groups.

If one uses the customary flux-weighted homogenized cross sections in Equation (3.1) for the construction of the coarse operator, then it is very unlikely that Equation (3.4) would be satisfied. The exception is full assembly homogenization or piecewise homogenization of an assembly consisting of a set of identical pins, in which case global balance (or local balance for the assembly with identical pins) ensures the conservation of reaction rates. However, for piecewise homogenization the individual macro-region reaction rates are most likely not preserved, because local leakage is not reproduced by the low-order operator. One may conclude that, in general, the coarse operator constructed by flux-weighting homogenization fails to reproduce macroscopic reaction rates.

To overcome this problem one must construct a *faithful* coarse operator, meaning an operator that preserves reference reaction rates for each macro-region and each macro-group as in Equation (3.4). Two techniques have been used to attain this goal: equivalence theory (EQV) and homogenization via Flux Discontinuity Factors (FDF). The former consists of directly computing an optimal set of cross sections, via iterative solution of nonlinear Equation (3.4). The latter, which applies only to elliptic coarse operators, consists of using flux-weighted cross sections, while introducing new degrees of freedom in the homogenization process, leading to a drastic modification of the coarse operator. Similarly to the FDF technique, the CMFD acceleration operator is also constructed with flux-weighted cross sections and introduces new degrees of freedom in order to preserve local balance for each macro-region and macro-group. However, it differs from the other one in the way the reference balance preservation is forced.

3.1.2 Equivalence theory

The idea behind equivalence theory, originally proposed by Kavenoky [46] and later refined by Hébert [47] and Sanchez *et al.* [48], is to obtain a faithful homogenization by numerically searching for a set of homogenized cross sections, called equivalent cross sections Σ^{eq}, which lead to a faithful coarse operator. Because of the dependence of the coarse fluxes on the coarse cross sections, the problem is nonlinear and it has been solved either i) by iteratively minimizing the functional

$$\mathcal{F}(\overrightarrow{\Sigma}^{eq}) = \sum_{R,G} \left[1 - \frac{\tau_R^{\mathrm{C},G}(\overrightarrow{\Sigma}^{eq})}{\tau_R^G} \right]^2 , \tag{3.11}$$

where $\overrightarrow{\Sigma}^{eq}$ is the set of equivalent cross sections for all macro-regions and macro-groups (the solution can be obtained for instance with a Newton algorithm [49]), or ii) by fixed-point iterations with Equation (3.4), which is then used to update the equivalent cross sections. The scheme of fixed-point iterations is shown in Figure 3.1.

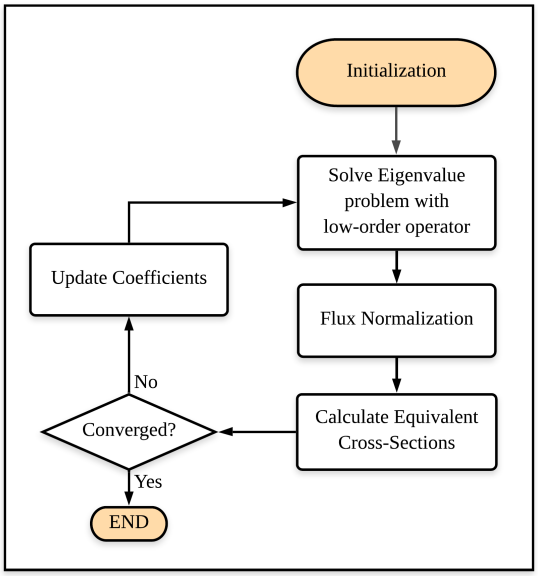

Figure 3.1. Fixed-point interations for the Equivalence method.

In both methods, the iterations are initialized with the flux-weighted cross sections and the updated values of the equivalent cross sections are used to compute the new flux $\Phi_R^{C,G}(\overrightarrow{\Sigma}^{eq})$, solution of the associated coarse equation. The difference between the two methods consists in the way the cross sections are updated: while in the functional method the set of equivalent cross sections is updated by a global minimization of the functional, in the fixed-point method each equivalent cross section is obtained directly from its associated reaction rate according to Equation (3.4).

As earlier explained, when conservative boundary conditions are applied, and in diffusion also for non-conservative conditions, the homogenization problem is degenerated [44, 49]. In order to choose one single solution, two different types of normalization are used in practice. The first consists of imposing the conservation of the domain's average reference scalar flux per macro-group, while in the second, known as Selengut's normalization [50], it is the total transport incoming current per macro-group that is preserved. In the particular case of full assembly homogenization with normalization of the average scalar flux, one has $\Sigma^{eq} = \Sigma^h$.

The advantage of equivalence theory is that it can be used with whichever low-order operator is adopted for the coarse calculation, which can also be a transport operator. However, it has been shown that the fixed point iterations may not converge, in particular for cases where transport effects are dominant [49].

3.1.3 Flux discontinuity factors

The homogenization via flux discontinuity factors was analyzed by Koebke [51, 52], Smith [53] and Sanchez [44]. This technique was initially applied for full assembly homogenization but we discuss it here in the general context of piecewise homogenization. The basic approach is to force the preservation of the reference net currents at each interface S of a macro-region so that, if flux-weighted homogenized cross sections are used in the coarse operator, the eigenvalue, the reactions rates and the local leakage are simultaneously reproduced for each macro-region and macro-group. However, as we mentioned earlier, in these conditions is very improbable that the resulting solution will be continuous at macro-region interfaces. This difficulty was circumvented thanks to Koebke's idea of introducing a relaxation in the continuity condition of the flux at each mesh interface [51] to allow for a discontinuity of the flux at the interface S between two adjacent macro-regions A and B:

$$f_{S_\mathrm{A}}\Phi^\mathrm{C}_{S_\mathrm{A}} = f_{S_\mathrm{B}}\Phi^\mathrm{C}_{S_\mathrm{B}} \Rightarrow \Phi^\mathrm{C}_{S_\mathrm{A}} = r_\mathrm{AB}\Phi^\mathrm{C}_{S_\mathrm{B}}, \tag{3.12}$$

where r_AB is called Flux Discontinuity Ratio (FDR). Note that $r_\mathrm{AB} = 1$ when no discontinuity is introduced, as well as at the boundaries with reflection conditions. Also, in Equation (3.12)

$$f_{S_\mathrm{A}} = \frac{\Phi_S}{\Phi^\mathrm{C}_{S_\mathrm{A}}} \tag{3.13}$$

is the Flux Discontinuity Factor (FDF), named heterogeneity factor by Koebke, defined as the ratio of the reference to the coarse averaged interface fluxes on surface S.

Koebke [51] was the first to use local balance for a macro-region to show that if one wanted to simultaneously use flux-weighted cross sections and preserve reaction rates, then the reference local net currents should also be preserved. He also concluded that this will also preserve the averaged macro-region fluxes and, furthermore, recognizes that most probably the resulting scalar flux will not be continuous at the interfaces between macro-regions. The solution thus was to implement the preservation of the reference transport net current at each interface between two macro-regions and accept flux discontinuity at the macro-region surfaces. In his seminal work, Koebke decided to impose the somewhat artificial condition that the discontinuity factors should be equal on the two opposite sides of each homogeneous rectangular macro-region. In order to achieve this, he had to introduce macro-region and direction dependent diffusion coefficients. For a two-dimensional homogenization mesh, the homogenization was thus achieved by adding four equivalence parameters per macro-region: a direction-dependent diffusion coefficient and a bilateral discontinuity factor for each one of the directions. Also, the diffusion coefficients have to be iteratively determined.

In order to avoid this iterative process, Smith [53] decided to use the typical volume averaged diffusion coefficient and defined his Generalized Equivalence Theory (GET) by relaxing the artificial symmetry constrain required by Koebke's homogenization and allowing for the two discontinuity factors associated to a given direction to be independent of each other. Hence, in Smith's GET a discontinuity factor is associated to each

interface that a macro-region may have with a neighbor macro-region, which is simply calculated via its definition in Equation (3.13). For a rectangular homogenization mesh this amounts to four FDFs, two for each direction.

The question that arises next is how to determine these factors when the reference core solution is not known. Smith made a distinction between Reference Discontinuity Factors (RDF) and Assembly Discontinuity Factors (ADF), calculated using the core solution and the assembly solution of the RHP, respectively. Following Koebke's steps, Smith showed for a 1D problem that if the RDFs are used with the homogenized cross sections weighted with the reference core flux, then the coarse operator reproduces exactly the reference average quantities. This suggests the possibility to construct an operator, as CMFD, which can be used as a nonlinear acceleration for the transport solution.

However, the objective of a homogenization paradigm is to predict the reference heterogeneous solution without actually solving the entire core problem. As Koebke has previously done by comparing the performance of his FDFs calculated with different environments of a given assembly type, Smith compared the impact of the RDFs calculated for each assembly type in different core environments, and showed that the results obtained using the ADFs computed with an infinite lattice model gave a good estimate of the average of all the actual RDF corresponding to that type of assembly in the core [53]. These ADFs cannot be exact because they do not account for the position or for the environment of the assembly. To determine the ADFs, he observed that for full assembly homogenization with periodic boundary conditions the coarse flux is constant. It follows that the coarse surface averaged flux in Equation (3.13) is equal to the coarse volume averaged flux, which in turn is also equal to the reference volume averaged flux. Hence, $\Phi_S^{\mathrm{C}} = \overline{\Phi}^{\mathrm{C}} = \overline{\Phi}$ so that the resulting ADFs are independent of the coarse solution for the RHP:

$$f_{\mathrm{GET}} = \left.\frac{\Phi_S}{\Phi}\right|_{\mathrm{RHP}}, \tag{3.14}$$

where $|_{\mathrm{RHP}}$ indicates evaluation for the RHP.

More recently, Sanchez [44] proposed a Black-Box (BB) homogenization model based on the use of flux-weighted cross sections wherein, instead of the reference averaged flux, it is the reference partial currents that are preserved at each interface. One of the advantages of this approach was to deal with diffusion as well as transport coarse operators. While in transport there were two Current Discontinuity Factors (CDFs) for each of the two opposite interface partial currents, for the diffusion operator one could use a single equivalent FDF, so that

$$J_S^{\pm,\mathrm{C}} = f\frac{\Phi_S^{\mathrm{C}}}{4} \pm \frac{J_S}{2}. \tag{3.15}$$

to achieve the conservation of the partial currents at the interface: $J_S^{\pm,\mathrm{C}} = J_S^{\pm}$. From

these conservations conditions, one derives the value of the equivalent FDF:

$$f_{S_A} = 2\frac{J_S^+ + J_S^-}{\Phi_{S_A}^{\mathrm{C}}}. \tag{3.16}$$

to be compared with Koebke and Smith's definition in Equation (3.13). Moreover, in the case of infinite lattice boundary conditions one has $J_S = 0$ so that $J_S^+ = J_S^-$ and for full assembly homogenization one obtains the simple formula

$$f_{\mathrm{BB}} = 4\frac{J_S^{\pm}}{\Phi}\bigg|_{\mathrm{RHP}}, \tag{3.17}$$

which is also independent of the discretization used with the coarse operator. The GET and BB homogenization models in Equations (3.14) and (3.17) give equal FDFs only in the extreme cases when the initial assembly is homogeneous or when the reference operator is also diffusion.

The result of the equivalent FDF is to introduce a jump from the partial currents at the interface of the homogenized macro-region:

$$\Delta J_S^{\pm,\mathrm{C}} = \pm(J_S^{\pm,\mathrm{C}} - \lim_{\epsilon\to 0_+} J_{S_\epsilon}^{\pm,\mathrm{C}}) = \pm\frac{(f-1)\Phi_S^{\mathrm{C}}}{4}\bigg|_{\mathrm{RHP}}, \tag{3.18}$$

where S_ϵ denotes the surface parallel at the interface at a distance ϵ towards the interior of the macro-region. As was previously observed [44], this jump is equivalent to inserting in the coarse model a singular surface anisotropic source emitting $\Delta J_S^{\pm,\mathrm{C}}$ neutrons in the outward direction and as many in the inward direction. We note that the GET FDF also leads to the interface values in Equation (3.15) and therefore exhibits also a partial current jump as in Equation (3.18), the only difference in the jump values is in the value of the flux discontinuity factor f.

The general case of piecewise homogenization, where the coarse operator has both internal and boundary interfaces, was recently investigated by Sanchez *et al.* [43] who computed the flux discontinuity ratios in Equation (3.12) induced by the simultaneous preservation of the net averaged currents at all the internal interfaces of the RHP, while using the reference surface averaged currents at the external interfaces as boundary conditions for the coarse RHP. These FDRs can be calculated from the minimization of the functional

$$\mathcal{F}(\overrightarrow{r}) = \sum_{S,G}\left[\frac{J_S^{\mathrm{C}}(\overrightarrow{r})}{J_S} - 1\right]^2, \tag{3.19}$$

where $\overrightarrow{r}$ is the set of all FDRs, one per internal interface and macro-group. Moreover, they considered the case when the diffusion discretization mesh is equal to the homogenization mesh and the numerical discretization of the diffusion operator has only one degree of freedom per interface, and computed an analytical solution for finite differences and nodal transverse discretizations. For these numerical schemes, the degree

of freedom can be identified with the interior limit of the averaged interface flux and these surface averaged fluxes can then be calculated from the solutions of an independent set of local diffusion problems, one per macro-region, where each macro-region is solved with the boundary conditions provided by the reference interface averaged currents. Finally, the FDRs are calculated from the surface averaged fluxes of the two macro-regions that share each interface.

When the diffusion discretization mesh is finer than the homogenization one, the solution cannot be computed analytically and has to be determined from the iterative minimization of the nonlinear functional in Equation (3.19). Numerical calculations showed that, while with finite differences the FDRs slowly converged with the number of sub-meshes, this was not the case for the transverse nodal method, giving thus a numerical advantage for which analytically determined FDRs for a single sub-mesh are a very good approximation for any other number of sub-meshes.

In the context of piecewise homogenization, the diffusion solution depends only on the flux discontinuity ratios and not on the individual flux discontinuity factors at both sides of each internal interface. Therefore, whether one uses GET FDFs as in Equation (3.13) of BB FDFs as in Equation (3.16) does not make any difference in the final values of the FDRs. This follows from the fact that the numerators of these two FDFs evaluations, $2(J_S^+ + J_S^-)$ and Φ_S, are reference transport values which depend only on the interface and not on the adjacent macro-regions and, therefore, simplify out when evaluating the FDR. It follows that the FDRs depend only on the method and the mesh adopted for the discretization of the coarse problem. However, for assemblies homogenized in separate RHPs one has to provide also the flux discontinuity factors at the boundary surfaces which will be used in the final whole core diffusion calculation, and it is here that the use of GET or BB makes a difference. The conclusion to this discussion is that while the FDRs are mathematically defined, the FDFs are based in a physical assumption regarding the behavior of the coarse flux at the interface between two adjacent assemblies: the GET model enforces the continuity of the reference flux, while the BB model preserves the exchanges between the assemblies as described by the reference partial currents.

When compared with equivalence theory, the homogenization technique based on FDFs has not only the advantage of improving the solution of core calculations, but it also offers the simplicity of using the physical transport flux for cross-section weighting plus the potential for a direct evaluation of the homogenization parameters that avoids problematic iterative solutions of nonlinear problems that might not always converge.

3.1.4 CMFD acceleration

With the same incentive of preserving the reference net currents at each mesh interface, which allows to use flux weighted cross sections while preserving reaction rates, another widely used technique is the Coarse Mesh Finite Difference method (CMFD) [54–59], which today it is often used as nonlinear acceleration for transport due to its fast solution and efficiency. As opposed to the FDF technique, the CMFD flux is continuous at the interfaces while an artificial drift term is added to the diffusion operator in order to preserve local balance. This is mediated by correcting the definition

of the net current:

$$J_{\mathrm{AB}} = -D_{\mathrm{AB}}(\Phi_{\mathrm{B}} - \Phi_{\mathrm{A}}) - \tilde{D}_{\mathrm{AB}}(\Phi_{\mathrm{B}} + \Phi_{\mathrm{A}}). \tag{3.20}$$

In this equation the first term is the expression for the traditional Fick's law obtained with a mesh-centered finite differences scheme,

$$D_{\mathrm{AB}} = \frac{2D_{\mathrm{A}}D_{\mathrm{B}}}{D_{\mathrm{A}}\Delta x_{\mathrm{B}} + D_{\mathrm{B}}\Delta x_{\mathrm{A}}}, \tag{3.21}$$

where D_Z and Δx_{Z} for $Z \in A, B$ are the diffusion coefficient and the size of a mesh element, respectively, and A and B stand for two adjacent meshes with B to the right of A. The diffusion coefficient D in a region is typically calculated by homogenizing in space and energy $\frac{1}{3\Sigma_{\mathrm{tr}}}$ by flux-volume weighting according to Equation (3.1). The coefficient $\tilde{D}_{\mathrm{AB}}$ of the corrective term is evaluated instead by substituting the reference transport currents and scalar fluxes of the previous iteration in Equation (3.20). Like in the FDF technique, for a given diffusion coefficient in a mesh, one has to define, respectively for 2D or 3D geometries, four or six equivalence parameters (one per interface). This does not apply, however, to the partial current-based Coarse Mesh Finite Difference (p-CMFD) method [38], where two corrective coefficients per interface are introduced in order to independently preserve the two partial currents, and therefore the net current. When the CMFD is used as an acceleration, the transport fluxes on the fine spatial and energy meshes are calculated at the end of each power iteration via rebalancing:

$$\psi_{r,h}^{g,l+1} = \psi_{r,h}^{g,l+1/2} \frac{\Phi_R^{\mathrm{C},G,l+1}}{\sum_{g\in G}\sum_{r\in R}\Phi_r^{g,l+1/2}}, \forall r \in R, \forall R \in D, \forall h, \forall g \in G, \tag{3.22}$$

where r,h,g are respectively the fine region, the angular moment and the energy group indexes of the angular flux ψ, l is the iteration index and Φ is the scalar flux. The sources for the next iterations are calculated with the accelerated flux and at convergence the flux ratio of Equation (3.22) must be equal to one. When a method of domain decomposition is used to solve the transport problem, the same rebalancing equation is applied to the outgoing angular flux of a subdomain before transmitting the information to its neighbors:

$$\psi_{s,d}^{+,g,l+1} = \psi_{s,d}^{+,g,l+1/2} \frac{\Phi_R^{\mathrm{C},G,l+1}}{\sum_{g\in G}\sum_{r\in R}\Phi_r^{g,l+1/2}}, \forall s \in \partial R, \forall \partial R \in \partial D, \forall d, \forall g \in G, \tag{3.23}$$

where + stands for outgoing, d is the direction index and s is the fine-transport surface element at the boundaries of the coarse region ∂R.

3.2 Cross-section Self-shielding

The first task required for a fine transport calculation is to produce the multigroup cross sections for each isotope according to Equation (2.1). This preliminary step is mandatory for any type of core calculation scheme with a *fully* deterministic approach. Because of this, the classical two-step approach becomes actually a three-step calculation scheme, and the direct 3D transport calculations that have been performed in literature are in effect a two-step calculation scheme. In this work, we will use in any case the traditional terms "two-step" and "direct" to refer respectively to the classical approach and the 3D core transport calculations.

Before introducing the main calculation schemes for core calculations, we will discuss firstly the most popular self-shielding approaches used in reactor physics for two reasons. The first one is that self-shielding models can be used for any type of calculation scheme and, secondly, they can be considered as a homogenization step, which is the topic of this chapter, but it is usually called cross-section condensation, since we substitute continuous energy cross sections, defined with hundreds thousands of points, to multigroup cross sections that typically have an energy mesh between 50 and 300 groups. An interesting feature of this homogenization step is that, unlike the second homogenization process between the fine transport and the low-order operators, here the number of output media is larger than the initial or real one. This is explained in the following discussion.

Equation (2.1) requires the knowledge of a weighting flux so as to produce effective cross sections that preserve reaction rates of a reference configuration. At this stage, the difficulty of a self-shielding model is to account for the resonant behavior of continuous cross sections, that exhibit a large number of peaks for heavy nuclides in the epithermal energy domain, that in turn cause flux depression at the corresponding energies. This results in a reduction of the neutron absorption rate at the resonance energies, known as the energy self-shielding effect. The spatial self-shielding effect, instead, is referred to the depression that neutron flux experiences from the peripheral surface to the center of the resonant medium. Because of this strong gradient that causes a spectrum change, the fuel pin is typically modeled with at least four concentric media that have different self-shielded cross sections, even if it has same nuclear properties. In multiphysics calculations, the number of concentric media also depends on the fuel radial temperature gradients, for which the continuous energy cross sections experience the Doppler broadening effect.

The main approaches used in self-shielding modeling are the ultrafine energy calculation, the equivalence theory and the subgroup method [60].
The former is based on a direct resolution on the continuous energy domain of the transport equation. This allows to obtain an accurate neutron flux, but it would make the cross-section condensation a useless step, since the transport solution is already available. This is why this method, as the other ones, typically solves a simplified equation that is the slowing-down transport equation, described in [2], and only for the resonance energy domain. The main assumptions at this stage are: the fission, spallation and upscattering sources are neglected, and the scattering source is isotropic

and elastic. These assumptions are justified by the fact that the former events and the inelastic scattering can be neglected for the considered energy domain. Although with this simplification, this approach is reliable, but requires a large amount of computational resources and, therefore, its application is limited to a pin cell or a small groups of pins [60].

3.2.1 Homogeneous-Heterogeneous Equivalence

The equivalence theory is a simple approach that introduces an ensemble of approximations that allow fast self-shielding calculations. It is based on an equivalence between the heterogeneous problem and a set of infinite homogeneous medium problems. The latter provides an analytical expression for the weighting spectrum in the continuous energy domain, that depends on a parameter called background cross section. This expression is obtained by introducing more approximations to the slowing-down equation. One of the most popular for the infinite homogeneous medium is the narrow resonance model, which utilizes the assumption that the resonance peaks are very narrow with respect to the energy loss of neutrons within the resonance energy range. It follows that the neutron source is mainly due to the neutron scattering from outside the resonance, which simplifies the slowing-down equation, yielding the following analytical expression:

$$\phi(E) = \frac{\sigma_{p,r} + \sigma_b}{\sigma_r(E) + \sigma_b} \frac{1}{E}, \tag{3.24}$$

where r stands for resonant isotope that has a potential scattering cross section $\sigma_{p,r}$ and a total cross section σ_r. Moreover, σ_b is the background cross section defined in an infinite homogeneous medium as:

$$\sigma_b = \frac{\sum_{i \neq r} N_i \sigma_{p,i}}{N_r}, \tag{3.25}$$

with N_i the isotopic concentration of isotope i contained in the medium. The background cross section is a fictitious cross section that accounts for the depression of the neutron flux at the resonance peak in an infinite homogeneous medium. The reader is directed to the reference [60] for more details on the derivation and approximations introduced to obtain Equation (3.24).
The continuous energy flux is tabulated with respect to this parameter and the heterogeneous problem is used to estimate the escape rate or the escape probability from the resonant medium. Ths probability can be computed using simplified physical models, such as the Dancoff correction, or with a numerical calculation that is typically performed with collision probabilities, such as in the Tone's method [60]. The escape rate is then expressed as an additional cross section that modifies the background cross section so as to obtain the equivalence between the heterogeneous problem and the set of equivalent media. The most important limits of this model are the approximations for the escape probabilities from the resonant medium, and that no resonance overlapping in isotopes mixtures is considered, that is a particular feature of depletion calculations where fission products and new actinides are produced, and for which other models are

required.

3.2.2 Subgroup Approach

The subgroup method is based on the subdivision of each energy group into a set of subgroups such that the effective or self-shielded cross section can be computed as follows:

$$\sigma_g(\mathbf{r}) = \frac{\sum_{sg\in g} \sigma_{sg}(\mathbf{r})\phi_{sg}(\mathbf{r})}{\sum_{sg\in g} \phi_{sg}(\mathbf{r})}, \tag{3.26}$$

where sg is the subgroup index. The weighting flux can be computed directly solving the slowing-down equation, but this is generally not done because of the high computational cost. Another approach is to use the probability tables where the subgroup cross sections are tabulated for different background cross sections, similarly to the equivalence approach. This tabulation results to be more accurate because the variation in energy of the subgroup cross sections is smaller than that of the effective multigroup cross section.
In this method the energy integration is substituted with a Lebesgue integration in the cross-section domain as it follows:

$$\int_{\Delta E_g} dE\phi(E) = \int_{\sigma_{g,min}}^{\sigma_{g,max}} d\sigma\phi(\sigma)p(\sigma), \tag{3.27}$$

where $p(\sigma)d\sigma$ is the probability density function of a given cross section that can be found in the energy group ΔE_g. Equation (3.27) is then employed for the effective cross sections as it follows:

$$\sigma_g(\mathbf{r}) = \frac{\sum_{sg\in g} \sigma_{sg}(\mathbf{r})\phi_{sg}(\mathbf{r})p_{sg}}{\sum_{sg\in g} \phi_{sg}(\mathbf{r})p_{sg}}, \tag{3.28}$$

where this time the flux is cross-section dependent and not energy dependent. A suitable set of the subgroup parameters σ_{sg} and p_{sg} is called probability table, and there are two main techniques that allow to determine it: the fitting method and the moment method. Once the probability tables are known, the subgroup flux is computed with a transport calculation, and then used in Equation (3.28).
The inconvenient of this approach is that the information of the energy dependency is lost when deriving the subgroup cross sections. It ensues that the temperature effects, in other words the Doppler broadening of resonances, are difficult to treat, posing some limitations to the method.

3.3 Classical Two-Step Approach

The classical two-step calculation scheme has been widely used for core modeling and design thanks to its efficacy of producing fast results at different core configurations. The calculation scheme is shown in Figure 3.2. The first of the two steps

consists of "off-line" 2D RHP calculations for each fuel assembly, performed on fine spatial and energy meshes with high order angular dependency. These calculations are called lattice calculations for some reason that will be discussed later. A library is produced where the homogenized microscopic cross sections are stored for different physical states and for the most significant isotopes that take part in the fuel depletion process, plus a residual that takes into account the remaining isotopes. Each state is associated to a set of physical parameters, such as burnup, moderator density, fuel temperature, etc. In the second step, a few-group 3D diffusion core solver is used for the actual 3D core depletion calculation. At this stage, the code searches and interpolates the library data to the actual state of the reactor, and performs the 3D calculation on coarse spatial and energy meshes. Recently, the 3D SP_3 and SP_5 operators have also been applied instead of diffusion to improve the pin-by-pin solution [61], while S_N operators are rarely applied to LWR cores.

Typically, the equivalent cross sections or the flux discontinuity ratios are determined and stored at the end of each lattice calculation and, in the second step, the parameterized library containing all the data necessary for the construction of the coarse operator is fed into the coarse core calculation, so that there is no need for the "equivalence box" in Figure 3.2. However, this requires that at the homogenization stage one has to know in advance which low-order operator will be used in the second step and, for the general case of piecewise homogenization with EQV or FDR with submeshing, the necessary coarse solver routines must be included in the same package than the lattice code. Another possibility to organize the two-step procedure is the one that is fully illustrated in the left of Figure 3.2 and in which the "equivalence box" is active. Here, the first step is used to compute a first parameterized library containing all transport results necessary for the homogenization stage, including volume and surface averaged fluxes, surface averaged partial currents and flux-weighted cross sections. In the second step, this library is used to perform the homogenization process and fabricate the final parameterized library that is then fed into the coarse core calculation. This operation is represented by the "equivalence box" which has direct access to the appropriate coarse solver routines available in the coarse core code. This procedure is more flexible in that it leaves the user free to adopt different core solvers, with the only limitation of fixing the number of coarse groups in the first step.

3.3.1 RHP in Two-step Approach

The motif that is chosen as Reference Homogenization Problem is a fuel assembly. After a self-shielding calculation, the multigroup transport equation is generally solved in a 2D geometry with a fine-transport operator that can treat all the heterogeneities and the geometrical details, such as MOC or Monte Carlo [45]. At this stage of the calculation scheme and for the self-shielding model, the surrounding environment of the assembly is not known. Reflection or conservative conditions are therefore imposed at the boundaries, as if the motif was repeated to infinity (the so called infinite lattice calculation), assuming that the exchanges between assemblies are negligible. It ensues that the solution is symmetric in space, so only one eighth of a PWR assembly or one sixth of a VVER assembly is computed. Another consequence is that the eigenvalue of the problem can be very different from one, which is the value in a steady-state core,

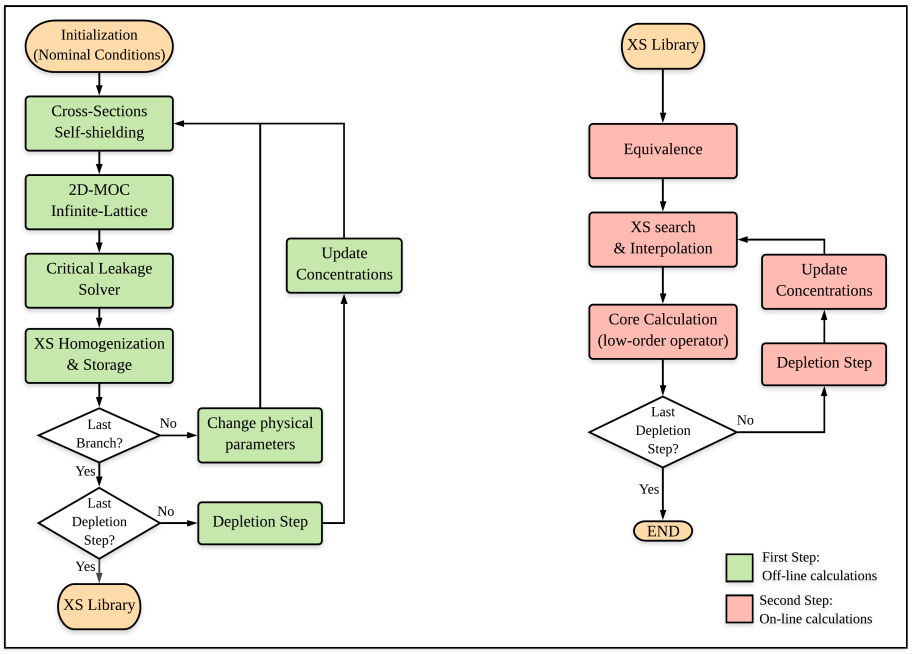

Figure 3.2. Two-step calculation scheme.

suggesting that the flux spectrum can be far from the actual situation.

It follows that the spectrum of condensation is adjusted introducing a critical-leakage model, so as to obtain an eigenvalue equal to one. In this model, three assumptions are introduced:

1. The neutron flux is written as the product of a macroscopic distribution in space $\phi(\mathbf{r})$ and a periodic fundamental mode, that is the transport solution within the motif (Equation (3.29)). It has been shown that this factorization is exact in the asymptotic situation where the core is composed of identical assemblies that contain regular pins;
$$\psi(\mathbf{r}, \mathbf{\Omega}, E) = \phi(\mathbf{r})\varphi(\mathbf{r}, \mathbf{\Omega}, E) \tag{3.29}$$

2. The macroscopic distribution is the asymptotic distribution in a homogeneous medium and solution of the Laplace equation (Equation (3.30)). The real number B^2 is the buckling of the macroscopic distribution;
$$\nabla^2\phi(\mathbf{r}) + \mathrm{B}^2\phi(\mathbf{r}) = 0 \Rightarrow \phi(\mathbf{r}) = \phi_0 e^{i\vec{\mathrm{B}}\cdot\mathbf{r}} \tag{3.30}$$

3. The fundamental mode is homogeneous, so it does not depend on the space variable (Equation (3.31)).
$$\psi(\mathbf{r}, \mathbf{\Omega}, E) = \varphi(\mathbf{\Omega}, E) e^{i\vec{\mathrm{B}}\cdot\mathbf{r}} \tag{3.31}$$

Substituting Equation (3.31) into the transport equation, then homogenizing in space,

integrating in angle, considering linear anisotropic scattering, and with some mathematical manipulations, we obtain the B_1 equations whose mathematical demonstration is here omitted:

$$[\Sigma^g + \mathrm{D}^g(\mathrm{B})\mathrm{B}^2]\varphi^g(\mathrm{B}) = \sum_{g'} \Sigma_{\mathrm{s0}}^{g'\to g}\varphi^{g'}(\mathrm{B}) + \frac{\chi^g}{k_{\mathrm{eff}}}\sum_{g'}\nu\Sigma_{\mathrm{f}}^{g'}\varphi^{g'}(\mathrm{B}),$$
$$\mathrm{D}^g(\mathrm{B}) = \frac{\gamma^g(\mathrm{B})}{\alpha^g(\mathrm{B})\Sigma^g}\left[1 + \sum_{g'}\Sigma_{\mathrm{s1}}^{g'\to g}\mathrm{D}^{g'}(\mathrm{B})\frac{\varphi^{g'}(\mathrm{B})}{\varphi^g(\mathrm{B})}\right], \tag{3.32}$$

with

$$\alpha^g(\mathrm{B}) = B^{-1}tg^{-1}\left(\frac{\mathrm{B}}{\Sigma^g}\right), \qquad \gamma^g(\mathrm{B}) = B^{-2}[1 - \Sigma^g\alpha^g(\mathrm{B})].$$

In Equation (3.32) the equivalent infinite homogeneous medium contains, for simplicity, only one fissile isotope. The three unknowns are the buckling B^2 of the macroscopic distribution, the leakage coefficient D in infinite homogeneous medium, and the fundamental spectrum φ^g. To close the system, a third condition is required, so the buckling is searched iteratively in such a way that the k_{eff} of the assembly is equal to one. At each iteration, for a given B the fundamental spectrum and the leakage coefficient can be directly calculated using Equation (3.32). The iterations are carried out by a Newton method until the zero of the function

$$f(\mathrm{B}) = \sum_g \nu\Sigma_{\mathrm{f}}\varphi^g(\mathrm{B}) - 1 \tag{3.33}$$

is found. The first bounding value for B of the interval of search is 0, corresponding to the case with no leakage, and the second one is estimated using the following equation:

$$\mathrm{B}^2 \approx \frac{k_\infty - 1}{M^2(0)}, \tag{3.34}$$

that has been obtained from the definition of k_{eff} and migration area respectively:

$$k_{\mathrm{eff}} = 1 = \frac{k_\infty}{1 + M^2(B)\mathrm{B}^2}, \tag{3.35}$$

$$M(\mathrm{B}) = \frac{\sum_g D^g(\mathrm{B})\varphi^g}{\sum_g \Sigma_a^g\varphi^g}. \tag{3.36}$$

Once the critical buckling is found, a fictive cross-section $\mathrm{D}^g\mathrm{B}_{cr}^2$ is added homogeneously

to the total cross-section to perform again a new heterogeneous calculation as follows:

$$[\mathbf{\Omega} \cdot \nabla + \Sigma^g(\mathbf{r}) + \mathrm{D}^g \mathrm{B}^2_{\mathrm{cr}}]\psi^g(\mathbf{r}) = Q^g(\mathbf{r}), \quad + \text{Reflective BC.} \tag{3.37}$$

The new heterogeneous flux is successively used for homogenization to produce the new cross sections of the equivalent infinite homogeneous medium. The iterations between the heterogeneous problem and its equivalent infinite-homogeneous medium problem are repeated until the k_{eff} of the heterogeneous problem equals one, as shown in Figure 3.3.

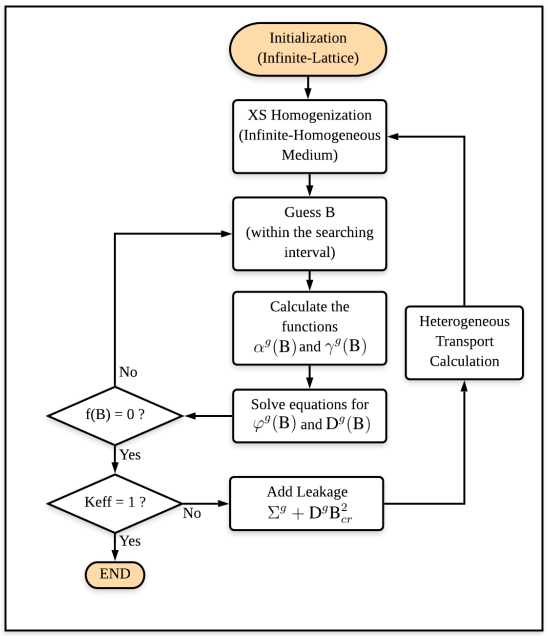

Figure 3.3. Critical Leakage Solver.

Finally, the heterogeneous transport solution at critical conditions is used as weighting function for cross-section homogenization, and the homogenized leakage coefficient, also called Benoist's coefficient, is stored in the few-group library as diffusion coefficient for the 3D core calculation.

It is worth to point out that the critical leakage model simulates the axial leakage as a term of absorption, which can be positive or negative depending on the k_∞ of the fuel assembly. The condition $k_{\mathrm{eff}} = 1$ gives then a global information on the environment, associated to the system state, but no information is provided about the position in the core and the isotopic content of the neighboring assemblies.

3.3.2 Limits of the Two-step Approach

Let us enumerate the approximations introduced by the two-step approach. At the RHP calculation stage, the surrounding environment of the assembly is not known, so conservative boundary conditions are typically imposed. This is the first approximation of the two-step approach, since 1) it assumes that the net exchanges between assemblies

are negligible. The weighting spectrum is then adjusted by introducing a homogeneous critical-leakage model, so as to obtain an assembly eigenvalue equal to one [62]. This model was developed on the assumption that 2) the transport solution is the product of a periodic fine distribution and a macroscopic distribution, the so called infinite medium fundamental mode assumption.

The sequence self-shielding and critical lattice calculations is repeated for each physical state to produce homogenized data. It is a usual practice 3) to perform the depletion calculation for only one assembly history with physical parameters that are typically the nominal ones, and successively using the isotopic concentrations of each burnup step for all the other branch calculations. That is why in Figure 3.2 the burnup parameter has a separate loop, associated to the depletion step, while an internal loop is used to do all the computations varying the values of the other parameters with fixed burnup value. This approach may fail when an assembly is actually depleted at physical conditions that are far from the nominal ones, like in the case of a rodded assembly [63]. This is the case also for BWRs where the vapor quality significantly changes axially, which requires to compute depletion histories for different values of that parameter.

An important issue that arises in the classical calculation scheme is how to define an adequate RHP for the reflector homogenization. Indeed, the reflector requires a different homogenization approach because no multiplication occurs and vacuum conditions are imposed on at least one boundary. Regarding this problem, there is a large number of procedures that have been adopted in the literature, such as 1D models, 2D calculations with one fuel assembly next to a reflector "assembly", or one row of 8 or 9 fuel assemblies next to each other including the reflector at the end, or even bigger motifs of 5×5 assemblies containing a reflector layer surrounding a mini-core. However, 4) the use of these reflector cross sections introduces further approximations because the RHPs used to compute them may contain assemblies with different fuels or irradiated at different conditions than those in the actual configuration in the core.

In addition to $\sigma_{x,i,R}^{h,G}$, one may want to store in the library the isotopic concentrations at each burnup step as well as the transport scalar flux integrated in energy and space, in order to be able to recalculate the reference reaction rates when performing the core calculation. Moreover, in order to calculate the flux discontinuity factors, one also needs to store surface quantities. In case of full assembly homogenization, the pin power form factors may also be stored, in order to reconstruct the power within a coarse mesh by 5) applying power reconstruction techniques that preserve the coarse nodal pin power results. Clearly, the size of the library containing all this information from the fine-transport calculation can quickly become very large. That is why in practice only a small set of values for each physical parameter are only considered, and 6) interpolation techniques are applied to calculate the actual state of the assembly in the core in terms of nearest states contained in the library.

3.4 3D Direct Transport

Three-dimensional direct transport core calculations are the most expensive alternative calculation scheme to the Two-step, in which no assumption on the environment is introduced in the flux solver. The transport solution is computed for the full reactor

problem with a high level of details within each fuel pin. The only sources of errors are due to the multigroup nuclear data, when the self-shielding model is not accurate for the actual configuration, and possibly to a coarse discretization of the phase space that introduces numerical dispersion. However, the latter can be usually overcome by simply refining the mesh or increasing the method order.

The most suitable numerical methods applied to this approach are the methods of long or short characteristics, since the heterogeneities can be treated exactly, in the geometrical sense, with no significant extra cost. Because of the large problem size, these calculations rely on domain decomposition methods (DDM) that can be massively parallelized by means of High Performance Computing (HPC) technology. The DDM performed in HPC not only gives the advantage of solving several problems with a smaller size, but also of distributing the memory requirements (both volatile and non-volatile) on several processes and nodes. In particular, the isotopic data in depletion calculations can be treated locally for each subdomain, minimizing the exchanges of information.

Apart from the DDM there are, in fact, other strategies for an HPC computation, that are based on the Koch-Baker-Alcouffe (KBA) parallel-wavefront sweep algorithm and aim to parallelize the full-domain transport sweeps. These algorithms are particularly efficient when the memory is shared by all processes and, therefore, are typically limited to computations with a single node. A combination of DDM and local KBA is generally the most suited code organization in large parallel calculations such as a 3D core.

We now give to the reader two recent examples of 3D direct transport core calculations found in literature, to give an idea of the necessary computational resources for a given discretization of the phase space.
A 3D MOC PWR core calculation was performed in 2019 with the code OpenMOC on the Argonne BlueGene/Q supercomputer [64]. The MPI libraries were used for the DDM, while OpenMP for the trajectory sweeps. The computational resources amount to 5780 nodes, one for each subdomain, with a total of 92480 CPU cores and a runtime of 7.76 hours. The core problem was discretized as it follows: $3.85 \cdot 10^8$ regions with a linear expansion for the flux and the source, corresponding to $3.44 \cdot 10^{12}$ track segments, 64 azimuthal angles and 10 polar angles, and transport corrected P_0 70-energy-group cross sections were produced for each unique material with OpenMC Monte Carlo simulations.

3D MOSC core calculations were performed with the IDT solver of the code APOLLO3® for both the PWR and the experimental reactor EOLE. The former [65] (2018) was computed with a P_3 26-energy-group cross section library, where the problem was discretized using more than 10 million regions with linear volumetric and surface expansions for the flux and 80 directions in the unit sphere. This calculation was run using only MPI libraries with 28 nodes of 12 CPU cores, for a domain decomposition of 19x19 3D assemblies that include the axial reflector. The runtime with 336 CPU cores was 7.8 hours in an Intel Xeon L5640 2.26 GHz machine. The EOLE calculation [66], instead, has a smaller number of regions (648434), since it is not a power reactor, but the problem contained 158647 different materials for which a P_3 281-energy-group library was used. The angular flux was represented with a linear volumetric and surface expansion and using an S_8 quadrature formula. The calculation was performed with

900 CPU cores, one for each subdomain, producing a runtime of 46 minutes applying the new acceleration CMFD-RMA method.

Clearly, a 3D direct transport calculation is a challenging task and a great effort has been put in increasing the number of degrees of freedom to compute the full reactor problem. In most of the works found in literature, the 3D solution has always shown good agreement with multigroup Monte Carlo, or with continuous energy Monte Carlo whose solution was used to provide the multigroup cross sections. However, it is still an open question how 2D self-shielding models work in this type of calculation schemes when compared to the continuous energy Monte Carlo solution, since they are fundamental step before for multiphysics and core depletion calculations.
Moreover, today it is still not clear with the increase of the computational resources if Monte Carlo simulations can be more advantageous than direct 3D transport calculation schemes, which entails that this approach has not found a "spot" in the nuclear industry applications yet.

3.5 2D/1D Fusion method

The 2D/1D Fusion method has been proposed by Cho et al. in 2002 [67, 68] as an alternative scheme for 3D core transport calculations, that takes advantage from the axially extruded geometries that are typically found in LWR cores. The idea is to use a transverse nodal approach to the 3D transport equation, so as to obtain two equations with a lower dimensionality, that are coupled by a term of transverse leakage source. An additional iteration loop is then required in order to converge on the transverse leakage source.

Applying the axial-averaging operator $T_k \cdot = \frac{1}{\Delta z_k} \int_k dz \cdot$ to the transport equation, where Δz_k is the height of an axial layer k, we get the equation for the axially averaged angular flux $\psi_k(\mathbf{r}_\perp, \mathbf{\Omega})$:

$$(\mathbf{\Omega}_\perp \cdot \nabla_\perp + \Sigma)\psi_k = Q_k - L_{z_k}, \tag{3.38}$$

with

$$L_{z_k}(\mathbf{r}_\perp, \mathbf{\Omega}) = \frac{\mu}{\Delta z_k} \psi(\mathbf{r}_\perp, z, \mathbf{\Omega}_\perp, \mu)\Big|_{z_k^-}^{z_k^+}. \tag{3.39}$$

In the last equations, $\perp$ stands for the radial plane, Q includes scattering and fission sources, μ is here defined as the cosine with respect to the z-axis and $z_k^\pm$ are the axial coordinates on top $(+)$ and bottom $(-)$ of the axial layer. Note that the group index has been omitted.

Equation (3.38) is a 2D problem that is typically solved with the MOC, and whose axial symmetry depends on the transverse leakage source. In the case of symmetric axial conditions with respect to the centered radial plane of an axial layer, we get $\psi(z_k^+, \mu, .) = \psi(z_k^-, \mu, .)$, so the axial source vanishes and Equation (3.38) becomes a 2D symmetric problem. Moreover, if the antisymmetric components of the entering axial fluxes are identical in absolute value, we get $\psi(z_k^\pm, \mu, .) = \psi(z_k^\mp, -\mu, .)$ and the 2D problem is also symmetric but with a non-null axial source. In all the other cases, the 2D problem is non-symmetric and requires a full angular expansion. However, when performing the 2D/1D Fusion method one may want to take all the advantages of a

classical 2D calculation, so the leakage source is typically symmetrized, by computing the average as it follows:

$$L_{z_k}(\mathbf{r}_\perp, \mathbf{\Omega}) \approx \frac{\mu}{2\Delta z_k}\Big[\psi(\mu, .) - \psi(-\mu, .)\Big]\Big|_{z_k^-}^{z_k^+}, \ \mu > 0\,, \tag{3.40}$$

that introduces the first approximation for the 2D/1D Fusion method, that is not necessary but allows to perform faster calculations.

In order to compute the axial leakage source, it is required the knowledge of the angular fluxes on top and bottom of the axial layer. This is mediated by a set of 1D axial problems for each radial region r, that are constructed applying the radial-average operator $T_r\cdot = \frac{1}{A_r}\int_r d\mathbf{r}_\perp \cdot$ to the transport equation, where A_r is the surface of region r in the radial plane, so as to obtain an equation for the radially averaged region flux $\psi_r(z, \mu, .)$:

$$(\mu\partial_z + \widehat{\Sigma}_k)\psi_r = Q_r - L_r, \tag{3.41}$$

where

$$\widehat{\Sigma}_k = \frac{\int_r d\mathbf{r}_\perp \Sigma(\mathbf{r}_\perp)\Phi_k(\mathbf{r}_\perp)}{\int_r d\mathbf{r}_\perp \Phi_k(\mathbf{r}_\perp)}, \tag{3.42}$$

and

$$L_r(z_k, \mathbf{\Omega}) = \frac{1}{A_r}\int_{\partial r} \psi_k(\mathbf{r}_\perp, \mathbf{\Omega})\mathbf{\Omega}\cdot\mathbf{n}dl. \tag{3.43}$$

It is worth to point out that $\widehat{\Sigma}_k$ is equal to Σ only if r coincides with a 2D region, which entails that no spatial homogenization is performed. However, the 1D problems are typically constructed for each fuel pin cell, introducing two further approximations: the first one concerns the representation of the axial source, which has constant value for both water and fuel within a pin cell; the second one, instead, concerns the homogenization process using the 2D scalar flux instead of the 2D angular moments.

At this point, it is common to introduce another approximation which is that of isotropic transverse leakage sources. This leads to a definition of the latter as a function of only the currents:

$$L_{z_k}(\mathbf{r}_\perp) \approx \frac{1}{4\pi}\int_{4\pi} d\mathbf{\Omega} L_{z_k}(\mathbf{r}_\perp, \mathbf{\Omega}) = \frac{1}{4\pi} J_r(z)\Big|_{z_k^-}^{z_k^+}, \tag{3.44}$$

$$L_r(z_k) \approx \frac{1}{4\pi}\int_{4\pi\, A_r} d\mathbf{\Omega} L_r(z_k, \mathbf{\Omega}) = \frac{1}{4\pi\, A_r}\int_{\partial r} J_k(\mathbf{r}_\perp)dl, \tag{3.45}$$

where J_r and J_k are respectively the 1D axial net current for the radial region r and the 2D radial net current for the axial layer k. Note that both currents are computed integrating in the unit sphere. This approximation automatically symmetrizes the transverse leakage sources, and consequently the 2D transport problem, and open up the possibility to solve Equation (3.41) with a simplified operator such as diffusion or

P_3. This approach is often called hybrid 2D/1D method, since it utilizes two methods of different orders for the 2D and 1D problems [69].

Apart from the order of the 1D operator, the approximations adopted for the transverse leakage sources also produce different solutions at the convergence of the iterative process. It can be shown, however, that whichever approximation is employed, the following condition must be satisfied in order to have a converged solution:

$$\overline{\Phi}_{r,k} = \frac{1}{A_r}\int_r d\mathbf{r}_\perp \Phi_k(\mathbf{r}_\perp) = \frac{1}{\Delta z_k}\int_k dz \Phi_r(z), \tag{3.46}$$

which is the condition sought by the fixed point iterations so as to achieve equivalence between the 2D and 1D problems. It follows that the Fusion method may be considered an advanced homogenization technique that, instead of preserving macroscopic reaction rates of a reference calculation, updates and modify the RHP so as to attain the preservation.

In literature a couple of calculation schemes for the Fusion method can be found. The pioneer codes are DeCART/nTRACER [59, 65] and MPACT [70, 71] and both utilize MOC as 2D operator and 3D CMFD as acceleration for the eigenvalue problem. The coefficients of this acceleration are constructed with the solutions of the 2D and 1D problems. In a traditional scheme, 2D and 1D calculations must iterate between each other in order to converge the transverse leakage sources. However, the research group of nTRACER has also explored the possibility to directly use the 3D CMFD solution to compute the isotropic and homogenized transverse leakage [65], causing two issues. The first one is that the CMFD operator must be constructed on the same energy mesh of the 2D and 1D operators, abandoning the possibility of energy condensation and, therefore, of the faster few-group CMFD calculation. The second issue is that the 2D and 1D operators only exchange information with the 3D CMFD operator, hence condition 3.46 is not necessarily satisfied.

In terms of computational cost, the 2D/1D Fusion method has a smaller number of regions and angular moments to deal with, thus the number of floating operations for a 2D and 1D transport sweeps are lower than in 3D direct MOC. On the other hand, an extra-cost is necessary because 2D and 1D calculations must be repeated for the fixed point iterations. Typically the parallel algorithm is organized as it follows: each node is used for the 2D MOC computation of each radial plane and OpenMP is employed to parallelize the trajectory sweeps. In [65] the performance comparison between nTRACER and IDT showed a smaller runtime for the former, but the comparison is hard to establish because they used two different machines with different architecture, memory management and power. The authors propose a comparison with the estimated sequential time, showing that IDT using MOSC is 1.75 faster than nTRACER using 2D/1D Fusion.

Part II

The Method of Dynamic Homogenization

Chapter 4

Development of the method of Dynamic Homogenization

4.1 Summary & Motivation

In nuclear reactor physics homogenization techniques play a fundamental role in core modeling because they allow to simplify such complicated systems, for which direct transport (DT) calculations are time demanding and require considerable computational resources. Moreover, the highly detailed information that DT can provide is generally not used for routine industrial applications.
We recall here the objectives of homogenization theory:

i) to reduce the problem size, either substituting detailed heterogeneous geometries with homogeneous ones, or averaging the energy dependencies;

ii) to construct a low-order operator that reproduces average transport quantities (typically the reaction rates) of the original system.

Since we do not know the reference fine transport solution in the core, the most delicate part of point i) is to define a Reference Homogenization Problem (RHP) that typically corresponds to an assembly calculation, whose solution is used as weighting function for cross-section homogenization. In order to obtain accurate results, the solution of the RHP must then be representative of the actual core conditions.

In the classical two-step approach, the RHP is defined per assembly type with infinite-lattice conditions. The multiplication constant can then be very different from that of a steady-state reactor, which is the only information on the environment that is known at the homogenization stage. The condition $k_{\text{eff}} = 1$ is therefore forced in the assembly transport calculation by introducing a critical leakage model so as to obtain a critical spectrum and the critical reaction rates to be preserved. This model is based on the assumption that the transport solution within an assembly is the product of a periodic solution and a macroscopic distribution: the so called infinite medium

fundamental mode assumption. It has been shown that this approximation is correct in the asymptotic situation where the core is composed of a large number of identical assemblies [72]. It follows that the assemblies in the core that are the most sensitive to the classical model are those at the peripheral area next to the reflector and those next to other types of assembly such as the UOx-MOx or Rodded-Unrodded interfaces [73]. Hence, the interest of developing new methodologies that are more reliable for core analysis.

An issue with the homogenization process is the loss of the detailed information on the cross sections. Thus, the coarse operator resulting from the homogenization can at most reproduce reference macroscopic reaction rates in macroregions and macrogroups when provided with a concurrent macroscopic description of references sources and boundary conditions. Moreover, with the exception of very limited cases, flux homogenized cross sections fail to reproduce reference reaction rates and it is then necessary to recur to special techniques, such as equivalence theory (EQV) [46, 47] or the use of flux discontinuity ratios (FDR) [44, 53] to reproduce the reference reaction rates in the RHP. Use of these techniques results in a marked improvement: for example, typical pin power errors are reduced from around 10-12% to roughly 5-7% in an LWR at nominal conditions for 2D configurations [14].

The question that arises at this point is whether the main source of these errors is due to the inadequacy of the adjusted low-order operator to describe the physics of the full-core problem, or that of the reference homogenization problem to provide a good approximation for the core flux, or even both.

Concerning the inadequacy of the low-order operator, in 2011 Grundmann and Mittag [61] computed the NEA PWR UO2/MOX Benchmark [74] with an 8-group pin-by-pin simplified P_3 operator, with and without equivalence, showing better results with respect to the other benchmark participants who adopted the nodal two-group diffusion, halving the standard deviation of the assembly power relative error, with a maximum of pin power error around 7-8%. Concerning the the inadequacy of the reference homogenization problem, many attempts have been made in the past to better account for the assembly environment at the homogenization stage. These can be divided into three classes: *i*) direct modeling, *ii*) cross-section correction techniques, and *iii*) iterative core-assembly calculations.

Direct modeling consists of running colorset calculations, combining each type of assembly in the core in order to homogenize with a more realistic environment. Typically, this approach is adopted for reflector homogenization [75] to improve its response. However, if one has to consider many combinations of assembly types in several configurations of refueling strategy or thermal feedback, the method can be expensive and the homogenized nuclear data can increase considerably.

The second technique approximates the environment effect by correcting the homogenized nuclear data. Rahnema *et al.* [76, 77] used a linear perturbation method to the assembly boundary conditions in order to calculate and tabulate the homogenized cross sections for a set of current-to-flux ratios. The latter were computed during the core calculation while the coefficients for the perturbation were determined from off-line assembly calculations, so that in the iterative process of cross-section

correction, no lattice calculation needed to be performed. With the same philosophy of off-line cross-section generation, Clarno *et al.* [78] used energy, angle, and space dependent albedo boundary conditions to "capture the effects of unlike neighbors in single-assembly calculations". Instead of using the core quantities, as first estimation these albedos were determined solving a 1D transport problem, that was representative of the 2D two-assembly problem. However, the cross sections used by the 1D solver were homogenized in space using the 2D assembly flux at infinite lattice conditions. A similar approach adopted by Palmtag for UOx-MOx interfaces [73] consists of using the two-group homogenized cross sections, the spectral index and several fitting coefficients to evaluate two types of spatially dependent corrections: a leakage correction that accounts for fast spectrum changes due to the leakage effects, and a spectrum correction that accounts for the spectrum changes of the sources. The set of correction coefficients was determined once and for all from a reference case calculation and then used for different problems.

The third class of methods is based on a very different philosophy, because it does not require any off-line calculation. A lattice solver is used as an "on-the-fly" cross-section generator for the core solver, where the boundary conditions are calculated by the low-order operator and updated at each iteration. This approach is definitely more expensive but it can be easily parallelized. The method was firstly called Dynamic Homogenization (DH), proposed by Mondot and Sanchez in 2003 [79] and tested for simple cases in 1D problems. In their work, the fine information on the environment came directly from the neighboring assemblies and from the core currents and eigenvalue. Each assembly has then different boundary conditions that account for its position in the core and for the isotopic content of the neighboring assemblies: both sources of gradients in a reactor. In 2008 Takeda *et al.* [80] applied a similar iterative process but, to redefine the RHP at each iteration, they adopted albedo boundary conditions determined with the core currents instead of using the outgoing angular flux of the neighbor. It ensues that each lattice calculation is independent of the others because it only depends on core quantities, which entails that the spectrum of the neighboring assemblies cannot be properly taken into account. In 2014 Colameco *et al.* [81] extended the DH method to a 2D configuration obtaining good agreement against reference transport calculation for a 2x2 cluster of UOx and MOx assemblies with reflection boundary conditions. The method was also adopted for Pebble Bed Reactors by Grimod and Sanchez in 2015 [82] where the pebbles were depleted with their own fine-group fluxes.

To sum up, in this context the RHP is a 2D assembly or a part of a 3D assembly, and the lowest homogenization model is to consider each RHP as independent of the neighboring assemblies and supply it with reflective boundary conditions. This is the classical homogenization technique traditionally used in the two-step core calculation method. A better model is to introduce albedo boundary conditions which can be iteratively calculated from the coarse core calculation. A step further up, the DH method consists of an iterative core homogenization where each assembly is provided with incoming fluxes that are obtained from the fluxes exiting neighboring assemblies or from adjacent reflector. Within the DH the reflector is also decomposed into "assembly"-like domains which are homogenized in a similar fashion.

The purpose of the method is then to eliminate all the approximations and limita-

tions of the classical two-step scheme discussed in Section 3.3.2, while avoiding expensive 3D transport calculations; it offers thus an interesting and promising alternative technique for the two-step core calculations.

A detailed description of the method of Dynamic Homogenization, its calculation scheme based on the domain decomposition method and the approximation used for the assembly boundary conditions are given in this chapter. Also, a problem with non-conservative boundary conditions is that particular care has to be used when applying equivalence theory or computing discontinuity factors. These two techniques will be discussed and adapted in the framework of a dynamic homogenization approach.

4.2 Domain Decomposition Method

We start by reviewing the use of the DDM for the solution of the whole core transport equation. Let D be the global geometrical domain, typically the reactor core including surrounding materials and reflector, with boundary Γ and N_D the number of subdomains, which comprise fuel and reflector "assemblies". Thanks to the DDM, the *global* core transport problem becomes a set of coupled *local* assembly transport problems, which is iteratively solved in parallel. At each iteration the solution of the local assembly problems with incoming boundary conditions is computed. In order to reproduce the reference solution obtained without DDM, two new conditions have to be imposed:

1) impose the same eigenvalue in all the subdomains;

2) enforce the continuity of the angular flux at the interfaces between subdomains.

The first condition is not necessary but ensures a robust convergence. The second condition is achieved by iteratively replacing the fluxes entering each assembly ($\psi_{\text{in},i}$) with those exiting the neighboring assemblies ($\psi_{\text{out},j}$):

$$\begin{cases} L_i\psi_i = H_i\psi_i + \frac{1}{\lambda}F_i\psi_i, \mathbf{r} \in D_i, \\ \psi_{\text{in},i} = \psi_{\text{out},j}, \mathbf{r} \in \Gamma_{ij} = \Gamma_i \cap \Gamma_j, \\ \psi_i = \beta_i\psi_i + \psi_{\text{in},i}, \mathbf{r} \in \Gamma_i \cap \Gamma, \end{cases} \tag{4.1}$$

where $D = \cup_{i=1,N_D} D_i$ is the partition of the core into N_D subdomains, D_i and Γ_i are, respectively, the subdomain i and its boundary and $\Gamma_{ij} = \Gamma_i \cap \Gamma_j$ is the common interface between neighboring assemblies i and j. Also, in this equation $L = \mathbf{\Omega} \cdot \boldsymbol{\nabla} + \Sigma$, operators H and F stand for scattering and fission production, β accounts for an albedo boundary condition and $\mathbf{r}$ is a generic position vector. The outermost loop of the iterative process, where interface conditions and eigenvalue are updated, consists of global iterations, while the fission source is locally updated at the subdomain level in the outer-iteration loop; in this loop a multigroup assembly transport problem with fixed eigenvalue and incoming angular fluxes is solved in parallel for each subdomain.

In practice, the maximum number of outer iterations is fixed to one because numerical experimentation has shown that in the DDM it is not worth to converge the multigroup problem, in particular if the boundary source is far from its converged value.

One of the easiest algorithms to solve the set of subproblems 4.1 is the Parallel Multigroup-Block Jacobi method (PMBJ), where the information is exchanged between subdomains through the multigroup angular fluxes "block" at the interface. In this algorithm, each subdomain uses as boundary conditions the flux at the interfaces coming from the neighboring subdomains that are calculated in the previous iteration. The interface flux is not updated throughout the inner iterations but only after each global iteration l. Because of this additional loop with respect to the direct method without decomposition, a higher number of outer iterations are required for the global problem to attain the convergence. The PMBJ method is shown in Algorithm 2.

Algorithm 2: Parallel Multigroup-Block Jacobi algorithm

```
Initialization of ψ, Fψ and λ
while λ, F_i ψ_i and ψ_{in,i} have not converged ∀i ∈ [1, N_D] do
    for i ∈ [1, N_D] do
        update ψ_{in,i} : ψ^{l+1}_{in,i} = ψ^l_{out,j}, ∀g ∈ [1, N_g], ∀r ∈ Γ_ij
        solve problem (4.1)
        update F_i ψ_i
    end
    update λ
end
```

In [3] it was shown that the PMBJ method deteriorates the convergence properties of the direct calculation and the authors presented some alternative techniques that improved the performance of the DDM. The idea is to minimize the exchanges of information that is computed in the previous iteration. Therefore, a set of subdomains will receive an interface flux computed in the current outer iteration while the others that of the previous iteration. This algorithm is called Parallel Multigroup-Block Gauss-Seidel (PMBGS) and it is presented in Algorithm 3.

This method is advantageous only if a processor has to compute more than one subdomain sequentially, otherwise each parallel task must wait for the information to be available. One can then define how to order the subdomain calculations. Considering that the domain is decomposed into a Cartesian structured geometry, the subdomains could be computed following the front of propagation: after one subdomain calculation, all of its neighbors that have no common interfaces between each other are calculated in parallel, and so on until the last subdomain. At each subdomain calculation then, three interfaces will have a flux of the previous global iteration, and the three others will have a flux updated to the current global iteration. It is common to begin the calculations from the external subdomains where the boundary conditions of the global problem are imposed, and let the propagation front develop to the center of the domain.

Another strategy is the "Red-Black" scheme, that gather the subdomains as if they were disposed in a chess board, so that the "red" half of subdomains are computed using the interface flux of the previous iterations (as in PMBJ scheme), and the "black" half using the updated interface flux (similarly to the PMBGS scheme but with the

Algorithm 3: Parallel Multigroup-Block Gauss-Seidel algorithm

```
Initialization of ψ, Fψ and λ
while λ, F_i ψ_i and ψ_{in,i} have not converged ∀i ∈ [1, N_D] do
    for i ∈ [1, N_D] do
        update ψ_{in,i} :
        if j < i then
            ψ^{l+1}_{in,i} = ψ^{l+1}_{out,j}, ∀g ∈ [1, N_g], ∀r ∈ Γ_ij
        end
        if j > i then
            ψ^{l+1}_{in,i} = ψ^{l}_{out,j}, ∀g ∈ [1, N_g], ∀r ∈ Γ_ij
        end
        solve problem (4.1)
        update F_i ψ_i
    end
    update λ
end
```

difference that the new information is imposed for the six interfaces). In [3] it is shown that the convergence properties of PMBGS and Red-Black methods are comparable.

To sum up, the PMBJ method is the one that requires the highest number of outer iterations to converge, but it is completely parallelizable because each subproblem is independent of the solution of the neighboring subdomains for the whole global iteration. The PMBGS methods have better convergence properties with respect to PMBJ but at the price of decreasing the level of parallelism, since part of the subproblems uses the solution of the same global iteration.

The method of domain decomposition not only offers the numerical advantage of an easy implementation of moderate to massive parallelization, but also provides a natural paradigm for homogenization techniques for full-core calculations, whereby increasingly sophisticated homogenization techniques lead to the 2D-1D fusion method, which uses homogenization for acceleration and eigenvalue calculation, and further up to truly 3D core transport calculations.

A multigroup full-core coarse operator can be used between two outer iterations for the acceleration of the eigenvalue and of the fission and boundary sources. A nonlinear acceleration may require a modification of the coarse operator to ensure that the acceleration process converges, as it is the case for the popular CMFD acceleration where an artificial drift term is added to Fick's law and computed from transport quantities. The multigroup acceleration is mediated by using the solution of the global coarse eigenvalue problem in the rebalancing Equations (3.22) and (3.23). In other words, each subdomain calculation is solved with imposed multiplication constant λ^{C}, and fixed incoming boundary sources $\psi_{\mathrm{in},i}$, where the former, being an integral parameter of the whole domain, is determined at the core level:

$$\lambda_{\mathrm{C}}^{k+1} = \lambda_{\mathrm{C}}^{k} \frac{\langle w, F^{\mathrm{C}} \Phi^{k+1} \rangle}{\langle w, F^{\mathrm{C}} \Phi^{k} \rangle}, \tag{4.2}$$

where C stands for coarse, F for fission operator, Φ for scalar flux, w for a weight function and k is the power iteration index for the coarse core operator. One could also compute the eigenvalue locally for each subdomain and require convergence into a unique value for the whole domain. However, it has been shown that imposing the same multiplication to all subdomains makes the iterative scheme more stable [3].

4.3 Reference Homogenization Problem in Dynamic Homogenization

We turn now to a discussion of the changes to be introduced to convert the full-core DDM calculation just outlined into a dynamic homogenization scheme. As mentioned in Section 4.2, the method of domain decomposition provides a natural paradigm to define an RHP, leading to homogenization techniques which can be applied to the local problem at each global iteration to construct a coarse operator that can reproduce exactly the average transport quantities on coarse spatial and energy meshes. This homogenization is necessarily a dynamic process because the homogenized cross sections and the equivalence parameters used to construct the coarse operator depend on the transport solution and, therefore, as long as the transport has not converged, the coarse operator keeps changing.

With the DH method, we invert the usual roles of the operators, where the coarse operator serves as an acceleration for the full-core transport solution, and consider instead **the low-order operator as the one that gives the solution of the core problem and the transport operator as the generator of homogenization parameters**. This approach can open new possibilities for reducing the computational time of the global problem at the cost of introducing some approximations. For instance, the coarse operator does not necessarily have to reproduce the exact average transport quantities, and the local RHP that generates the homogenization parameters can be simplified with respect to the true situation in the core. A clear example of this is to adopt a 3D low-order operator and a 2D transport problem for the RHP.

Suppose that the whole core transport reference solution is known, and for some reason we are interested in recomputing a subdomain contained in the global problem using the exact incoming boundary conditions. This situation is shown in Figure 4.1, where the circle represents the full-core problem and the dotted square the subdomain to be recomputed, such as a fuel assembly.

The exact solution within the subdomain can be recovered with two different types of calculations. The first one consists in solving an eigenvalue problem with fixed incoming boundary source. Because the latter comes directly from the reference solution, the transport flux in the subdomain and the reference eigenvalue of the whole problem are exactly reproduced. The second type of calculation is the one typically used in DDM, and it consists in a fixed boundary source problem where the reference eigenvalue is imposed. Also in this case, the reference transport flux is exactly reproduced. In DDM calculations accelerated by CMFD, it is possible to impose the multiplication constant of this coarse operator because it is constructed so as to preserve average transport reaction rates and, therefore, the reference eigenvalue. Clearly, any other

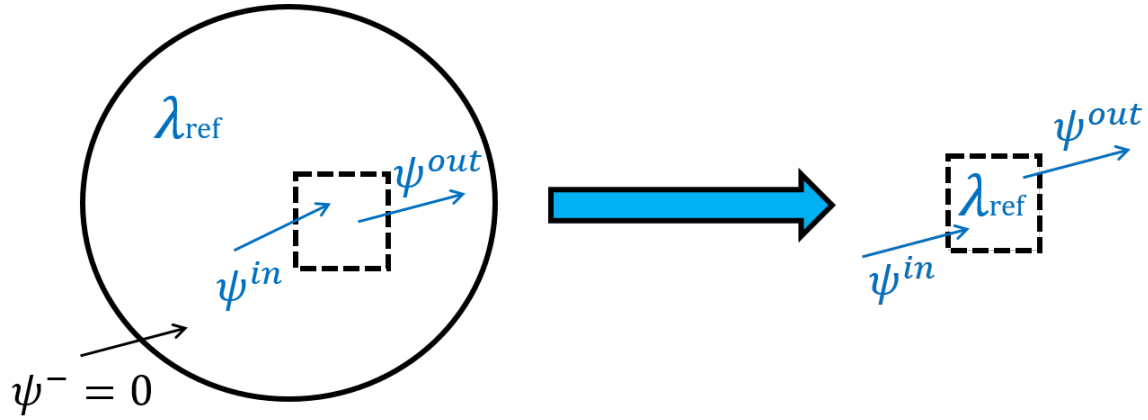

Figure 4.1. Sketch of recomputing a subdomain imposing the exact boundary conditions.

boundary source and/or any other imposed eigenvalue can only produce a different solution, as long as it exists. In other words, there exists only one pair $(\lambda, \psi_{\text{in}})$ that can reproduce the reference solution.

We now analyze the scenario where the solution of the problem is attained iteratively and the flux leaving a subdomain is used as boundary source for the neighbor. This means that the single subdomain calculation is no more isolated but it is coupled with the neighboring subdomains.

For this scenario an issue comes up because each local transport problem is solved with a boundary source, that is solution of the neighboring transport problem, and with the imposed eigenvalue from the low-order operator, which in a DH framework does not necessarily have to reproduce the eigenvalue of the full-transport calculation. Moreover, because of the subdomain coupling, the issue resides in the fact that it is not possible anymore to simultaneously assure that:

1) the core eigenvalue is the same everywhere in D;

2) the fine angular flux at the interfaces between subdomains is continuous.

Therefore, to construct an iterative process where both the assembly homogenization and the global coarse operator converge, it is necessary to introduce a relaxation in the continuity condition of the angular flux by using a normalization factor that preserves the coarse incoming partial current:

$$\psi_i^{-,g}(\mathbf{r},\mathbf{\Omega})\mid_{\Gamma_{ij}}^{l+1} = \psi_j^{+,g}(\mathbf{r},\mathbf{\Omega})\mid_{\Gamma_{ij}}^{l} \times \frac{J_i^{-,\mathrm{C},G}(\mathbf{r})\mid_{core}^{l+1}}{\sum_{g\in G}\int \mid \mathbf{n}\cdot\mathbf{\Omega} \mid \psi_j^{+,g}(\mathbf{r},\mathbf{\Omega})d\mathbf{\Omega}\mid_{\Gamma_{ij}}^{l}} \qquad \forall g \in G, \quad (4.3)$$

where l denotes the global iteration index, $\mathbf{n}$ the unit vector normal to the interface and g G the fine (transport) and coarse energy groups. Note that the ψ^+ from the neighbor gives the fine distribution in space, energy and angle that allows to define the transport boundary conditions of each local RHP, normalized so as to preserve the coarse incoming partial current J^- defined per macro-group and macro-surface. In this

formula, we have used the same global iteration index for the incoming angular flux and the coarse incoming current to express that for each local RHP the transport and the coarse calculations are normalized by the same boundary source.

It is important to point out that the level of detail employed for the boundary source in Equation (4.3) is equivalent to that of a 2D direct transport calculation solved by DDM. This means that we are providing to each subdomain a very detailed information (ψ^+) but with an accuracy corrupted by the current normalization (J^-). However, by introducing the discontinuity of the entering angular flux at the interfaces, we do not only ensure the convergence of the iteration process by preserving the eigenvalue of the low-order operator, but we also allow for the use of a simplified, rough distribution in space and angle of the incoming angular flux in Equation (4.3). The shape of the energy distribution as given by the angular flux exiting the adjacent subdomain is, on the other hand, mandatory.

We want now to stress the differences between the Two-step and DH reference homogenization problems in terms of which environment information is taken into account and how it is modeled. The comparison of the two RHPs is synthesized in Table 4.1.

In the classical approach, one could use a model to correct the homogenized cross sections, as discussed in Section 4.1. However, this additional step is not always employed, and the only environment information resides in the imposed multiplication constant, that generally equals one, for the homogeneous critical leakage model. The critical leakage is expressed as a term of additional absorption to the total cross section, so it is a volumetric quantity distributed uniformly in the assembly. On the other hand, in DH the imposed core eigenvalue gives the global information of the actual reactor state, the macroscopic current gives the information on the position of the assembly in the core, and the outgoing angular flux allows to account for the spectral properties of the neighboring assemblies that may have a different isotopic content. The leakage is then a surface quantity and it is different for each interface of the subdomain.

It follows that the 2D transport problem is no more symmetric in space and one has to compute the whole assembly instead of one height, as it is done in the Two-step scheme for LWR cores. Moreover, each assembly in the core has its own boundary conditions so all of them must be computed. On the other hand, in the classical approach the lattice calculation is performed for each assembly type.

Finally, the DH model is richer than the classical one in terms of environment information, so the weighting flux employed for cross-section homogenization is expected to be closer to the actual situation in the core and to produce, then, homogenization parameters of better quality.

4.4 Iterative Scheme

The iterative scheme of the method of Dynamic Homogenization is shown in Figure 4.2 and it can be seen as a mirror image of a nonlinear acceleration scheme for a direct transport calculation based on the Domain Decomposition Method (DDM).

In the direct approach, in fact, the update box in the inner loop of Figure 4.2 not only concerns the boundary source and the eigenvalue, but also the fission source that is computed with the accelerated transport flux. On the other hand, in DH

	Two-step	Dynamic Homogenization
Environment	global: λ_C	global: λ_C position in the core: J_C^- neighbor: $\psi_{s,d,g}^+$
Leakage	volumetric (distributed uniformly)	surface (source imposed on the boundary)

Table 4.1. Weighting flux from reference homogenization problem.

the acceleration of the fission source arises at the local transport calculation in the "Assembly Calculation" box of Figure 4.2. Moreover, in DH we consider only 2D assembly calculations because we want to avoid expensive 3D transport calculations.

To ensure convergence of the DH method we check the following criteria between two successive global iterations l and $l+1$:

- Eigenvalue λ_{C}: $|\lambda_{\mathrm{C}}^{l} - \lambda_{\mathrm{C}}^{l+1}| < \varepsilon_{\lambda}$;
- Fission Integral F_r per transport region r: $|1 - \frac{F_r^l}{F_r^{l+1}}| < \varepsilon_{\mathrm{f}}$;
- Incoming flux $\psi_{s,d}^{-,g}$ per surface element s, direction d and group g: $\|1 - \frac{\psi_{s,d}^{-,g,l}}{\psi_{s,d}^{-,g,l+1}}\|_2 < \varepsilon_{\psi}$;

where ε_{λ}, ε_{f} and ε_{ψ} are the tolerances accepted for convergence. The same criteria are used in direct transport calculation based on DDM.

We also considered the possibility to reiterate on the self-shielded cross sections in order to account for the environment information. The latter could be simplified by employing an albedo boundary condition in the self-shielding model. Nonetheless, in the present work only static calculations for a given set of macroscopic cross sections are considered and self-shielding and depletion calculations in the external loops of Figure 4.2 are not studied.

In Figure 4.3 we show a possible parallel organization of the DH iterative scheme that has been developed in a mock-up code for analysis and studies of the method. There are three MPI phases, which cannot be performed if all the processors have not finished the previous one. In the first one, the multigroup transport calculation and the homogenization process are performed independently for each subdomain. The second one concerns the core calculation with the low-order operator that is also based on DDM, and therefore an exchange of information is required that is indicated in Figure 4.3 with the green arrows.

Our code organization was conceived so that both transport and coarse operators rely on the same spatial decomposition, in order to keep all data only locally available in memory and, therefore, not accessible by the other processors. It ensues that the only information that is exchanged between processors involves the following quantities at the interfaces between subdomains: the angular flux for transport, the scalar flux and the homogenization parameters for CMFD and the partial currents for parabolic nodal diffusion (NEM2). In addition, the quartic nodal diffusion (NEM4) requires both

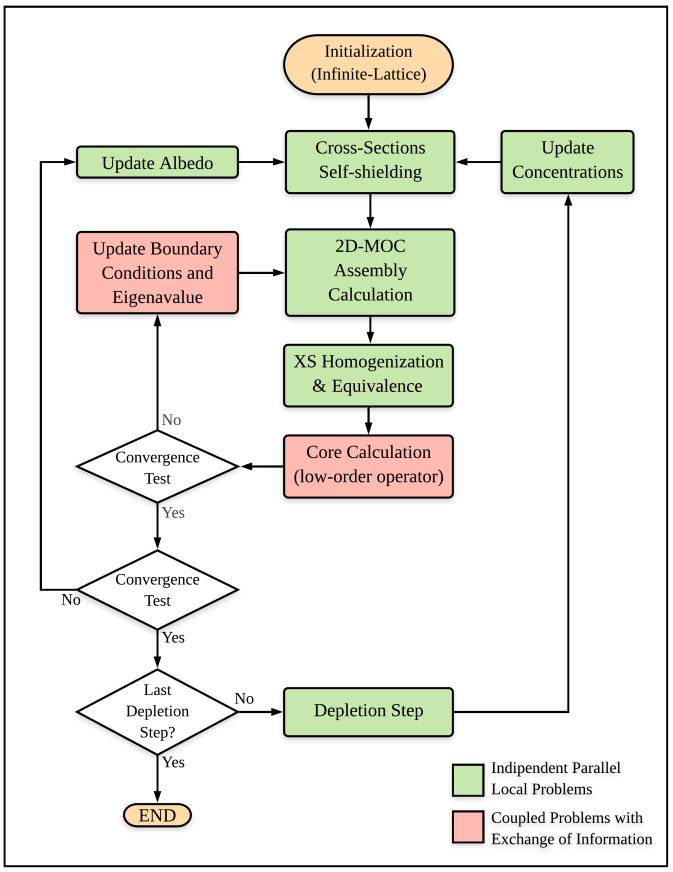

Figure 4.2. Dynamic Homogenization calculation scheme.

partial currents and transverse leakage of the regions adjacent to the interfaces. One may notice that the few-group diffusion calculation could be performed efficiently without DDM. This is kept to preserve the consistency in the code organization, especially important for the 3D calculations.

The third phase consists in exchanging the fine-transport information at the interfaces, while the coarse current and the eigenvalue are already accessible in the local memory because of MPI phase 2.

It is worth to point out that the same code organization allows to perform efficiently both DDM Transport and Dynamic Homogenization calculations. It is also possible to perform a Two-step calculation, with the inconvenient of computing more than one time the same assembly type that may be repeated in the core geometry. However, these computations are parallel so they do not affect the computational time for the construction of the homogenized cross-section library.

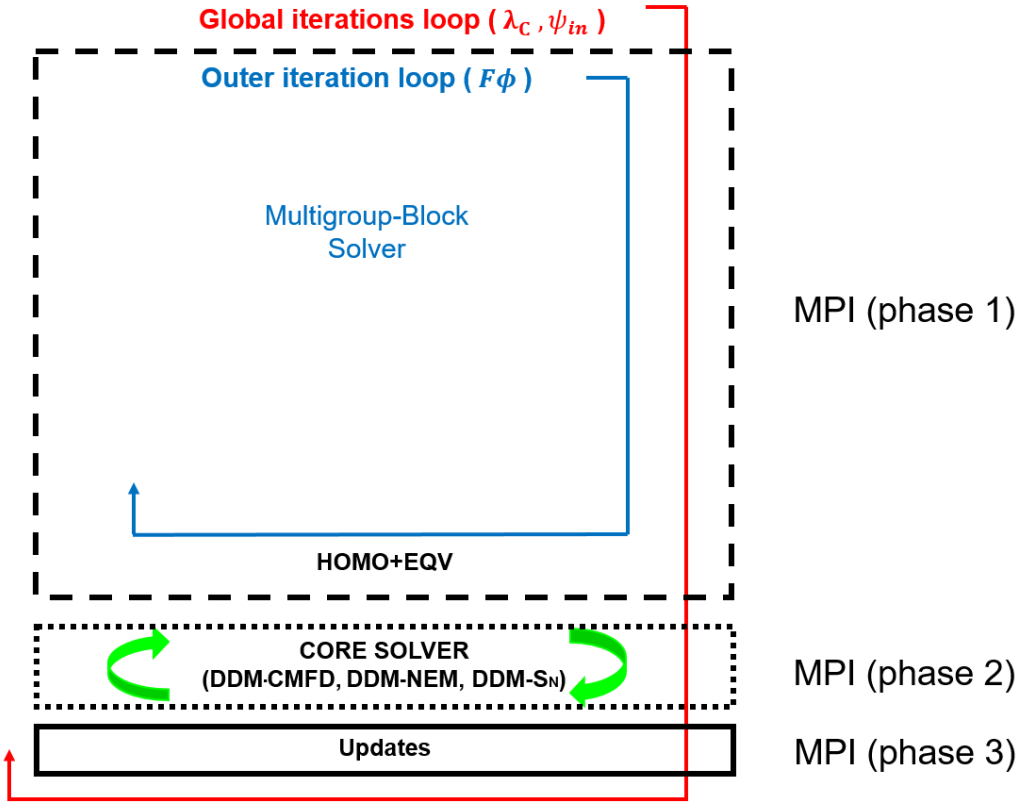

Figure 4.3. Parallel Organization for a Dynamic Homogenization iterative scheme.

4.5 Construction of the Low-Order Operator

Because the DH solution depends on the low-order operator and the transport information is locally available and can be used at negligible cost, it is expedient to introduce the advanced homogenization techniques, which we presented in Chapter 3. We revisit next these techniques to analyze them in the context of the DH-like RHPs with non-zero surface leakage.

4.5.1 Equivalence theory

With the presence of non-zero surface leakage in a reference homogenization problem, the preservation of the reaction rates per macro-group and macro-region is insufficient to ensure that the homogenized RHP will have the same eigenvalue as the reference transport calculation, since the eigenvalue also depends on the total leakage, which is not necessarily reproduced by the low-order operator. In order to preserve the reference balance, one must add an additional condition to the equivalence problem. This condition can be either 1) the preservation of the reference net current at the boundaries per macro-surface and macro-group, which is only possible in diffusion theory, or 2) the preservation of the reference eigenvalue with same incoming boundary source per macro-surface and macro-group, which is possible for any operator, let be

it transport or diffusion like.

Let us define three types of problems acting in equivalence theory. The first one is the assembly RHP solved by the transport operator to obtain the average reference reaction rates. The second one is the homogenized assembly problem solved by the low-order operator to compute the equivalent cross sections that are operator dependent. The third one is the core problem solved by the same coarse operator of the second problem.

The option 1) of preserving the reference net current of problem 1 at the boundaries of problem 2 implies the resolution of the local diffusion eigenvalue problem if the subdomain is fissile. It reproduces the core eigenvalue only if the equivalence iteration process converges. However, this possibility can be considered a weak equivalence and it is not encouraged by the author because it is not guaranteed that at the convergence of the DH method the total net leakage of each assembly $\sum_{S\in\partial D} A_S J_S^C$ is the same for both transport assembly calculation and diffusion core calculations. This is explained by the fact that the incoming currents are not necessarily preserved and, therefore, the core conditions are not properly accounted in problem 2.

In the DH framework, it is advantageous instead to apply the second option, because the equivalence problem is naturally defined since the RHP is solved with imposed core eigenvalue and fixed incoming boundary source that is normalized so as to preserve the core coarse partial current. Hence, in the balance Equations (3.5) and (3.6) we have then $J^- = J^{-,\mathrm{C}} = J^-_{core}$ for each $S \in \partial D$ and G, and $\lambda = \lambda_{\mathrm{C}} = k^{core}_{\mathrm{eff}}$. The equivalence is then achieved between three problems mentioned earlier.
Moreover, the boundary source dictates the norm of both the transport and the homogenized local problems, so if the method converges there exists a unique coarse operator that reproduces the reference balance for a given core state. It ensues that the homogenized problem and the core problem will also reproduce the total outgoing current per macro-group $\sum_{S\in\partial D} A_S J_S^+$ in each assembly, but not necessarily for each surface element S. Because of this, the fine angular flux is still discontinuous at the interfaces with neighbors, but the method offers the advantage of having the same local coarse power density for both transport and coarse problems, which can be used to perform a depletion calculation on the fine transport mesh. This is definitely an advantage of this option.

4.5.2 Flux Discontinuity Ratios

We remind that this method can only be used with coarse operators that are diffusion-like. The basic idea here is to compute FDRs for all internal coarse surfaces of a subdomain. As for the equivalence homogenization, the RHP for the transport problem has an incoming boundary condition, but the RHP coarse problem is provided with reference net transport currents. Both problems have the same fixed eigenvalue. In these conditions, for the general case when the coarse operator has a submeshing the FDRs are computed from the iterative minimization of the functional in Equation (3.19), whereas in the case with no submeshing they can be obtained by solving a set of independent local problems, one per coarse region, with net currents boundary conditions and for which an analytical expression for the FDR can be directly obtained.

Regardless of the case, the computation requires the values of the net reference currents on all coarse surfaces and the final coarse core operator has discontinuity conditions at all internal coarse surfaces.

Recall that the boundary condition for the coarse operator which consists of taking the coarse net current equal to its transport counterpart allows to preserve the reference balance and therefore the reference reaction rates. However, as for any other local homogenization model, at convergence the interface currents are not necessarily those that would extant for the full-core transport calculation. Similarly to the equivalence technique with option 1 discussed in Section 4.5.1, in this case it would follow that transport and coarse full-core solutions have different assembly power densities. The reason behind this is that the normalization in Equation (4.3) makes the transport solution to be discontinuous at the subdomain interfaces.

We now describe how the Flux Discontinuity Ratios can be analytically computed for a diffusion nodal operator with a parabolic (NEM2) and quartic (NEM4) flux expansion, which have been employed in our analysis and calculations in Chapters 5 and 6.

4.5.2 FDR for Diffusion NEM

In this section we use the same notation employed in Section 2.6.2 for the physical quantities involved in the nodal expansion method. When the Flux Discontinuity Factors technique is applied, both scalar flux and partial currents are no more continuous and at the interface of two nodes k and $k-1$ one has:

$$f_{x_+^{k-1}}\Phi_{x_+^{k-1}} = f_{x_-^k}\Phi_{x_-^k} \Rightarrow f_{x_+^{k-1}}(J^{out}_{x_+^{k-1}} + J^{in}_{x_+^{k-1}}) = f_{x_-^k}(J^{out}_{x_-^k} + J^{in}_{x_-^k}), \tag{4.4}$$

while the net current is continuous:

$$(J^{out}_{x_+^{k-1}} - J^{in}_{x_+^{k-1}}) = -(J^{out}_{x_-^k} - J^{in}_{x_-^k}). \tag{4.5}$$

In the last equations, $\pm$ indicates the right $(+)$ and left $(-)$ interfaces of a node, J^{out} and J^{in} are respectively the outgoing and incoming currents, and x is a Cartesian axis. Using Equations (4.4) and (4.5) we can express the incoming partial current as a function of the outgoing currents of the neighboring nodes and that of the node itself:

$$J^{in}_{x_-^k} = \frac{2f_{x_+^{k-1}}}{f_{x_+^{k-1}} + f_{x_-^k}} J^{out}_{x_+^{k-1}} + \frac{f_{x_+^{k-1}} - f_{x_-^k}}{f_{x_+^{k-1}} + f_{x_-^k}} J^{out}_{x_-^k}.$$

In practice, only the Flux Discontinuity Ratios $r_{x_\pm^k} = \frac{f_{x_\mp^{k\pm1}}}{f_{x_\pm^k}}$ are used to solve the system, and the last equation written for both right and left surfaces of the node becomes:

$$J^{in}_{x_\pm^k} = \frac{2r_{x_\pm^k}}{r_{x_\pm^k} + 1} J^{out}_{x_\mp^{k\pm1}} + \frac{r_{x_\pm^k} - 1}{r_{x_\pm^k} + 1} J^{out}_{x_\pm^k}. \tag{4.6}$$

Clearly, if the two discontinuity factors in an interface are the same, there is no discontinuity so the ratio equals one, the second term of Equation (4.6) vanishes and we find again the continuity condition of the partial current. We rewrite Equations (2.119) and (2.125) so as to take into account the discontinuities:

$$(\mathbf{A}_x - \mathbf{B}_x \cdot \mathbf{F1}_x)\mathbf{J}_x^{out} = \mathbf{B}_x \cdot \mathbf{F2}_x \mathbf{J}_{x^{\mathrm{nk}}}^{out} + \mathbf{Q}_x, \quad \forall k \in [1, N_x], \tag{4.7}$$

where

$$\mathbf{F1}_x = \begin{bmatrix} \frac{r_{x_-}-1}{r_{x_-}+1} & 0 \\ 0 & \frac{r_{x_+}-1}{r_{x_+}+1} \end{bmatrix}, \quad \mathbf{F2}_x = \begin{bmatrix} \frac{2r_{x_-}}{r_{x_-}+1} & 0 \\ 0 & \frac{2r_{x_+}}{r_{x_+}+1} \end{bmatrix}, \forall k \in [1, N_x].$$

At this point we need to determine the FDRs to feed the operators $\mathbf{F1}_x$ and $\mathbf{F2}_x$ in Equation (4.7). When submeshing is not applied to a zone of homogenization, the FDFs can be calculated directly and *a priori* according to Equation (3.13) or Equation (3.16) without employing any iterative process. In the last equations, the numerators are transport quantities, which are available at the homogenization stage, while one needs an expression for the coarse surface flux Φ_S^{C} at the denominator as a function of the average transport flux in the node and the average transport net current at the surfaces, since both are the quantities to be preserved. Note that for a direct computation of the FDR, only the knowledge of coarse surface flux Φ_S^{C} is required.

For the parabolic nodal operator (NEM2), this expression can be determined by combining Equations (2.115) and (2.116):

$$\Phi_{S_\pm}^{\mathrm{C=NEM2}} = \Phi_R \mp \frac{\Delta x_R}{6D_R}(2J_{S_\pm} + J_{S_\mp}). \tag{4.8}$$

In Equation (4.8) $S_\pm$ are the right (+) and the left (-) surfaces of a coarse region R, Δx_R is its size along an axis x, Φ_R and $J_{S_\pm}$ are respectively the average transport scalar flux in R and the transport net currents across $S_\pm$, and the diffusion coefficient D_R can be arbitrarily chosen. Note that for a given D_R a set of six FDFs is completely defined (one for each surface in a 3D mesh) and when it is used in Equation (4.7), the average reference transport reaction rates are exactly reproduced.

For the quartic nodal operator (NEM4), an approach to determine $\Phi_{S_\pm}^{\mathrm{C}}$ is to use Equation (2.113) that requires the knowledge of average transport scalar flux and the values of the four flux moments. The scalar flux is one of the quantities to be preserved, while the spatial moments can be computed using the following four conditions: preservation of the net currents on the right and left surfaces of a node along a direction; preservation of the average transverse leakage of the right and left adjacent nodes. Because of Equation (2.122), the flux moments are coupled by the scattering and fission sources, which entails that a multigroup system of equations has to be solved:

$$\mathbf{A}_x^G \mathbf{\Phi}_x^G = \mathbf{Q}_x^G + \mathbf{J}_x^G, \quad \forall G, \tag{4.9}$$

where

$$\mathbf{A}_x^G = \begin{bmatrix} 2 & 6 & 12 & 20 \\ 2 & -6 & 12 & -20 \\ \Sigma_{\mathrm{r}} & 0 & 60d & 0 \\ 0 & \Sigma_{\mathrm{r}} & 0 & 140d \end{bmatrix}_R^G, \quad \mathbf{\Phi}_x^G = \begin{bmatrix} \phi_{x,1} \\ \phi_{x,2} \\ \phi_{x,3} \\ \phi_{x,4} \end{bmatrix}_R^G, \quad \mathbf{Q}_x^G = \begin{bmatrix} 0 \\ 0 \\ q_{x,1} \\ q_{x,2} \end{bmatrix}_R^G, \quad \mathbf{J}_x^G = \begin{bmatrix} d\Delta x J_{x_+} \\ d\Delta x J_{x_-} \\ -L_{x,1} \\ -L_{x,2} \end{bmatrix}_R^G,$$

where

$$d = -\frac{D}{(\Delta x)^2}, \quad q_{x,n}^G = \sum_{G' \neq G} \Sigma_{s0}^{G' \to G} \phi_{x,n}^{G'} + \frac{\chi^G}{\lambda} \sum_{G'} \nu \Sigma_{\mathrm{f}}^{G'} \phi_{x,n}^{G'}.$$

In Equation (4.9) the indexes R and G mean that the vector and matrix elements are evaluated for the macro-group G and coarse region R. The first two equations of the system are obtained from Equation (2.114), while the last two equations from Equation (2.122). The moments of the leakage source $L_{x,1}$ and $L_{x,2}$ are calculated according to Equation (2.126), where the average leakage of the adjacent nodes are determined with the transport net currents in the transverse direction, while to evaluate the source moments $q_{x,n}^G$ the reference eigenvalue has to be imposed, adding an additional condition to the equivalence problem. Note that the classical notation was used for the cross sections and the fission spectrum. The system of Equation (4.9) is composed of $4N_G$ equations, with N_G the number of macro-groups, and it can be solved by direct inversion or by iterating on the source $\mathbf{Q}_x$. Once the flux moments are computed, the coarse surface flux for the NEM4 operator is determined with:

$$\Phi_{S_\pm}^{\mathrm{C=NEM4}} = \Phi_R + \sum_{n=1}^{4} (\pm)^n \phi_{R,x,n}, \tag{4.10}$$

where we have omitted the group index.

4.5.3 Leakage coefficient as diffusion coefficient

In our analysis in Chapters 5 and 6 we will compare the DH and the Two-step solutions obtained with the same transport solver options, homogenization options and diffusion solver options. For a fair comparison, we wanted to employ as diffusion coefficient in the fuel assemblies the leakage coefficient resulting from the homogeneous critical leakage model, while in the reflector it was equal to $\frac{1}{3\Sigma_{tr}}$.

The critical leakage model in the Two-step calculation scheme is based on the fundamental mode assumption, and the experience has shown that the leakage coefficient used as diffusion coefficient produces better results than $\frac{1}{3\Sigma_{tr}}$ [15]. The role of the leakage model in the classical approach is to adjust the heterogeneous spectrum flux so as to obtain the critical fundamental mode used as weighting function for cross-section homogenization. As described in Section 3.3.1, in order to obtain the critical condi-

tions, it is necessary to iterate between the equivalent homogeneous medium and the heterogeneous problem, because the former provides the homogeneous leakage rate, that is injected in the heterogeneous problem to change the weighting spectrum, which in turn produces a new equivalent homogeneous medium.

On the other hand, the heterogeneous problem in DH has already realistic core conditions as described in Section 4.3, so there is no need for flux adjustment. However, it is possible to create an equivalent homogeneous medium using the heterogeneous solution, and subsequently compute the homogeneous leakage rate that gives a multiplication constant equal to a given k_{eff}^{core}, that is the one in both RHP and core problem. The purpose of using a homogeneous leakage model in a DH framework is uniquely to compute the leakage coefficient and use it as diffusion coefficient.

We remind the reader that the model is based on the assumption that flux in the reactor can be expressed as a product of a macroscopic distribution in space, that is equal for all the energy groups, and a fine distribution in energy that is characteristic of the equivalent homogeneous medium:

$$\Phi^g(\mathbf{r}) = \varphi^g e^{i\vec{\mathrm{B}}\cdot\mathbf{r}}. \tag{4.11}$$

In the last equation, we have omitted the angular dependence because it is supposed that the reactor is homogeneous and the scalar flux is solution of the diffusion equation. Consequently, using the last equation one can express the leakage rate as it follows [83]:

$$\nabla \cdot J^g(\mathbf{r}) \;=\; -D^g\nabla^2\Phi^g(\mathbf{r}) \;=\; -D^g\varphi^g\nabla^2 e^{i\vec{\mathrm{B}}\cdot\mathbf{r}} \;=\; D^g\mathrm{B}^2\varphi^g e^{i\vec{\mathrm{B}}\cdot\mathbf{r}} \;=\; D^g\mathrm{B}^2\Phi^g(\mathbf{r}). \tag{4.12}$$

In a DH framework, the leakage $D^g\mathrm{B}^2\varphi^g$ is not necessarily equal for each energy group to the actual surface leakage computed in the heterogeneous problem. However, the energy-integrated leakage must correspond to the heterogeneous situation in order to preserve the balance and, therefore, the multiplication constant. This may explain why the leakage coefficient contains more physical insight than $\frac{1}{3\Sigma_{tr}}$, estimating a better diffusion coefficient that produces more accurate results. In Chapter 5 a comparison of the leakage coefficient against $\frac{1}{3\Sigma_{tr}}$ is provided, showing the improvements on the core diffusion solution also in the DH methodology.

4.6 DH as a nonlinear acceleration

We now discuss the particular case when the method of Dynamic Homogenization becomes a nonlinear acceleration scheme, which means the solution of the low-order operator reproduces average transport reaction rates.

A necessary condition to obtain a nonlinear acceleration scheme is that both transport and low-order operators have the same space dimensionality, which is not necessarily the case in a DH calculation. On the contrary, one of the most important features of the method is indeed to avoid expensive 3D transport calculations.

At the convergence of the iterative process, the current ratio in Equation (4.3) is

typically not equal to one, but there exists two particular cases where it is. The first and less interesting one is when the coarse and the transport operators are exactly the same, so no homogenization arises. The second case is when a coarse operator is constructed so as to preserve the transport coarse partial currents at each coarse surface of the homogenized problem including the surfaces on the interfaces between assemblies. This entails that when the transport and coarse solutions converge, the current ratio equals one and the angular transport flux becomes continuous at the interfaces, that means one obtains the exact full-core transport solution. Clearly, in these circumstances the coarse operator acts as a nonlinear acceleration for the transport solution. In all other cases, the solution of the global problem depends on the low-order operator and the process is a truly dynamic homogenization method.

In Chapter 5 on 2D core calculation, this feature of the DH method will be analyzed with respect to the more popular CMFD acceleration. Moreover, in Chapter 6 on 3D core calculations the author provides a further discussion based on the particular case where the 3D low-order operator preserves the average transport reaction rates on the whole radial plane, as it is done in the 2D/1D Fusion method.

The feature of preserving the average transport quantities arises from the FDR technique, for which two different implementations are here examined. These implementations differ on the coarse conditions used at the interface between subdomains.

The first approach is the one introduced in Section 4.5.2, where we use continuity conditions for the flux of the low-order operator at the assembly interfaces and this leads to a typical DH method. Indeed, because of the normalization in Equation (4.3), at convergence the final transport solution is discontinuous at the interfaces and so are then the transport flux and net current. This implies that the current used as boundary conditions for the local subdomains are not those of a full-core transport calculation. Note that this also applies if we compute FDFs at the interface using either the GET or BB prescriptions in Equations (3.13) and (3.16) and use them to construct FDRs to be used as assembly interface conditions for the full coarse operator.

In the second approach instead, we enforce the continuity of the transport flux at the assembly interfaces and use them to construct a fully coherent coarse core operator with FDR conditions at the interfaces between subdomains. Since the interface FDRs are computed using as coarse boundary conditions continuous transport currents, the iterations converge to the exact transport solution and the converged coarse operator reproduces exactly the coarse transport reaction rates.

Let us explain how one enforces continuity of the angular flux at the interfaces while accelerating the incoming angular flux via Equation (4.3). Consider the interface between two subdomains A and B. At the $l+1$ global iteration the transport solution for subdomain A is computed using the normalized incoming angular flux from the previous iteration, the $\psi_A^{-,l+1}$ given in Equation (4.3), and produces an exiting angular flux $\psi_A^{+,l+1}$. These are the angular fluxes which are used to compute the current boundary conditions for the coarse operator in the first approach discussed in Section 4.5.2. Clearly, the transport flux is not continuous at the interface between A and B because $\psi_A^{\pm,l+1} \neq \psi_B^{\mp,l+1}$. In order to re-establish flux continuity, in the present implementation we proceed to sweep the incoming fluxes before constructing the coarse operator so that now $\psi_A^{-,l+1} = \psi_B^{+,l+1}$ and $\psi_B^{-,l+1} = \psi_A^{+,l+1}$. Because in the parallel DDM implementation the sweep operation is done by an exchange of data between subdomains, the main

difference between the two approaches based on the use of FDRs is that in the former the sweep is done after the construction of the coarse operator, while in the second it is prior to it. The second difference resides in that in the second approach one computes the FDRs at the interfaces.

Although a diffusion NEM operator can admit boundary conditions either for the net currents, or for the partial currents, or for the boundary flux, we recall here that when an RHP has non-zero surface leakage it is not possible to determine the FDF beyond the boundaries so, in order to reproduce the transport balance, one has to impose the preservation of the transport boundary net currents.

When Equation (4.7) is used as nonlinear acceleration, the matrix coefficients depend on the transport flux and net currents, thus they change at each iteration:

$$(\mathbf{A}_x - \mathbf{B}_x \cdot \mathbf{F1}_x)^{l+1/2}\mathbf{J}_x^{out,l+1} = (\mathbf{B}_x \cdot \mathbf{F2}_x)^{l+1/2}\mathbf{J}_{x^{\mathrm{n}k}}^{out,l+1} + \mathbf{Q}_x^{l+1}, \quad \forall k \in [1, N_x],$$

and

$$\overline{\Phi}^{l+1} = \frac{1}{\Sigma_{\mathrm{r}}^{l+1/2}}[\overline{Q}_x^{l+1} - \frac{1}{\Delta x}(J_{x_+}^{l+1} - J_{x_-}^{l+1})].$$

Note that $(l + 1/2)$ stands for the last available transport quantities, on which the coefficients of $\mathbf{Q}_x$ also depend, but the source is computed using the coarse flux. The angular flux solved by DDM is typically accelerated with:

$$\psi_{r,h}^{g,l+1} = \psi_{r,h}^{g,l+1/2}\frac{\Phi_R^{\mathrm{C},G,l+1}}{\sum_{g\in G}\sum_{r\in R}\Phi_r^{g,l+1/2}}, \forall r \in R, \forall h, \forall g \in G, \forall R \in D,$$

$$\psi_{s,d}^{+,g,l+1} = \psi_{s,d}^{+,g,l+1/2}\frac{\Phi_R^{\mathrm{C},G,l+1}}{\sum_{g\in G}\sum_{r\in R}\Phi_r^{g,l+1/2}}, \forall s \in \partial R, \forall d, \forall g \in G, \forall \partial R \in \partial D, \qquad (4.13)$$

where h and d stand respectively for angular moment and direction. The accelerated outgoing angular flux becomes in the next global iteration the boundary source for the neighbors.

However, for some coarse operators the incoming interface currents are different from the transport ones, so the DH current normalization in Equation (4.3) acts as a nonlinear acceleration for the transport solution if the BB definition in Equation (3.16) is used, since the latter preserves the average transport partial currents. This means that the acceleration Equation (4.13) for the outgoing flux can be replaced by the DH condition Equation (4.3), where the macroscopic core current is computed as it follows:

$$J_S^{-,\mathrm{C},G}\,|_{core}^{l+1} = f_{\mathrm{BB},S}^{G,l+1/2}\frac{\Phi_S^{\mathrm{C},G,l+1}}{4} - \frac{J_S^{\mathrm{C},G,l+1}}{2}.$$

This is not possible with the GET definition of the FDF because it preserves the reference transport surface flux, which entails that in this case one has to apply Equation (4.13) instead of Equation (4.3).

When convergence is achieved, the coarse operator reproduces simultaneously the eigenvalue, the reactions rates and the partial currents of the fine transport operator on coarse energy and spatial meshes.

Chapter 5

2D Core Calculation based on Dynamic Homogenization

This chapter is devoted to core calculations in a 2D configuration and it is divided into four sections. The first one presents the two problems that we he computed for our analysis and numerical tests, where the second one is the 2D core problem. In the second section, we show some numerical tests and analysis on the coarse operator that justify the choice of two-group diffusion theory as core solver and the interest of exploring in the context of the method of Dynamic Homogenization (DH) the advanced homogenization techniques that are typically used in the classical approach. The third section is the highlight of this chapter where equivalence theory (EQV) and the Flux Discontinuity Ratio (FDR) technique are applied to the 2D core calculation based on DH, whose solutions are compared with the classical two-step (DB2) calculation scheme against Direct Transport (DT) reference calculation. The last section is a discussion on the results, in terms of accuracy and performance, given by DH.

5.1 2D Problem descriptions

In this section we describe the two problems that have been employed for our numerical tests in 2D configurations.

The first one is a cluster of three-by-three assemblies that have 17x17 pin-cells and are of three different types: UO_2, UO_2 with burnable absorber of PYREX material (borosilicate), and UO_2 rodded with AIC control rods, as illustrated in Figures 5.1a and 5.1c. The problem has reflection boundary conditions on each side. In order to perform fast calculations, we employed a library of macroscopic cross sections that have been pre-treated so as to obtain homogenized pin-cells, 26 energy groups, P_1 scattering order and one isotope only. The reference power distribution is shown in Figure 5.1b after normalization such that the total power equals 10000 W. More details about the reference and DH calculations will be given in Section 5.2.1 while presenting our analysis on the influence of the coarse operator to the local transport solution.

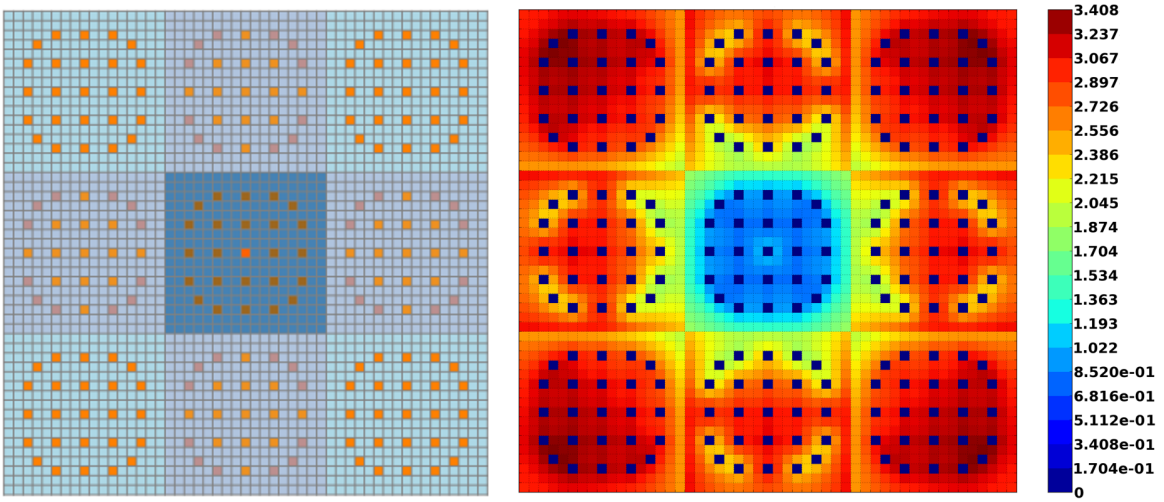

(a) 2D Cluster of three-by-three assemblies of three different types.

(b) Normalized reference power distribution for the 2D cluster problem.

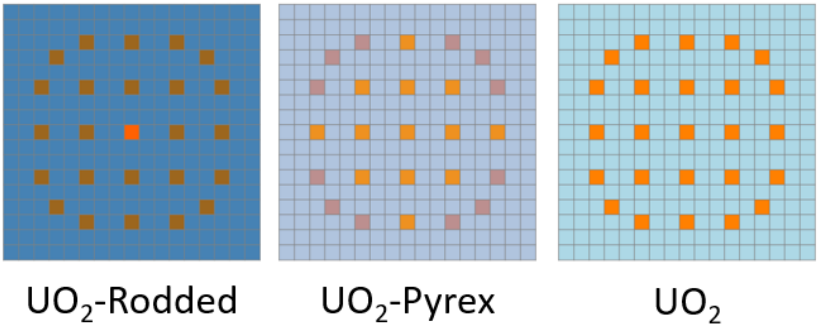

(c) Assembly types for the 2D cluster test.

The second problem that we have solved for most of our analysis in this chapter was inspired by the NEA PWR MOX/UO2 Core Transient Benchmark [74], adopting some simplifications in order to have smaller data library to process for preliminary calculations. We considered only two types of assemblies instead of four, the UOx

with 4.5% enrichment and the MOx with an average content of Pu-fissile of 4.3%. Both assemblies have been irradiated at critical infinite-lattice conditions to obtain the necessary macroscopic cross sections at three average burnup levels: fresh fuel at 0 GWd/t, once-burned at 20 GWd/t and twice-burned at 35 GWd/t. The core layout is shown in Figure 5.2. The UOx assemblies contain guide tubes, fuel pins with and without IFBA (Integral Fuel Burnable Absorber). The MOx assemblies contain guide tubes with and without WABA rods (Wet Annular Burnable Absorber), and a three-zone MOx fuel with 5.0%, 3.0% and 2.5% fissile Pu (in respectively the interior, periphery and corner positions). The two assembly types are represented in Figure 5.3.

Nominal power conditions have been considered to generate burnup dependent fuel and absorber compositions and the corresponding self-shielded cross sections assuming a unique average power density for each assembly. In our core application, the transport solver used a macroscopic self-shielded cross-section library in 172 energy groups with transport corrected P_0 scattering. The self-shielding calculation was performed so as to obtain two self-shielding regions for each fuel pin and, subsequently, the effective multigroup cross sections have been averaged for the same fuel pin type. As for the first problem, all the details of the reference, DH and two-step calculations will be given in the proper sections.

The reference power per pin and per assembly is presented in Figure 5.4 after normalization such that the average power per fuel pin or per fuel assembly is equal to one. The hot point can be found in a once-burned UOx assembly at the position B2 of the core (see Figure 5.2).

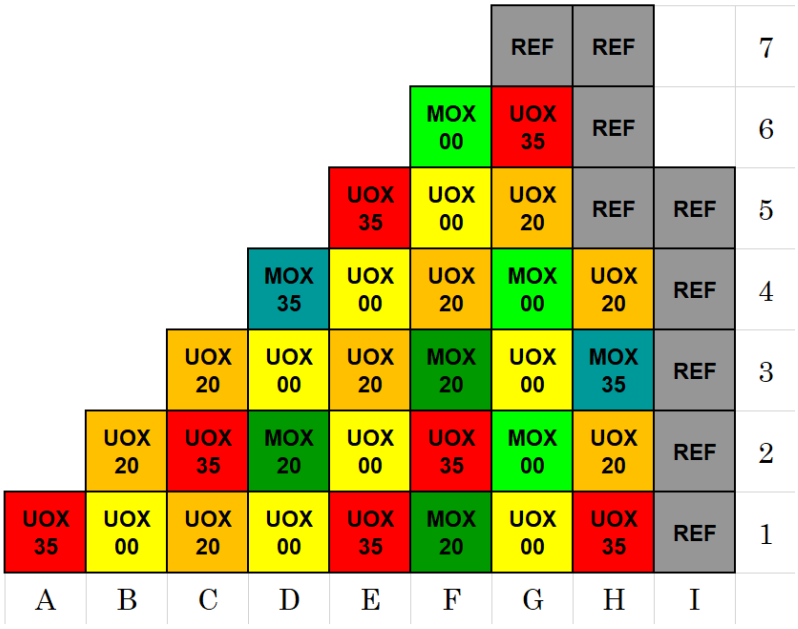

Figure 5.2. Core layout of NEA Benchmark [74].
It contains two types of assembly (UOx, MOx) at three burnup (0, 20, and 35 GWd/t).

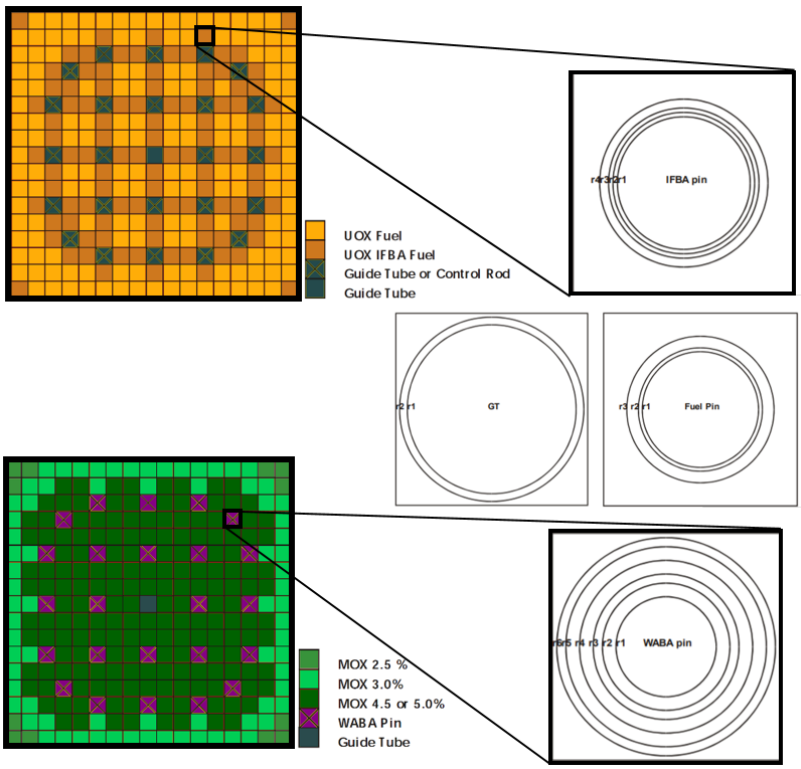

Figure 5.3. Assembly types in the NEA Benchmark [74].

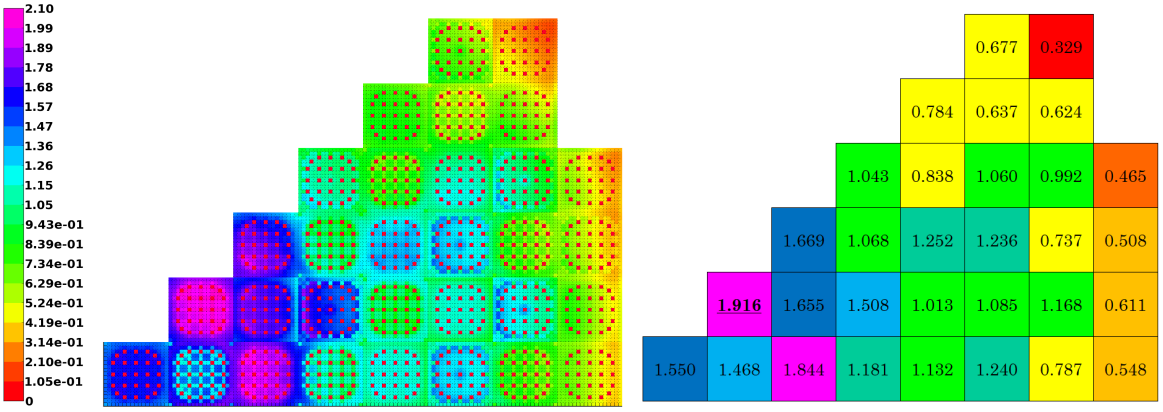

(a) Pin Power **(b)** Assembly Power

Figure 5.4. Normalized reference power distribution for the 2D core problem.

5.2 Preliminary tests

After the implementation of the Domain Decomposition Method (DDM) as described in Section 4.2, the first step of our work was to understand if a two-group diffusion operator is a good candidate as low-order operator for full-core DH calculations. The interest in this type of operator comes from two aspects. In one hand it performs very fast calculations, that will be a necessary feature for 3D full-core calculations. On the other hand, it is the typical core solver employed for routine industrial applications in a two-step approach, so it is very well known that this operator is well accepted by the industrial standards although its limited applicability.

We have firstly tested different types of spatial and energy homogenization options, with both diffusion and transport coarse operators. Note that in this section we are only interested in the accuracy of the DH method given by a coarse operator that is constructed with only flux-volume homogenization with no equivalence technique. The latter and the performances of the method will be analyzed in Section 5.3.

5.2.1 Investigation on the influence of the coarse operator to the local transport solution

As explained in Section 4.1, the results of the DH approach depend on the low-order operator, since the latter is the one that gives the solution of the global problem. However, the coarse operator is also the one that imposes the problem eigenvalue and the macro-incoming currents to define the Reference Homogenization Problem (RHP), which in turn produces the homogenization parameters used to construct the low-order operator. In this first section, we wanted to analyze how the local transport solution that generates the homogenized cross sections is affected by different types of coarse operator.

The local fine-transport problems were solved by an S_{16} operator with linear short characteristics approximation. This operator was fixed for all the cluster calculations and also used to obtain the direct reference solution, whose power distribution is shown in Figure 5.1b after normalization such that the total power equals 10000 W. The normalization for the DH calculation is performed as follows: the total power given by the coarse operator is equal to 10000 W, as for the reference calculation, and this normalization is performed at each global iteration, so that the norm of the transport solution is dictated by the incoming source given by the low-order operator.

At this point we played on the degradation of the angular, energy and geometrical representation for the coarse operator, where the last two are directly given by the homogenization process. For each variable we considered two options: S_2 and S_{16} for the angle, 6 and 26 groups for the energy, a 4x4 and a 17x17 grid of identical meshes for the output homogenization geometry. For all these options the spatial representation for the coarse flux was given by the linear characteristics approximation.

The S_2 formula was chosen because it is supposed to give a solution of similar quality to diffusion theory. Moreover, the spatial mesh for the coarse flux was consistent to that of the fine-transport flux, so it was composed of meshes with pin-cell size. This was

also true in the 4x4 spatial homogenization option, but the current normalization was performed for each surface of the homogenization geometry, even if the coarse current had a finer distribution due to its spatial mesh. This is justified by the fact that in a realistic core configuration, one may want to employ a high order nodal diffusion operator, like it is done in the classical approach for full-assembly homogenization. This operator, in fact, gives the advantage of employing one spatial mesh for each output homogenization media, resulting in a reduced computational cost.

Note that since each pin-cell is homogeneous, the coarse operator with S_{16} quadrature formula, 26 energy groups and 17x17 spatial mesh corresponds to the fine-transport operator, so the DH solution must reproduce the reference fine-transport solution. As explained in Section 4.6, this is due to the fact that the eigenvalue and the assembly incoming currents for the fine-transport and coarse problems are identical. We performed this test for code validation purposes and the errors with respect to the direct calculation are not shown for obvious reasons.

At this point we compare the pin power distribution given by the union of the local fine-transport problems, which are discontinuous between each other. Therefore, it must be clear that one should rather look at the coarse solution but in this section we are interested in how far the RHP is from the direct reference solution due to the low-order operator. For a more rigorous analysis, one should investigate on the macroscopic reaction rates obtained by the local transport solution for each macro-group and macro-region. However, we are here interested in the energy-integrated fission rates, assuming that if the latter are very different from the reference counterpart, then the macroscopic reaction rates are not representative of the actual situation for some "unknown" macro-group.

In Figure 5.5 the pin power relative errors are shown for the seven coarse operators presented earlier and Table 5.1 sums up the results for the seven calculations. In this table, k_C is the eigenvalue computed by the coarse operator and the pin power relative errors are calculated as follows:

$$e_i = \frac{P_i - P_i^{\text{ref}}}{P_i^{\text{ref}}} \tag{5.1}$$

where P_i stands for pin power.

Coarse Operator	k_C-k_{ref}	MAX($\lvert e_i \rvert$)	**RMS**
S_{16} - 26g - 17x17	k_{ref}=0.98502	ref	ref
S_2 - 26g - 17x17	-110 pcm	1.8%	0.3%
S_{16} - 6g - 17x17	109 pcm	2.25%	0.6%
S_2 - 6g - 17x17	11 pcm	3.5%	0.9%
S_{16} - 26g - 4x4	-156 pcm	9.8%	1.15%
S_2 - 26g - 4x4	-198 pcm	9.75%	1.1%
S_{16} - 6g - 4x4	-60 pcm	11%	1.55%
S_2 - 6g - 4x4	-95 pcm	11%	1.6%

Table 5.1. Comparison of DH local transport problems for different coarse operators.

According to these results, it is evident that the spatial homogenization is the main source of the errors introduced in the coarse operator. In particular, the most sensitive pins are those at the corner of the rodded assembly because they undergo to two current normalization (one for each interface with the neighbors) that has been computed along a larger surface (one quarter of the assembly pitch). Next, we can attribute the second source of errors to the energy homogenization, which is mainly due to the fast-spectral variations of the spectrum caused by the control rods. The assemblies UO_2 and UO_2-Pyrex instead, do not show any considerable sensitivity to the energy homogenization, as represented in Figures 5.5b and 5.5c. Clearly, the combination of spatial and energy homogenization gives the worst results in terms of pin power distribution within the assemblies, and Figure 5.5g can be seen as a superposition of Figures 5.5c and 5.5e. Finally, the angular representation for the coarse flux is not the main responsible of the pin power errors, as shown in Figure 5.5a, but it introduces a discrepancy of -110 pcm from the reference eigenvalue. This means that the nine RHPs are close to the reference configuration, but the coarse quadrature formula is not sufficient to deal with the heterogeneities within the assemblies. This discrepancy is of the same order of magnitude of the one due to the energy homogenization, but with opposite sign, and that of the space homogenization with same sign.

It is hard to generalize the conclusions of this test case to the more complicated core calculation, which is never performed with the coarse operators that we have employed and, in addition to that, our reference calculations did not have heterogeneous pin-cells with all the fuel and cladding descriptions. However, whenever the following conclusions are not true for future tests in the rest of the work, it will be explicitly disclosed.

From this first analysis, we may conclude that if one wants to perform a Dynamic Homogenization calculation with no EQV or FDR techniques, the spatial homogenization should be as close as possible to the actual geometry in order to have a better RHP. A coarse energy homogenization could be justified by the presence of types of assembly with similar isotopic content, but in strongly heterogeneous configurations it may easily fail. Finally, a low-order operator such in diffusion theory with a good diffusion coefficient might produce acceptable results for a limited range of configurations.

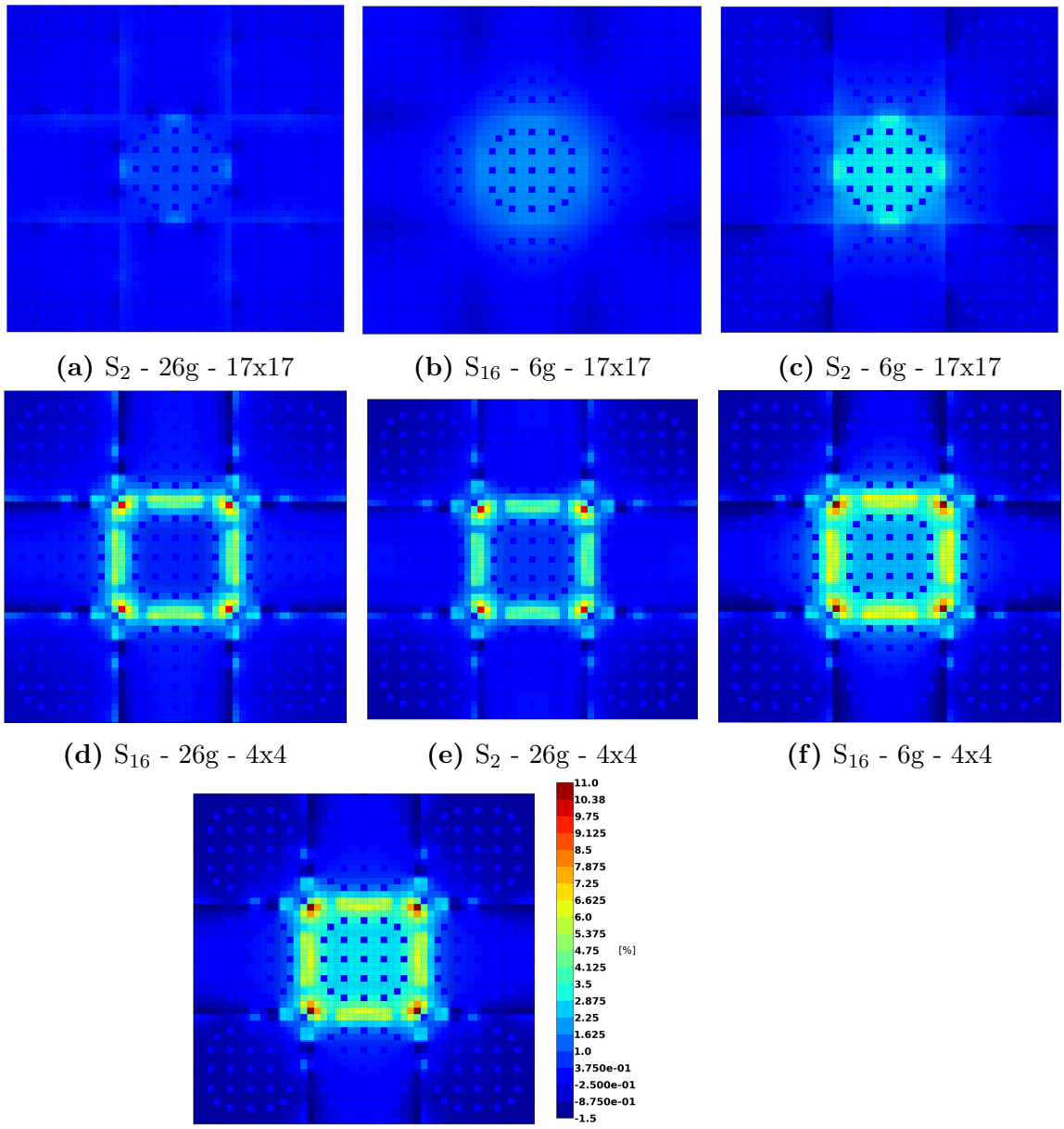

(a) S_2 - 26g - 17x17 **(b)** S_{16} - 6g - 17x17 **(c)** S_2 - 6g - 17x17

(d) S_{16} - 26g - 4x4 **(e)** S_2 - 26g - 4x4 **(f)** S_{16} - 6g - 4x4

(g) S_2 - 6g - 4x4

Figure 5.5. Pin power relative errors of the local fine-transport solution in DH with respect to direct reference calculation for different coarse operators.

5.2.2 Investigation on the solution of the coarse operator

We now turn our analysis to the solution of the coarse operator constructed with flux-volume homogenization. We are interested here only in pin-by-pin homogenization for two reasons. The first one is that a pin-by-pin coarse solution is supposed to produce a better reference homogenization problem as shown in Section 5.2.1. The second one is explained by the following discussion.

The inconvenient of performing pin-by-pin homogenization is that the coarse problem has a large number of degrees of freedom, due to the large number of homogeneous media, especially in a 3D core calculation. This is the reason why this homogenization option is not popular in the two-step calculation scheme. However, an important aspect in favor of the pin-by-pin homogenization resides in the fact that a DH calculation is performed in a MPI parallel environment where the memory and the tasks are distributed for each assembly problem in the core. This means that the coarse core calculation can be easily performed using the same DDM of the transport problem, taking advantage of the parallel calculation that reduces the computational time. If one wants to perform a coarser space homogenization for faster core calculations using a single node, then the amount of computational resources would keep unchanged.

The objective of this section is to verify if the cross sections used to construct the coarse operator, that are homogenized taking into account the environment, can be sufficient to produce accurate solutions for the core problem without relying in advanced homogenization techniques. It is not trivial to answer this question because, on one hand, through homogenization we are simplifying the heterogeneous pin to a homogeneous one, so the accuracy of the coarse solution can be compromised by simply the homogenization process itself and, on the other hand, if this is not the case, then it means that the accuracy is compromised by the low-order flux approximations that are typically employed for the coarse operator.

The problem that we solved for this analysis is the PWR core inspired by the NEA PWR MOX/UO2 Core Transient Benchmark [74] as described in Section 5.1. The details of the reference calculation are here omitted, as it is not the topic of the section, and it will be presented in Section 5.3.1 when compared with DH and two-step. The most important aspect that the reader should retain is that the fine-transport operator employed in DH is the same as in the reference calculation, which utilizes a level symmetric S_{16} quadrature formula and linear short characteristics approximation for the angular flux.

We considered both diffusion and transport for the coarse operator and, in the second case, we employed the same angular flux representation used for the fine-transport operator (S_{16} and Linear MOSC) in order to avoid ambiguity on the error sources. In diffusion theory we have investigated two diffusion coefficient options: $\frac{1}{3\Sigma_{tr}}$ and the leakage coefficient (D_{leak}) from the infinite homogeneous leakage model as discussed in Section 4.5.3. The energy homogenization has been performed in 2, 6, 26 and 172 macrogroups (N_G), where the latter means space homogenization only.

Table 5.2 presents the range of the pin power relative errors and the RMS for each calculation, while Figure 5.6 shows the distribution of the pin power errors in the core.

First of all, we can clearly see that increasing the number of macrogroups in diffusion theory does not improve the solution of the core operator. This can be justified by the

Coarse Operator	$\mathbf{N_G}$	k_C-k_{ref}	**MIN**(e_i)	**MAX**(e_i)	**RMS**(e_i)
Diffusion - D_{leak}	2g	-131 pcm	-4.8%	5.0%	1.94%
Diffusion - D_{leak}	6g	-201 pcm	-7.06%	5.51%	2.49%
Diffusion - D_{leak}	26g	-223 pcm	-7.15%	5.34%	2.33%
Diffusion - D_{leak}	172g	-248 pcm	-7.07%	5.32%	2.23%
Diffusion - $\frac{1}{3\Sigma_{tr}}$	2g	-302 pcm	-7.09%	13.04%	2.89%
Diffusion - $\frac{1}{3\Sigma_{tr}}$	6g	-368 pcm	-7.82%	12.84%	3.10%
Diffusion - $\frac{1}{3\Sigma_{tr}}$	26g	-415 pcm	-7.33%	13.17%	2.90%
Diffusion - $\frac{1}{3\Sigma_{tr}}$	172g	-455 pcm	-7.09%	13.38%	2.80%
Transport	2g	+156 pcm	-6.40%	7.08%	3.32%
Transport	6g	+94 pcm	-5.41%	4.75%	2.40%
Transport	26g	-29 pcm	-3.07%	2.32%	0.96%
Transport	172g	-52 pcm	-2.91%	2.22%	0.88%

Table 5.2. Comparison of DH solutions for different pin-by-pin coarse operators.

discussion in Section 2.6 on the minimization of the first-angular moment of the group-to-group scattering source by coarsening the energy groups. Secondly, we observe that the leakage coefficient always produces more precise results with respect to a diffusion coefficient equal to $\frac{1}{3\Sigma_{tr}}$. This can be explained by the more physical meaning of the leakage coefficient over the other, especially in the two-group coarse energy mesh. In both cases, it is evident from Figure 5.6 that the assemblies containing IFBA pins exhibit peaks of errors distributed as in a chessboard, due to the strong absorption around the fuel pin.

As opposite to diffusion, the transport operator has a tendency to improve the solution as the number of macrogroups increases. In particular, at 26 and 172 groups the RMS of the pin power relative errors is lesser than 1%. However, for a coarse energy mesh the transport solution can be even worse than diffusion. This is particularly true for the two-group case, and it may be justified by the fact that the linearly anisotropic flux assumption in diffusion theory introduces errors of opposite sign with respect to those introduced by the two-group energy mesh, thus partially compensating.

It is important to point out that the pin-by-pin space homogenization in the DH framework is not the main source of errors, since the solution from the operator S_{16} with 172g has good agreement with the reference solution. The bias of the pin-by-pin homogenization itself can be quantified to an RMS equal to 0.88%. We remind the reader that the same operator constructed with cross sections that are homogenized with critical infinite lattice conditions does not necessarily produce the same accuracy as in DH.

We may conclude in this section that the pin power errors introduced by diffusion theory in a DH framework with pin-by-pin homogenization are mainly due to the assumption of linearly anisotropic flux, since increasing the number of macrogroups does not improve the solution. On the other hand, a transport core operator can be accurate if the coarse energy mesh is fine enough to reproduce the spectral effects,

otherwise it does not exhibit particular advantages over diffusion.

5.2.3 Reasons for choosing two-group diffusion

In the last sections, we have discussed the advantage of applying the pin-by-pin homogenization. The latter is motivated by two aspects: 1) the RHPs are closer to the actual situation in the core, and 2) in an HPC calculation the diffusion calculation can be parallelized so that it is not the main responsible of the calculation cost. For instance, in the 2D core calculation presented in Section 5.2.2 the total time elapsed in the two-group diffusion calculations was up to 20 seconds over a wall-clock time of 50 minutes.

In order to quantify the loss of accuracy introduced by a coarser spatial homogenization, we run a similar 2D core calculation, where the coarse operator is two-group diffusion with the leakage coefficient, but the homogenization was performed so as to produce a 3x3 grid output geometry for each assembly. The homogenization grid was defined so as to divide the 17 pin-cells in a row into groups of 5, 7 and 5 pins. Because the meshes are coarser, we employed the nodal diffusion operator with quartic expansion for the flux representation, so as to have one spatial mesh for each output medium. The diffusion calculations cost 3 seconds in total, but the power error of each output medium with respect to the spatially integrated reference solution was between -4.2% and 7.2% with an RMS equal to 2.4%. The error distribution of the coarse solution is shown in Figure 5.7, and the highest errors are found in the internal region of the homogenized IFBA assembly and at the external regions of the other types of assembly.

We now turn our discussion on why we discard transport as core operator. We have concluded in Section 5.2.2 that in order to have accurate results with a transport coarse operator one should increase the number of macrogroups, let us suppose around 30. However, this operator in a 3D core calculation would be too time consuming, probably more than the 2D fine-transport operator, with no guarantee that the desired accuracy is achieved for any core configuration. Note that we do not presents here the run-times of the core calculations of Section 5.2.2, because at the time when we did this analysis, the acceleration for the core power iterations was not implemented yet, making the comparison meaningless.

In order to overcome these two problems we decided to investigate the advanced homogenization techniques (AdH), such as equivalence and flux discontinuity ratios, since the transport solution is locally available and can be used advantageously. When these techniques are applied and converge, the average RHP reaction rates are preserved by the low-order operator *regardless* of the discretization and of the representation for the angular flux. Clearly, if the RHP reaction rates are close to the actual situation in the core, a converging AdH technique can guarantee that the desired accuracy is preserved in most of the configurations. Therefore, there is an interest in employing the most efficient operator that can perform fast core calculations while preserving RHP reaction rates. It is worth to point out that the last feature is not helpful if the RHP is far from the actual situation in the core. So the interest also resides in the verification that a fast operator such as two-group diffusion can provide accurate boundary source and eigenvalue to the local-fine transport problems.

For these reasons, we chose to investigate from now on only two-group diffusion as coarse operator for the rest of analysis, also allowing a fair comparison with the classical two-step approach, where this operator is extensively used and combined with the aforementioned AdH techniques.

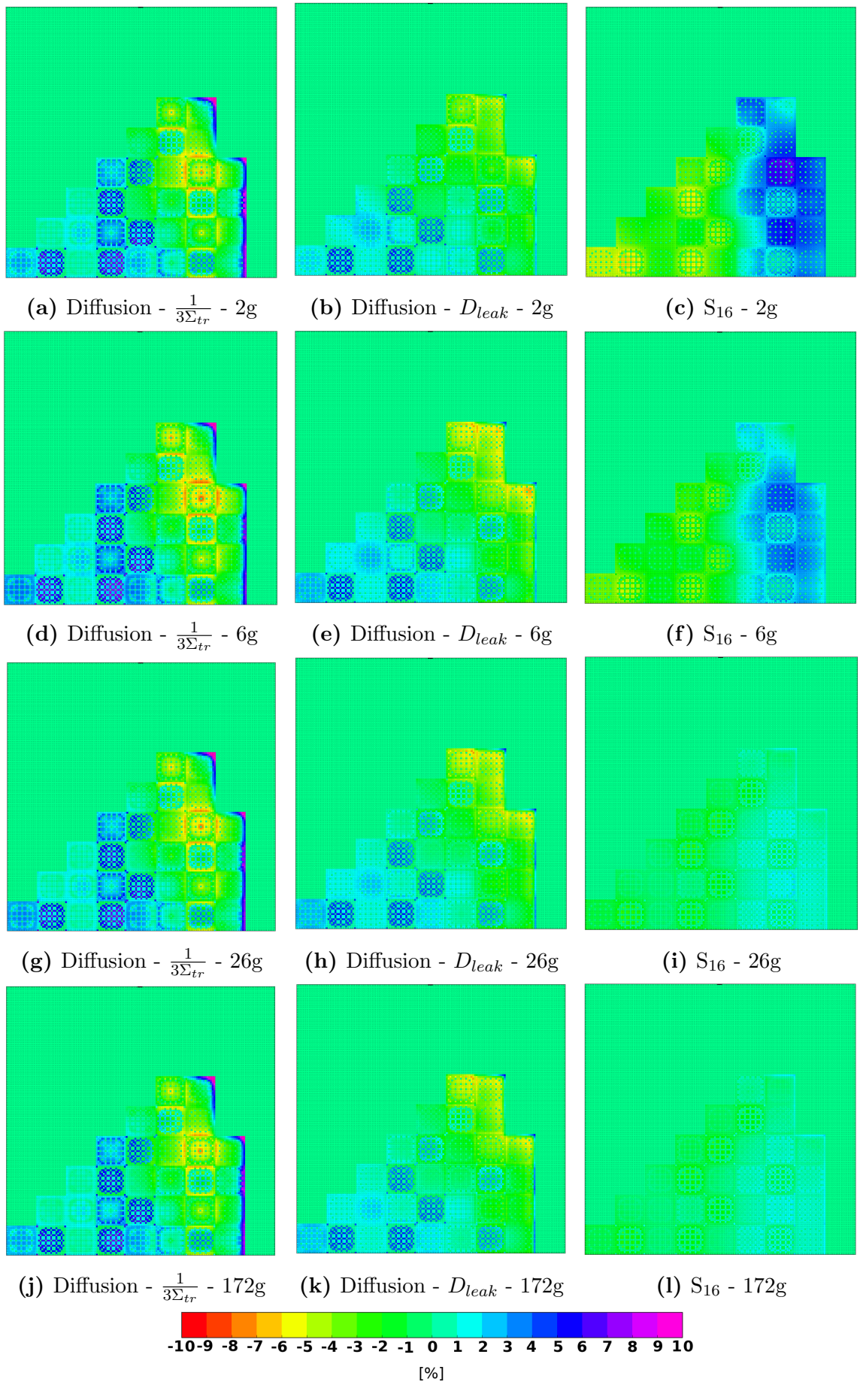

(a) Diffusion - $\frac{1}{3\Sigma_{tr}}$ - 2g **(b)** Diffusion - D_{leak} - 2g **(c)** S_{16} - 2g

(d) Diffusion - $\frac{1}{3\Sigma_{tr}}$ - 6g **(e)** Diffusion - D_{leak} - 6g **(f)** S_{16} - 6g

(g) Diffusion - $\frac{1}{3\Sigma_{tr}}$ - 26g **(h)** Diffusion - D_{leak} - 26g **(i)** S_{16} - 26g

(j) Diffusion - $\frac{1}{3\Sigma_{tr}}$ - 172g **(k)** Diffusion - D_{leak} - 172g **(l)** S_{16} - 172g

Figure 5.6. Pin power relative error of the DH solution with pin-by-pin flux-volume homogenization.

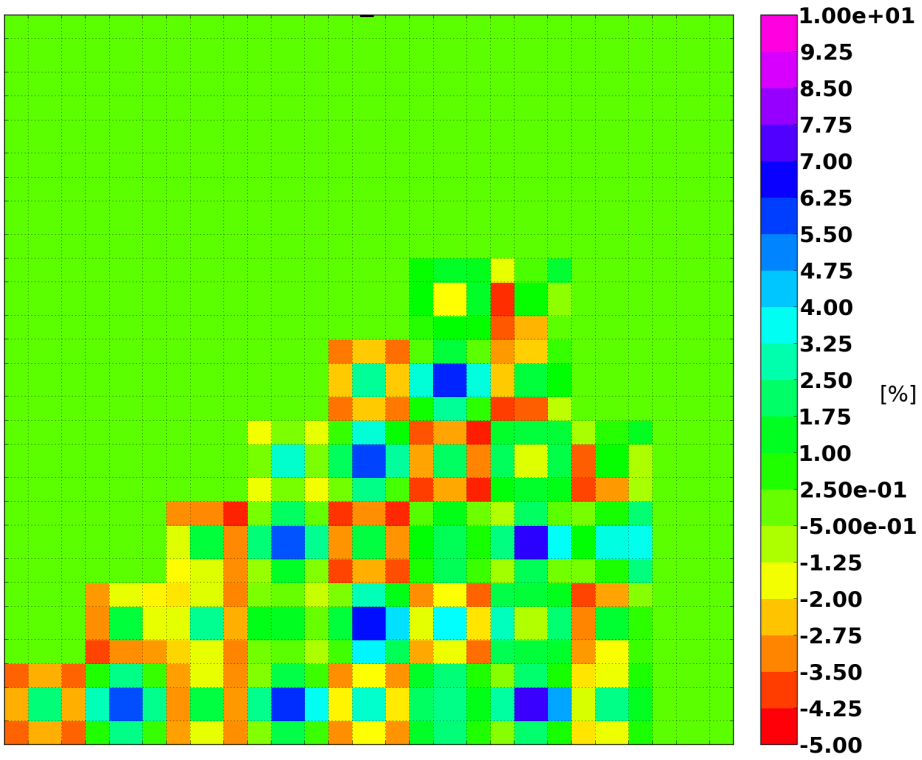

Figure 5.7. Power relative error of the DH solution with coarse mesh flux-volume homogenization and two-group diffusion (NEM4).

5.3 Application of advanced homogenization techniques

In this section we investigate the equivalence (EQV) and flux discontinuity ratios (FDR) techniques presented in Section 4.5 for a DH calculation, as we are interested in improving the two-group diffusion solution. The problem that we solved is the 2D core described in Section 5.1.

Three approaches are compared: Direct Transport (DT) considered as reference, two-step (DB2) and DH. To make a fair comparison, the same fine-transport operator was used for the three cases, and the same diffusion operator as coarse operator for the two-step and DH approaches. The two-dimensional model problem in this core configuration is not critical. In order to avoid additional criticality searches in each of these calculations, for instance via boron concentration or control rods, the multiplication factor in the DB2 leakage model is forced to be equal to reference k_{eff} value. It follows that the comparisons of the presented methods are not compromised.

The same domain decomposition is also applied to the three approaches so that each subdomain corresponds to an assembly in the core, including the reflector assemblies. The benchmark problem is symmetric with respect to the diagonal, so we computed one eighth of the reactor geometry with a total of 40 subdomains to be treated. We run all the calculations in a MPI parallel environment using 40 processors, so that each processor task concerns the computation and the homogenization of only one subdomain.

Our code organization was conceived so that both transport and coarse operators rely on the same spatial decomposition, in order to keep all data in private memory and, therefore, not accessible by the other processors. It ensues that the only information that is exchanged between processors involves the following quantities at the interfaces between subdomains: the angular flux for transport, the scalar flux and the homogenization parameters for CMFD and the partial currents for parabolic nodal diffusion (NEM2). In addition, the quartic nodal diffusion (NEM4) requires both partial currents and transverse leakage of the regions adjacent to the interfaces. In Section 2.6.2 we described in detail the Nodal Expansion Method that was adopted in our calculations and we also presented in Section 4.6 how the method is used as nonlinear acceleration for transport.

One may notice that the few-group diffusion calculation could have been performed efficiently without DDM. However, DDM was used to keep the consistency in the code organization, which is especially important for the future 3D calculations.

5.3.1 Direct Transport approach

The standalone solver IDT of the code APOLLO3® was used as transport solver, which is a multigroup discrete ordinates short-characteristic solver [17, 26, 62, 65]. The source iterations are carried out using the standard transport sweep, CMFD is used as nonlinear acceleration for the global iterations and the Boundary Projection Acceleration (BPA) for the inners. As said earlier, in our core application the transport

solver used a macroscopic self-shielded cross-section library in 172 energy groups with transport corrected P_0 scattering. A S_{16}, level symmetric quadrature formula was adopted for the angular discretization and the linear characteristics expansion for the spatial representation of the angular flux. We divided each side of a pin-cell into 3 sub-surfaces for the projection on the polynomial basis of the surface flux. Note that the fission source is updated at each outer iteration using the accelerated flux moments.

A preliminary analysis was performed to find the optimal choice of coarse energy groups to be used for a pin-by-pin CMFD acceleration. We compared the overall calculation time using 172, 26, 6 and 2 group flux rebalancing according to Equations (3.22) and (3.23). Results showed that transport accelerated by two-group pin-by-pin CMFD had the lowest computational time, thus we considered this case to compare the performance with the DH approach. We refer to this reference case as DT-CMFD. This choice is in agreement with the analysis effectuated by Cho *et al.* in [84] and Lenain *et al.* in [85]. The former showed that CMFD is effective when the optical thickness of the coarse mesh is smaller than one mean-free-path and it becomes unstable for the optically larger cells. The latter also showed that the collapsing in energy does not significantly affect the convergence properties of the iterative scheme, allowing actually to perform faster coarse calculations.

In a further analysis, we compared two DT calculations with same transport operator, but accelerated using Equations (3.22) and (3.23) by two different coarse operators: in the first case by two-group pin-by-pin CMFD and in the second case by two-group pin-by-pin Parabolic Nodal Diffusion with Flux Discontinuity Ratios (DT-NEM2+FDR). We observed that the number of outer iterations was the same in both calculations (12) and that the run-times and the total number of inner iterations in transport were very close. Despite the fact that the computational cost of the two corrected diffusion operators is negligible with respect to transport, (up to 20 seconds over 58 minutes of whole run-time), CMFD is computationally less expensive than NEM2+FDR since the number of unknowns is lower. So we did not observe any particular advantage of NEM2+FDR over CMFD, but further studies on the stability of the iterative scheme will be done in future work.

In this work then, we will consider transport accelerated by two-group pin-by-pin CMFD as the best option for the reference calculation. Moreover, we also considered a coarse mesh homogenization for this low-order operator in order to fairly compare the convergence properties against other cases described later. The geometrical details for the coarse mesh homogenization will be presented with more details in the next paragraph and we refer to this case as DT-CMFD3x3, since the coarse mesh was constructed so that the assembly is homogenized on a three-by-three grid. Using this homogenization option, we also analyzed a calculation where transport is accelerated by an NEM4 operator with FDR according to Equations (3.22) and (3.23) (DT-NEM4+FDR).

The distribution of relative power errors per pin or per assembly and the root mean square with respect to the reference are calculated using Equation (6.24):

$$e_i = \frac{P^i - P^i_{\text{ref}}}{P^i_{\text{ref}}}, \qquad \text{RMS} = \sqrt{\frac{\sum_i^{N_i} e_i^2}{N_i}}, \tag{5.2}$$

where i is either the fuel pin, or the assembly index, with N_i being the total number of fuel pins.

5.3.2 DH approach

For the DH calculations, we used the same transport operator described in Section 5.3.1 based on the IDT solver and nodal diffusion as coarse operator. The transport solution is locally accelerated by BPA for the inners and by CMFD for the outers, where the latter uses the multigroup structure of transport. The number of local (per subdomain) outer iterations was fixed to one. Moreover, as discussed earlier, we decided to homogenize in energy from 172 to 2 groups.

The diffusion coefficient in the fuel assemblies is equal to the leakage coefficient resulting from the homogeneous leakage model that corresponds to the imposed reactor eigenvalue, while in the reflector it is equal to $\frac{1}{3\Sigma_{tr}}$.

We explored two types of spatial homogenization: the pin-by-pin and the coarse mesh.
With pin-by-pin homogenization, we applied the NEM2 diffusion operator and we checked that the spatial mesh was fine enough and there was no need for higher order expansion. We preferred this operator rather than finite differences because we observed that the fixed point iterations used for the search of the equivalent cross sections showed much slower convergence rate than that of NEM2. With finite difference, it was possible to reach the 10^{-4} pin-wise precision in reaction rates only by sub-meshing the pin-cells. This suggests that NEM2 has a spatial representation of the within-cell flux much closer to the transport solution than finite differences. Moreover, the computational cost of diffusion is negligible with respect to transport, so the choice of one of the two diffusion operators does not compromise the overall run-time.

We recall here that this type of spatial homogenization provides a detailed power distribution per pin, such that the impact of different homogenization options will be analyzed by comparing the pin power distributions against the reference. Here will be presented the diffusion solutions with the following options: a homogenization using only the flux-volume weighting (DH-NEM2), the one with equivalence (DH-NEM2+EQV), using flux discontinuity ratios at the interior surfaces (DH-NEM2+FDR), and also with the Black-Box discontinuity factors at the external surfaces (DH-NEM2+FDR+BB). The latter is the case when DH becomes a nonlinear acceleration and it differs from the cases discussed in Section 5.3.1 in two aspects: *i*) it does not apply the rebalancing Equations (3.22) and (3.23) but Equation (4.3) only; *ii*) the fission source is accelerated locally using a 172-group pin-by-pin CMFD operator.

The coarse mesh homogenization is performed on a three-by-three spatial grid per assembly, where the assembly subdivision is done such that the 17 pin-cells are grouped in three sets of 5, 7 and 5 along each Cartesian direction. For this type of homogenization, we used the NEM4 diffusion operator. For comparison purposes, we are allowed to directly use the local transport solution, only if the coarse operator preserves the transport reaction rates in each coarse spatial mesh. This allows us to analyze finely the homogenization options with equivalence (DH-NEM4+EQV) and with flux discontinuity factors applied to all the coarse surfaces (DH-NEM4+FDR+BB).

The stopping criteria of the iterative processes introduced in Section 4.4 were set to:

$\varepsilon_\lambda = 10^{-5}$, $\varepsilon_\mathrm{f} = 10^{-4}$ and $\varepsilon_\psi = 10^{-4}$. The same criteria were used for DT calculations.

5.3.3 Two-step approach

The two-step calculation scheme is considered only in its pin-by-pin homogenization variant, since for the comparison, a coarse mesh homogenization would require a power reconstruction technique, which is not the objective of this work. We adopted the NEM2 diffusion operator for the reasons explained in Section 5.3.2. To homogenize the cross sections we applied the same transport operator as for the DT and DH approaches and, in order to have a consistent comparison, we forced the homogeneous critical leakage model to reproduce the reference core eigenvalue that is $k_\mathrm{eff} = 0.97449$. As in the DH approach, the diffusion coefficient in the fuel assemblies was the leakage coefficient determined by the homogeneous leakage model, while in the reflector it was $\frac{1}{3\Sigma_{tr}}$.

One of the important points in the two-step scheme, as discussed in Section 3.3, is the reflector homogenization because it requires a separate calculation. In our work we investigated two different models for the reflector, and none of them uses cross sections weighted by the reference transport flux, because it would mean knowing a priori the solution, which is not always the case. The first model performs a transport calculation of a motif composed of one UOx assembly burned at 20 GWd/t next to a reflector assembly. Vacuum boundary conditions were imposed at the outermost side of the reflector. We produced the two-group cross sections for only one "output" medium mixing iron and water in the reflector. The homogenized data of this model were used for the whole reflector surrounding the core.

The second model considers four different motifs, representative of the periphery of the core as shown in Figure 5.8, and this time we produced for each motif two "output" media, one for the iron and one for the water. The first two motifs are clusters of 2x1, where the fuel assembly is once-burned UOx and twice-burned MOx respectively for the first and second motifs, and the reflector assembly has vacuum at the outer side. The other two motifs are clusters of 2x2 assemblies. In particular, motif 3 has one UOx assembly burned at 20 GWd/t and three reflector assemblies with vacuum boundary conditions on the outer sides. This motif is used to homogenize the part of the reflector on top right. Motif 4, instead, has two once-burned UOx assemblies on top left and bottom right, one fresh MOx assembly on bottom-left, one reflector assembly on top right, and conservative boundary conditions on all sides. Finally, for each part of the reflector surrounding the core we matched the cross sections homogenized using the most representative motif among the four.

At this point, we wanted to analyze the impact of both reflector models on the power distribution. To do that, for the two cases, where only the reflector cross sections differ, we used the fuel assembly cross sections obtained with the classical two-step approach applying the equivalence theory. We compared the power distribution of the two cases with the direct calculation, and observed that the one-medium reflector model exhibits higher pin power errors at the interface with the reflector, with a maximum of around 18% and a global root mean square of 3.02%. Using the four-motif model instead, the maximum pin power error was around 6% and the global root mean square 1.91%. Figure 5.9 and Figure 5.10 show respectively the pin power error and the assembly

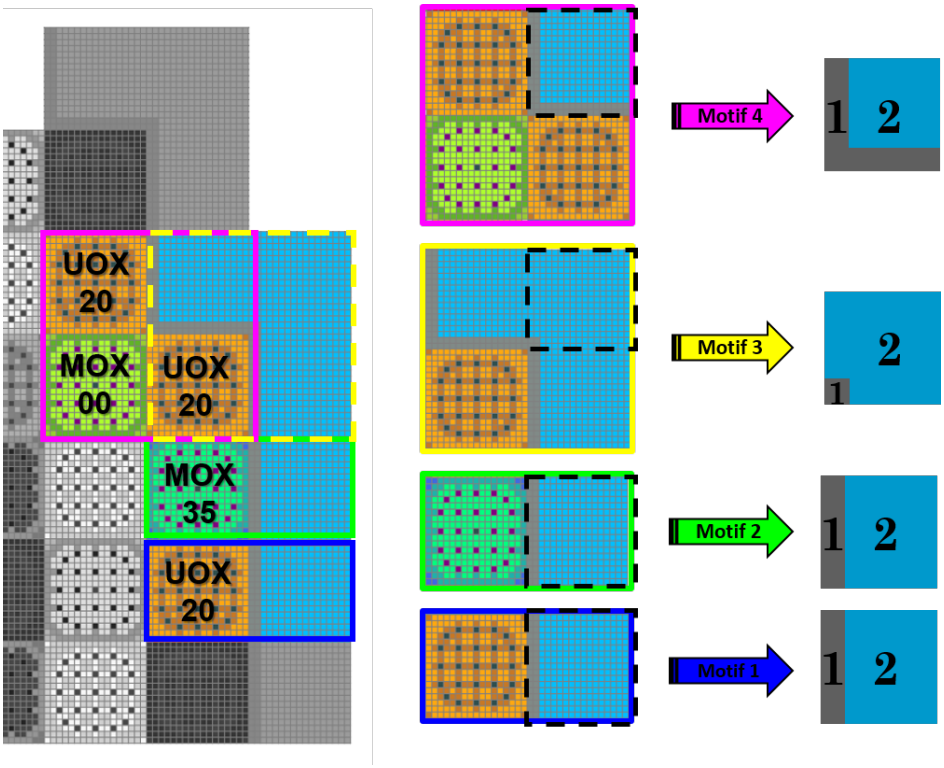

Figure 5.8. Reflector homogenization. Four-motif model.

power error for the two reflector models of the two-step scheme.

This difference of errors at the reflector interface was predictable, since one model utilizes more details than the other. Even if the peripheral region of the core may have a lower importance, since the power is low, it is worth to point out that the two cases that have same fuel cross sections and different reflector ones, result in a different diffusion power distribution, even in the center of the core. As the periphery assemblies are greater in number, the change in local power next to the reflector induces a significant change on power density in the center of the core if the total power of the reactor is maintained constant. In the UOx-20 assembly at position B2, which is the hot point of the core, the assembly power varies from 2.35% to 0.98%, while the power of the UOx-00 assembly at position B1 from 4.66% to 3.21%. Clearly, the core eigenvalue problem redistributes the power so that a higher underestimation next to the reflector produces a higher overestimation in the center of the core. It follows that if the solution that we obtain is different for each reflector model that we adopt, the prediction of the hot points in the center of the core becomes more uncertain, which is an undesirable issue. For all the following comparisons, when referring to two-step, the reflector cross sections are those produced with the four-motif model. Like we did for DH, in order to show the impact of each homogenization option on the final solution we considered the following cases: leakage model only (DB2), leakage model with equivalence (DB2+EQV) and leakage model with Flux Discontinuity Factors (DB2+FDF). Note that for the latter we used the acronym FDF and not FDR because the discontinuities are introduced in all surfaces including the assembly interfaces. Moreover, for the reflector assemblies no FDFs were applied.

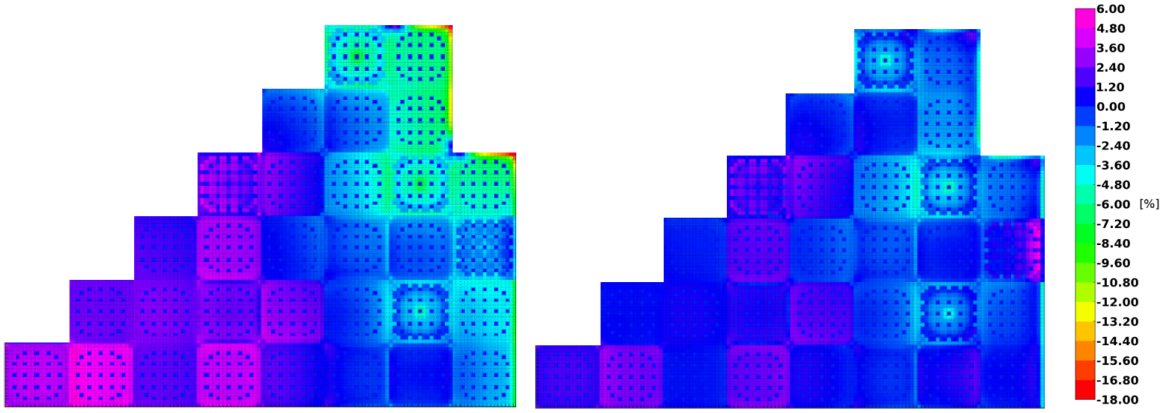

(a) One-medium reflector model. **(b)** Four-motif reflector model

Figure 5.9. Effects of reflector modeling in the two-step scheme. Pin power errors.

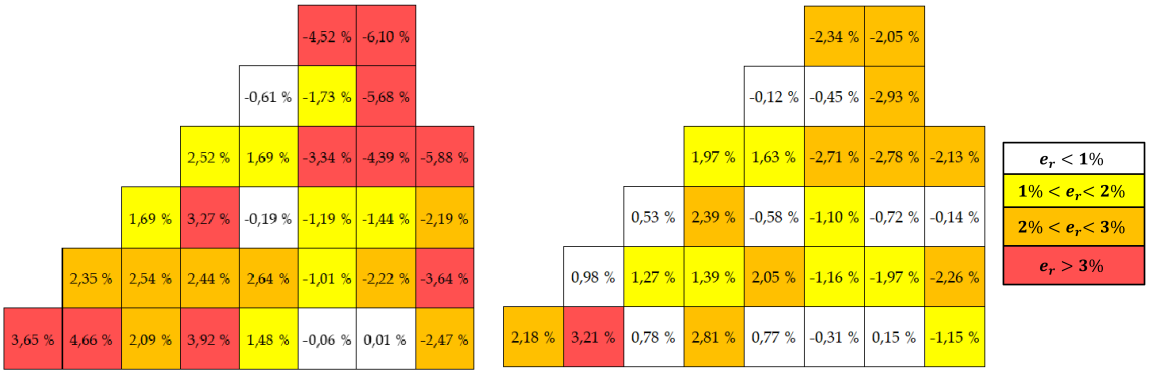

(a) One-medium reflector model. **(b)** Four-motif reflector model

Figure 5.10. Effects of reflector modeling in the two-step scheme. Assembly power errors.

5.3.4 DH vs DB2

Figure 5.11 shows the relative pin power errors respectively for the two-step and DH approaches, applying flux-volume homogenization only, the equivalence and the flux discontinuity factors techniques. In Table 5.3 the maximum, minimum and RMS of the relative pin power errors are presented for each assembly in the core. The errors of the DH cases with Black-Box discontinuity factors at the interfaces between assemblies are not presented since the reference solution is exactly reproduced.

First of all, for both of the approaches we can clearly see that the choice of a homogenization option that adjusts the low-order operator, such as EQV or FDF, does globally improve the solution of the two-group diffusion operator. The RMS of the relative pin power errors in the two-step approach is 2.2%, 1.91% and 1.7% respectively for the flux-volume homogenization, the equivalence, and the flux discontinuity factors options. In the DH approach with pin-by-pin homogenization, instead, the RMS is 1.9%, 0.94%, 0.65% and 0% respectively for the options flux-volume only, EQV, FDR

and FDR+BB. The EQV and the FDF techniques result to be more effective in DH than in two-step thanks to the environment information. There is no guarantee, in fact, that an equivalence technique used in the two-step approach always improves the solution everywhere in the core, because the distribution of the reaction rates determined by solving the RHP can be very different from the actual one in the core, so forcing the low-order operator to reproduce it is not always advantageous. An example of this can be seen for the fresh MOx assemblies at peripheral positions G2, G4 and F6, that show a peak of error in the central pins of the assembly for the case DB2+EQV, while for the case DB2 they are not as prominent. In other words, the choice of RHP may be inadequate, that is, at the homogenization stage the assembly solution was symmetric while in the core close to the reflector they experience strong gradients. More rigorous procedure would be to generate the homogenized cross sections for the peripheral assemblies using a fuel-reflector motif as RHP, like it was done for the reflector zones, but in general, while preparing the cross sections for the core calculation the position of a specific type of assembly is in general not known in advance. However, for local phenomena like the strong absorption in the fresh UOx assemblies containing IFBA, we can clearly observe that EQV and FDF properly adjust the diffusion solution in both two-step and DH approaches.

In the two-step scheme, some other error peaks are found because of the absence of the environment information in the model, such as the UOx-MOx interfaces, but also for the UOx-UOx interfaces with different burnup. In particular, the fresh UOx assemblies containing IFBA in positions B1, D1, E2 and D3, which belong to the interior part of the core, show a sensitivity to the environment influence with a maximum relative pin power error between 3% and 4%. These errors, however, result to be lower in the case of the FDF option, probably because of the discontinuities at the assembly interfaces. On the other hand, in DH the errors introduced by the infinite lattice approximation at the interfaces between different types of assembly were eliminated and the maximum error remains lower than 2%, that typically arises in the corner pins of the assemblies in the inner part of the core.

The power distribution in the peripheral part of the core is predicted by two-step with a comparable quality using the three homogenization options, with peaks of errors between 4.5% and 6.5%, while in DH the behavior is different. In our DH calculations, the reflector cross sections were homogenized into a 17x17 grid geometry, with the same mesh size as that of a fuel cell. We observed that in DH-NEM2+EQV the equivalence did not converge in the reflector subdomains, either due to the inefficiency of fixed point iterations in a problem with strong flux gradients or to the weak values of the flux at the outer boundary. Therefore, the flux-volume weighted homogenized cross sections were used in the reflector coarse geometry instead of the equivalent cross sections. The case DH-NEM2+EQV shows an improved solution close to the reflector with respect to two-step, but this region still remains the most difficult to solve, since it strongly depends on the reflector properties that might not be well modeled by two-group diffusion, especially if no equivalence is applied. However, an enormous advantage of DH is the possibility to calculate directly the FDR also in this region of the reactor without applying any iterative process that may not converge, thanks to the fact that the geometry used for homogenization is locally available in each subdomain composing the reflector, while this is not possible in the two-step scheme.

Finally, because of the correction of the diffusion operator also in reflector assemblies, the case DH-NEM2+FDR exhibits the best reflector response and, therefore, the best solution. This definitely shows how important the reflector homogenization is in reactor modeling.

In Figure 5.12 the coarse mesh homogenization option is shown for the DH approach with equivalence, where the pin power has been computed using the local transport flux of each assembly. Recall that the errors of DH-NEM4+FDR+BB are not shown since the reference solution is exactly reproduced. The coarse mesh homogenization option with equivalence shows a similar behavior of DH-NEM2+EQV in the interior part of the core, with slightly higher errors at the corners of the interfaces between assemblies, due to the coarser representation of the currents. On the other hand, the reflector response is not as well predicted as in the pin-by-pin case. In the latter, the fixed point iterations for the search of the equivalent cross section also converged in the reflector subdomains but the EQV technique does not show any significant improvement in the quality of the solution at the peripheral area. This can be explained by two reasons: the first one is related to the type of operator, because Fick's law fails to describe the physics of the problem in this region; the second one can be related to the choice of the mesh for cross-section homogenization, which is too coarse to represent the rapid spectrum change in the reflector.

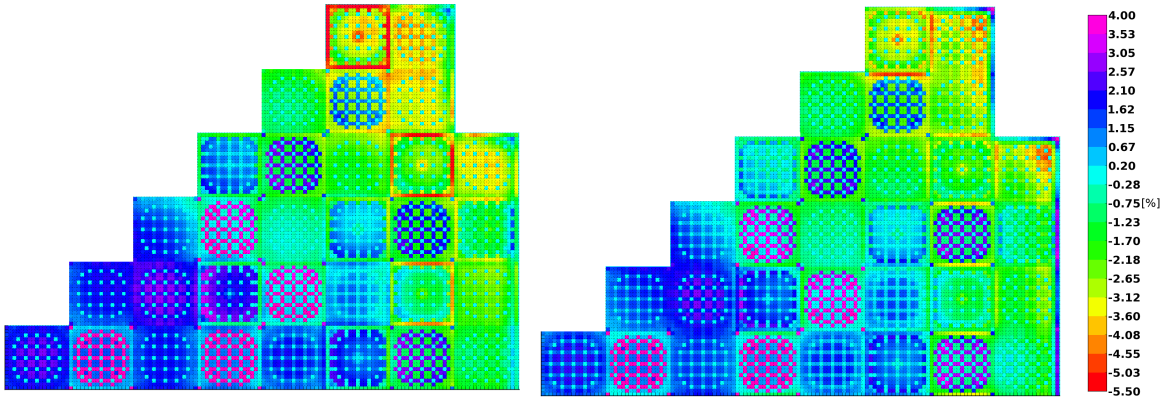

(a) Two-step: leakage model only (DB^2)
MIN=-6.2%, MAX=5.4%, RMS=2.20%

(b) Dynamic homogenization (DH-NEM2)
MIN=-4.8%, MAX=5.0%, RMS=1.9%

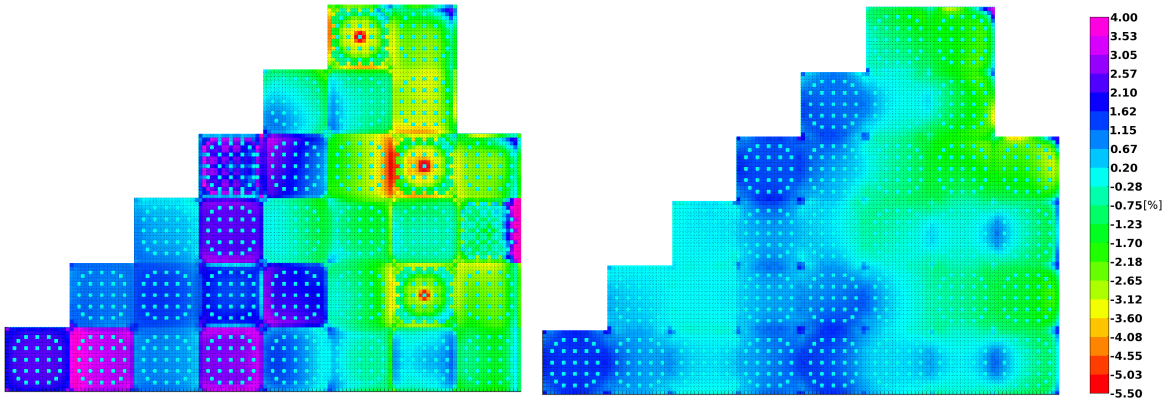

(c) Two-step: leakage model with equivalence (DB^2+EQV)
MIN=-5.8%, MAX=6.4%, RMS=1.91%

(d) Dynamic homogenization with equivalence (DH-NEM2+EQV)
MIN=-3.6%, MAX=3.2%, RMS=0.94%

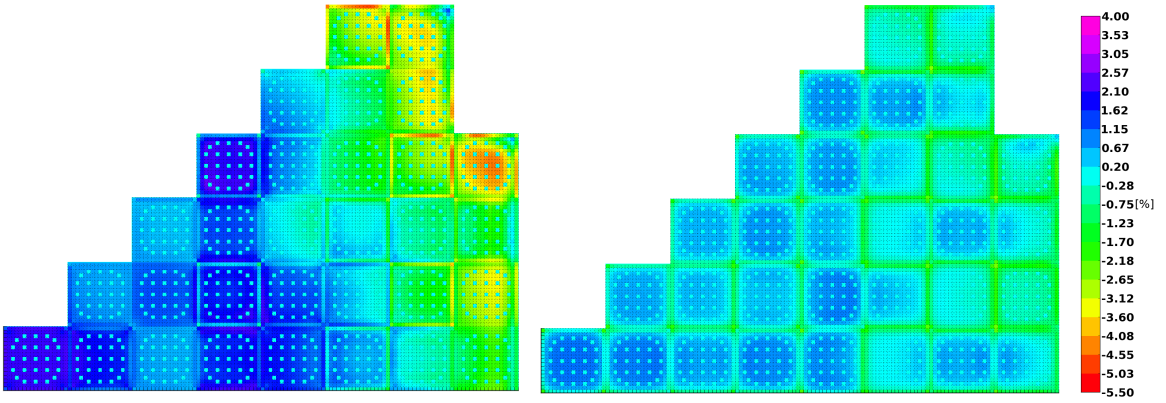

(e) Two-step: leakage model with flux discontinuity factors (DB^2+FDF)
MIN=-4.7%, MAX=2.5%, RMS=1.70%

(f) Dynamic homogenization with flux discontinuity factors (DH-NEM2+FDR)
MIN=-2.6%, MAX=1.0%, RMS=0.65%

Figure 5.11. Relative pin power errors.

max e_i					0.	1.24	
min e_i					**-6.24**	-4.3	
RMS					**3.99**	3.14	
				0.	1.62	0.	
				-2.65	-4.55	-4.13	
				1.39	2.56	3.23	
			1.89	2.94	0.	0.	1.01
			-2.09	-3.03	-3.29	-5.45	-4.27
			1.12	2.04	1.95	3.05	2.96
		2.15	4.53	0.55	1.62	2.51	1.6
		-0.41	-1.71	-1.72	-3.13	-3.02	-3.83
		1.25	2.44	0.69	1.25	1.9	1.78
	2.16	2.93	3.34	4.5	1.5	0.57	0.
	0.	0.	-1.47	-1.37	-0.48	-4.64	-2.86
	1.63	2.28	1.98	2.51	0.62	2.07	2.12
2.69	**5.4**	2.01	5.09	1.97	2.38	3.19	0.39
0.	0.	0.	-0.36	0.	-2.31	-2.8	-1.97
1.98	3.25	1.51	3.02	1.28	1.4	1.93	1.24

DB^2

				0.	3.94	
				-4.38	**-4.8**	
				2.78	**2.95**	
			0.	1.83	1.77	
			-2.79	-4.94	-4.15	
			1.36	2.29	2.56	
		1.42	2.79	0.	0.	4.31
		-1.52	-2.72	-3.43	-3.49	-4.8
		0.62	1.9	1.7	1.83	2.66
	2.32	4.28	0.	1.77	3.18	3.32
	-0.71	-1.97	-1.81	-1.48	-3.86	-2.92
	0.99	2.14	0.83	0.64	2.16	1.38
2.33	2.72	3.04	4.35	1.44	0.7	2.98
0.	0.	-0.48	-1.92	-1.54	-2.44	-3.13
1.29	1.78	1.35	2.23	0.72	1.06	1.89
2.2	**5.03**	1.85	4.82	1.67	2.3	3.56	2.67
0.	-0.18	0.	-1.27	-0.22	-0.58	-3.48	-2.32
1.41	2.77	1.18	2.59	0.91	1.07	2.14	1.22

DH-NEM2

				0.89	2.46	
				-5.46	-3.3	
				2.62	2.1	
			1.75	0.95	0.	
			-2.05	-3.15	-4.02	
			0.72	0.78	2.92	
		4.13	3.13	0.	0.38	2.2
		-0.07	-1.14	-5.23	**-5.82**	-3.29
		2.11	1.84	2.9	3.	2.19
	0.99	2.94	0.8	0.62	0.13	**6.4**
	-0.09	0.	-1.65	-2.91	-3.48	-2.93
	0.57	2.41	0.75	1.26	0.86	2.17
2.43	1.59	2.67	3.07	0.28	0.36	0.
0.	0.	0.	-0.59	-3.63	-4.94	-3.31
0.98	1.26	1.45	2.09	1.49	2.24	2.28
2.83	3.86	1.41	3.26	1.63	1.27	1.09	0.22
0.	0.	0.	0	-0.18	-1.97	-2.34	-1.81
2.17	**3.22**	0.79	2.82	0.87	0.69	0.54	1.18

DB^2+EQV

				1.28	**3.24**	
				-1.91	-3.04	
				1.	1.72	
			1.66	0.91	1.09	
			0.	-1.15	-3.43	
			1.01	0.35	1.58	
		2.23	1.79	0.92	0.	2.11
		0.	-0.45	-1.46	-2.37	**-3.61**
		1.28	0.74	0.79	1.55	**2.05**
	0.88	1.39	1.03	0.25	0.7	1.48
	-0.17	0.	-0.59	-0.97	-0.89	-1.24
	0.13	0.69	0.32	0.41	0.3	0.71
1.6	0.19	2.03	1.59	1.11	0.05	1.42
-0.04	-0.2	0.	0.	-0.57	-1.19	-2.08
0.32	0.07	0.66	0.94	0.4	0.71	1.39
1.75	1.54	0.75	1.57	1.53	0.69	1.04	1.46
0.	0.	-0.17	0.	0.	-0.3	-0.52	-1.13
1.41	0.78	0.26	0.88	1.16	0.31	0.31	0.67

DH-NEM2+EQV

				0.	1.28	
				-4.71	-3.67	
				2.84	2.81	
			1.2	0.28	0.	
			-1.07	-2.19	-4.1	
			0.6	0.97	2.97	
		2.46	1.82	0.	0.	0.52
		-0.68	-0.65	-2.08	-4.54	-4.41
		1.87	0.87	1.31	2.71	**3.37**
	0.87	2.08	0.74	0.7	0.55	0.24
	0.	0.	-0.61	-2.47	-1.25	-3.46
	0.57	1.41	0.35	0.62	0.69	1.67
1.5	1.94	2.17	2.25	1.42	0.	0.
0.	0.	-1.03	0.	-0.25	-3.75	-3.43
0.83	1.25	1.52	1.33	0.56	1.71	2.69
2.28	2.2	1.14	2.33	1.94	1.23	0.82	0.
0.	0.	0.	0.	0.	-1.57	-1.41	-2.44
2.15	1.67	0.72	1.71	1.5	0.72	0.54	1.63

DB^2+FDF

				0.	0.46	
				-1.99	**-2.64**	
				0.67	0.83	
			0.81	0.81	0.54	
			-2.52	-1.44	-2.18	
			0.67	0.62	0.71	
		0.7	0.79	0.4	0.	0.44
		-1.97	-1.06	-2.3	-2.18	-2.57
		0.54	0.6	0.64	0.77	0.97
	0.59	0.8	0.64	0.35	0.62	0.48
	-2.15	-1.07	-2.16	-2.03	-1.49	-2.25
	0.52	0.61	0.57	0.5	0.63	0.69
0.66	0.55	0.55	0.95	0.59	0.04	0.
-1.87	-1.95	-1.9	-1.08	-2.3	-2.11	-2.55
0.53	0.56	0.44	0.69	0.68	0.55	**1.02**
1.04	1.03	0.8	0.92	0.86	0.42	0.77	0.71
-1.96	-0.85	-1.63	-0.97	-2.21	-1.88	-1.41	-2.3
0.82	0.72	0.57	0.67	0.68	0.46	0.64	0.66

DH-NEM2+FDR

Table 5.3. MAX, MIN and RMS of relative pin power error [%] within assembly.

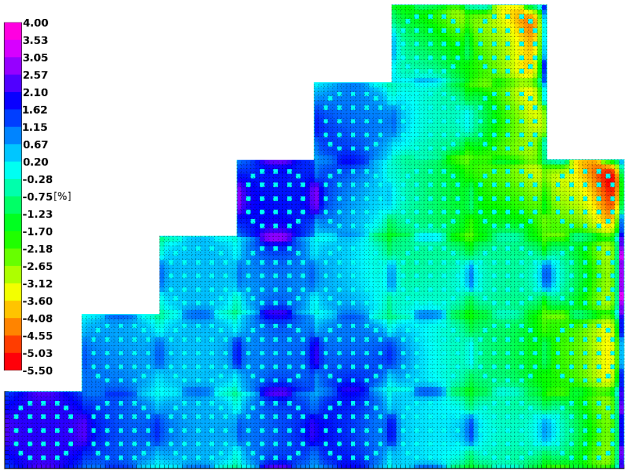

(DH-NEM4+EQV) MIN= -5.3%, MAX=3.3%, RMS=1.47%

max e_i					0.44	1.56	
min e_i					-2.76	-4.33	
RMS					1.33	2.71	
				1.63	1.01	0.43	
				-0.5	-2.43	-3.48	
				0.96	0.63	2.15	
			2.78	2.64	0.09	0.	1.78
			0.	-1.52	-2.37	-3.17	**-5.29**
			1.74	0.89	1.03	1.94	**3.08**
		1.06	2.81	0.91	0.76	1.04	**3.34**
		-0.69	-0.41	-1.44	-2.1	-2.25	-2.92
		0.49	1.05	0.43	0.57	0.81	1.71
	1.28	1.51	2.23	2.12	1.27	0.06	2.06
	-0.47	-0.46	0.	-0.78	-1.66	-2.37	-3.53
	0.82	0.6	1.15	1.09	0.5	1.12	2.27
2.42	2.46	1.31	2.4	1.97	1.56	1.28	2.52
0.	0.	-0.58	-0.29	-0.06	-1.37	-1.73	-2.68
2.03	1.3	0.67	1.27	1.32	0.47	0.59	1.62

DH-NEM4+EQV

Figure 5.12. Dynamic homogenization with equivalence and coarse mesh homogenization. Relative errors [%] of the reconstructed pin power.

5.3.5 Convergence Rate and Runtimes

Table 5.4 presents the eigenvalue error, the RMS of pin power errors, the number of global iterations and the calculation run-time for each case that we investigated. All calculations were performed with 40 parallel process, where each process computes only one assembly.

As expected and explained in Section 5.3.1, CMFD constructed on coarse spatial mesh is less effective than pin-by-pin, resulting in a total of 18 global iterations instead of 12, and therefore a calculation run-time of 81 minutes instead of 58. This is due to two reasons: *i*) the average fission source is accelerated on a coarser mesh, so the transport operator needs more iterations for the pointwise convergence on the fine mesh; *ii*) the linear flux approximation of the finite difference scheme is insufficient for this mesh size to describe the flux gradients everywhere in the core, which ensues that the average flux is not well predicted and the acceleration becomes less effective. Therefore, we wanted to analyze the case DT-NEM4+FDR for the following reasons: the algorithm of the iterative scheme is identical for both calculations, the transport flux moments are accelerated using the same equations and same spatial and energy meshes, and the only difference is that the coarse flux is represented by a higher order polynomial expansion which is sufficient for the size of the chosen coarse mesh. This acceleration shows a convergence rate of the transport fission source, which situates between the two CMFD operators, resulting in 13 global iterations with a run-time of 68 minutes. Figures 5.13a and 5.13b show the error decay as a function of the global iteration number, respectively for the transport fission source and the boundary angular fluxes.

In Figure 5.13c we have plotted the number of core iterations needed by the coarse operator to converge as a function of the global iteration number, since at convergence

it equals one. Note that the global coarse problem is solved using the same DDM like in transport; as for the core iteration, we refer to a power iteration solved by DDM, where at the end of each iteration we update the coarse fission source, the eigenvalue and the coarse boundary conditions of each subdomain; our two-group diffusion operator is not accelerated.

At the beginning of the iterative process, we can see that the pin-by-pin CMFD for the first five global iterations reaches the maximum number of core iterations that was fixed to 500. A similar behavior is observed with the CMFD3x3 operator for the first two global iterations, while the NEM4+FDR operator exhibits a better convergence rate with less than 100 core power iterations after the first global iteration. On the other hand, during the last global iterations, where the solution is close to the convergence, we observe that the number of core iterations decreases slowly in the case of two coarse mesh operators with respect to the pin-by-pin operator, which entails that they are less effective in accelerating the pointwise convergence of the transport fission source.

The fact that pin-by-pin CMFD and coarse mesh NEM4+FDR have good properties in different phases of the iterative process may be of interest to develop a nonlinear acceleration with an adaptive mesh scheme, in order to take advantage of both operators and improve the convergence rate of the overall process. We suppose that this strategy may be convenient especially for 3D calculations, since the pin-by-pin CMFD is no more computationally negligible. However, in this work we only show the feasibility of using different operators as nonlinear acceleration and further analysis on the properties of discontinuous operators will be investigated in future.

We now analyze the cases DH-NEM2+FDR+BB and DH-NEM4+FDR+BB. First of all, the former converges in 11 global iterations while the latter in 13, resulting respectively in 60 minutes and 75 minutes of run-time. This can be explained by the use of a coarser mesh to accelerate the transport convergence but, unlike the DT cases, here the coarse scalar flux is not used at all to accelerate either the fission source or the outgoing angular flux, but instead the coarse partial currents are used to accelerate the incoming boundary source. In Figure 5.13b we observe that the boundary source of DH-NEM2+FDR+BB converges faster than in all the other cases, in part because of the use of the Equation (4.3) instead of Equation (3.23), since the former has more physical insight, and in part because of the multigroup local acceleration. When comparing DH-NEM2+FDR+BB with DT-CMFD and DH-NEM4+FDR+BB with DT-NEM4+FDR, we can clearly see in Figure 5.13a that the convergence rate of the fission source does not significantly change, even if the fission source is accelerated differently, either using the local information (DH) or the global information from the diffusion solution (DT). This is explained by the fact that fission is an internal source, while the eigenvalue and the boundary flux depend on the external environment information and in both cases (DT and DH) the convergence of these quantities are similarly accelerated using the coarse solution that, somehow, contains this information.

these q is accelerated using coarse quantities that somehow contain . Nevertheless, we can observe a difference of the two approaches for non-fissile subdomains. In Figure 5.13d we have plotted the total number of transport inner iterations, where total stand for the sum of all subdomains, fissile and not. For the first five global iterations the transport operator in all the cases reaches the maximum number of inner iterations which was fixed to 3 in fissile subdomains and 50 in non-fissile subdomains, where there

is no outer loop on fission source. We can observe that DH-NEM2+FDR+BB requires more inners than DT-CMFD and DH-NEM4+FDR+BB more than DT-NEM4+FDR. This is explained by the lack of using Equation (3.22) in the DH cases, since it gives the advantage of accelerating the convergence of the multigroup problem also in non-fissile subdomains. We checked, in fact, that the increase of the number of inner iterations occurs mainly in the reflector subdomains. It follows that the overall run-time of DH-NEM2+FDR+BB and DH-NEM4+FDR+BB is slightly higher than the respective DT cases with same coarse mesh homogenization option.

All of Dynamic Homogenization cases show on average a run-time that is comparable to Direct Transport accelerated by pin-by-pin CMFD. The fastest cases are DH-NEM2 and DH-NEM2+EQV mainly due to the lesser number of global iterations (10 instead of 12) with a run-time of 50 minutes for both, since EQV iterations have a negligible cost. We have observed that in these cases the diffusion solution after 5 iterations does not change significantly, which means that cross sections are close to the converged values, but the process needs 5 more iterations to converge the transport quantities. We think that the slightly lower number of global iterations is due to the fact that when using a low-order operator that preserves net currents, even if the homogenized cross sections do not change very much, its matrix coefficients also depend on the homogenized transport currents and surface fluxes per coarse region, adding then additional dependencies from transport. This is why the convergence rate of the cases DH-NEM2+FDR, DH-NEM2+FDR+BB and DT-CMFD cannot be very different.

Comparing the cases DH-NEM2+EQV and DH-NEM4+EQV we observe that they have the same eigenvalue, even if the power distribution is different, with a RMS of relative errors being respectively 0.94% and 1.47%. As we observed for the direct calculations, the coarse mesh homogenization option exhibits a higher number of inner iterations in transport as shown in Figure 5.13d. Therefore, even if the coarse diffusion calculation (NEM4+EQV) is computationally less expensive than the pin-by-pin diffusion (NEM2+EQV) calculation (respectively 3 seconds and 10 seconds cumulated at convergence), the overall run-time of the latter is lower because almost all of the computing time is spent for transport.

Finally, the two-step calculations, also shown in Table 5.4, are the most rapid and the least accurate as expected. The run-time of DB2 cases includes only the diffusion calculation. For the interested reader, the initialization of DH and DT cases consists of infinite lattice calculations that produce the first weighting flux for cross-section homogenization and, therefore, the zeroth global iteration can be considered as a two-step calculation. The initialization has a computational cost of roughly 10 minutes and it is, evidently, included in the total run-times. In our two-step cases, the lattice calculation takes 12 minutes instead of 10 because of the critical buckling search and the critical fundamental mode that is not performed in DH and DT. However, it is hard to include this additional cost of generating the homogenized cross sections in the overall two-step computational cost for several reasons: *i*) one eighth of assembly is typically computed to take advantage of the geometrical symmetries, while in our cases for simplicity of implementation we computed the whole assembly also for two-step; *ii*) the separate calculation for reflector homogenization is not included in the 12 minutes discussed earlier, and in our two-step case the code read an external library for only

the reflector cross sections. The highest computational cost for generating the reflector library among the 4 motifs was 25 minutes associated to motif 3 (see Figure 5.8), that was solved using a 2x2 domain decomposition, 4 parallel process, same transport operator accelerated by two-group pin-by-pin CMFD.

In summary, the results show that the DH approach does not exhibit any considerable advantage for 2D configurations in terms of computational cost with respect to a two-step approach (which is obvious) nor to a direct transport with a nonlinear acceleration. We observed that the diffusion solutions of the cases DH-NEM2 and DH-NEM2+EQV did not change significantly after five global iterations, which entails that the homogenized cross sections are close to the converging values, but the transport operator needs more iterations to converge the local multigroup problem. We conclude then that the convergence rate of the iterative process is more sensitive to the convergence of the local fission source than the convergence of the incoming source.

Case	$\mathbf{k-k_{ref}}$	**RMS**	**N. global iterations**	**Run-Time**
DT-CMFD	k_{ref}=0.97449	ref	12	58 min
DT-CMFD3x3	ref	ref	18	81 min
DT-NEM4+FDR	ref	ref	13	68 min
DH-NEM2+FDR+BB	ref	ref	11	60 min
DH-NEM4+FDR+BB	ref	ref	13	75 min
DH-NEM2+FDR	-21 pcm	0.65%	11	57 min
DH-NEM2+EQV	-35 pcm	0.94%	10	50 min
DH-NEM4+EQV	-35 pcm	1.47%	11	56 min
DH-NEM2	-131 pcm	1.9%	10	50 min
DB2+FDF	-20 pcm	1.7%	0	10 sec
DB2+EQV	-38 pcm	1.9%	0	6 sec
DB2	-104 pcm	2.2%	0	6 sec

Table 5.4. Run-time comparison. All calculations use 40 parallel process.

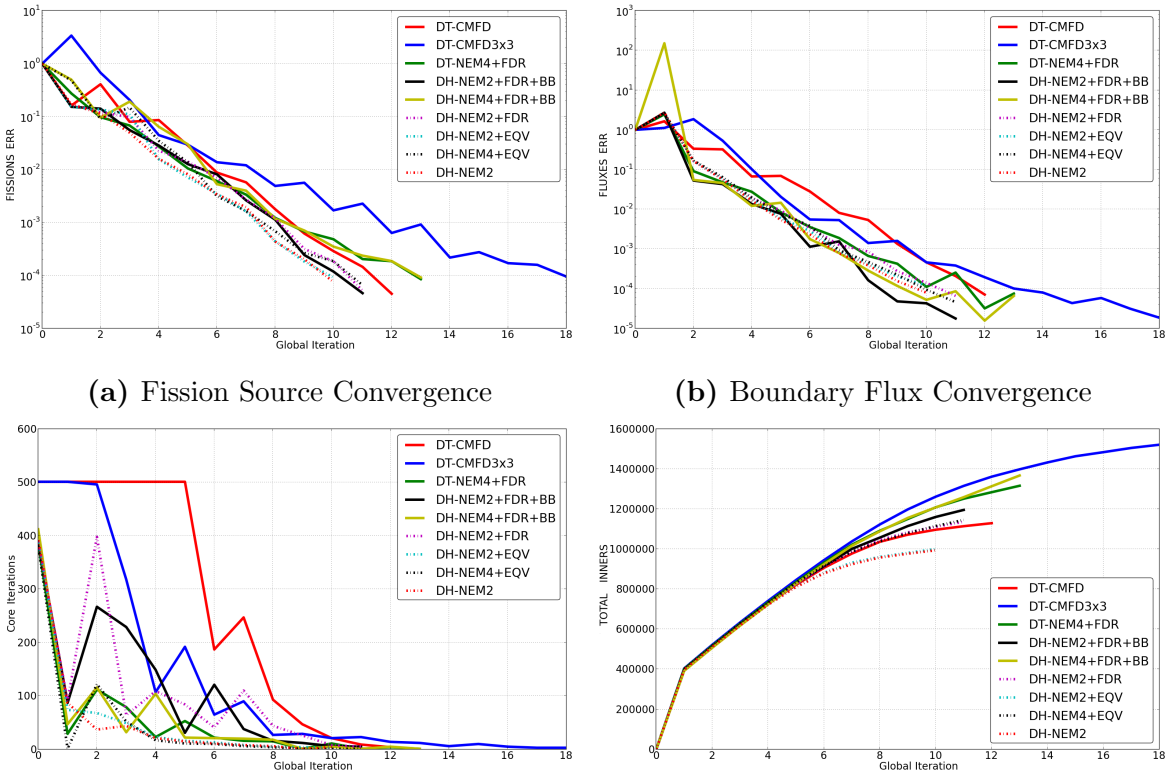

(a) Fission Source Convergence

(b) Boundary Flux Convergence

(c) Core Iterations per Global Iteration

(d) Total Number of Transport Inner Iterations

Figure 5.13. Convergence Properties

5.3.6 Reducing the interface angular information

We also investigated the possibility of simplifying the information transmitted at the boundaries so as to relax the constraints of the iterative process, with the purpose of reducing the number of global iterations and, therefore, the computational cost. We introduced the approximations to the boundary conditions by reducing the level of details of the fine distribution in angle and space of the incoming angular flux in Equation (4.3).

To do that, we considered the case DH-NEM2+EQV, since it showed the lowest number of globals, and imposed an isotropic boundary flux averaged in space per each coarse surface. With the solver options that we used, this results in 1 value per pin side and per group at the assembly interfaces that is transmitted to the neighbors instead of 432 values per cell side and per group. This reduction accounts for 72 directions, 3 sub-surfaces of flux projection over a linear polynomial basis (2 surface moments).

Figure 5.14 shows a comparison of the case DH-NEM2+EQV with and without angular simplification for the boundary source imposed to each assembly problem. The calculation exhibited a RMS of the relative pin power errors of 0.97% instead of 0.94% for the case without approximations at the boundaries, which means that in our configuration the reduction of the surface information do not drastically impact the accuracy of the solution.

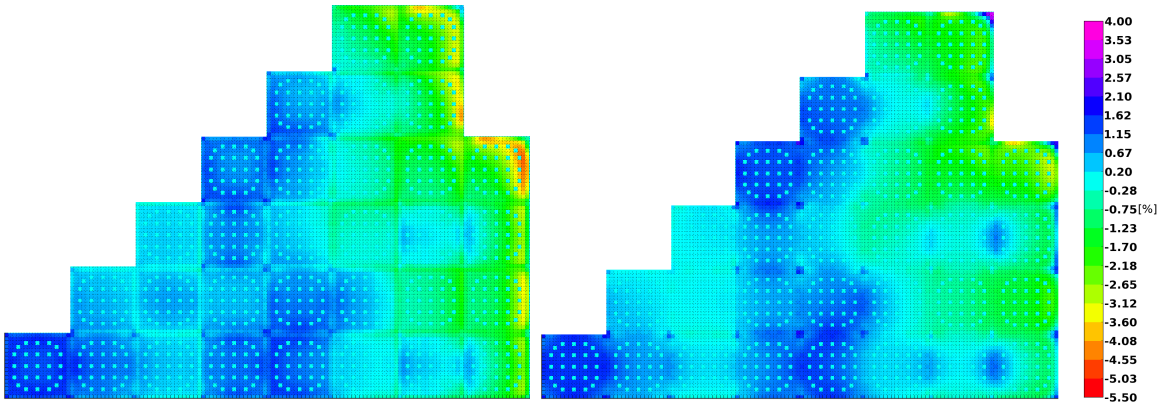

(a) (DH-NEM2+EQV)with DP_0 boundary source
MIN=-4.2%, MAX=1.4%, RMS=0.99%

(b) (DH-NEM2+EQV) with full angular description
MIN=-3.6%, MAX=3.2%, RMS=0.94%

Figure 5.14. Comparison of boundary source with full angular description and DP_0 approximation.

Moreover, the total number of inner iterations was slightly reduced, while the number of global iterations did not change (10 iterations). As already said in the last section, we suppose then that the convergence rate of the iterative process is more sensitive to the fission source than the incoming source. Also, the time required by the MPI exchanges was lesser, since the amount of memory is reduced, but compared to the total run time the gain is negligible. This might also be due to the fact that the MPI messages were sent and received by CPUs of the same node, which otherwise would have required more time.

We conclude that there is no particular interest in reducing the interface angular information of the boundary source transmitted to the neighbors. However, with the method of long characteristics this option could be convenient since the number of values for the interface fluxes depend on the trajectories and could be much larger than in MOSC.

5.3.7 D_{leak} vs $\frac{1}{3\Sigma_{tr}}$

In this section we compare again the two options for the diffusion coefficient that we have considered in Section 5.2.2. However, here we are interested in applying equivalence theory and the FDR technique with $D = \frac{1}{3\Sigma_{tr}}$ in order to verify that, for all homogenization options, the D_{leak} always produces more accurate results.

Figure 5.15 shows a comparison of the two diffusion coefficient for equal homogenization options in DH. The results produced by D_{leak} and presented in the last section are shown again.

The results show that the leakage coefficient halves the RMS of the pin power errors produced by $\frac{1}{3\Sigma_{tr}}$ for the cases with flux-volume homogenization and equivalence theory. In particular, the RMS equals 1.94% and 2.89% respectively for the D_{leak} and $\frac{1}{3\Sigma_{tr}}$ options with flux-volume homogenization, and it equals 0.94% and 1.93% for the equivalence theory case.

For the FDR technique instead, the leakage coefficient still produces better results, but the difference in the RMS of the two options is much lesser and it is equal to 0.65% and 0.74%, respectively for the D_{leak} and $\frac{1}{3\Sigma_{tr}}$ options.

This can be explained by the fact that FDRs adjust the coarse operator so as to reproduce the average RHP net currents given by the local fine-transport problem. The set of six or four FDRs, respectively in a 3D or 2D geometry, is completely defined for a given diffusion coefficient. So the only difference between the two cases resides in the assembly interface currents that are exclusively computed in diffusion with no transport adjustment.

Clearly, the case with Black-Box assembly discontinuity factors is not presented, since the reference solution is exactly reproduced.

We may conclude that particle exchanges between assemblies in the core are better computed with a diffusion coefficient that accounts for the total leakage.

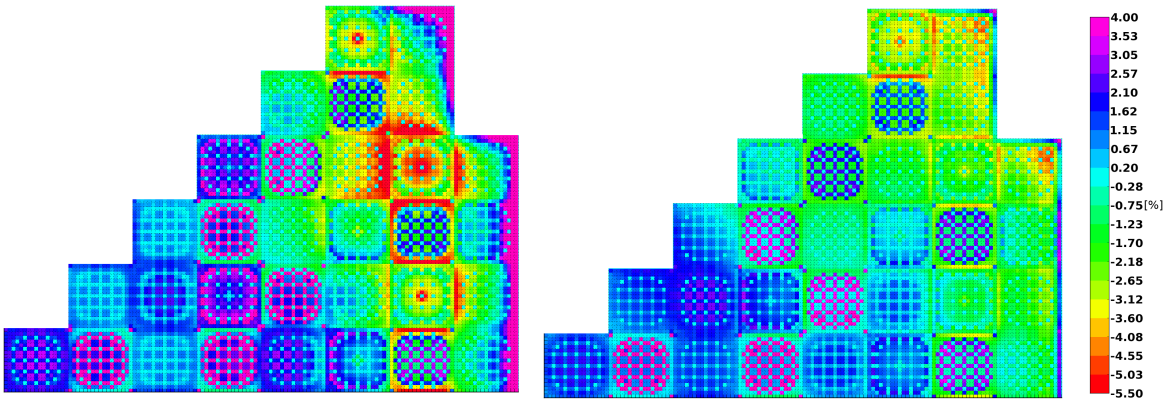

(a) DH-$\frac{1}{3\Sigma_{tr}}$
MIN=-7.1%, MAX=13.0%, RMS=2.89%

(b) DH-D_{leak}
MIN=-4.8%, MAX=5.0%, RMS=1.9%

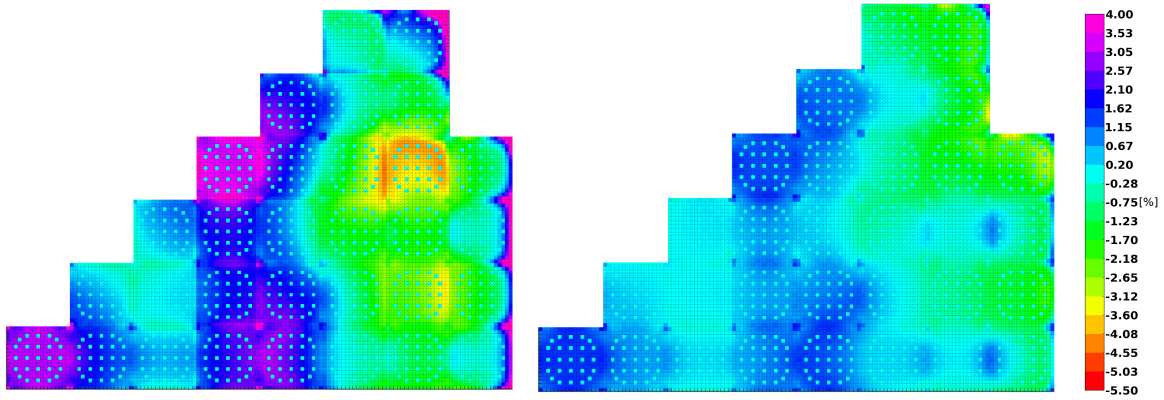

(c) DH-$\frac{1}{3\Sigma_{tr}}$+EQV
MIN=-4.4%, MAX=10.3%, RMS=1.93%

(d) DH-D_{leak}+EQV
MIN=-3.6%, MAX=3.2%, RMS=0.94%

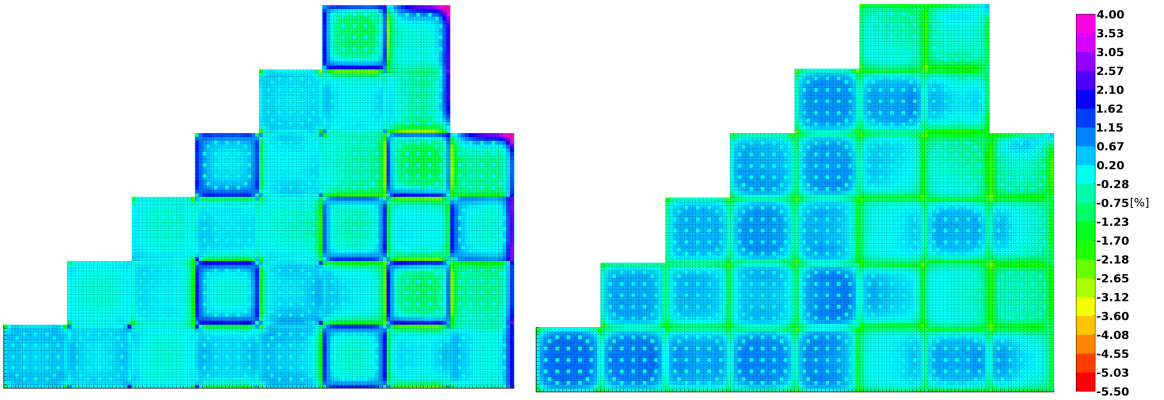

(e) DH-$\frac{1}{3\Sigma_{tr}}$+FDF
MIN=-2.7%, MAX=4.8%, RMS=0.74%

(f) DH-D_{leak}+FDR
MIN=-2.6%, MAX=1.0%, RMS=0.65%

Figure 5.15. Comparison of two diffusion coefficient options in DH with flux-volume homogenization, EQV and FDR.

5.4 Conclusions

In this chapter we have investigated different options for the method of Dynamic Homogenization (DH), and we have applied the method to a core calculation for a two-dimensional configuration. Before incurring to the 3D, with the present 2D analysis we firstly wanted to verify whether the main source of the typical two-step errors is due to the inadequacy of the adjusted low-order operator to describe the physics of the full-core problem, or that of the reference homogenization problem to provide a good approximation for the core flux, or even both. A nuclear reactor is radially more heterogeneous than axially, therefore a diffusion operator can more easily fail. Moreover, for our 2D core calculations 40 processes were sufficient, so they turned in a desktop machine, but a real 3D core calculation would require much more computational resources.

Despite the influence of the environment information accounted at the homogenization stage for the core solution, we studied the applicability and the impact in DH of the two main techniques used to preserve the transport reaction rates: equivalence theory and flux discontinuity ratios. The evidence that comes out from our calculations is that these techniques result to be more effective in DH than in two-step, where the homogenization parameters are affected by the fundamental mode approximation. We also showed how any coarse operator constructed with the flux discontinuity ratios technique can be used as nonlinear acceleration for the full-core transport problem.

For equal homogenization options, DH always shows a better quality of the solution with respect to the classical two-step approach, mainly due to the elimination of the typical error peaks at the interface between assemblies of different types and to the improvement of the reflector response, where two-step easily fails. The RMS of the DH diffusion relative pin power errors is, in fact, 1.9%, 0.94% and 0.65% respectively with flux-volume homogenization option, with equivalence and with flux discontinuity ratios at the interior surfaces of the assembly. The RMS of the diffusion pin power errors for the two-step approach is instead 2.2%, 1.9% and 1.7% respectively for the same aforementioned homogenization options. Note that the pin power errors are calculated with respect to a direct transport calculation considered as reference.

We also explored a coarse mesh homogenization, where the assembly is homogenized in a 3-by-3 grid. Especially for this type of homogenization, the transport flux that is locally available can be directly used to compute the power within the pin. This is a sort of reconstruction of a fine distribution that, in a DH framework, reduces to simply a normalization of the transport solution. This normalization requires the average transport power and the diffusion power to be equal for each coarse mesh. This is possible only if the equivalence or the flux discontinuity ratios in all surfaces are applied. The last case is a nonlinear acceleration, while in the first case the RMS of relative errors of the reconstructed pin power is 1.47%. The higher errors of the coarse homogenization case with respect to the pin-by-pin homogenization arise mainly at the reflector interfaces, which entails that these homogenization options (coarse mesh with equivalence) may not be sufficient to model the reflector response and the inadequacy comes from the nature of the coarse operator.

When the discontinuities are also introduced at the assembly interfaces so as to

preserve the transport net currents in each macro-surface, the diffusion operator reproduces exactly the transport reaction rates, which entails that it can be used to accelerate the convergence of the fission and boundary transport sources. A comparison between CMFD and the parabolic nodal diffusion operator with two-group pin-by-pin homogenization showed comparable transport convergence properties in our configuration. However, the two-group CMFD constructed on coarse spatial mesh is less effective than a quartic nodal diffusion operator with same homogenization options, with a total number of global iterations of 18 and 13 respectively. This is due to the linear flux approximation of the finite difference scheme that might be insufficient to describe the flux gradients everywhere in the core for the mesh size that we considered (an assembly homogenized on a 3-by-3 grid), which ensues that the average flux is not as well predicted as with the higher order flux expansion of the nodal operator.

In 2D configurations the DH method exhibits a convergence rate which is comparable with respect to a direct calculation accelerated by two-group pin-by-pin CMFD. This also means that the calculation run-times are very close. The largest but not appreciable difference is 10 global iterations instead of 12, which results in 50 minutes instead of 58, associated to the DH cases with flux-volume homogenization and equivalence options. Therefore, using the same computational resources than the direct transport calculation, the DH method does not show considerable advantages for 2D configurations in terms of performances.

However, the objective of this analysis was to investigate, above all, that the solution of the DH approach has an excellent agreement in the radial plane with the reference calculation. Moreover, results demonstrate that the choice of a two-group diffusion operator with appropriate homogenization parameters is largely valid for core modeling and design even for highly heterogeneous configurations. We do think that improvements in the performance are promising for the 3D core problem via DH, where no 3D transport computation is needed.

Chapter 6

3D Core Calculation based on Dynamic Homogenization

This chapter is devoted to the application of the method of dynamic homogenization (DH) to 3D core calculations. The first section presents a simplified leakage model that is used to axially couple the 2D transport problems. A discussion on the advanced homogenization techniques and the possibility to compute a fine distribution of the power using the transport solution of the heterogeneous problem follows.

We then analyze two different core problems and compare the two-step, the DH and the direct 3D transport calculations.
The first problem is the one described in Chapter 5, with an extrusion of the 2D radial plane for the whole active length of the core. We call this problem "Axially uniform 3D core", where the only axial heterogeneity takes place at the interface with the axial reflector. The second problem is inspired by the first one, but we partially inserted three banks of control rods in order to test the methodology in a configuration where the axial gradients are dominant. We call this problem "Partially rodded 3D core". The chapter concludes on the accuracy and performance of the Dynamic Homogenization method against two-step and direct 3D transport.

6.1 The RHP for 3D configurations

In this section we examine the Reference Homogenization Problem (RHP) in the context of a 3D core problem solved by the method of Dynamic Homogenization (DH).

In Chapter 5 we have seen that in 2D configurations the DH approach does not show any considerable advantages over Direct Transport (DT) calculations in terms of computational cost and, of course, accuracy. This is explained by the fact that almost all the run-time was spent in solving the transport problems, since they have by far a larger number of degrees of freedom than the diffusion problem. In a 2D core calculation both DH and DT approaches have to solve the same transport problems that have different boundary source but same size. We may claim then that for a 3D core calculation there is no advantage in solving 3D transport problems as RHP with a DH approach, because the computational cost will be comparable to a 3D DT calculation.

As said earlier, one of the most interesting features of the method of Dynamic Homogenization is the possibility to simplify the RHP with respect to the actual situation in the core. It follows that as a matter of performances we choose to solve only 2D transport problems, which make the methodology more attractive.

The 3D core problem is radially decomposed as for a 2D configuration, where the subdomains have fuel and "reflector" assembly size. The axial decomposition instead is imposed by the axial discontinuities of the media, due for instance to temperature gradients, fuel depletion or the presence of core components such as control rods, instrumentation or assembly grids. In any case, each 3D subdomain has an axial height Δz, that can be different for each axial layer, along which the macroscopic radial incoming current has to be averaged for the 2D transport problem as follows:

$$J^{-,\mathrm{C}}(\mathbf{r}_\perp) = \frac{1}{\Delta z}\int_{\Delta z} dz J^{-,\mathrm{C}}(\mathbf{r}_\perp, z), \quad \forall G, \tag{6.1}$$

where we have decomposed the position vector into the radial and axial components $\mathbf{r}_\perp$ and $z\mathbf{k}$, C stands for coarse and G is the macrogroup index.

We now start to consider the RHP presented in Section 4.3, where each transport problem is solved with imposed core eigenvalue computed by the low-order operator, and fixed boundary source normalized so as to preserve the axially averaged macroscopic radial incoming current. Technically, one is free to use the RHP as just discussed also in a 3D DH calculation because the discontinuity of the angular flux at the assembly interfaces guarantees the convergence of the iterative process, but this would involve the following consequences.

First of all, the imposed multiplication constant accounts for the macroscopic axial leakage while the 2D transport calculation has no information in this regard. It follows that the RHP does not consider the influence of the adjacent axial neighbors and that the macroscopic axial leakage would be rather converted in radial leakage by the 2D transport operator in order to preserve the core eigenvalue.

Secondly, when the equivalence theory is applied the average transport reaction rates can be preserved only in the homogenized 2D assembly problem that, according

to the discussion in Section 4.5.1, corresponds to the second problem acting in the equivalence iterative process. Because the 3D core problem has axial leakage, the average reaction rates from transport cannot be preserved by the 3D coarse operator. It would follow that transport and coarse full-core solutions have different power densities in each subdomain. This was also the case for the Flux Discontinuity Ratios (FDR) technique in 2D configurations, as well as in 3D, where the average net interface currents of each subdomain are not necessarily the same in the transport and full-core problems. Moreover, in the case where the FDRs are also applied at the assembly interfaces allowing to avoid a discontinuous angular flux, there is no guarantee that the iterative scheme converges since the imposed eigenvalue may not be consistent with the local transport solution.

Thirdly, this approach can also cause some problems when applying it to the RHP for the axial reflector, where no multiplication occurs and the only source is the incoming flux at the boundaries. The axial reflector computation must then be driven by another type of source coming from the core.

In order to avoid all the aforementioned issues, we decided to include in the reference homogenization problem a simplified axial leakage model that should have some features that we discuss next.
Firstly, the model *i)* should take into account the environment of each subdomain and use the spectral information of the adjacent neighbors. This permits to axially couple the 2D transport calculations of an axial layer with the ones on top and bottom, suggesting that the iterative process must also converge on another quantity that is representative of the axial leakage in a subdomain.
The axial leakage model to be used for the RHP *ii)* should preserve the axial net current computed by the low-order operator. Despite improving the radial response of each subdomain, preserving the macroscopic axial exchanges also allows to apply the aforementioned advanced homogenization techniques so as to obtain the same axially averaged particle balance by both transport and full-core problems, and therefore the same average transport reaction rates. Clearly, as said earlier, this is not the case for the FDR technique applied uniquely to the interior interfaces of an assembly.
Finally, even if the DH methodology allows it, in our first implementation for 3D modelization we chose to adopt a very rough model for the axial leakage, that is simple, robust and avoids the computation of axially dependent solutions, such as in 3D transport, or in 1D as it is done in the 2D/1D Fusion method. This is justified by the interest of avoiding this additional cost and making the methodology more effective.

We now turn our discussion on the construction of the axial leakage model. The latter is based on the transverse nodal approach as in the 2D/1D Fusion method [67, 68] that takes advantage from the axially extruded geometries that are typically found in LWR cores.

Applying the axial-averaging operator $T_k\cdot = \frac{1}{\Delta z_k}\int_k dz\cdot$ to the 3D transport equation:

$$(\mathbf{\Omega}_\perp \cdot \nabla_\perp + \mu\partial_z + \Sigma)\psi(\mathbf{r}_\perp, z, \mathbf{\Omega}_\perp, \mu) = Q, \tag{6.2}$$

where Δz_k is the height of the axial layer k, we get the equation for the axially averaged

angular flux $\psi_k(\mathbf{r}_\perp, \mathbf{\Omega})$:

$$(\mathbf{\Omega}_\perp \cdot \nabla_\perp + \Sigma)\psi_k = Q_k - L_{z_k}, \tag{6.3}$$

with

$$L_{z_k}(\mathbf{r}_\perp, \mathbf{\Omega}) = \frac{\mu}{\Delta z_k}\psi(\mathbf{r}_\perp, z, \mathbf{\Omega}_\perp, \mu)\Big|_{z_k^-}^{z_k^+}. \tag{6.4}$$

In the last equations, $\perp$ stands for radial coordinates, Q includes scattering and fission sources, μ is the cosine with respect to the z-axis and $z_k^\pm$ are the axial coordinates on top $(+)$ and bottom $(-)$ of the axial layer. Note that the group index has been omitted.

Equation (6.3) is a 2D problem whose axial symmetry depends on the transverse leakage source defined in Equation (6.5). In the case of symmetric axial conditions with respect to the centered radial plane of an axial layer, we get $\psi(z_k^+, \mu, .) = \psi(z_k^-, \mu, .)$, so the axial source vanishes and Equation (3.38) becomes a 2D symmetric problem. Moreover, if the antisymmetric components of the entering axial fluxes are identical in absolute value, we get $\psi(z_k^\pm, \mu, .) = \psi(z_k^\mp, -\mu, .)$ and the 2D problem is also symmetric but with a non-zero axial source. In all the other cases, the 2D problem is non-symmetric and requires a full angular expansion. However, we want to take all the advantages of a classical 2D transport calculation, so we symmetrize the leakage source by computing the average as it follows:

$$L_{z_k}(\mathbf{r}_\perp, \mathbf{\Omega}_\perp, |\mu|) \approx \frac{\mu}{2\Delta z_k}\Big[\psi(z, \mu, .) - \psi(z, -\mu, .)\Big]\Big|_{z_k^-}^{z_k^+}, \quad \text{with} \mu > 0\,. \tag{6.5}$$

This is the first approximation that we introduce for the leakage model that allows to perform faster 2D transport calculations.

Note that one would need to symmetrized only the fluxes entering on top and bottom surfaces of the axial layer, because the angular fluxes leaving a symmetric problem are necessarily symmetric. However, we choose to keep Equation (6.5) because the leakage model can produce asymmetric outgoing fluxes, that must then be used for the computation of the leakage source.

At this point, it is common to introduce another approximation which is that of isotropic transverse leakage sources. This leads to a definition this source as a function of only the currents:

$$L_{z_k}(\mathbf{r}_\perp) \approx \frac{1}{4\pi}\int_{4\pi} d\mathbf{\Omega} L_{z_k}(\mathbf{r}_\perp, \mathbf{\Omega}) = \frac{1}{4\pi} J_z(\mathbf{r}_\perp, z)\Big|_{z_k^-}^{z_k^+}, \tag{6.6}$$

where J_z is the net current along the axial direction z defined in each point $\mathbf{r}_\perp$ of the radial plane. This approximation automatically symmetrizes the transverse leakage sources, and consequently the 2D transport problems.

In order to couple the 2D problems one has to compute the axial leakage source using Equation (6.5), which depends on the interface fluxes at the top and bottom of

the axial layer. In the 2D/1D Fusion method this is mediated by solving a set of 1D axial problems, per radial region or per radial pin-cell, that are constructed in a similar fashion than the 2D problems, thus imposing a radial leakage source. As discussed in Section 3.5, in the case where the 1D problem is constructed for the pin-cell, a spatial homogenization is required and further approximations are introduced. In this work, however, we do not apply this strategy.

Another, simpler, way to estimate the fluxes on top and bottom of the axial layer is to approximate the angular behavior of the fluxes exiting the axial layer by the angular behavior of the axially averaged 2D flux in the layer, so that:

$$\psi^g(\mathbf{r}_\perp, z_k^\pm, \mathbf{\Omega}_\perp, \mu) \approx f_k^g(\mathbf{r}_\perp, z_k^\pm)\psi_k^g(\mathbf{r}_\perp, \mathbf{\Omega}_\perp, \mu), \tag{6.7}$$

where $f^g(\mathbf{r}_\perp, z_k^\pm)$ is a shape factor that is defined for each radial region and is group dependent. Because we want to ensure that the 3D core and 2D transport problems have the same macroscopic axial leakage, we compute the shape factor as it follows:

$$f_k^g(\mathbf{r}_\perp, z_k^\pm) = \frac{J_R^{+,C,G}(z_k^\pm)}{J_R^{+,G}\big|_k}, \quad \forall \mathbf{r}_\perp \in R, \quad \forall g \in G, \tag{6.8}$$

where R and G are respectively the coarse surface and the coarse energy group, which are defined by the homogenization process for the low-order operator, where R is also the 2D coarse region of the homogenized problem. Moreover, $J_R^{+,C,G}(z_k^\pm)$ is the axial coarse partial current from the 3D operator exiting the axial layer k, and $J_R^{+,G}$ is the partial axial transport current averaged over the area of R as follows:

$$J_R^{+,G}\big|_k = \frac{1}{V_R}\sum_{g\in G}\int_R d\mathbf{r}_\perp \int_{2\pi} d\mathbf{\Omega}_\perp \int_0^1 d\mu\mu\psi_k^g(\mathbf{r}_\perp, \mathbf{\Omega}_\perp, \mu). \tag{6.9}$$

In the last equation, V_R is the area of the coarse surface R, and the integral over μ can also be applied in $[-1, 0]$ order to compute the bottom outgoing current, if the radial flux has a full angular description. As said before, in our work the angular flux is symmetric with respect to the radial plane, so the average outgoing axial transport current in Equation (6.9) is equal on both top and bottom of the axial layer.

This approximation is equivalent to assuming the angular flux axially constant in each layer, which entails that i tis discontinuous at the interfaces between two axial neighbors. The continuity of the angular flux can be only ensured by a direct 3D transport calculation, and in any dynamic homogenization calculation this property would be lost in any case because of the current normalization from the coarse operator.

The axial leakage source can now be computed using the four "blocks" of concurring fluxes as follows:

$$L_{z_k} = \frac{\mu}{2\Delta z_k}\left[\psi_{k,\text{out}}^{\text{top}} + \psi_{k,\text{out}}^{\text{bot}} - \psi_{k,\text{in}}^{\text{top}} - \psi_{k,\text{in}}^{\text{bot}}\right], \quad \mu > 0, \tag{6.10}$$

where we have omitted the spatial and angular dependency and defined:

$$\psi_{k,\text{out}}^{\text{top}} = \psi_k \frac{J^{+,C}(z_k^+)}{J_k^+}, \quad \psi_{k,\text{out}}^{\text{bot}} = \psi_k \frac{J^{+,C}(z_k^-)}{J_k^+}, \tag{6.11}$$

and

$$\psi_{k,\text{in}}^{\text{top}} = \psi_{k+1} \frac{J^{+,C}(z_{k+1}^-)}{J_{k+1}^+}, \quad \psi_{k,\text{in}}^{\text{bot}} = \psi_{k-1} \frac{J^{+,C}(z_{k-1}^+)}{J_{k-1}^+}. \tag{6.12}$$

Note that since the solution of the coarse operator is axially continuous, it holds:

$$J^{+,C}(z_{k\pm1}^{\mp}) = J^{-,C}(z_k^{\pm}). \tag{6.13}$$

Finally, from Equation (6.12) it is clear that the definition of the angular fluxes on top and bottom that we have introduced allows to couple each axial layer with its neighbors while preserving the macroscopic axial leakage from the coarse operator.

Since at each global iteration the transport and core solutions change, one needs also to introduce an additional stopping criterion for the axial leakage source in order to ensure the convergence of the DH method. To do that we check the following criteria between two successive global iterations l and $l+1$:

$$\left\| \frac{L_{0z,r}^{g,l+1} - L_{0z,r}^{g,l}}{\max\left(|L_{0z,r}^{g,l+1}|, |\Sigma_r^g \Phi_r^{g,l+1}| \right)} \right\|_2 < \varepsilon_z \tag{6.14}$$

where L_{0z} is the angle integrated axial leakage source, ε_z is the tolerance criteria, and $\Sigma_r^g \Phi_r^g$ is the total transport reaction rate in the fine energy group g and region r. Introducing this quantity in the computation of the relative error ensures that the method does not iterate in vain if the leakage source is equal to zero or negligible with respect to the other transport sources.

6.2 Equivalence Theory and Flux Discontinuity Ratios

In this section we discuss how the average transport reaction rates can be preserved by the low-order operator in the 3D core problem.

We have already analyzed the application of the equivalence theory and the flux discontinuity ratios technique to 2D problems in order to preserve the transport reaction rates in Section 3.1.1, so we omit the discussion to construct an equivalent homogenized problem. We consider instead the third problem acting in the equivalent process, which is the full-core problem, and we start our discussion from the balance equations in a subdomain for the fine and the 3D coarse problems, which for a macrogroup G

read:

$$\sum_{S\in\partial D_\perp} A_S\Delta z(J_S^{+,G}-J_S^{-,G})+\sum_{R\in D_\perp}\Sigma_R^{h,G}V_R\Delta z\Phi_R^G=\sum_{R\in D_\perp}V_R\Delta z(Q_R^G-L_{z,R}^G), \quad (6.15)$$

$$\sum_{R\in D_\perp} V_R(J_{z^+,R}^{\mathrm{C},G}+J_{z^-,R}^{\mathrm{C},G})+\sum_{\substack{S\in\partial D_\perp\\ i\in Z}} A_S\mathrm{d}z_i(J_{S,i}^{+,\mathrm{C},G}-J_{S,i}^{-,\mathrm{C},G})+\sum_{\substack{R\in D_\perp\\ i\in Z}}\Sigma_R^{\mathrm{C},G}V_R\mathrm{d}z_i\Phi_{R,i}^{\mathrm{C},G}=\sum_{\substack{R\in D_\perp\\ i\in Z}} V_R\mathrm{d}z_iQ_{R,i}^{\mathrm{C},G}, \quad (6.16)$$

$$Q=H_0\Phi+\frac{1}{\lambda}F\Phi, \quad (6.17)$$

$$Q^{\mathrm{C}}=H_0^{\mathrm{C}}\Phi^{\mathrm{C}}+\frac{1}{\lambda^{\mathrm{C}}}F^{\mathrm{C}}\Phi^{\mathrm{C}}. \quad (6.18)$$

In these equations, we have considered the axial subdomain $D=D_\perp\times Z$ where the radial domain $D_\perp=\cup_R V_R$ and the axial domain $Z=\cup_i\mathrm{d}z_i$, such that $\sum_i\mathrm{d}z_i=\Delta z$, and the boundary $\partial D_\perp$ has been partitioned into a set of macro-surfaces noted S of length A_S. Moreover, C stands for coarse, Q and Q^{C} are the isotropic sources comprising scattering (H_0) and fission (F) as in Equations (6.17) and (6.18) and $J_{S,i}^{\pm}$ are the outgoing ($+$) and incoming ($-$) partial currents crossing the radial surface S, at axial coordinate i where needed. We also note that the balance equations have been obtained by direct integration in angle and energy over the entire 3D geometric domain of the original equations (transport, diffusion, etc.) and express a relation between the cross sections and the solution (fluxes, currents) of the equations constructed with those cross sections. In Equation (6.15) Σ^h is the homogenized total cross section, while Σ^{C} in Equation (6.16) is the coarse cross section that can be either the homogenized one or the equivalent total cross section for the coarse problem. In addition to that, the cross sections $\Sigma_R^{\mathrm{C},G}$ used for the 3D full-core problem are piecewise functions that are constant along an axial layer k of height Δz_k. It is convenient to rewrite Equation (6.16) using axially averaged quantities that are obtained applying the $T_k\cdot$ as follows:

$$\sum_{R\in D_\perp} V_R(J_{z^+,R}^{\mathrm{C},G}+J_{z^-,R}^{\mathrm{C},G})+\sum_{S\in\partial D_\perp} A_S\Delta z(J_S^{+,\mathrm{C},G}-J_S^{-,\mathrm{C},G})+\sum_{R\in D_\perp}\Sigma_R^{\mathrm{C},G}V_R\Delta z\Phi_R^{\mathrm{C},G}=\sum_{R\in D_\perp} V_R\Delta zQ_R^{\mathrm{C},G}, \quad (6.19)$$

where the index i for the axial coordinate has been removed in favor of the average coarse scalar fluxes and currents, similarly to Equation (6.1).

We now use the definition of the axial leakage source defined in our model (Equa-

tion (6.10)) and integrate it in space, angle and energy as follows:

$$V_R \Delta z L^G_{z,R} = \sum_{g \in G} \int_{\Delta z} dz \int_R d\mathbf{r}_\perp \int_{2\pi} d\mathbf{\Omega}_\perp 2 \int_0^1 d\mu \frac{\mu}{2\Delta z} \left[\psi^{g,\text{top}}_{\text{out}} + \psi^{g,\text{bot}}_{\text{out}} - \psi^{g,\text{top}}_{\text{in}} - \psi^{g,\text{bot}}_{\text{in}} \right], \tag{6.20}$$

which, substituting the definitions in Equations (6.11) and (6.12) and using Equation (6.9), simplifies to:

$$V_R \Delta z L^G_{z,R} = V_R \left[J^{+,C,G}_{z^+_k,R} - J^{+,C,G}_{z^-_{k+1},R} + J^{+,C,G}_{z^-_k,R} - J^{+,C,G}_{z^+_{k-1},R} \right] \tag{6.21}$$

and finally, because of the continuity condition of the coarse partial currents according to Equation (6.13) it reads:

$$V_R \Delta z L^G_{z,R} = V_R (J^{\text{C},G}_{z^+,R} + J^{\text{C},G}_{z^-,R}) \tag{6.22}$$

where we have omitted the axial layer index k and used the definition $J = J^+ - J^-$.

Clearly, Equation (6.19) corresponds to the balance equation for a macrogroup G of the 2D homogenized problem, which entails that if the equivalence theory is successfully applied, the 3D full problem reproduces the same average reaction rates of the transport problem. The conditions that assure the equivalence between 2D transport, 2D homogenized and 3D core problems are the following: *i*) the equivalent cross section is axially constant; *ii*) the 2D homogenized problem is solved with homogenized sources from transport, including the axial leakage source; *iii*) the eigenvalue is imposed by the 3D core operator; *iv*) the incoming boundary source of the fine transport and 2D coarse problems is normalized so as to preserve the axially averaged 3D incoming radial current; *v*) the axial leakage source is normalized so as to preserve the total axial net current of the 3D coarse operator.

The FDRs technique requires the same aforementioned conditions in order to achieve the equivalence with the exception of the points *i* and *iv*). Concerning the former, the homogenized cross sections do have to be axially constant in each axial layer, as well as the flux discontinuity ratios in the 3D coarse problem as follows:

$$\text{FDR}^G_{S,i} = \text{FDR}^G_{S,\text{2D}}, \quad \forall i \in Z, \tag{6.23}$$

where S is an interface between two radial regions, and FDR_{2D} is the flux discontinuity ratio computed for the 2D homogenized problem. As discussed in Section 4.6, if the condition *iv*) is used, then the average reaction rates are preserved only in the 2D homogenized problem but not in the 3D full-core problem. One has then to impose the continuity of the angular flux at the radial interfaces between subdomains and, clearly, the preservation of the net transport currents at these interfaces. In the 2D core configuration, this condition led to the particular case where DH becomes a nonlinear acceleration for the full transport problem, because the coarse operator preserves

exactly the homogenized reaction rates. However, in a 3D configuration this is not the case because the transport problem is simplified with respect to the actual problem, and depends on 3D coarse quantities such as the leakage source and the eigenvalue. It follows that the solution of the global problem is necessarily the one given by the 3D low-order operator and the process is a truly dynamic homogenization method. Nevertheless, we can say that the homogenization option that uses FDRs in all radial interfaces, including interior and external surfaces of a fuel of "reflector" assembly, is still a particular case, where the paradigm of the reference homogenization problem (RHP) is no more at the assembly level but it becomes the whole reactor radial plane. It ensues that the quality of the DH solution comes very close to that of the 2D/1D Fusion method.

Despite the model used to compute the axial leakage source, another difference of DH with respect to the 2D/1D Fusion method resides in the fact that the RHP is not solved directly but rather through a domain decomposition method, where the 3D coarse operator partially acts as a nonlinear acceleration for the fission and boundary transport sources of the 2D whole core radial plane problem. We used the term "partially" because the 3D operator is also the one that imposes the axial leakage and the core eigenvalue.

Finally, when the three problems (2D fine transport, 2D homogenized, 3D coarse) acting in the subdomain homogenization process have same average reaction rates per macrogroup and macroregion, the 2D transport solution can be directly used to compute the power within each pin-cell in the core. It follows that the 3D full-core problem and the local transport problem have same coarse power density in each subdomain, which can be directly used to perform a depletion calculation on the fine transport mesh.

6.3 Problem 1: Axially uniform 3D core

The first 3D problem that we have analyzed is inspired by the NEA PWR MOX/UO2 Core Transient Benchmark [74] adopting some simplifications described in Section 5.1 in order to have smaller data library to process. The 3D reactor has an active fuel length of 365.76 cm and the axial reflector is modeled with an axial layer of 20.32 cm containing only water on top and bottom of the core. Since the global core geometry has been constructed by simply extruding a radial plane, we call this problem the "axially uniform 3D core" problem.

6.3.1 Direct 3D transport approach

The transport operator used a macroscopic self-shielded cross-section library in 172 energy groups with transport corrected P_0 scattering. The self-shielding calculation was performed so as to obtain two self-shielding regions for each fuel pin and, subsequently, the effective multigroup cross sections have been averaged for the same fuel pin type. The standalone multigroup discrete ordinates short characteristics solver IDT of the code APOLLO3® [17, 26, 62, 65] was used to produce the 3D reference solution. The source iterations are carried out using the standard transport sweep, the two-group CMFD operator is used as nonlinear acceleration for the global iterations and the Boundary Projection Acceleration (BPA) for the inners. A S_8 level symmetric quadrature formula was adopted for the angular discretization and the linear characteristics expansion for the spatial representation of the angular flux. Each 3D heterogeneous Cartesian cell has a size of 1.26x1.26x2.54 cm^3 where 1.26 cm is the pin pitch, and each surface has been subdivided into nine sub-surfaces of same area (three subdivisions for each axis) for the projection of the surface angular fluxes.

In order to use less computational resources and because of the core symmetry in the radial plane, we computed one height of the 3D full problem. The latter is also symmetric with respect to the centered radial plane, but we run the calculation for the whole height of the reactor for code validation.

The total number of 3D regions is equal to $5.9\,10^6$, in each of which the angular flux is represented with 4 spatial moments, 80 discrete directions for the angle integration and 172 energy groups. The angular source is isotropic with transport corrected cross sections. The surface angular flux is projected onto 54 sub-surfaces of the 3D Cartesian cell (9 in each side), with 3 spatial moments in each. The CMFD operator which serves as nonlinear acceleration for the transport sources is obtained with a pin-cell homogenization, resulting in $1.8 \cdot 10^6$ regions and 2 energy groups for the coarse flux representation.

The machine used for our calculations was the Intel® Xeon® Broadwell/2.4 Ghz processor of the "Centre de Calcul Recherche et Technologie" (CCRT) at CEA, where each node has 28 cores with a memory of 128 GB.

The reference calculation was performed in a MPI framework decomposing the global domain into 6240 subdomains and using the same number of cores. No shared memory parallelism was used for our calculations. The geometrical domain was decomposed as follows: for a radial plane each assembly was divided into a 3x3 grid

of subdomains with a size of 6, 5 and 6 pin-cells respectively, while the axial height was 20.32 cm resulting in 8 pin-cells on the axial direction. The maximum number of 3D heterogeneous Cartesian cells for one subdomain was then 288. We refer to this reference case as DT-CMFD.

The stopping criteria of the iterative process introduced in Section 4.4 were set to: $\varepsilon_\lambda = 10^{-5}$, $\varepsilon_\mathrm{f} = 10^{-4}$ and $\varepsilon_\psi = 10^{-4}$.

The 3D reference power distribution per each pin-cell is shown in Figure 6.2 while Figures 6.1a and 6.1b show respectively the axially and radially integrated powers. The normalization is performed such that the average power per unit cell (in 3D, 2D or 1D respectively) equals one.

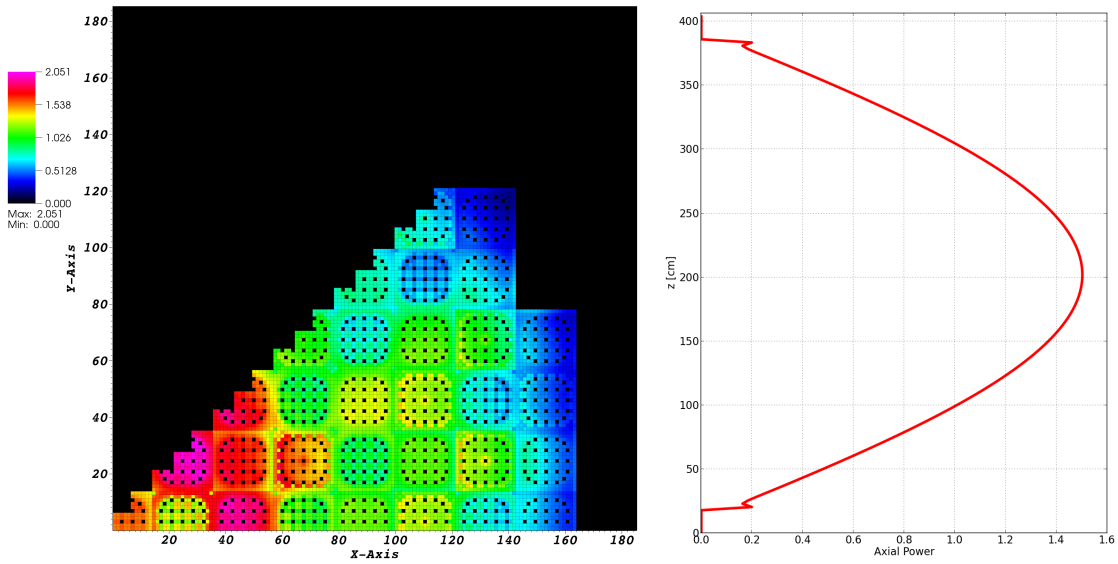

(a) Radial power **(b)** Axial power

Figure 6.1. Axially (a) and Radially (b) integrated reference power distribution normalized such that the average power over the pin-cells equals one.

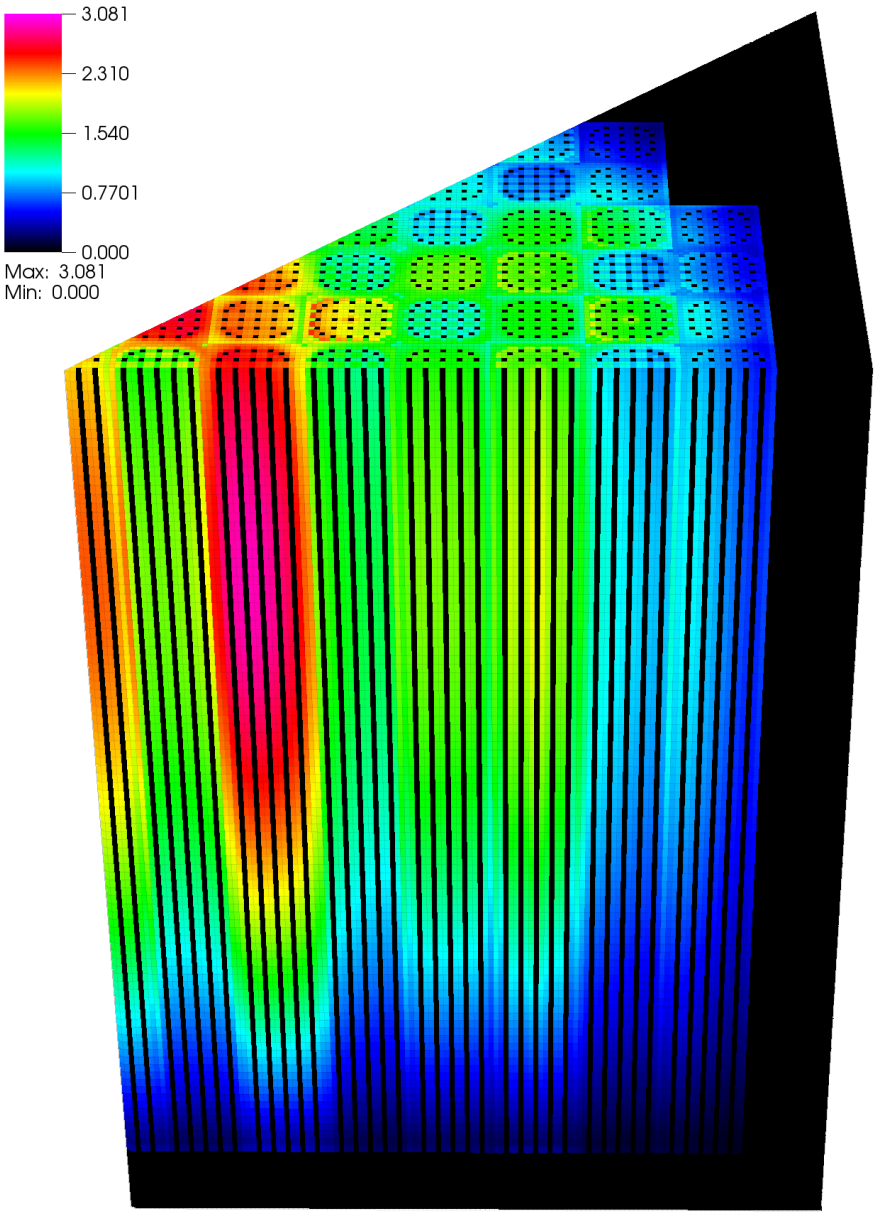

Figure 6.2. 3D Reference power distribution normalized such that the average power per pin-cell equals one. For a better representation, the core geometry has been cut at the height $z = 260$cm.

6.3.2 Dynamic Homogenization approach

For the DH calculations, we used the same transport operator in 2D described in Section 6.3.1 which is based on the IDT solver. The transport solution is locally accelerated by BPA for the inners and by CMFD for the outers, which uses the multigroup structure of transport. The number of local (per subdomain) outer iterations was fixed to one.

We remind the reader that in our analysis the leakage source is always symmetrized with respect to the radial plane, as discussed in Section 6.1. A preliminary analysis was performed to study the influence of the radial anisotropy of the leakage source. We observed that the accuracy of the diffusion solution was not affected at all by the angular representation of the leakage source. On the other hand, the highly detailed angular information increases the run-time of the calculation because the computation of the directional source requires more floating operations. Therefore, for all the cases that we shall present for our analysis we set the axial leakage source isotropic and defined per each fine transport region and energy group.

The only exception to this option is at the interfaces between axial neighbors that use different 2D transport geometries. In this case, we average over the pin-cell the outgoing fluxes on top or bottom of the axial layer. This simplification arises for instance at the interface between the axial reflector and the fuel assembly. We also run a calculation where the 2D transport geometry of both axial reflector and fuel assembly was the same, with the only difference of containing different media (the axial reflector contains water only). The accuracy of the solution was not affected by this specification, and we decided to use a 17x17 grid for the 2D transport geometry of the axial reflector in order to reduce its size and perform faster calculations. In addition, this is consistent with the source representation in the 3D direct transport calculation.

The stopping criteria of the iterative process are those previously used for the DT calculation, plus $\varepsilon_z = 10^{-4}$ as introduced in Section 6.1.

The total number of 2D transport regions is equal to $0.74 \cdot 10^6$, in each of which the angular flux is represented with 3 spatial moments, 40 discrete directions for the angle integration and 172 energy groups. The angular source is isotropic with transport corrected cross sections. The surface angular flux is projected onto 12 sub-surfaces of the 2D Cartesian cell (3 in each side), with 2 spatial moments in each. These solver options are consistent with those used for the DT calculation.

The energy homogenization is performed from 172 to 2 macrogroups and we applied the nodal diffusion as coarse operator. The diffusion coefficient in the fuel assemblies is equal to the leakage coefficient resulting from the homogeneous leakage model that corresponds to the imposed reactor eigenvalue, while in the reflector it is equal to $\frac{1}{3\Sigma_{tr}}$. We explored two types of spatial homogenization: the pin-by-pin and the coarse mesh.

With pin-by-pin homogenization we applied the parabolic nodal diffusion operator (NEM2), since in the 2D core configuration we checked that the spatial mesh was fine enough. We did not use the finite difference scheme because we observed in the 2D configuration that the fixed point iterations used for the search of the equivalent cross sections showed much slower convergence rate than that of NEM2. With finite differences, it was possible to reach the 10^{-4} pin-wise precision in reaction rates only by

sub-meshing the pin-cells. Moreover, the NEM2 operator also allows to use a smaller number of pin-cells with larger axial size. In our calculations, the axial size of the diffusion mesh was equal to 2.54 cm which is consistent with the CMFD operator in the DT calculation.

We recall here that this type of spatial homogenization provides a detailed power distribution per pin, such that the impact of different homogenization options will be analyzed by comparing the pin power distributions against the reference. Here, the diffusion solutions will be presented with the following options: a homogenization using only the flux-volume weighting (DH), the one with equivalence (DH+EQV), using flux discontinuity ratios at the interior surfaces (DH+FDR), and also with the Black-Box discontinuity factors at the external surfaces (DH+FDR+BB), which is the case where the RHP in DH becomes the whole reactor radial plane as discussed in Section 6.2. As for the CMFD problem in the reference calculation, the NEM2 diffusion problem size results in $1.8 \cdot 10^6$ regions in each of which 7 spatial moments are required for the coarse flux representation and 2 energy groups.

The coarse mesh homogenization is performed on a three-by-three spatial grid per assembly, where the assembly subdivision is done such that to divide the 17 pin-cells in a row into groups of 5, 7 and 5 pins. In this type of homogenization, we applied the quartic nodal diffusion operator (NEM4) and the axial size of the diffusion mesh was equal to 6.77 cm so as to obtain a diffusion subdomain with 3x3x3 meshes. It follows that the NEM4 diffusion problem size results in 21600 regions in each of which 13 spatial moments are required for the coarse flux representation and 2 energy groups.

For the comparison purposes, we are allowed to compute the pin power distribution with the aid of the local transport solution, only if the coarse operator preserves the transport reaction rates in each coarse spatial mesh. For this type of spatial homogenization, we considered then only the option with flux discontinuity ratios applied to all the coarse radial surfaces (DH-NEM4+FDR+BB), as the EQV option did not give satisfying results in the 2D core configuration presented in Section 5.3.4. Note that the computed pin-wise power distribution can be compared only in average for each axial layer.

For all the aforementioned DH cases, we decomposed the domain into 800 subdomains which have the size of a fuel assembly, and we run the calculations with the same number of cores on the same machine at CCRT that was used for the DT calculation. We decided to use this DDM because our code considers each subdomain a separate RHP, and we wanted each subdomain to be an assembly paradigm. In the DT calculation, this was not possible for memory and run-time requirements.

6.3.3 Two-step approach

The two-step calculation scheme is considered only in its pin-by-pin homogenization variant, since for the comparison, a coarse mesh homogenization would require a power reconstruction technique, whose study and comparison was not the objective of this work. We adopted the NEM2 diffusion operator as in DH, with the same spatial and energy discretization. To homogenize the cross sections we applied the same transport operator as for the other approaches and, in order to have a consistent comparison, we forced the homogeneous critical leakage model to reproduce the reference core eigen-

value that is $k_{\text{eff}} = 0.96821$. As in the DH approach, the diffusion coefficient in the fuel assemblies was equal to the leakage coefficient determined by the homogeneous leakage model, while in the reflector it was equal to $\frac{1}{3\Sigma_{tr}}$.

One of the important points in the two-step scheme, as discussed in Section 3.3, is the reflector homogenization because it requires a separate calculation. For this analysis we used the same set of homogenized cross sections obtained with the four-motif model described in Section 5.3.3. Moreover, for the axial reflector the homogenized water cross section that was used is the one obtained from the motif 1 (see Figure 5.8), since the assembly UOX-20GWd/t is the most frequent in the core.

Like we did for DH, in order to show the impact of each homogenization technique on the final solution we considered the following cases: leakage model only (DB2), leakage model with equivalence (DB2+EQV) and leakage model with Flux Discontinuity Factors (DB2+FDF). Note that for the latter we used the acronym FDF and not FDR because the discontinuities are introduced in all surfaces including the assembly interfaces, where we applied the GET definition. Moreover, for the reflector assemblies no FDFs were applied. We recall the reader that the FDFs in the radial vertical surfaces are the same along the axial layer, while on the axial direction they were set to one as in DH.

The diffusion calculations of the two-step cases were also performed via DDM with equal decomposition of the DH calculations and same number of cores (800).

6.3.4 DH vs DB2

In order to compare the classical and DH calculation schemes against a 3D reference calculation, we decided to observe different types of relative errors and the root mean square that we shall define. The first one is a 3D distribution of the relative error per pin-cell computed as follows:

$$e(i,j,k) = \frac{P(i,j,k) - P_{\text{ref}}(i,j,k)}{P_{\text{ref}}(i,j,k)}, \qquad \text{RMS}_{\text{3D}} = \sqrt{\frac{\sum_i \sum_j \sum_k e^2(i,j,k)}{N_p}}, \tag{6.24}$$

where i, j and k are the coordinate indexes of the pin-cell, and N_p is the total number of 3D pin-cells with non-zero power. We then define the RMS of the axial power errors per pin as follows:

$$\text{RMS}_{\text{1D}}(i,j) = \sqrt{\frac{\sum_k e^2(i,j,k)}{N_k}}, \tag{6.25}$$

where N_k is the number of pin-cells in the axial direction that have non-zero power. Finally, in order to see the axial behavior of the solution, we define the MAX and the RMS of the relative pin power error per radial plane as follows:

$$\text{MAX}_{\text{2D}}(k) = \|e(:,:,k)\|_\infty, \quad \text{RMS}_{\text{2D}}(k) = \sqrt{\frac{\sum_i \sum_j e^2(i,j,k)}{N_{ij}}}, \tag{6.26}$$

where we used the symbol ":" in order to indicate that the search range is on the whole radial plane, and N_{ij} is the number of pin-cells in the radial plane with non-zero power. Note that unless specified, the error $\mathrm{MAX}_{\mathrm{2D}}$ is by definition always positive.

For calculation comparisons we used the ensemble of the criteria as just presented in order to put in evidence which zone in the core is more sensitive to the limits of each approach with different options.

Figure 6.3 shows the root mean square of the axial power errors per pin ($\mathrm{RMS}_{\mathrm{1D}}$) respectively for the two-step and DH approaches, applying flux-volume homogenization only, the equivalence and the flux discontinuity factor techniques. The same quantity for the DH cases with Black-Box discontinuity factors at the interfaces between assemblies is presented in Figure 6.4 for the cases with pin-by-pin (NEM2) and coarse mesh (NEM4) homogenization options. Note that in the NEM4 case, the pin power per axial layer is computed using the local transport solution. Figure 6.5 shows instead the MAX and the RMS of the relative pin power error per radial plane for all the solutions with pin-by-pin homogenization.

First of all, for both DH and the two-step approaches we can clearly see that the choice of a homogenization option that adjusts the low-order operator, such as EQV or FDF, does globally improve the solution of the two-group diffusion operator. This is particularly true for local phenomena like the strong absorption in the fresh UOx assemblies containing IFBA. However, it must be clear that there is no guarantee that an equivalence technique always improves the solution everywhere in the core, because the distribution of the reaction rates determined by solving the RHP can be very different from the actual one in the core, so forcing the low-order operator to reproduce it is not always advantageous.

In the two-step scheme, the EQV and FDF options give results of same quality with an $\mathrm{RMS}_{\mathrm{2D}}$ of nearly 2% and a $\mathrm{MAX}_{\mathrm{2D}}$ around 5.5% in the interior part of the core. Clearly, the efficacy of these techniques are limited by the fundamental mode assumption that not always provides realistic homogenization parameters. As expected, the highest errors are found close to the radial and axial reflectors, with a maximum of 11% at the corner between the two. Some other error peaks are found because of the absence of the environment information in the model, such as the UOx-MOx interfaces, but also for the UOx-UOx interfaces with different burnup. In particular, the fresh UOx assemblies containing IFBA in positions B1, D1, E2 and D3, which belong to the interior part of the core, show a sensitivity to the environment influence with a maximum $\mathrm{RMS}_{\mathrm{1D}}$ between 3% and 4%. On the other hand, in DH the errors introduced by the infinite lattice approximation at the interfaces between different types of assembly were eliminated and the maximum $\mathrm{RMS}_{\mathrm{1D}}$ with the EQV and FDR options remains lower than 2%, that typically arises in the corner pins of the assemblies in the inner part of the core. However, as observed for 2D configurations, the DH-EQV case particularly suffers at the peripheral area, which suggests that the technique is not sufficient to properly reproduce the radial reflector response. As a result of this, the power of the diffusion operator is redistributed in such a way that the assembly in the center of the core at position A1 exhibits higher errors. The FDRs instead, a more robust technique that is particularly effective for the reflector response, totally eliminates these discrepancies.

The main difference between the cases DH-FDR and DH-FDR+BB resides in the

fact that the radial transport solution is continuous, which entails that the errors at the assembly interfaces are totally wiped out. This is the case also for the DH-NEM4-FDR+BB calculation which differs from the pin-by-pin case DH-FDR+BB only in the coarse mesh and, therefore, on the spatial representation of the leakage source. The latter in fact is computed using Equation (6.10) with a shape factor that is constant in a larger coarse region for the DH-NEM4-FDR+BB calculation. This means that in this configuration the leakage model and the coarser discretization for the low-order operator does not affect the accuracy of the global solution, and it might even improve the solution as we shall discuss.

Figure 6.6 shows the $\mathrm{MAX_{2D}}$ and $\mathrm{RMS_{2D}}$ of the relative error of the average pin power in axial layer, that has been computed by simply averaging the solution of the pin-by-pin cases along Δz, or using the local transport solution in the coarse mesh case. The response of the axial reflector results to be better reproduced in the DH-NEM4-FDR+BB case because the $\mathrm{RMS_{2D}}$ of the top and bottom axial layer in the core is close to one. It ensues that the solution is globally more accurate, thus it exhibits a lower $\mathrm{RMS_{1D}}$ as shown in Figure 6.4.

As a first analysis, we may conclude that all the cases for both approaches show their maximum discrepancies at the interface with the axial reflector, that is justified by the following reasons. In the two-step calculations, we did not employ any model for the homogenization of the axial reflector and we used the same two-group cross sections for the water that we obtained by the radial reflector models. However, the errors in the interior part in the core are in agreement with the analysis that we performed for the 2D core calculations, thus the solution in this zone of the reactor does not show a sensitivity on the axial reflector cross sections. In the DH framework instead, the RHP for the axial reflector is probably not the best one that one can adopt, because the diffusion operator uses axially constant cross sections which should be weighted by a flux that experiences strong gradients. Nonetheless, we think that the accuracy of the solution is definitely acceptable for this region in the core where the power is much lower.

Finally, the most remarkable fact that we did not observe in 2D core calculations, is that in the dynamic homogenization framework the equivalence theory is not sufficient to improve the overall quality of the diffusion solution with respect to the two-step approach. The $\mathrm{RMS_{2D}}$ in the core center is not the same that we obtained in a 2D calculation. This might be justified by the additional bias that is introduced by an inadequate axial reflector response.

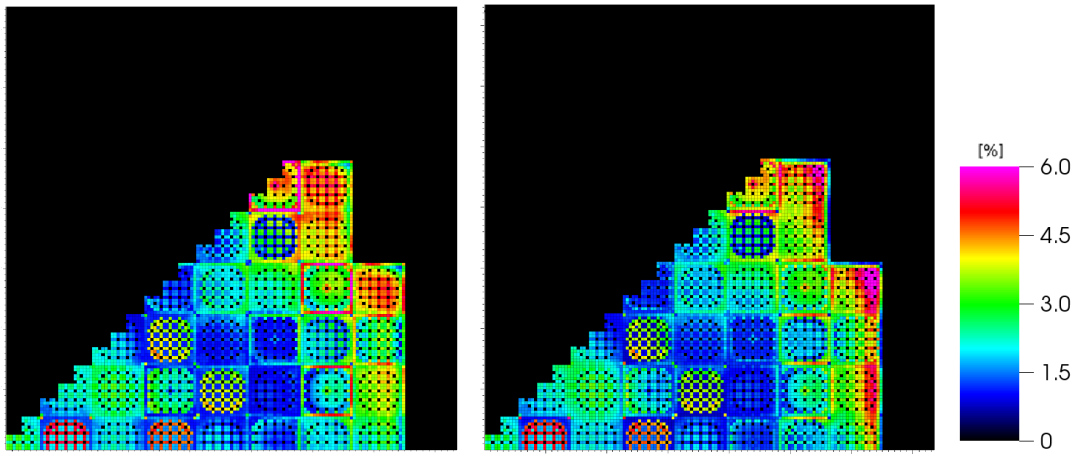

(a) Two-step: leakage model only (DB^2) $\max(RMS_{1D}) = 7.2\%$

(b) Dynamic homogenization (DH) $\max(RMS_{1D}) = 7.0\%$

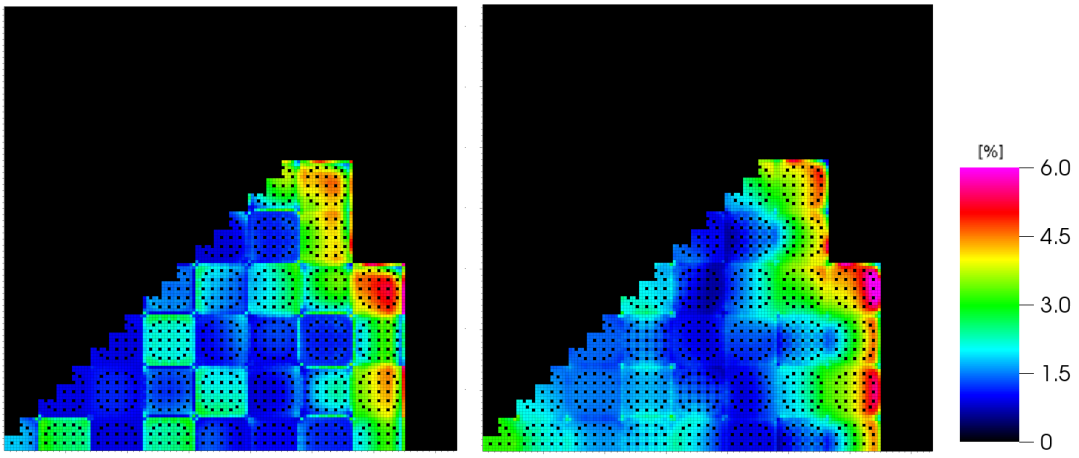

(c) Two-step: leakage model with equivalence (DB^2+EQV) $\max(RMS_{1D}) = 6.0\%$

(d) Dynamic homogenization with equivalence (DH+EQV) $\max(RMS_{1D}) = 6.5\%$

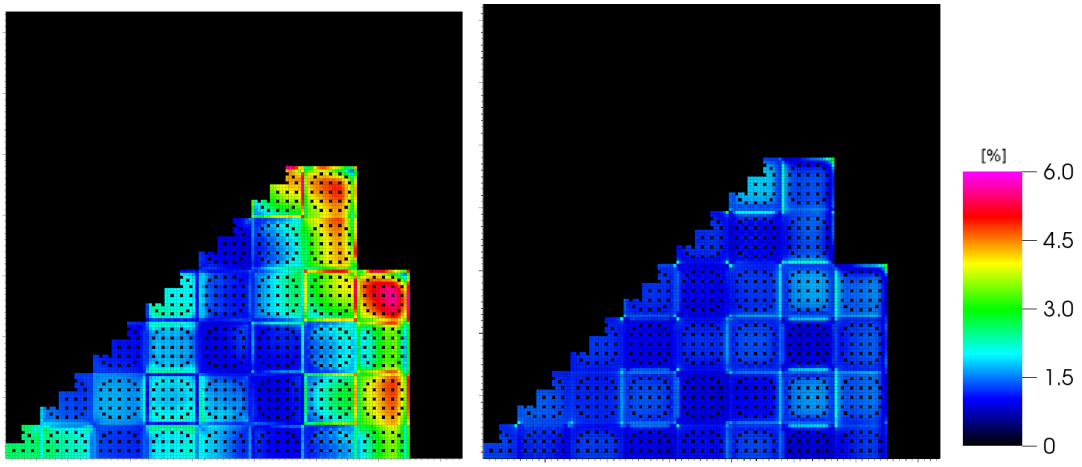

(e) Two-step: leakage model with flux discontinuity factors (DB^2+FDF) $\max(RMS_{1D}) = 5.7\%$

(f) Dynamic homogenization with flux discontinuity ratios (DH+FDR) $\max(RMS_{1D}) = 3.1\%$

Figure 6.3. Root mean square of axial power errors per pin (RMS_{1D}) for problem 1, as defined in Equation (6.25). For each case we have given the maximum value.

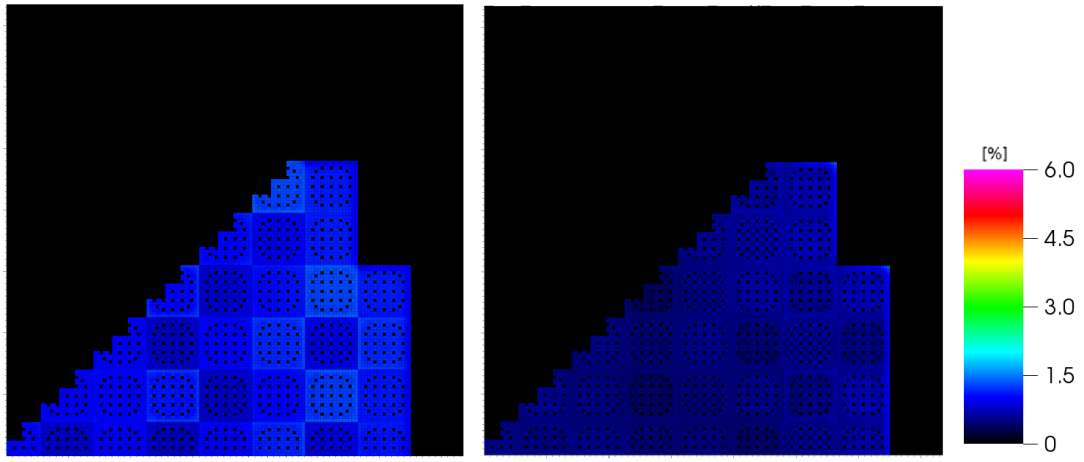

(a) Pin-by-pin homogenization and NEM2 diffusion operator (DH+FDR+BB) $\max(\text{RMS}_{1D}) = 1.38\%$

(b) Coarse mesh homogenization and NEM4 diffusion operator (DH-NEM4+FDR+BB) $\max(\text{RMS}_{1D}) = 1.33\%$

Figure 6.4. Root mean square of axial power errors per pin (RMS_{1D}) for problem 1, as defined in Equation (6.25), for the cases of Dynamic homogenization with flux discontinuity ratios and BB factors at the assembly interfaces. The coarse mesh homogenization result is based on the pin power computed with the local transport solution.

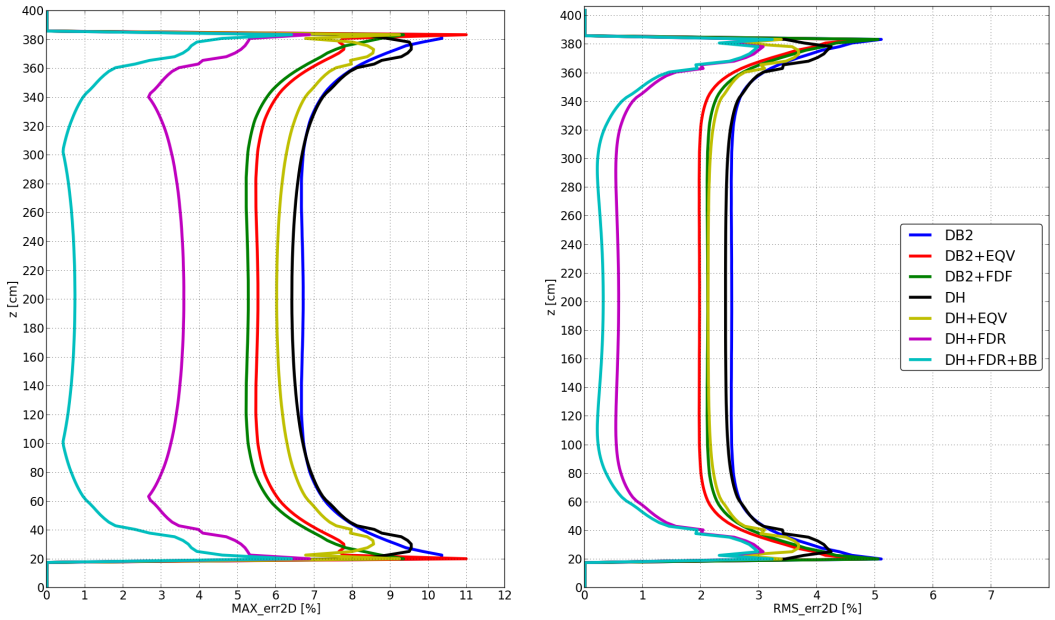

(a) MAX_{2D}

(b) RMS_{2D}

Figure 6.5. MAX and RMS of the relative pin power error per radial plane for all the solutions with pin-by-pin homogenization for problem 1. (The legend is used once for both figures).

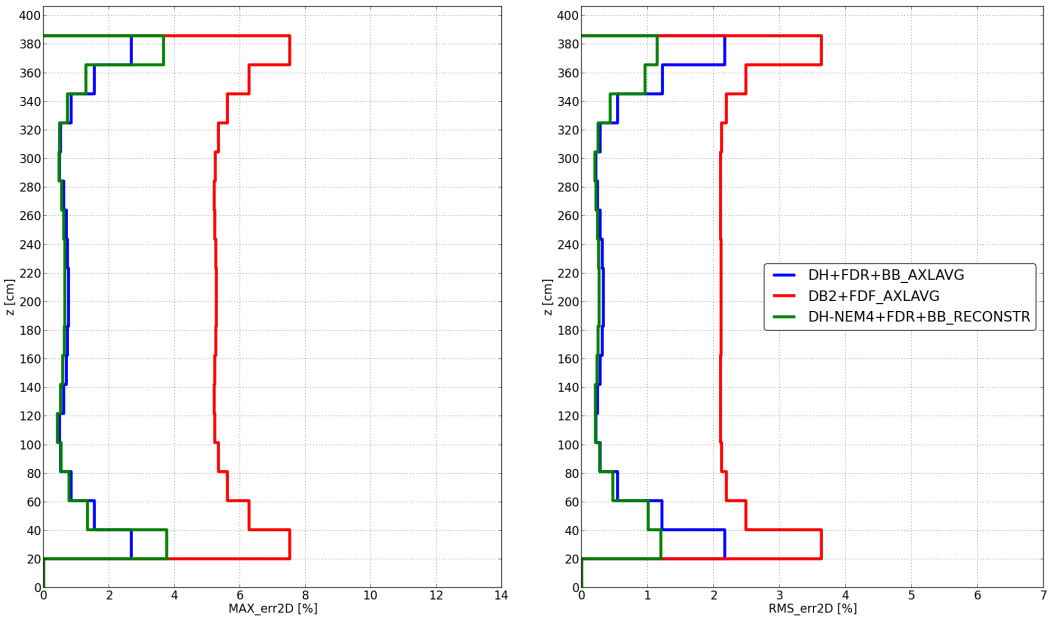

(a) MAX_{2D} **(b)** RMS_{2D}

Figure 6.6. MAX and RMS of the relative error of the average power per pin and per axial layer for problem 1. The latter has been computed by averaging along the axial layer the solution of DH+FDR+BB and DB2+FDF, while using the local transport solution in DH-NEM+FDR+BB. (The legend is used once for both figures).

6.3.5 Performance comparison

We now analyze with global parameters the accuracy and the computational cost of each calculation for the axially uniform core problem. Table 6.1 shows the difference of the core eigenvalue with respect to the reference DT calculation, the $\mathrm{RMS_{3D}}$ computed according to Equation (6.24), the range of the 3D relative pin power errors and the number of global iterations for each case. In the particular case of coarse homogenization, we considered the 3D errors that are defined per pin and per axial layer (20.32 cm of height) that are obtained with the local transport solution. The best solution is the one given by DH-NEM4+FDR+BB for the reasons explained in Section 6.3.4. All the two-step cases and the DH cases without FDRs show similar accuracy with an $\mathrm{RMS_{3D}}$ above 2%. As expected, the cases with flux-volume homogenization option are the least accurate.

It ensues that in order to improve the two-group diffusion solution, the environment information is not sufficient and one should rather use the flux discontinuity ratios technique to obtain an $\mathrm{RMS_{3D}}$ of 1.4% in the case DH-NEM2+FDR and of 1.0% in the case DH-NEM2+FDR+BB. We remind the reader that these values are computed with pin-cells of size $1.26 \times 1.26 \times 2.54\mathrm{cm}^3$.

Since the reference calculation has been performed with a different number of CPUs and the computational cost is proportional to the number of employed CPUs and the whole calculation run-time, in order to compare the performances of the different approaches we have used a Figure Of Merit (FOM) defined as follows:

$$\mathrm{FOM} = \frac{\#\mathrm{CPU}_{\mathrm{ref}} \times RT_{\mathrm{ref}}}{\#\mathrm{CPU}_{\mathrm{case}} \times RT_{\mathrm{case}}}, \tag{6.27}$$

where RT stands for Run-Time. This definition of FOM does not take into account the accuracy of the solution, but we wanted to separate the two types of information because the applicability of two different approaches is not necessarily the same. Moreover, we consider the $\mathrm{RMS_{3D}}$ as a global parameter to compare the accuracy of each method.

It is worth to point out that in order to avoid inconsistencies for performance comparisons against the DH and the two-step approaches, we also tried a different domain decomposition for the reference calculation, where the subdomains had the assembly size and therefore the number of CPUs was equal to 800 instead of 6240. However, this calculation could not fairly be compared because of the following reasons. Firstly, the calculation run-time was too long for the time limits of the service required by the computing center, so storing the 3D flux and recovering it for another run could have compromised the number of global iterations, and therefore the whole run-time.

Secondly, since our code did not use shared memory parallelism, the 28 CPUs of a node were supposed to compute 28 3D subdomains of the assembly size. However, the ensemble of these assembly problems required a memory storage that was much higher than a single node capacity, and we were obliged to adopt a "depopulation" parallel strategy, where four cores for each subdomain were not used at all in the calculation just to free up the memory space for the other cores. It followed that the computational

cost of the reference calculation would have been biased by this non-optimal strategy, and we rather preferred to reduce the size of the subdomains in order to take all the advantages of the available computational resources.

Table 6.2 shows the whole run-times of each calculation and the percentage of the time elapsed in transport and diffusion. The remaining fraction is mainly due to the MPI transport exchanges and processors waiting, while the homogenization has a negligible cost with respect to the whole run-time.

Clearly, regardless of the homogenization option, what really makes the difference in terms of computational cost is: *i*) the absence of transport calculations in the two-step approach; *ii*) in DH the 2D transport calculations are the main tasks of the overall run-time (around 80%); *iii*) the 3D transport calculations in DT. The homogenization options in DH slightly change the convergence properties of the iterative process and the difference in the run-time is essentially due to the different number of global iterations.

As we observed in 2D configurations, the coarse mesh homogenization case cuts the diffusion cost down because of the lesser number of degrees of freedom, but the iterative process requires more global iterations in order to converge the fine-transport fission and boundary sources.

For the two-step cases, we did not include the time required for lattice calculation, as we performed it the full assembly problem. However, for the interested reader we report this information in Table 6.2.

We shall conclude that in average DH was 200 times less expensive than a direct 3D transport calculation.

Case	$\mathbf{k-k_{ref}}$	$\mathbf{RMS_{3D}}$ [%]	e [%] **range**	**# globals**
DT-CMFD	k_{ref}=0.96789	ref	ref	23
DH+FDR+BB	14 pcm	1.0	$-4.5 \div 6.4$	15
DH-NEM4+FDR+BB	14 pcm	0.57*	$-3.8^* \div 0.6^*$	18
DH+FDR	3 pcm	1.4	$-5.8 \div 6.9$	16
DH+EQV	-48 pcm	2.4	$-8.5 \div 9.2$	22
DH	-121 pcm	2.7	$-9.5 \div 8.3$	13
DB2+FDF	-13 pcm	2.4	$-9.3 \div 3.1$	0
DB2+EQV	-31 pcm	2.3	$-11 \div 3.6$	0
DB2	-96 pcm	2.8	$-10.3 \div 6.1$	0

Table 6.1. Global comparison for problem 1. The symbol "*" means that the value has been computed per pin and per axial layer using the local transport solution.

Case	# CPUs	Run-Time	Transport	Diffusion	FOM
DT-CMFD	6240	13.67 h	74%	21%	1
DH+FDR+BB	800	29.1 min	80%	16%	220
DH-NEM4+FDR+BB	800	34.4 min	90%	0.48%	186
DH+FDR	800	30.8 min	80 %	16%	207
DH+EQV	800	37.7 min	74%	14%	170
DH	800	26.5 min	82%	14%	241
DB2+FDF	800	3.6 min	(4.6 min)	100%	1761
DB2+EQV	800	3.5 min	(4.7 min)	100%	1837
DB2	800	3.5 min	(4.5 min)	100%	1837

Table 6.2. Performance comparison for problem 1. The time elapsed in transport and diffusion is expressed as a percentage of the whole run-time. For the two-step cases, the time spent in transport includes a full assembly lattice calculation with leakage model and homogenization.

6.4 Problem 2: Partially rodded 3D core

The second 3D problem that we analyzed is the same core described in Section 6.3.2 with three controlled assemblies where the rods are inserted at half height of the core. We call then this problem the "partially rodded 3D core" problem. We are interested in this analysis because we believe it is a good scenario to test the limits of the axial leakage model that we have introduced in the RHP for 3D calculations. We have inserted the control rods in the assemblies at positions A1, C1 and E5 that are indicated with a black circle in Figure 6.7 and correspond to the Control Rod Banks A and D of the NEA Benchmark [74].

All the calculations that we run for this problem have the same solver options and flux discretization that we used for the axially uniform core problem described in Section 6.3, so we shall omit here this discussion. However, it is worth to stress the fact that for the two-step calculations we used the same homogenized reflector cross sections of problem 1, and in the fuel assemblies we forced the leakage model to reproduce the reference eigenvalue of 0.96331. The 3D reference power distribution per each pin-cell

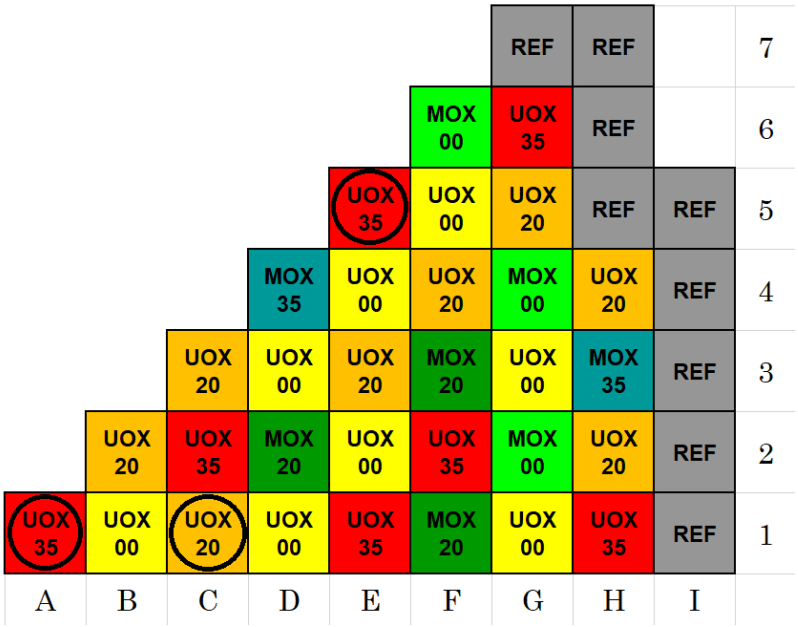

Figure 6.7. Partially rodded core layout [74].

is shown in Figures 6.9 and 6.10 normalized such that the average power over the pin-cells equals one. The first figure shows a vertical section of the geometry, while the second one a diagonal section so that the three controlled assemblies are shown.

Figures 6.8a and 6.8b show the power distribution on the radial planes at heights of 260cm and 140cm respectively, which are located in the rodded and unrodded parts of the core. Figure 6.8c shows the radially integrated power distribution.

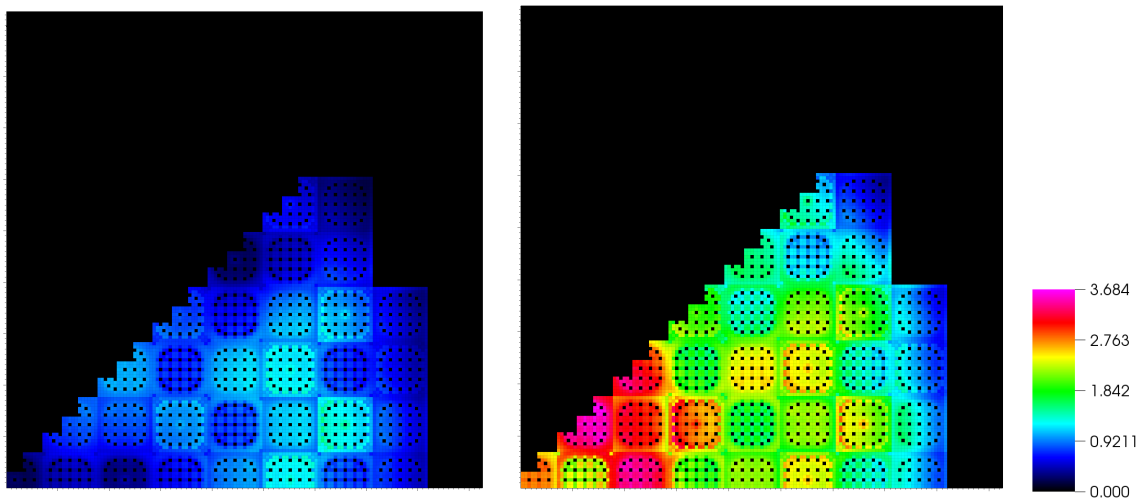

(a) Rodded part **(b)** Unrodded part

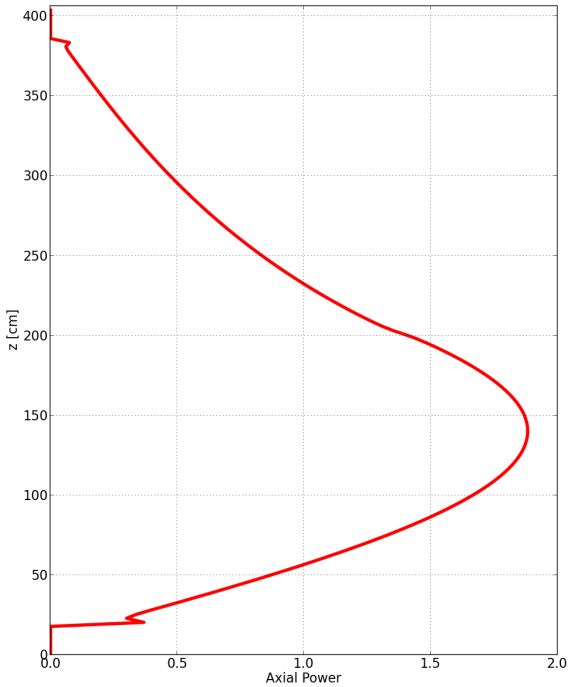

(c) Axial power

Figure 6.8. Radial power distribution on the (a) top (rodded) and (b) bottom (unrodded) parts of the core. The two radial planes are located at a height of 260cm and 140cm respectively for the top and bottom core parts. (c) Radially integrated reference power distribution such that the average power per unit cell equals one.

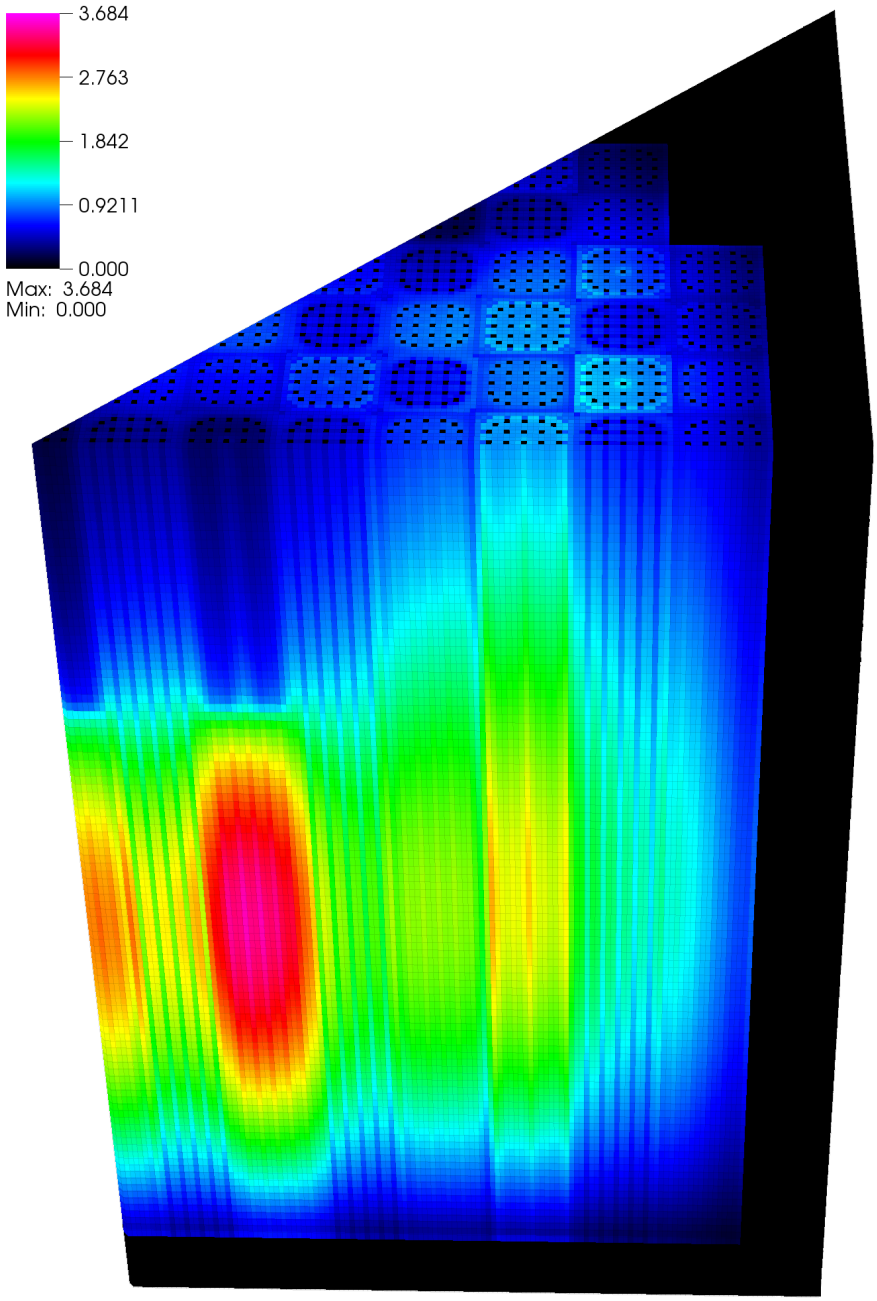

Figure 6.9. 3D Reference power distribution normalized such that the average power per pin-cell equals one. For a better representation, the core geometry has been chopped at the height $z = 260$cm.

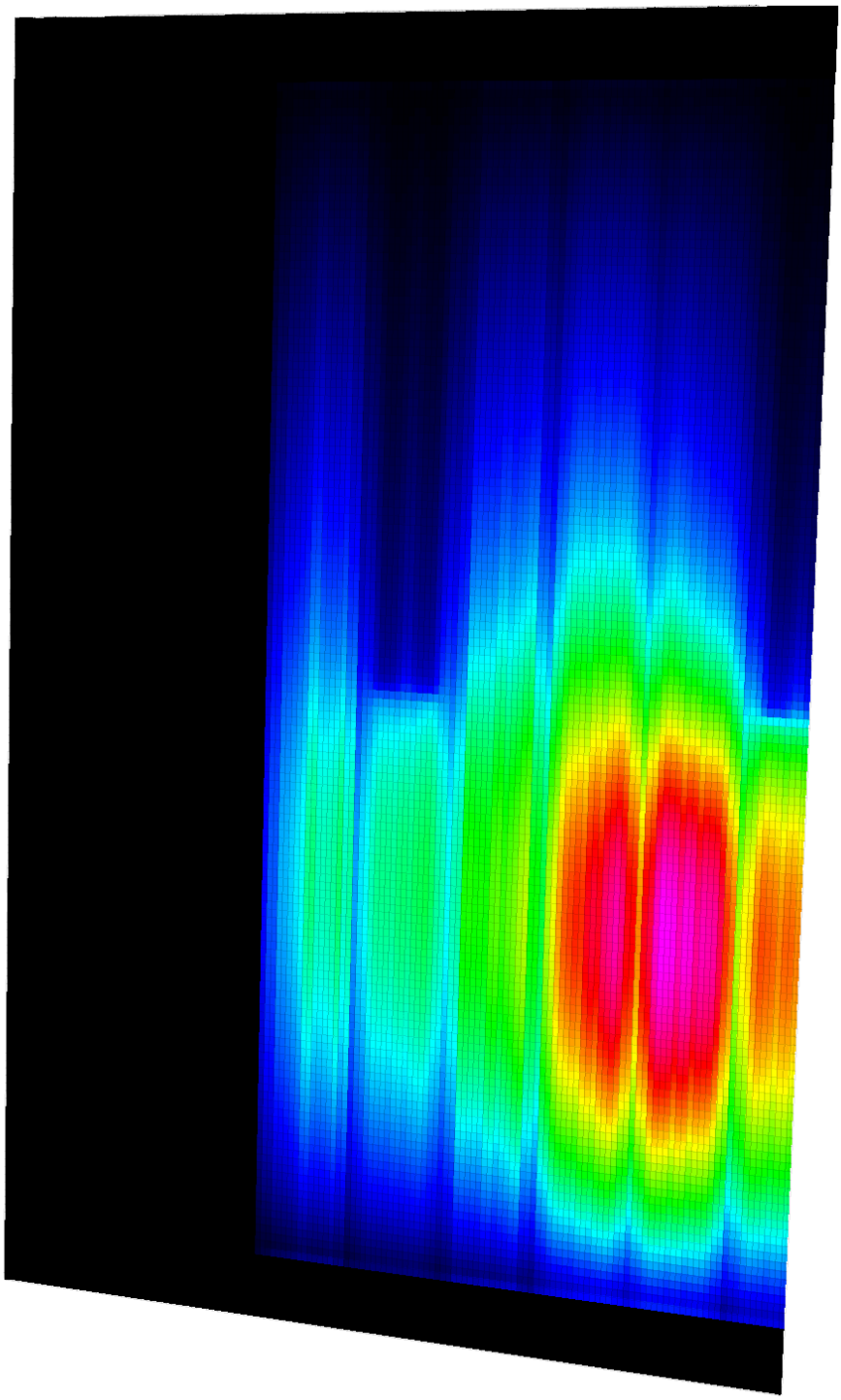

Figure 6.10. 3D Reference power distribution normalized such that the average power per pin-cell equals one. In this figure the core geometry has been cut through the diagonal plane. Same legend scale as Figure 6.9.

6.4.1 DH vs DB2

For this comparison we shall use the same definitions of MAX and RMS given in Section 6.3.4.

Figure 6.11 shows the root mean square of the axial power errors per pin (RMS_{1D}) respectively for the two-step and DH approaches, applying flux-volume homogenization, the equivalence and the flux discontinuity factors techniques. Note that the cases with flux-volume homogenization option have a different scale for a better interpretation of the errors.

The RMS_{1D} for the DH cases with Black-Box discontinuity factors at the interfaces between assemblies is presented in Figure 6.12 with pin-by-pin (NEM2) and coarse mesh (NEM4) homogenization options. As said earlier, in the last case the pin power per axial layer is computed using the local transport solution. Figure 6.13 shows instead the MAX and the RMS of the relative pin power error per radial plane for all the solutions with pin-by-pin homogenization.

The most remarkable behavior is that both DH and the two-step approaches do not predict well the reference solution when only the flux-volume homogenization option is used. The maximum relative errors in absolute value are -29.7% and -26.5% for the DH and DB2 cases respectively, that are found at the interface with the axial reflector. The MAX_{2D} and RMS_{2D} for these cases have the tendency to increase from the center plane of the core to the axial reflector on top of the core. It follows that the radial environment information is of little help in this configuration, and the errors introduced by the coarse discretization of the diffusion operator are largely more important.

On the other hand, when the equivalence theory and the flux discontinuity factors are applied, we observe a totally different behavior of the solution, where the RMS_{2D} keeps constant along all the top or bottom part of the core and reaches its maxima at the axial reflector interfaces. This suggests that EQV and FDFs techniques improve the solution of the 3D diffusion operator both radially and axially.

The RMS_{2D} of the cases DB2+EQV and DB2+FDF in the unrodded part of the core has increased with respect to the axially uniform core problem, and this can be justified by the presence of stronger gradients and a different axial bottom reflector response for which the homogenized cross sections are not representative. This is certainly the case of the axial top reflector.

The solution given by the dynamic homogenization with equivalence theory option results to be more penalized by the axial and radial reflector homogenization rather than the control rods. This can be seen by the values of RMS_{1D} in Figure 6.11, which are lower in the controlled assemblies than the two-step cases.

The best scenarios are given by the dynamic homogenization approach with flux discontinuity ratios. The radial solution of the cases DH+FDR and DH+FDR+BB, in fact, exhibits no considerable sensitivity by the presence of the control rods, as shown in Figure 6.11 where the RMS_{1D} in the controlled assemblies remains lower than 1.3%. Excluding the axial reflector interfaces, the local maximum errors are found inside the axial layers above and below the control rod discontinuity. In particular, the rodded axial layer has a positive maximum relative error of less than 4%, and the pin-cell power in the unrodded axial layer is underestimated by at most 2%. Figure 6.13 shows only the absolute values of the errors, but for a deeper analysis the reader is directed

to Appendix B, where seven assemblies with different environments and characteristics are analyzed more in detail.

We now turn our attention to the coarse mesh homogenization option in DH. Figure 6.14 shows the MAX_{2D} and the RMS_{2D} of the errors per pin and per axial layer. This type of homogenization (DH-NEM4+FDR+BB) still produces a slightly better axial reflector response with respect to the pin-by-pin case DH+FDR+BB, but at the control rod discontinuity it does not. Figure 6.12 clearly shows that the controlled assemblies are the most sensitive in DH-NEM4+FDR+BB, but the RMS_{1D} is not larger than 1.20%. The maximum error on the average pin power in the axial layer is found for both cases in the rodded part, with a MAX_{2D} equal to 2.5% and 3.8% respectively for the DH+FDR+BB and the DH-NEM4+FDR+BB cases. This is the pin power density that could be used for core depletion calculations, while the two-step solution introduces in the same axial layer a maximum bias of 9% as shown in Figure 6.14.

The less accurate prediction at the control rod discontinuity of the case DH-NEM4+FDR+BB with respect to DH+FDR+BB can be justified by the coarser discretization of the low-order operator that provides the shape factors for the axial leakage source. On the other hand, the improved pin power distribution at the axial reflector interface of the former over the latter remains unexplained.

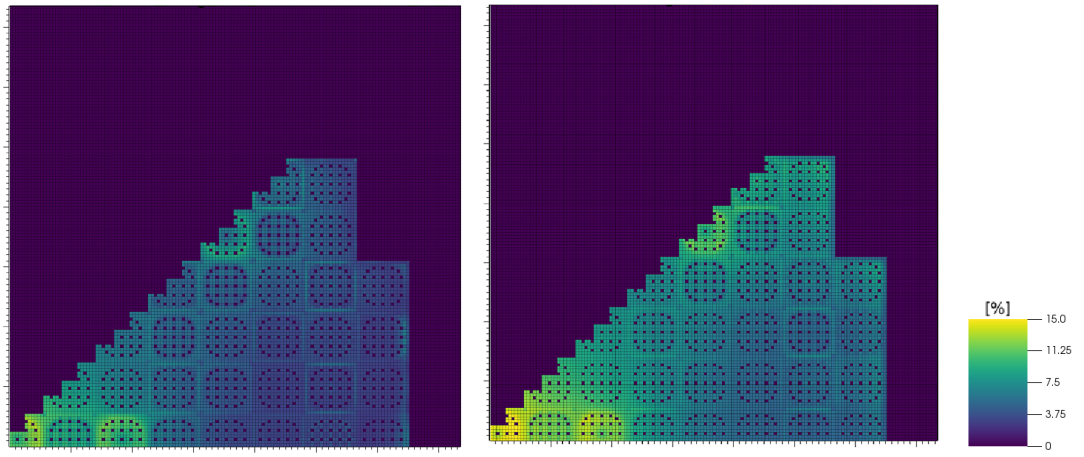

(a) Two-step: leakage model only (DB^2) $\max(RMS_{1D}) = 13.5\%$

(b) Dynamic homogenization (DH) $\max(RMS_{1D}) = 16\%$

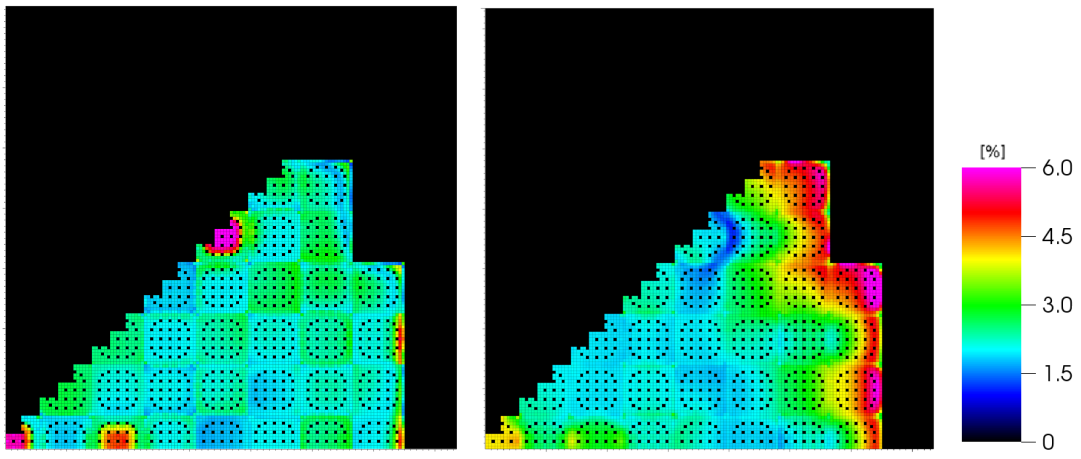

(c) Two-step: leakage model with equivalence (DB^2+EQV) $\max(RMS_{1D}) = 6.9\%$

(d) Dynamic homogenization with equivalence (DH+EQV) $\max(RMS_{1D}) = 6.9\%$

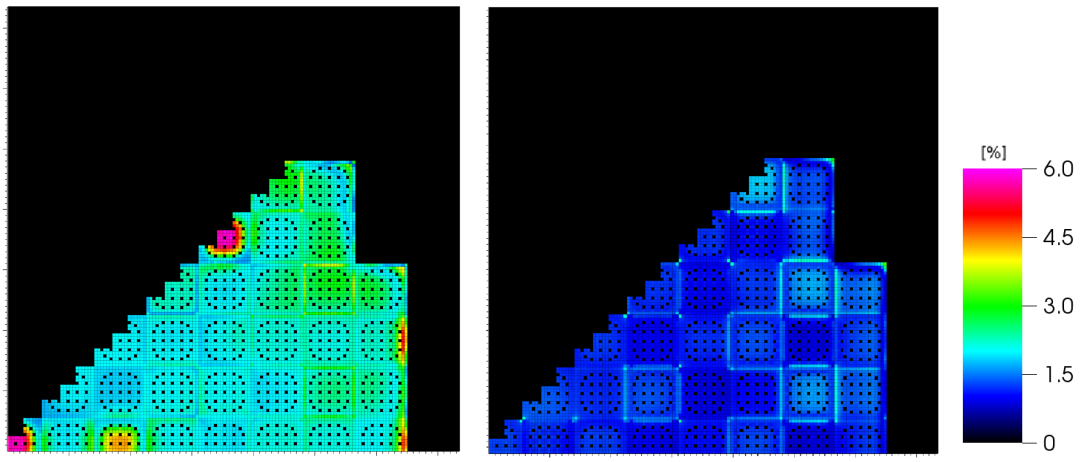

(e) Two-step: leakage model with flux discontinuity factors (DB^2+FDF) $\max(RMS_{1D}) = 5.9\%$

(f) Dynamic homogenization with flux discontinuity ratios (DH+FDR) $\max(RMS_{1D}) = 3.2\%$

Figure 6.11. Root mean square of axial power errors per pin (RMS_{1D}) for problem 2, as defined in Equation (6.25). For each case we have given the maximum value.

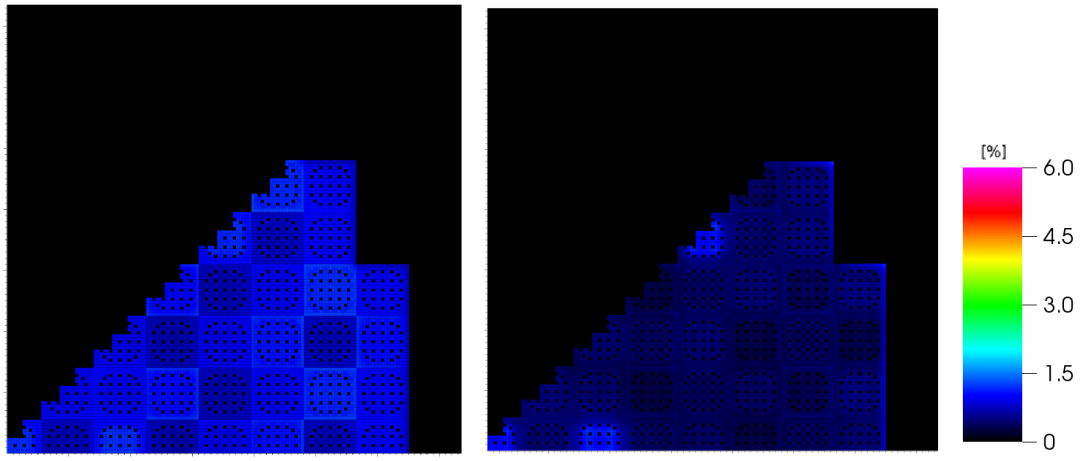

(a) Pin-by-pin homogenization and NEM2 diffusion operator (DH+FDR+BB) $\max(\text{RMS}_{1D}) = 1.28\%$

(b) Coarse mesh homogenization and NEM4 diffusion operator (DH-NEM4+FDR+BB) $\max(\text{RMS}_{1D}) = 1.20\%$

Figure 6.12. Root mean square of axial power errors per pin (RMS_{1D}) for problem 2, as defined in Equation (6.25), for the cases of Dynamic homogenization with flux discontinuity ratios and BB factors at the assembly interfaces. The coarse mesh homogenization result is based on the pin power computed with the local transport solution.

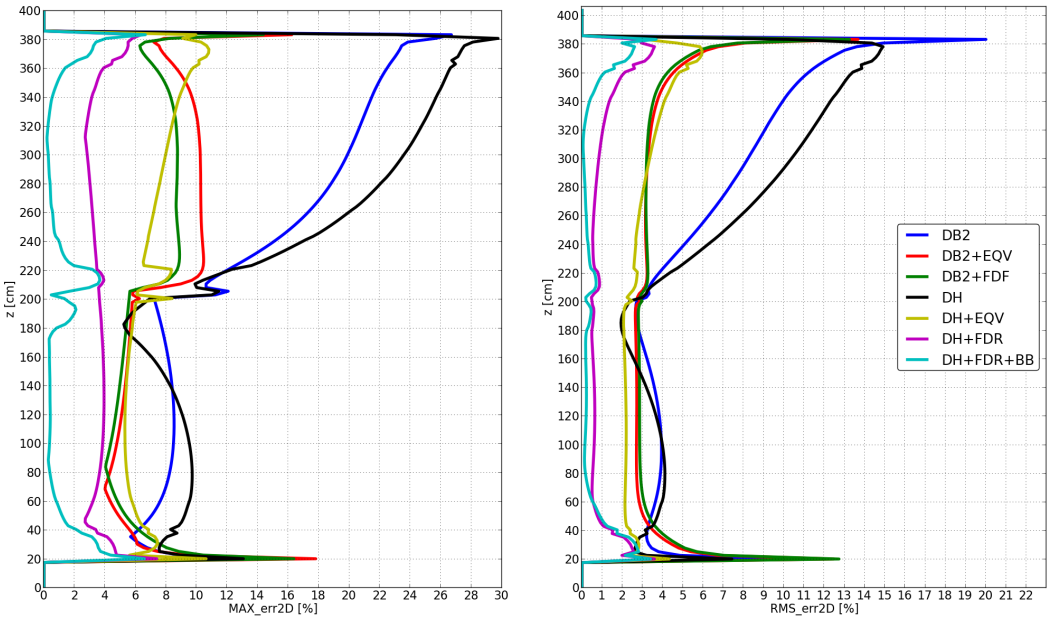

(a) MAX_{2D}

(b) RMS_{2D}

Figure 6.13. MAX and RMS of the relative pin power error per radial plane for all the solutions with pin-by-pin homogenization for problem 2. (The legend is used once for both figures).

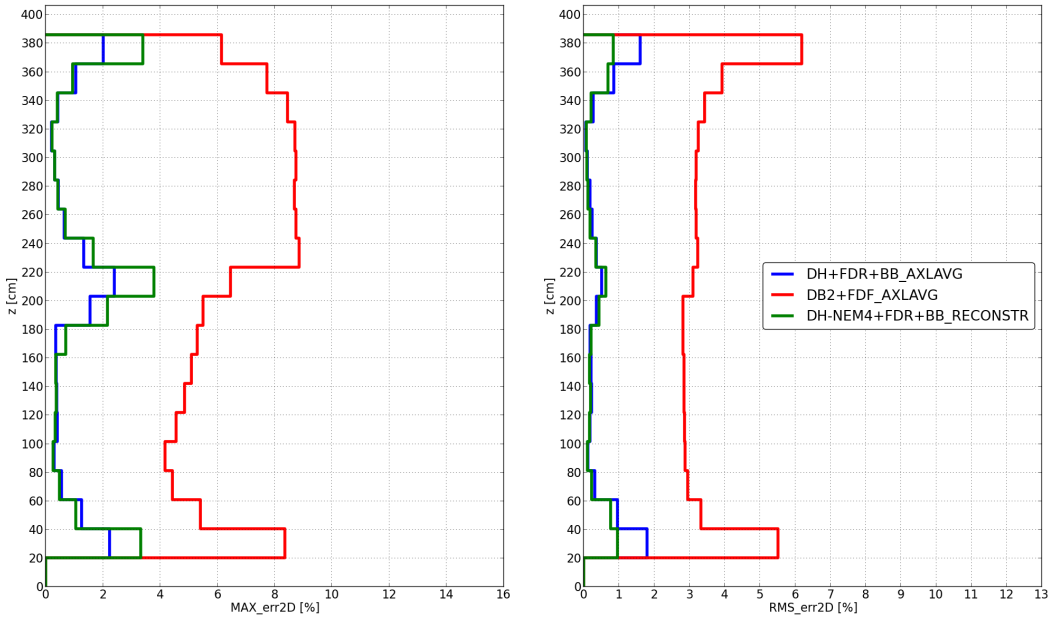

(a) $\mathrm{MAX_{2D}}$ **(b)** $\mathrm{RMS_{2D}}$

Figure 6.14. MAX and RMS of the relative error of the average power per pin and per axial layer for problem 2. The latter has been computed by averaging along the axial layer the solution of DH+FDR+BB and DB2+FDF, while using the local transport solution in DH-NEM+FDR+BB. (The legend is used once for both figures).

6.4.2 Performance comparison

Table 6.3 shows the global parameters for problem 2. With respect to the axially uniform core problem, the results do not show globally any particular difference in terms of accuracy for the DH approach with flux discontinuity ratios option. The differences in the core eigenvalue and the $\mathrm{RMS_{3D}}$ have in fact similar values. Also the 3D relative errors have a comparable range that is dictated by the simplified model for the axial reflector homogenization. All the other cases show instead larger errors, particularly the flux-volume homogenization cases where the $\mathrm{RMS_{3D}}$ has a factor of around 2.5 with respect to problem 1.

All the calculations, including the reference, require more global iterations to converge than the axially uniform core problem, which can be explained by the presence of stronger gradients in the power distribution. It ensues that the computational cost of all the approaches in this configuration is higher. The percentage of time elapsed in the transport and diffusion solvers keeps practically unchanged with respect to problem 1 but the figure of merit does not.

The DH calculations have an average FOM equal to 150 instead of 200, while for the two-step cases in average equals 750 instead of 1800. The reason why the two-step calculations are more penalized than DH is the following. The former must converge once for the eigenvalue problem to the desired precision on the fission sources and multiplication constant. On the other hand, in DH there is no need for that because the 3D diffusion calculation is repeated at each global iteration, and if the homogenization parameters are not close to the convergence values, it can be time-

consuming to perform more diffusion power iterations than necessary. It follows that in all DH calculation we limited the number of diffusion power iterations to 100.

In problem 2, for instance, the case DB2+FDF performed a total of 1200 diffusion power iterations in order to converge, while the case DH+FDR+BB performed a total of 1800 diffusion power iterations, although the diffusion solver was called 21 times. Clearly, in the last 6 global iterations, the diffusion solver converged with a decreasing number of power iterations, since its solution gets closer and closer to convergence at each global iteration. Note that our nodal diffusion solver did not use any acceleration or preconditioning method for the inner, thermal or outer iterations.

We also observed that for problem 2, DH with coarse mesh homogenization and flux discontinuity factors converged with one global iteration less than pin-by-pin homogenization option with flux discontinuity factors (20 and 21 respectively), that is a different result than in problem 1. However, the whole run-time of the pin-by-pin case was shorter than the coarse case of around 3 minutes. This was explained by the total number of transport inner iteration (including all subdomains) that was equal to 57×10^6 and 41×10^6 respectively for the coarse mesh and the pin-by-pin homogenization options. This difference can be justified by the fact that the imposed core eigenvalue converged after 7 iterations instead of 10 respectively for the cases DH+FDR+BB and DH-NEM4+FDR+BB, and by the boundary source normalization that is applied to a coarser mesh in the NEM4 case.

Case	$\mathbf{k-k_{ref}}$	$\mathbf{RMS_{3D}}$ [%]	e [%] **range**	**# globals**
DT-CMFD	k_{ref}=0.96331	ref	ref	23
DH+FDR+BB	11 pcm	0.94	$-4.4 \div 6.6$	21
DH-NEM4+FDR+BB	10 pcm	0.45*	$-3.4^* \div 3.8^*$	20
DH+FDR	7 pcm	1.2	$-5.8 \div 7.4$	25
DH+EQV	-65 pcm	3.0	$-10.8 \div 10.6$	26
DH	-151 pcm	7.5	$-29.7 \div 13.1$	23
DB2+FDF	7 pcm	3.7	$-20.7 \div 11.6$	0
DB2+EQV	-13 pcm	3.8	$-21.9 \div 12.3$	0
DB2	-99 pcm	6.6	$-26.5 \div 9.9$	0

Table 6.3. Global comparison for problem 2. The symbol "*" means that the value has been computed per pin and per axial layer with the local transport solution.

Case	# CPUs	Run-Time	Transport	Diffusion	FOM
DT-CMFD	6240	15.12 h	74%	21%	1
DH+FDR+BB	800	42.8 min	80%	15%	165
DH-NEM4+FDR+BB	800	45.5 min	90%	0.47%	155
DH+FDR	800	47.9 min	80%	15%	148
DH+EQV	800	46.2 min	82%	12%	153
DH	800	44.7 min	82%	12%	158
DB2+FDF	800	9.5 min	(6.6 min)	100%	745
DB2+EQV	800	9.3 min	(6.7 min)	100%	761
DB2	800	9.7 min	(6.6 min)	100%	730

Table 6.4. Performance comparison for problem 2. The time elapsed in transport and diffusion is expressed as a percentage of the whole run-time. For the two-step cases, the time required in transport includes a full assembly lattice calculation with leakage model and homogenization.

6.4.3 Analysis on the axial layer height Δz

In this section we shall explore the behavior of the DH method when the axial layers are defined for different heights Δz. This analysis has no particular interest for actual multiphysics or depletion calculations in a DH framework, because the size of the axial layers depends on the axial mesh used to model the structural components, the temperature gradients or the isotopic content in the core.

However, for some modelizations these axial meshes can be coarser or finer than our "nominal" $\Delta z \approx 20$cm, that has been used in all of the calculations so far. If for different Δz the DH method exhibits the same accuracy and stability properties of the calculations showed in the last sections, then there is an interest in reducing the number of axial layers. This means, in fact, that the number of subdomains can be reduced advantageously and, therefore, the amount of computational resources.

For this analysis we considered only the pin-by-pin homogenization option with flux discontinuity factors in all the internal and external surfaces of the homogenized assembly. We chose this option because in the last two sections it showed the best run-time and one of the best accuracies that the DH methodology can provide. This means that we are exploring the particular case where the RHP is the whole reactor radial plane.

We considered the partially rodded 3D core problem and we produced the 3D core solution with the same nodal diffusion operator (NEM2) that has identical spatial and energy discretization described in Section 6.3.2. The axial reflectors are also modeled in a similar way, with one single axial layer of 20.32cm for the RHP. This feature does not change in the calculations that we shall analyze.

We shall consider four calculations with the core is divided into 2, 4, 8 and 18 axial layers with respectively a Δz equal to 182.88cm, 91.44cm, 45.72cm and 20.32cm. Note that half of the core axial layers are rodded and the other half are unrodded for all the cases. The radial decomposition of the domain is instead fixed with 40 subdomains of the assembly size for each axial layer. It follows that the calculations have a total number of 3D subdomains equal to 160, 240, 400 and 800 respectively. These calculations are performed with a number of cores equal to the number of subdomains. We shall name the cases as "40x4", 40x6", "40x10" and "40x20" respectively.

We also explored the case with an axial layer of 10.16cm, but the iterative process was unstable in the radial reflector subdomains just on top or bottom of the axial reflector. The instability was caused by negative transport fluxes that, when used for cross-section homogenization, produced negative cross sections for diffusion theory. Because of a lack of time, we did not investigate further.

It must be clear that even if the domain decomposition is different, the transport problems to be solved have identical size in all the cases, while the coarse problems have subdomains of different axial size in order to preserve the active fuel length and the total number of 3D pin-cells.

Figure 6.15 shows the MAX and the RMS of the relative pin power error per radial plane for different Δz, while Table 6.5 shows the difference in the core eigenvalue, the RMS_{3D}, the error range and the number of global iterations for each case. Finally, Table 6.6 shows the run-times and the figure of merit for each case.

In terms of accuracy, all the results show a solution that has better quality than two-

step calculations and the cases DH-FDR and DH-EQV presented in the last sections. This means that the weighting spectrum for cross-homogenization must be similar for the ensemble of axial layers belonging to the same part of the core (rodded or unrodded). Moreover, the nominal case $\Delta z = 20$cm exhibits a peak of error at the control rod interface that is higher than the other cases.

The number of global iterations is also similar for all the calculations with a tendency of augmenting when the number of subdomains increases. The figure of merit instead shows a critical point between the two extreme cases with 4 and 20 axial layers. The highest FOM is equal to 285 and it is produced by the case with 6 axial layers.

We may conclude then that where possible, coarsening the axial layer to define the 3D RHP may improve the performance of the method without losing in accuracy.

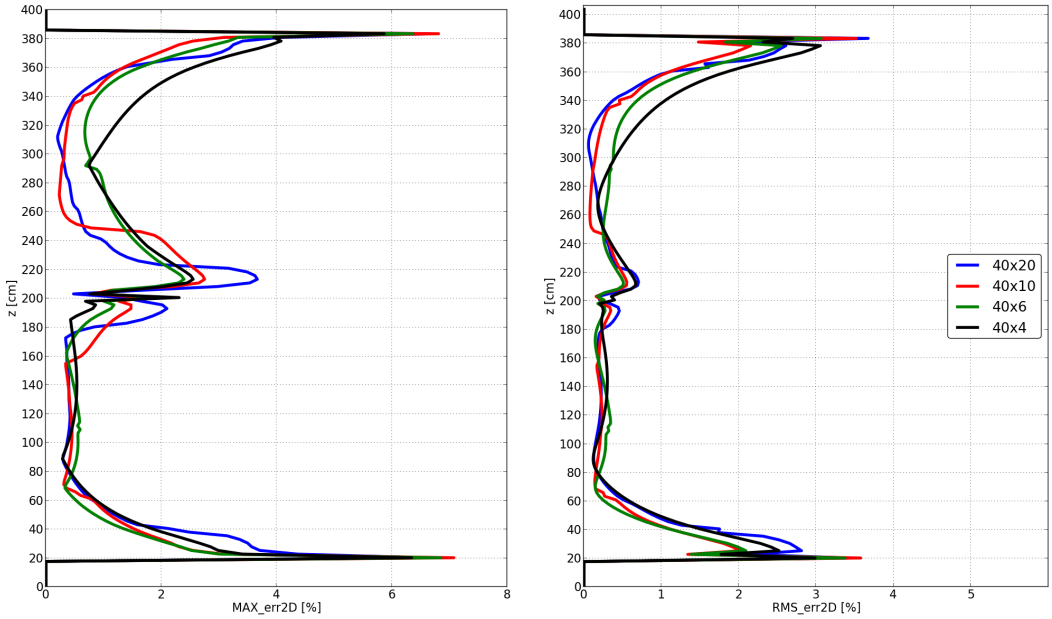

(a) MAX_{2D} **(b)** RMS_{2D}

Figure 6.15. MAX and RMS of the relative pin power error per radial plane for different Δz. (The legend is used once for both figures).

Case	$\mathbf{k-k_{ref}}$	$\mathbf{RMS_{3D}}$ [%]	e [%] range	# globals
DT-CMFD	k_{ref}=0.96331	ref	ref	23
40x20	11 pcm	0.94	$-4.4 \div 6.6$	21
40x10	13 pcm	0.77	$-3.1 \div 7.1$	20
40x6	15 pcm	0.84	$-3.3 \div 6.8$	18
40x4	16 pcm	1.0	$-4.1 \div 6.3$	17

Table 6.5. Global comparison for different Δz.

Case	# CPUs	Run-Time	Transport	Diffusion	FOM
DT-CMFD	6240	15.12 h	74%	21%	1
40x20	800	42.8 min	80%	15%	165
40x10	400	53.6 min	63%	34%	264
40x6	240	1.38 h	37%	61%	285
40x4	160	3.19 h	14%	84%	185

Table 6.6. Performance comparison for different Δz. The time elapsed in transport and diffusion is expressed as a percentage of the whole run-time.

6.5 Conclusions

In this chapter we have applied and investigated the dynamic homogenization method for 3D core calculations.

In the first part, we have introduced a model for the axial leakage in the reference homogenization problem that is solved in order to provide the homogenization parameters. This leakage source is normalized so as to preserve the total net axial current of the low-order operator. Despite the influence on the core solution of the environment information accounted at the homogenization stage, we studied the applicability and the impact in DH of the two main techniques used to preserve the transport reaction rates: the equivalence theory and the flux discontinuity ratios. Thanks to these techniques and the axial leakage model, we showed that it is possible to force the transport and the coarse problems to preserve the same average reaction rates.

We compared three different approaches: 3D direct Transport, Dynamic Homogenization and two-step, where the former was our reference calculation. The evidence that comes out from our analysis is that only with flux discontinuity factors and with the environment information, that are both provided in the DH method, the coarse operator can produce very accurate results, with a root mean square of the relative pin power error inferior to 1.5%. When the RHP becomes the whole reactor radial plane, it is less than 1%. All the other cases, including two-step and DH with equivalence theory, are less precise, especially for the partially rodded configuration.

The methodology showed that the most sensitive part of the core is at the axial reflector interface. This may be caused by the fact that the approximation that we introduced for the axial leakage in the 2D transport calculation may not be sufficient to describe the actual behavior of the solution, since the problem has strong axial gradients axial and leakage is dominant.

Excluding the axial reflector interfaces, in the partially rodded core problem DH exhibited a maximum of relative error per 3D pin-cell of 3.8% in the rodded axial layer at the control rod interface plane.

We also explored a coarse mesh homogenization, where the assembly is homogenized in a 3-by-3 grid. It is only for this type of homogenization that the transport flux which is locally available can be used to compute the power within the pin. This operation requires the average transport power and the diffusion power to be equal for each coarse mesh. This is possible only if the equivalence or the flux discontinuity ratios in all surfaces are applied. In this chapter we investigated the last option only, and the results had a root mean square lower than 1% for both the axially uniform and partially rodded core problems.

Results demonstrate that the choice of a two-group diffusion operator with appropriate homogenization parameters is amply valid for core modeling and design even for highly heterogeneous configurations, such as the presence of different fuels and control rods.

The DH approach avoids 3D transport calculations, and produces a figure of merit with respect to the reference between 150 and 250. This results makes the methodology attractive for multiphysics applications and core depletion calculations. We have also shown that in some core modelizations it is possible to reduce the number of subdo-

mains, requiring a smaller amount of computational resources. Thus, DH is a good candidate as technique for core analysis and design that may run in future desktop machines.

Chapter 7

Conclusions

In this work we have investigated a dynamic homogenization method as an alternative methodology for core calculations and analysis.

The objective of the method is to solve the full 3D core problem with a one-step approach via an iterative process, between fine-transport assembly calculations and two-group diffusion core calculation, preserving assembly macro-exchanges. In contrast with an iterative scheme used in a nonlinear acceleration for the transport problem, in this approach the transport operator does not serve as the core solver, but instead as a generator of homogenization parameters, which entails that the quality of the solution depends on the coarse core operator. However, the advantage of knowing the actual conditions in the core and the environment of each assembly, allows the dynamic homogenization method to seek for a better reference homogenization problem, providing thus a weighting flux for cross sections homogenization which is closer to the real situation than the one given by the critical infinite lattice conditions adopted in the classical two-step calculation scheme.

We have applied and adapted the most popular homogenization techniques used in reactor physics, equivalence theory and flux discontinuity factors, in the framework of our methodology, where the reference homogenization problems have non-zero surface leakage. As opposite to the classical approach, this requires particular care in order to force the three calculations acting in the homogenization process, that are associated respectively to the fine-transport problem, the 2D homogenized problem and the 3D core problem, to produce same the average reaction rates on coarse spatial and energy meshes of the 3D core problem. In particular, we have shown that the flux discontinuity factors are the most efficient homogenization option, because they always produce the most accurate results in a DH framework and, in addition to that, they can be computed analytically at negligible cost without employing any iterative process that may not always converge.

Moreover, we noted that this technique can be used in place of the $\hat{D}$ correction in the popular CMFD operator, in order to construct a low-order operator that serves as nonlinear acceleration for the converge of the core eigenvalue problem and of the fission and boundary transport sources. The main difference with respect to the CMFD technique resides in the fact that $\hat{D}$ has been computed in literature only for a finite

difference scheme, while the flux discontinuity factors can be computed for any type of operator that can admit them. In our case, we applied them to parabolic and quartic nodal diffusion operators.

Our work shows the importance of using the aforementioned techniques in both the classical and DH methodologies, without which two-group diffusion can very drastically fail in severe conditions, such as in the presence of partially inserted control rods. In any case, the most delicate and difficult part was to produce the homogenized reflector cross sections for the two-group calculations, which are the paramount responsible of the accuracy for this calculation scheme. Moreover, the reflector modelization in the classical calculation scheme introduces some uncertainties in the prediction of the two-step power distribution, because it is not guaranteed that the model used for reflector homogenization in a core configuration (in terms of refueling strategy or thermal-hydraulic states) is valid for any other configuration.

This region of the reactor is also not very well predicted by DH with equivalence option, because we observed that this homogenization technique is not sufficient to properly reproduce the reflector response. On the other hand, DH eliminates the reflector uncertainties in the two-step scheme discussed earlier, because the homogenized reflector cross sections are computed with realistic 2D heterogeneous geometry and actual environment for each core configuration. We consider this reliability a significant advantage.

Besides avoiding the infinite lattice approximation and the critical leakage model, the DH approach has then the following advantages: (i) no need for a power reconstruction technique, since the transport solution is locally available in every assembly; (ii) no need for a multiparametrized cross-section library and, therefore, no need for interpolation of the homogenized data, since the assembly transport calculation can be performed at the actual core conditions. Moreover, (iii) the depletion calculation can be performed using transport fluxes at the pin-level and imposing the assembly power density from the actual power distribution; as said earlier, the method offers (iv) the possibility to homogenize the reflector using a 2D heterogeneous geometry and taking into account the real environment of the core. Furthermore, (v) the method avoids expensive 3D transport calculations.

We have seen in this work that there is no particular interest in performing a DH calculation for a 2D core configuration, because the computational cost and the memory requirements are comparable with a direct transport calculation. However, for 3D core problems we have observed a remarkable gain in terms of computational cost (around 200 times less expensive than a direct calculation) and memory requirements, which is mainly due to the point (v) discussed earlier. 3D transport has to deal with a larger number of degrees of freedom and floating operations per inner iteration, which make the approach unfeasible for today current machines.

The DH approach is also feasible only in a parallel framework, because each assembly in the core has to be computed separately in order to obtain a solution with a reasonable time. However, the amount of computational resources are by far inferior to 3D transport, which makes DH a good candidate as one-step calculation scheme for core analysis and design in future desktop machines.

Perspectives and future work

The method of dynamic homogenization offers a wide range of new possibilities for core analysis.

Multiphysics calculations can take advantage from the fact that DH can be coupled at two different scales depending on the phenomenon to be modeled. For instance, local phenomena such as the fuel thermo-mechanics can exchange information only with the fine-transport solver that uses detailed 2D geometries. On the other hand, macroscopic phenomena like the core thermal-hydraulics could be coupled with the diffusion solver. Or one could choose to couple all the other physics directly with transport. So new explorations are possible.

The depletion calculation could be performed using the detailed transport information that is locally available. This allows to deplete each fuel pin annulus with its own power density that is constant along the axial layer. For this application, it would be interesting to use the method of long characteristics instead of MOSC as transport solver, because the former does not use coefficients, that would be different for each pin-cell and may require large memory storage.

Also, most of the methodology developed for diffusion transient calculations can have a direct application.

We discuss now some interesting future research work around the neutronics in DH methodology.

Accuracy

We did not have enough time to verify if the anisotropy order for the scattering source can affect the accuracy of the method. For the same reason, we did not explore different models for the axial leakage source, as well as their impact on the stability properties of the iterative process.

The reflector problems encountered in DH with equivalence theory may be overcome by a different domain decomposition. One should include a part or the radial reflector in the same subdomains of the peripheral fuel assemblies, so that the reflector response would be better determined by the transport operator. This approach was not explored in our work for a lack of time, because it requires the possibility for each subdomain to communicate with more than one neighbor in each side, the so called non-conforming DDM.

The axial reflector merits a different reference homogenization problem. For instance, one could solve a 1D model of the whole fuel assembly element that is constructed so as to preserve the core eigenvalue and the net leakage of the 2D transport problem. Since in the axial reflector the transport problem is strongly axial, this would allow to produce axially dependent homogenized reflector cross sections and the associated FDRs for the 3D diffusion operator that may improve the axial reflector response.

In order to improve the solution at the material discontinuities in the axial direction, one may use the Generalized Equivalence Theory or the Black Box theory in order to estimate the axial discontinuity factors for the 3D diffusion operator. The difficulty of this approach is to be consistent with the coarse axial leakage from the 3D low-order

operator. However, we believe that an investigation is worth.

The iterative scheme should include self-shielding models with leakage. A comparison against reference Monte Carlo solution would be interesting in order to understand if the errors introduced by the multigroup formalism have larger or smaller magnitude than those introduced at the two-group diffusion level.

Another interesting comparison would be against the 2D/1D Fusion method where the axial leakage is computed by an ensemble of 1D axial problems that use multigroup pin-wise homogenized cross sections. If the quality of the 2D/1D Fusion solution is comparable to DH even in the most severe configurations, then the 1D axial problems performed on the homogenized pin-cells are of little help and time-consuming. On the other hand, if the use of the 1D axial problems can improve the solution of a 3D transport problem, then one could employ the 2D/1D Fusion method locally in a 3D subdomain, so as to obtain improved homogenization parameters for the 3D two-group diffusion operator.

Performance

As for any approach based on domain decomposition, the run-time of the DH method is corrupted by the reflector calculation for the following reasons. This type of subdomain experiences strong gradients and has a fixed boundary source. Moreover, the great amount of water that is found in it requires a high number of inner iterations in order to converge the self-scattering source, which can be easily reduced with an acceleration method. In our calculation, for instance, we applied the BPA. However, we used a thermal rebalancing method that was not so effective in converging the up-scattering source. Thus, especially for the first global iterations, the processors that compute fuel assembly subdomains had to wait for the reflector calculations.

Also, shared memory parallelism may be introduced for faster transport sweeps.

Acceleration or preconditioning methods could be employed to accelerate the convergence of the 3D diffusion problem.

A different iterative strategy could also be explored, where the 2D transport problem for the whole reactor radial plane converges before applying homogenization theory for the 3D coarse operator.

The axial leakage model can be used with a different iterative strategy. The coefficients used in the computation of the leakage source with the outgoing flux on top and bottom of the axial layer can be used as fictitious leakage cross section that is added to the total one. It follows that one would use the angular flux of the current iteration in order to accounts for the axial leakage, instead of the one of the previous iteration, and the volumetric leakage source would include only the incoming components that are always positive. Moreover, the scattering ratio would decrease, producing a faster convergence of the self-scattering source. This allows to have a more stable and reliable iterative scheme, since it avoids negative fluxes and, possibly, negative homogenized cross sections for diffusion.

We did not explore this strategy because the method of short characteristics would have required the computation of the interface-current matrix coefficients at each global iteration and, therefore, it would have increased the computational cost of the method. However, it could be interesting to test instead this strategy with a long characteristic

solver.

APPENDIX A

A DERIVATION OF THE 3D P_N SYSTEM OF EQUATIONS

The P_N method employs the spherical harmonics as basis functions for the projection of the integrodifferential equation. The choice of this basis is explained by the fact that the scattering source is already expanded in spherical harmonics, thus the projection technique simplifies the initial equation. Following the approach shown in Section 2.3, the P_N equations are given by expanding and projecting Equation (2.15), yielding:

$$\nabla \cdot \left[\sum_{\ell'}^{N} \frac{2\ell'+1}{4\pi} \sum_{m'=-\ell'}^{\ell'} \phi_{\ell',m'}(\mathbf{r}) \int_{4\pi} d\mathbf{\Omega} \mathbf{\Omega} Y_{\ell,m}(\mathbf{\Omega}) Y_{\ell',m'}(\mathbf{\Omega}) \right] + \Sigma(\mathbf{r}) \phi_{\ell,m}(\mathbf{r}) = Q_{\ell,m}(\mathbf{r}), \tag{A.1}$$

where the group index has been omitted, the indexes ℓ' and m' are those for the flux expansion while ℓ and m for the projected equation, and N is the order of the flux approximation, and we have used the orthogonality condition in the collision term and the source. Note that N must be greater than or equal to the order of anisotropy for the scattering source ($N \geq L$), but it is generally higher in order to better represent the anisotropy of the flux.

At this point we need to rearrange the term $\mathbf{\Omega} Y_{\ell,m}$ in Equation (A.1) so as to obtain the dependence among the angular moments and the system of P_N equations. To do that, we need to use the following recurrence relations :

$$\mu P_\ell^{|m|}(\mu) = \frac{\ell - |m| + 1}{2\ell + 1} P_{\ell+1}^{|m|}(\mu) + \frac{\ell + |m|}{2\ell + 1} P_{\ell-1}^{|m|}(\mu), \tag{A.2}$$

$$\sqrt{1-\mu^2} P_\ell^{|m|}(\mu) = \frac{-1}{2\ell + 1} \left[P_{\ell+1}^{|m+1|}(\mu) - P_{\ell-1}^{|m+1|}(\mu) \right], \tag{A.3}$$

$$\sqrt{1-\mu^2} P_\ell^{|m|}(\mu) = \frac{(\ell - |m| + 1)(\ell - |m| + 2)}{2\ell + 1} P_{\ell+1}^{|m-1|}(\mu) - \frac{(\ell + |m|)(\ell + |m| - 1)}{2\ell + 1} P_{\ell-1}^{|m-1|}(\mu), \tag{A.4}$$

$$\cos(\varphi) T_m(\varphi) = \frac{1}{2} \left[T_{m+1}(\varphi) + T_{m-1}(\varphi) \right], \tag{A.5}$$

$$\sin(\varphi) T_m(\varphi) = -\frac{1}{2} \left[T_{-(m+1)}(\varphi) - T_{-(m-1)}(\varphi) \right] \tag{A.6}$$

where the functions $P_\ell^{|m|}(\mu)$ and $T_m(\varphi)$ are defined respectively in Equations (1.32)

and (1.33).
We firstly analyze the x direction of the streaming term, for which $\mathbf{\Omega}\cdot\mathbf{i}=\Omega_x=\mu$:

$$\begin{aligned}
&\Omega_x Y_{\ell,m}(\mathbf{\Omega}) = N_\ell^m T_m(\varphi)\mu P_\ell^{|m|}(\mu)\\
=&N_\ell^m T_m(\varphi)\left[\frac{\ell-|m|+1}{2\ell+1}P_{\ell+1}^{|m|}(\mu)+\frac{\ell+|m|}{2\ell+1}P_{\ell-1}^{|m|}(\mu)\right]\\
=&\frac{\ell-|m|+1}{2\ell+1}\frac{N_\ell^m}{N_{\ell+1}^m}Y_{\ell+1,m}(\mathbf{\Omega})+\frac{\ell+|m|}{2\ell+1}\frac{N_\ell^m}{N_{\ell-1}^m}Y_{\ell-1,m}(\mathbf{\Omega}),
\end{aligned}$$

then substituting in Equation (A.1) and using the orthogonality property, the streaming term along the x-axis becomes:

$$\frac{\ell-|m|+1}{2\ell+1}\frac{N_\ell^m}{N_{\ell+1}^m}\frac{\partial\phi_{\ell+1,m}(\mathbf{r})}{\partial x}+\frac{\ell+|m|}{2\ell+1}\frac{N_\ell^m}{N_{\ell-1}^m}\frac{\partial\phi_{\ell-1,m}(\mathbf{r})}{\partial x}. \tag{A.7}$$

The streaming along y is obtained similarly applying the appropriate recurrence relations to $\Omega_y Y_{\ell,m}$ as follows:

$$\begin{aligned}
&\Omega_y Y_{\ell,m}(\mathbf{\Omega}) = N_\ell^m \cos(\varphi)T_m(\varphi)\sqrt{1-\mu^2}P_\ell^{|m|}(\mu)\\
=&N_\ell^m\frac{1}{2}\Big[T_{m+1}(\varphi)+T_{m-1}(\varphi)\Big]\sqrt{1-\mu^2}P_\ell^{|m|}(\mu)\\
=&\frac{N_\ell^m}{2(2\ell+1)}\Bigg[T_{m+1}(\varphi)\Big(P_{\ell-1}^{|m+1|}(\mu)-P_{\ell+1}^{|m+1|}(\mu)\Big)+\\
&+T_{m-1}(\varphi)\Big((\ell-|m|+1)(\ell-|m|+2)P_{\ell+1}^{|m-1|}(\mu)-(\ell+|m|)(\ell+|m|-1)P_{\ell-1}^{|m-1|}(\mu)\Big)\Bigg]\\
=&\frac{N_\ell^m}{2(2\ell+1)}\Bigg[\frac{Y_{\ell-1,m+1}(\mathbf{\Omega})}{N_{\ell-1}^{m+1}}-\frac{Y_{\ell+1,m+1}(\mathbf{\Omega})}{N_{\ell+1}^{m+1}}+(\ell-|m|+1)(\ell-|m|+2)\frac{Y_{\ell+1,m-1}(\mathbf{\Omega})}{N_{\ell+1}^{m-1}}\\
&-(\ell+|m|)(\ell+|m|-1)\frac{Y_{\ell-1,m-1}(\mathbf{\Omega})}{N_{\ell-1}^{m-1}}\Bigg],
\end{aligned}$$

that produces the streaming operator for the y-axis:

$$\frac{1}{2(2\ell+1)}\frac{N_\ell^m}{N_{\ell-1}^{m+1}}\frac{\partial\phi_{\ell-1,m+1}(\mathbf{r})}{\partial y} - \frac{1}{2(2\ell+1)}\frac{N_\ell^m}{N_{\ell+1}^{m+1}}\frac{\partial\phi_{\ell+1,m+1}(\mathbf{r})}{\partial y} + \frac{(\ell-|m|+1)(\ell-|m|+2)}{2(2\ell+1)}\frac{N_\ell^m}{N_{\ell+1}^{m-1}}\frac{\partial\phi_{\ell+1,m-1}(\mathbf{r})}{\partial y} - \frac{(\ell+|m|)(\ell+|m|-1)}{2(2\ell+1)}\frac{N_\ell^m}{N_{\ell-1}^{m-1}}\frac{\partial\phi_{\ell-1,m-1}(\mathbf{r})}{\partial y}. \quad \text{(A.8)}$$

Finally, $\Omega_z Y_{\ell,m}$ is rearranged as follows:

$$\begin{aligned}
&\Omega_z Y_{\ell,m}(\mathbf{\Omega}) = N_\ell^m \sin(\varphi) T_m(\varphi)\sqrt{1-\mu^2}P_\ell^{|m|}(\mu)\\
=& -N_\ell^m\left[T_{-(m+1)}(\varphi) - T_{-(m-1)}(\varphi)\right]\sqrt{1-\mu^2}P_\ell^{|m|}(\mu)\\
=& -\frac{N_\ell^m}{2(2\ell+1)}\left[T_{-(m+1)}(\varphi)\left(P_{\ell-1}^{|m+1|}(\mu) - P_{\ell+1}^{|m+1|}(\mu)\right)+\right.\\
&\left. - T_{-(m-1)}(\varphi)\left((\ell-|m|+1)(\ell-|m|+2)P_{\ell+1}^{|m-1|}(\mu) - (\ell+|m|)(\ell+|m|-1)P_{\ell-1}^{|m-1|}(\mu)\right)\right]\\
=& -\frac{N_\ell^m}{2(2\ell+1)}\left[\frac{Y_{\ell-1,-(m+1)}(\mathbf{\Omega})}{N_{\ell-1}^{m+1}} - \frac{Y_{\ell+1,-(m+1)}(\mathbf{\Omega})}{N_{\ell+1}^{m+1}} - (\ell-|m|+1)(\ell-|m|+2)\frac{Y_{\ell+1,-(m-1)}(\mathbf{\Omega})}{N_{\ell+1}^{m-1}}\right.\\
&\left. + (\ell+|m|)(\ell+|m|-1)\frac{Y_{\ell-1,-(m-1)}(\mathbf{\Omega})}{N_{\ell-1}^{m-1}}\right],
\end{aligned}$$

and the streaming term along the z-axis turns into:

$$-\frac{1}{2(2\ell+1)}\frac{N_\ell^m}{N_{\ell-1}^{m+1}}\frac{\partial\phi_{\ell-1,-(m+1)}(\mathbf{r})}{\partial z} + \frac{1}{2(2\ell+1)}\frac{N_\ell^m}{N_{\ell+1}^{m+1}}\frac{\partial\phi_{\ell+1,-(m+1)}(\mathbf{r})}{\partial z} + \frac{(\ell-|m|+1)(\ell-|m|+2)}{2(2\ell+1)}\frac{N_\ell^m}{N_{\ell+1}^{m-1}}\frac{\partial\phi_{\ell+1,-(m-1)}(\mathbf{r})}{\partial z} - \frac{(\ell+|m|)(\ell+|m|-1)}{2(2\ell+1)}\frac{N_\ell^m}{N_{\ell-1}^{m-1}}\frac{\partial\phi_{\ell-1,-(m-1)}(\mathbf{r})}{\partial z}. \quad \text{(A.9)}$$

By recasting Equations (A.7) to (A.9) in Equation (A.1) it yields:

$$
\begin{aligned}
&\frac{\ell-|m|+1}{2\ell+1}\frac{N_\ell^m}{N_{\ell+1}^m}\frac{\partial\phi_{\ell+1,m}(\mathbf{r})}{\partial x}+\frac{\ell+|m|}{2\ell+1}\frac{N_\ell^m}{N_{\ell-1}^m}\frac{\partial\phi_{\ell-1,m}(\mathbf{r})}{\partial x}\\
&+\frac{1}{2(2\ell+1)}\frac{N_\ell^m}{N_{\ell-1}^{m+1}}\left[\frac{\partial\phi_{\ell-1,m+1}(\mathbf{r})}{\partial y}-\frac{\partial\phi_{\ell-1,-(m+1)}(\mathbf{r})}{\partial z}\right]\\
&-\frac{1}{2(2\ell+1)}\frac{N_\ell^m}{N_{\ell+1}^{m+1}}\left[\frac{\partial\phi_{\ell+1,m+1}(\mathbf{r})}{\partial y}-\frac{\partial\phi_{\ell+1,-(m-1)}(\mathbf{r})}{\partial z}\right]\\
&+\frac{(\ell-|m|+1)(\ell-|m|+2)}{2(2\ell+1)}\frac{N_\ell^m}{N_{\ell+1}^{m-1}}\left[\frac{\partial\phi_{\ell+1,m-1}(\mathbf{r})}{\partial y}+\frac{\partial\phi_{\ell+1,-(m-1)}(\mathbf{r})}{\partial z}\right]\\
&-\frac{(\ell+|m|)(\ell+|m|-1)}{2(2\ell+1)}\frac{N_\ell^m}{N_{\ell-1}^{m-1}}\left[\frac{\partial\phi_{\ell-1,m-1}(\mathbf{r})}{\partial y}+\frac{\partial\phi_{\ell-1,-(m-1)}(\mathbf{r})}{\partial z}\right]\\
&+\Sigma(\mathbf{r})\phi_{\ell,m}(\mathbf{r})=Q_{\ell,m}(\mathbf{r}),\qquad \ell\in[0,N],\quad m\in[-\ell,\ell],
\end{aligned}
\tag{A.10}
$$

which is the recursive equation for the $\mathrm{P_N}$ method. The latter is used to produce as many equations as desired that approximate the angular flux up to the order N. The system to be solved is composed of $(N+1)^2$ first order differential equations in a 3D problem. The space-dependent solution is generally found using the finite difference or the finite element methods.

APPENDIX B

AXIAL DISTRIBUTION OF THE DISPERSION OF RELATIVE PIN-POWER ERRORS WITHIN THE ASSEMBLY. PARTIALLY RODDED 3D CORE PROBLEM.

This annex includes complementary analysis for the Partially rodded 3D core problem.

The plots are given for representative assemblies in the core: three assemblies with control rods, one facing the controlled assembly and one facing the reflector. The abscissa represents the axial coordinate. The relative errors are given in percent. Each figure contains the plots for different methods, all having the same plot range that is set to the max error values across the methods for the plotted assembly.

The author thanks Igor Zmijarevic for his generous help in analyzing and providing all the plots in this section with its unique elegance.

Figure B.1. Controlled assembly at position A1. Axial distribution of the dispersion of relative pin-power errors within the assembly. The two curves per plot denote extreme lower and upper error values.

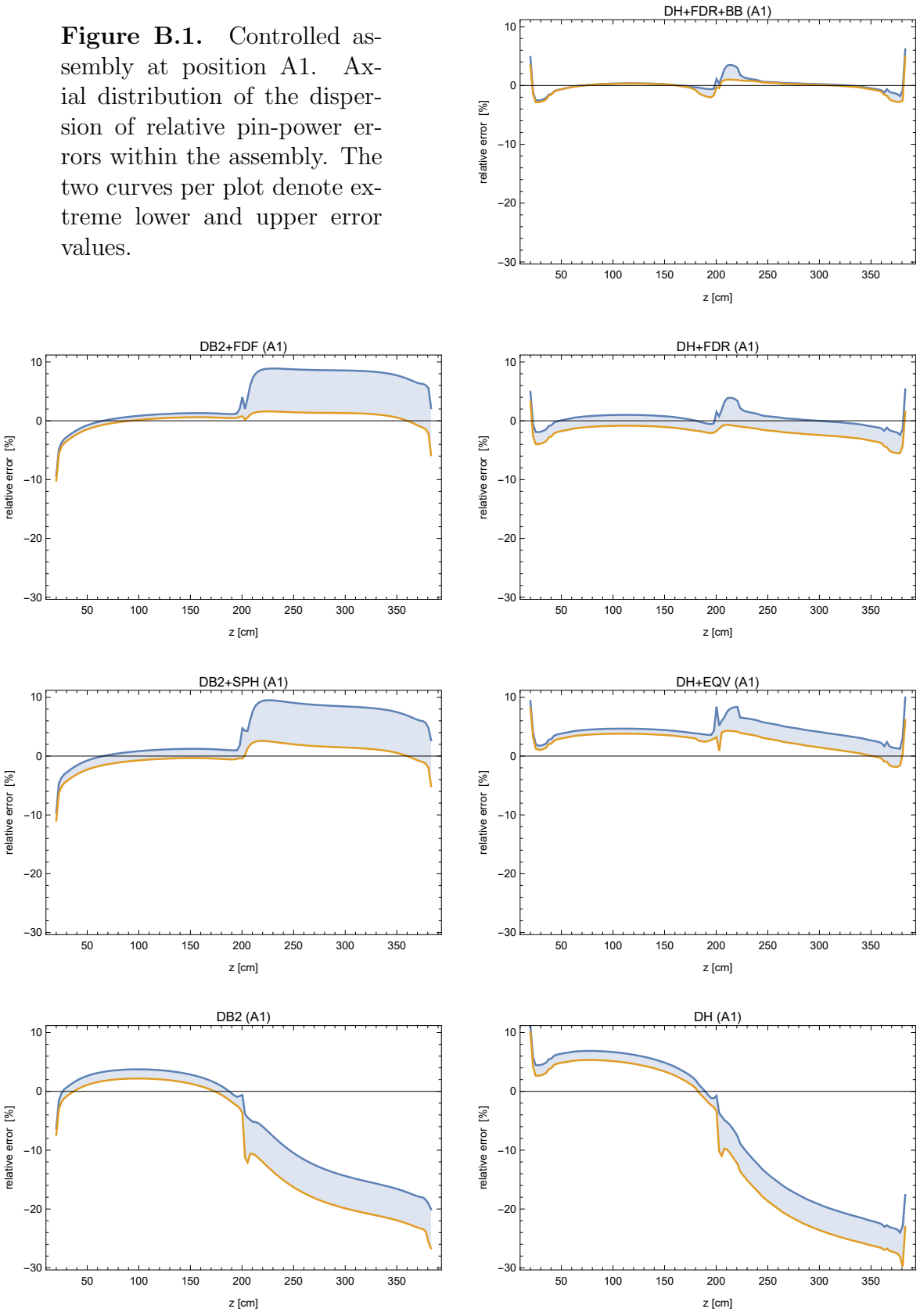

Figure B.2. Controlled assembly at position C1. Axial distribution of the dispersion of relative pin-power errors within the assembly. The two curves per plot denote extreme lower and upper error values.

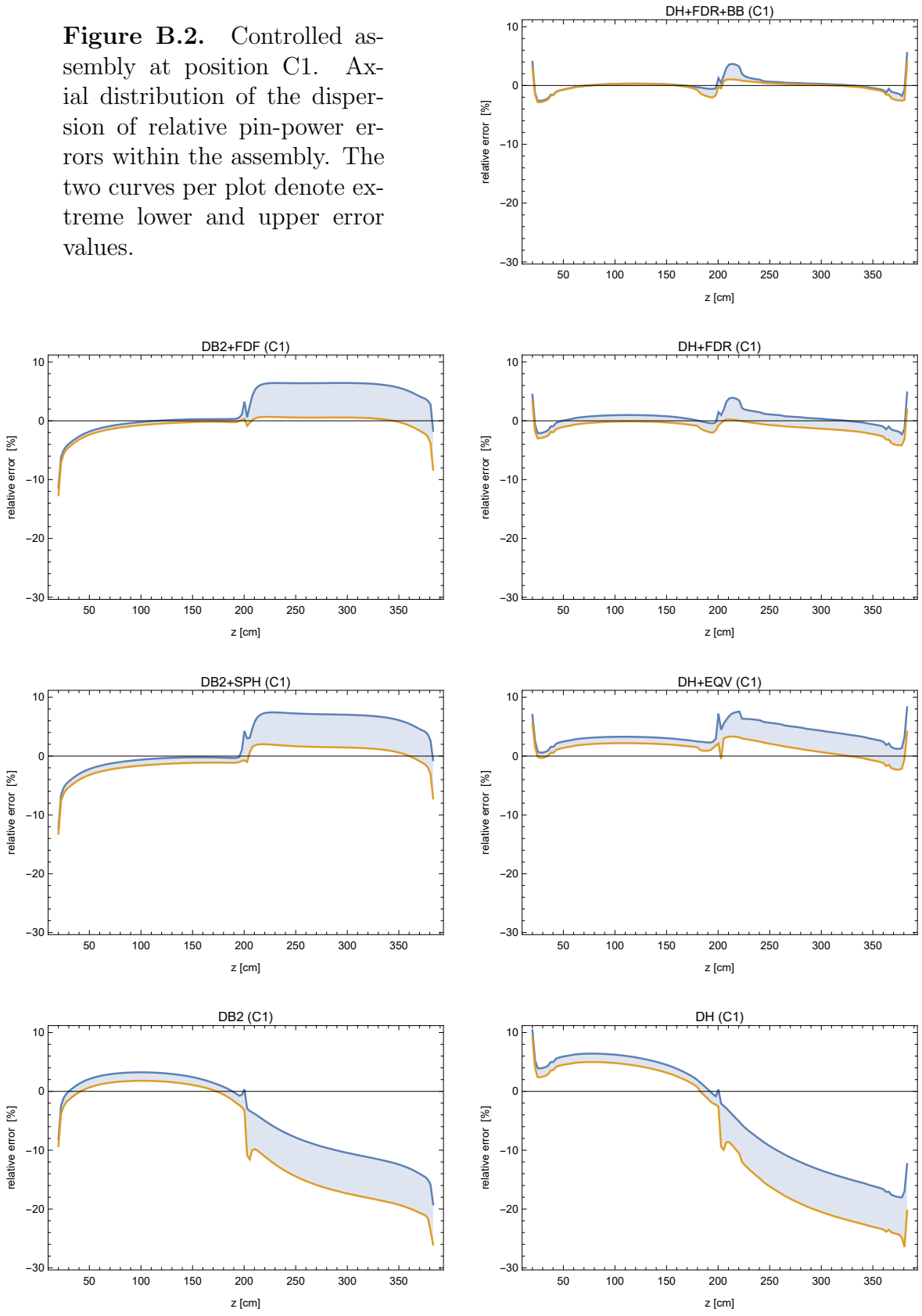

Figure B.3. Controlled assembly at position E5. Axial distribution of the dispersion of relative pin-power errors within the assembly. The two curves per plot denote extreme lower and upper error values.

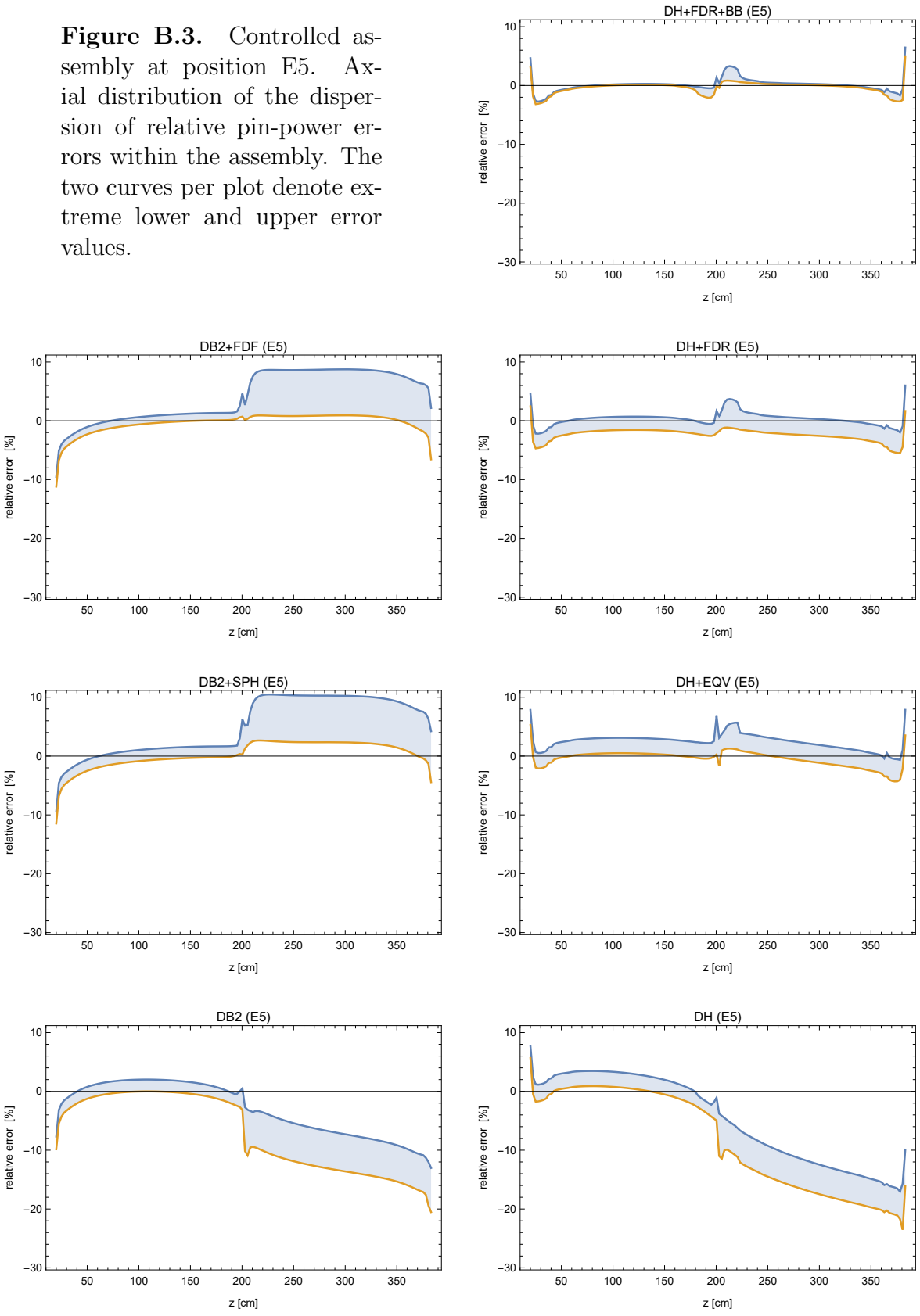

Figure B.4. Fresh UO2 assembly at position E4 adjacent to the controlled assembly. Axial distribution of the dispersion of relative pin-power errors within the assembly. The two curves per plot denote extreme lower and upper error values.

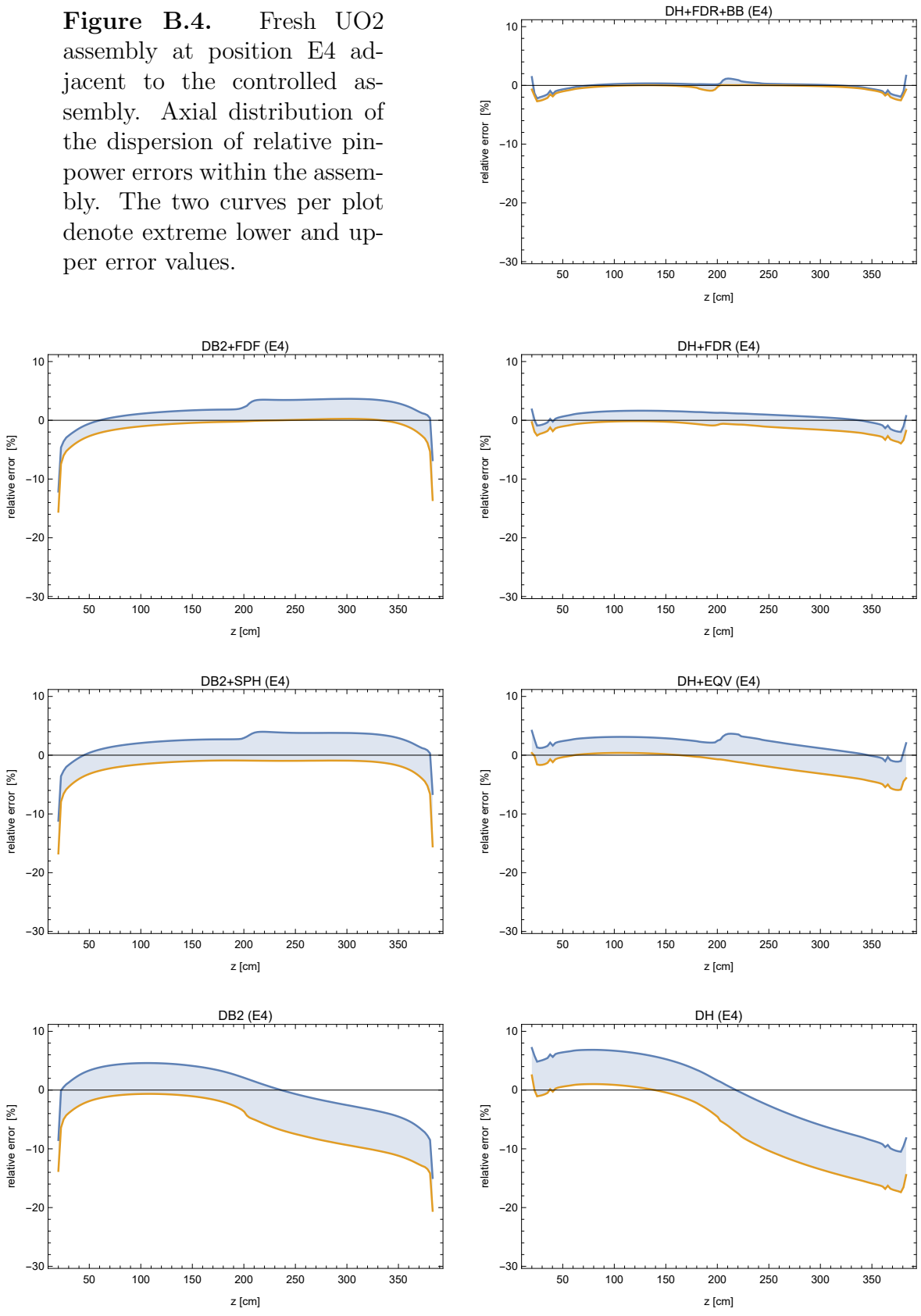

Figure B.5. Fresh MOX assembly at position F6 adjacent to the controlled assembly. Axial distribution of the dispersion of relative pin-power errors within the assembly. The two curves per plot denote extreme lower and upper error values.

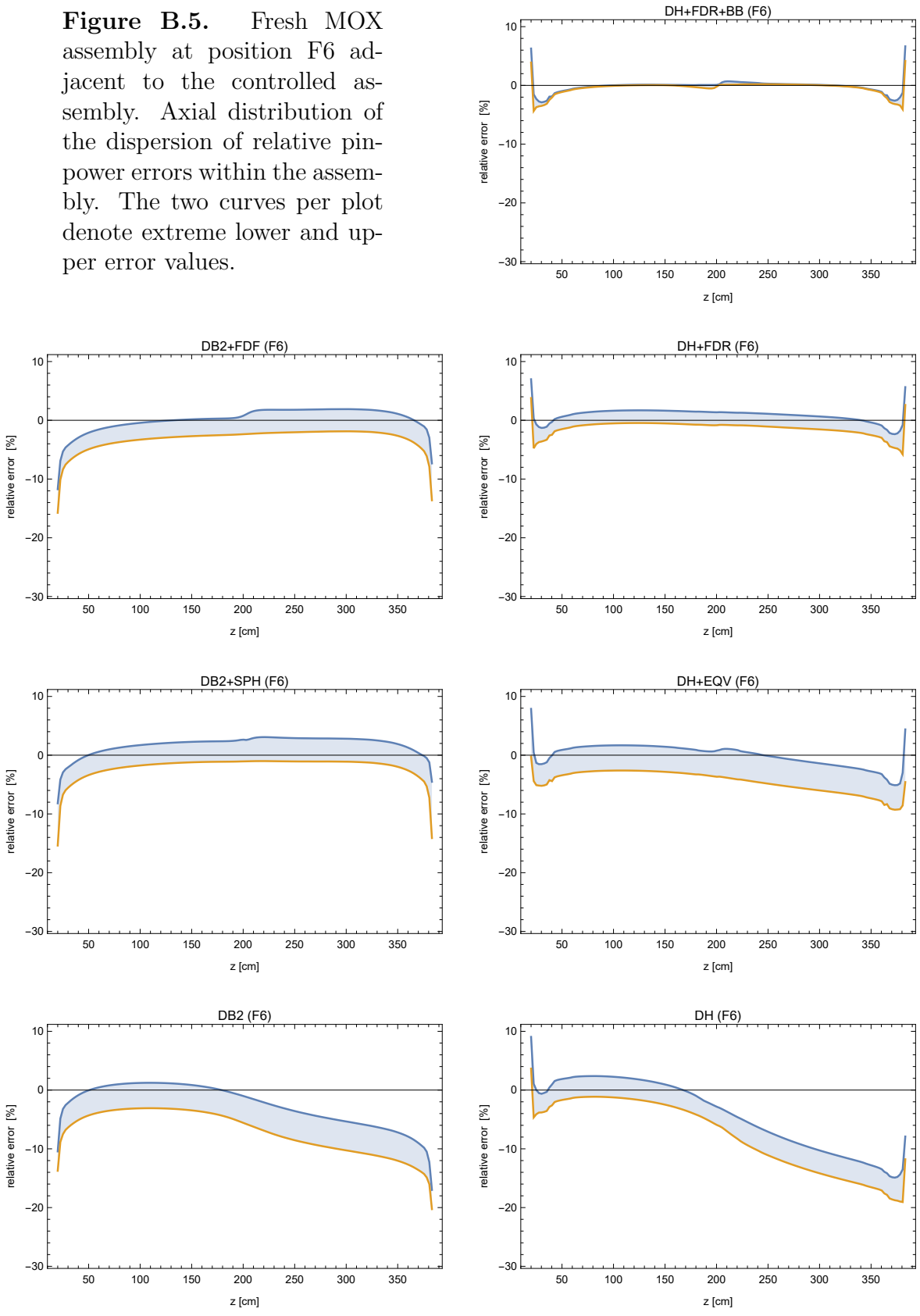

Figure B.6. Twice burned UO2 assembly at position G6 adjacent to the reflector. Axial distribution of the dispersion of relative pin-power errors within the assembly. The two curves per plot denote extreme lower and upper error values.

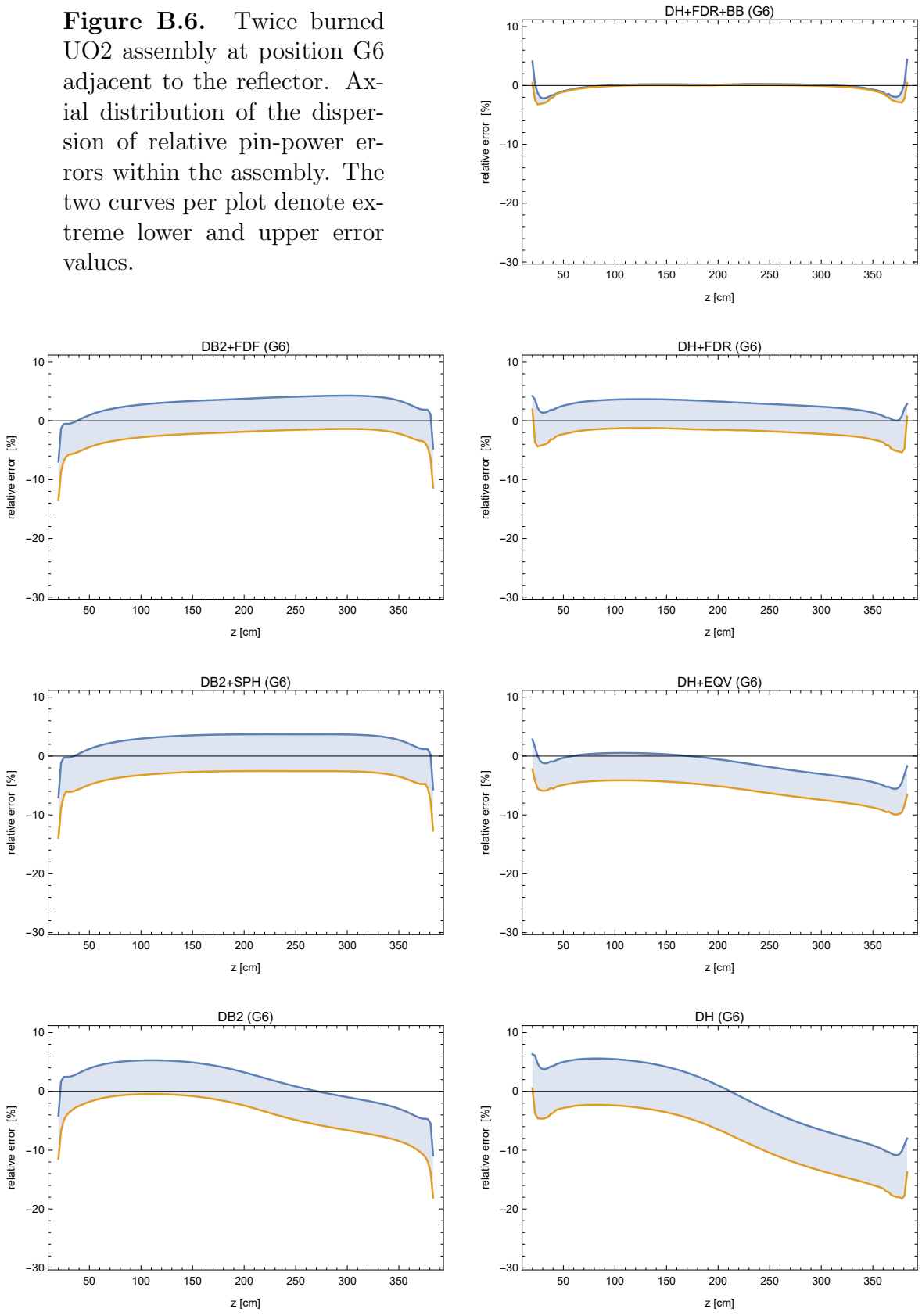

Figure B.7. Twice burned MOX assembly at position H3 adjacent to the reflector. Axial distribution of the dispersion of relative pin-power errors within the assembly. The two curves per plot denote extreme lower and upper error values.

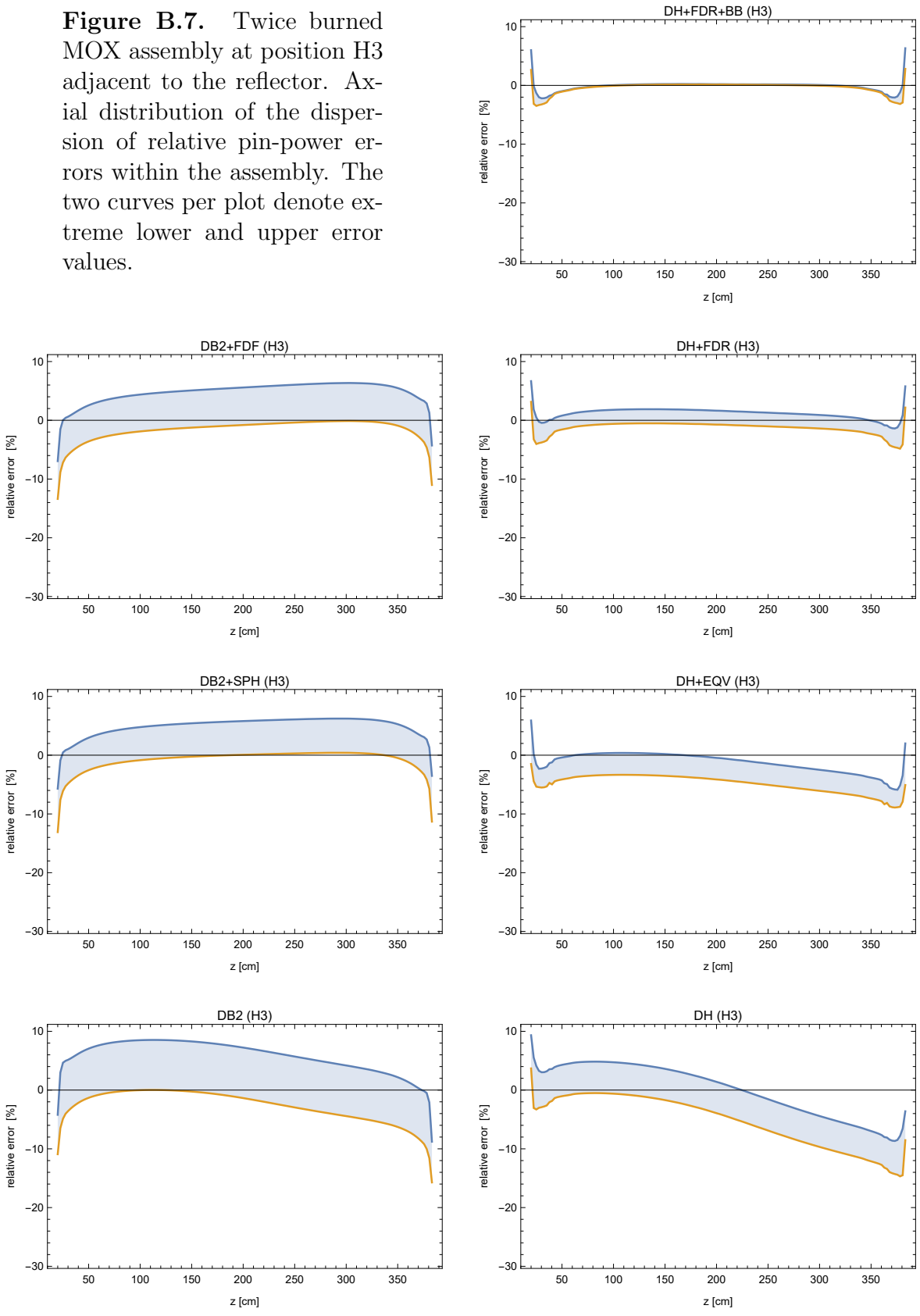

References

[1] A. Weinberg and E. Wigner. *The Physical Theory of Neutron Chain Reactors*. Publications (University of Chicago. Committee on Publications in the Physical Sciences). University of Chicago Press, 1958.

[2] A. Hébert. *Applied Reactor Physics*. Collection cursus. Presses internationales Polytechnique, 2016. ISBN 9782553016981.

[3] R. Lenain. *Contribution to the development of methods for nuclear reactor core calculations with APOLLO3 code : domain decomposition in transport theory for 2D and 3D geometries with nonlinear diffusion acceleration*. Ph.D. thesis, Université Paris Sud - Paris XI, September 2015.

[4] N. Z. Cho. Fundamentals and recent developments of reactor physics methods. *Nuclear Engineering and Technology*, 37(1):25 – 78, 2005.

[5] S. Choi, K. Smith, H. C. Lee, and D. Lee. Impact of inflow transport approximation on light water reactor analysis. *Journal of Computational Physics*, 299:352 – 373, 2015. ISSN 0021-9991.

[6] G. I. Bell, G. E. Hansen, and H. A. Sandmeier. Multitable treatments of anisotropic scattering in sn multigroup transport calculations. *Nuclear Science and Engineering*, 28(3):376–383, 1967.

[7] G. I. Bell and S. Glasstone. Nuclear reactor theory. 1970.

[8] F. d. H. K. M. Case and G. Placzek. *Introduction to the theory of neutron diffusion*. Los Alamos, N. M.: Los Alamos Scientific Laboratory., 1953.

[9] E. E. Lewis. *Second-Order Neutron Transport Methods*, pages 85–115. Springer Netherlands, Dordrecht, 2010.

[10] R. Sanchez and N. J. McCormick. A review of neutron transport approximations. *Nuclear Science and Engineering*, 80(4):481–535, 1982.

[11] E. M. Gelbard. Spherical harmonics methods: Pl and double-pl approximations. 1968.

[12] R. E. Marshak. Note on the spherical harmonic method as applied to the milne problem for a sphere. *Phys. Rev.*, 71:443–446, Apr 1947.

[13] E. M. Gelbard. Applications of spherical harmonics method to reactor problems. 1960.

[14] P. Mala, A. Pautz, S. Canepa, and H. Ferroukhi. Nodal and pin-by-pin calculations comparison with codes simulate-5 and dyn3d. *Proceedings of M&C 2017*, April 2017. doi:Jeju,Korea.

[15] J. C. Ragusa. Steady state analysis of multigroup diffusion and spn methods in an mslb-like situation using the cronos code system. *Proceedings of M&C 2003*, April 2003. doi:Gatlinburg,TN.

[16] B. G. Carlson and G. I. Bell. Solution of the transport equation by the sn method. 1958.

[17] I. Zmijarevic. Multidimensional discrete ordinates nodal and characteristics methods for the apollo2 code. *Proc. Mathematics and Computation and Reactor Physics and Environmental Analysis in Nuclear Applications, Madrid, Spain*, page 1587, September 1999.

[18] I. Zmijarevic. *Résolution de l'équation de transport par des méthodes nodales et des caractéristiques dans les domaines à deux et trois dimensions*. Ph.D. thesis, Université de Provence Aix-Marseille I, 1998.

[19] J. R. Askew. A characteristics formulation of the neutron transport equation in complicated geometries. *United Kingdom Atomic Energy Authority, Reactor Group, Winfrith (United Kingdom).*

[20] D. Sciannandrone. *Acceleration and higher order schemes of acharacteristic solver for the solution of the neutron transport equation in 3D axial geometries.* Ph.D. thesis, Université Paris Sud, 2015.

[21] R. M. Ferrer and J. D. R. III. A linear source approximation scheme for the method of characteristics. *Nuclear Science and Engineering*, 182(2):151–165, 2016.

[22] S. Santandrea, R. Sanchez, and P. Mosca. A linear surface characteristics approximation for neutron transport in unstructured meshes. *Nuclear Science and Engineering*, 160(1):23–40, 2008.

[23] R. Sanchez. Prospects in deterministic three-dimensional whole-core transport calculations. *Nuclear Engineering and Technology*, 44, 03 2012.

[24] F. Févotte. *Techniques de traçage pour la méthode des caractéristiques appliquée à la résolution de l.équation du transport des neutrons en domaines multidimensionnels.* Ph.D. thesis, Université Paris Sud 11, November 2008.

[25] Personal conversation with em.

[26] E. Masiello, R. Sanchez, and I. Zmijarevic. New numerical solution with the method of short characteristics for 2-d heterogeneous cartesian cells in the apollo2 code: Numerical analysis and tests. *Nucl. Sci. Eng.*, 161(3):257–278, 2009.

[27] E. Masiello, R. Lenain, and W. Ford. Linear short characteristics applied tp 3d heterogeneous cartesian cells for transport-based core simulations. *Proceedings of M&C 2019*, 10 2019.

[28] H. L.A. and Y. D.M. *Applied iterative Methods.* Academic Press, New York, 1981.

[29] M. L. Adams and E. W. Larsen. Fast iterative methods for discrete-ordinates particle transport calculations. *Progress in Nuclear Energy*, 40(1):3 – 159, 2002. ISSN 0149-1970.

[30] G. R. Cefus and E. W. Larsen. Stability analysis of coarse-mesh rebalance. *Nuclear Science and Engineering*, 105(1):31–39, 1990.

[31] E. M. Gelbard and L. A. Hageman. The synthetic method as applied to the sn equations. *Nuclear Science and Engineering*, 37(2):288–298, 1969.

[32] W. H. Reed. The effectiveness of acceleration techniques for iterative methods in transport theory. *Nuclear Science and Engineering*, 45(3):245–254, 1971.

[33] R. E. Alcouffe. Diffusion synthetic acceleration methods for the diamond-differenced discrete-ordinates equations. *Nuclear Science and Engineering*, 64(2):344–355, 1977.

[34] R. D. Lawrence. An interface current approach to synthetic acceleration of three dimensional discrete ordinates transport methods. *Transactions of the American Nuclear Society*, 53(280), 1986.

[35] M. L. Adams and W. R. Martin. Boundary projection acceleration: A new approach to synthetic acceleration of transport calculations. *Nuclear Science and Engineering*, 100(3):177–189, 1988.

[36] P. F. Nowak and M. L. Adams. Anxy-geometry analysis of an "s2-like" synthetic acceleration scheme. *Transactions of the American Nuclear Society*, 55(354), 1987.

[37] K. S. Moon, N. Z. Cho, J. M. Noh, and S. G. Hong. Acceleration of the analytic function expansion nodal method by two-factor two-node nonlinear iteration. *Nuclear Science and Engineering*, 132(2):194–202, 1999.

[38] S. Yuk and N. Z. Cho. Whole-core transport solutions with 2-d/1-d fusion kernel via p-cmfd acceleration and p-cmfd embedding of nonoverlapping local/global iterations. *Nuclear Science and Engineering*, 181(1):1–16, 2015.

[39] J. M. Aragonés and C. Ahnert. A linear discontinuous finite difference formulation for synthetic coarse-mesh few-group diffusion calculations. *Nuclear Science and Engineering*, 94(4):309–322, 1986.

[40] W. Ford, E. Masiello, C. Calvin, F. Fevotte, and B. Lathuilliere. The response matrix acceleration method for the discrete-ordinate transport equation. *Proceedings of M&C 2019*, August 2019. doi:Portland,OR.

[41] W. Ford. *The Advancement of Stable, Efficient and Parallel Acceleration Methods for the Neutron Transport Equation.* Ph.D. thesis, Université Paris-Saclay,, November 2019.

[42] D. Sciannandrone, L. Graziano, and S. Santandrea. Memory footprint reduction of a multi-group dpn transport operator for 3d moc acceleration. 08 2019. doi:Portland,OR.

[43] R. Sanchez, G. Dante, and I. Zmijarevic. Diffusion piecewise homogenization via flux discontinuity ratios. *Nucl. Eng. Technol.*, 45(6):707 – 720, 2013. ISSN 1738-5733.

[44] R. Sanchez. Assembly homogenization techniques for core calculations. *Progress in Nuclear Energy*, 51(1):14 – 31, 2009. ISSN 0149-1970.

[45] G. Ilas and F. Rahnema. A monte carlo based nodal diffusion model for criticality analysis of spent fuel storage lattices. *Annals of Nuclear Energy*, 30(10):1089 – 1108, 2003. ISSN 0306-4549.

[46] A. Kavenoky. The sph homogenization method. *Procedings of a Specialists' Meeting on Homogenization Methods in Reactor Physics*, 1978. doi:Lugano,Switzerland.

[47] A. Hébert. A consistent technique for the pin-by-pin homogenization of a pressurized water reactor assembly. *Nucl. Sci. Eng.*, 113(3):227–238, 1993.

[48] R. Sanchez, J. Mondot, Z. Stankovski, A. Cossic, and I. Zmijarevic. Apollo2: a user oriented, portable, modular code for multigroup transport assembly calculations. *Nucl. Sci. Eng.*, 100:352 – 362, 1988.

[49] J. Ortensi, Y. Wang, A. Laurier, S. Schunert, A. Hébert, and M. DeHart. A newton solution for the superhomogenization method: The pjfnk-sph. *Annals of Nuclear Energy*, 111:579 – 594, 2018. ISSN 0306-4549.

[50] A. Hébert and G. Mathonnière. Development of a third-generation superhomogénéisation method for the homogenization of a pressurized water reactor assembly. *Nuclear Science and Engineering*, 115(2):129–141, 1993.

[51] K. Koebke. A new approach to homogenization and group condensation. *IAEA-TECDOC*, (231):303, 1980.

[52] K. Koebke and L. Hetzelt. On the reconstruction of local homogeneous neutron flux and current distributions of light water reactors from nodal schemes. *NNucl. Sci. Eng.*, 91:123–131, 10 1985.

[53] K. Smith. Assembly homogenization techniques for light water reactor analysis. *Progress in Nuclear Energy*, 17(3):303 – 335, 1986. ISSN 0149-1970.

[54] K. S. Smith, A. F. Henry, and R. Lorentz. Determination of homogenized diffusion theory parameter for coarse-mesh nodal analysis. *Proc. ANS Topl. Mtg. Advanced in Reactor Physics and Shielding, Sun Vallay, Idaho*, page 224, 1980.

[55] K. S. Smith. Nodal method storage reduction by nonlinear iteration. *Transactions of the American Nuclear Society*, 44:265–266, 1983.

[56] J. M. Aragonés and C. Ahnert. A linear discontinuous finite difference formulation for synthetic coarse-mesh few-group diffusion calculations. *Nuclear Science and Engineering*, 94(4):309–322, 1986.

[57] K. Smith and J. Rhodes. Full core, 2-d, lwr core calculations with casmo-4e. *Proceedings of PHYSOR 2002*, October 2002. doi:Seoul,Korea.

[58] B. Kelley and E. Larsen. Cmfd acceleration of spatial domain-decomposed neutron transport problems. *International Conference on the Physics of Reactors 2012, PHYSOR 2012: Advances in Reactor Physics*, 1:715–727, 01 2012.

[59] Y. S. Jung, C. B. Shim, C. H. Lim, and H. G. Joo. Practical numerical reactor employing direct whole core neutron transport and subchannel thermal/hydraulic solvers. *Ann. Nucl. Energy*, 62:357 – 374, 2013. ISSN 0306-4549.

[60] D. G. Cacuci, editor. *Handbook of Nuclear Engineering*. Springer US, 2010. ISBN 978-0-387-98130-7, 978-0-387-98149-9, 978-0-387-98150-5.

[61] U. Grundmann and S. Mittag. Super-homogenisation factors in pinwise calculations by the reactor dynamics code dyn3d. *Ann. Nucl. Energy*, 38(10):2111 – 2119, 2011. ISSN 0306-4549.

[62] R. Sanchez, I. Zmijarevic, M. Coste-Delclaux, E. Masiello, S. Santandrea, E. Martinolli, L. Villate, N. Schwartz, and N. Guler. Apollo2 year 2010. *Nuclear Engineering and Technology*, 42, 10 2010.

[63] D. Tomatis, A. Galia, S. Pastoris, and I. Zmijarevic. Quantification of history effects in pwr modelling. *Nuclear Engineering and Design*, 325:205–217, 12 2017.

[64] G. Gunow, B. Forget, and K. Smith. Full core 3d simulation of the beavrs benchmark with openmoc. *Annals of Nuclear Energy*, 134:299 – 304, 2019. ISSN 0306-4549.

[65] Y. S. Ban, E. Masiello, R. Lenain, H. G. Joo, and R. Sanchez. Code-to-code comparisons on spatial solution capabilities and performances between ntracer and the standalone idt solver of apollo3®. *Ann. Nucl. Energy*, 115:573 – 594, 2018. ISSN 0306-4549.

[66] W. Ford, E. Masiello, C. Calvin, F. Févotte, and B. Lathuilière. The response matrix acceleration: A new non-linear method for the 3d discrete-ordinate transport equation. *Annals of Nuclear Energy*, 146:107642, 2020. ISSN 0306-4549.

[67] N. Cho, G. Lee, and C. Park. Fusion of method of characteristics and nodal method for 3-d whole-core transport calculation. *Trans. Am. Nucl. Soc.*, 86, 2002.

[68] N. Z. Cho. Fundamentals and recent developments of reactor physics methods. *Nuclear Engineering and Technology*, 37, 02 2005.

[69] S. Yuk and N. Z. Cho. Comparison of 1-d/1-d fusion method and 1-d/1-d hybrid method in two-dimensional neutron transport problems: Convergence analysis and numerical results. *Nuclear Science and Engineering*, 184(2):151–167, 2016.

[70] B. W. Kelley. *An Investigation of 2D/1D Approximations to the 3D Boltzmann Transport Equation*. Ph.D. thesis, University of Michigan, 2015.

[71] M. G. Jarrett. *A 2D/1D Neutron Transport Method with Improved Angular Coupling*. Ph.D. thesis, University of Michigan, 2018.

[72] E. W. Larsen. Diffusion theory as an asymptotic limit of transport theory for nearly critical systems with small mean free paths. *Annals of Nuclear Energy*, 7(4):249 – 255, 1980. ISSN 0306-4549.

[73] S. Palmtag and K. Smith. Two-group spectral corrections for mox calculations. *Proc. of the Int. Conf. on the Physics of Nuclear Science and Technology*, 1, 1998. doi:LongIsland,NewYork,USA.

[74] T. Kozlowski and T. J. Downar. Pwr mox/uo2 core transient benchmark (final report). *NEA/NSC/DOC(2006)20*, 6048, 2007. ISSN ISBN 92-64-02330-5.

[75] P. Mala, A. Pautz, and H. Ferroukhi. Epr fuel cycle depletion with pin-by-pin code tortin and nodal code simulate5. *Proceedings of M&C 2019*, August 2019. doi:Portland,OR.

[76] F. Rahnema and E. M. Nichita. Leakage corrected spatial (assembly) homogenization technique. *Ann. Nucl. Energy*, 24(6):477 – 488, 1997. ISSN 0306-4549.

[77] F. Rahnema and M. S. Mckinley. High-order cross-section homogenization method. *Ann. Nucl. Energy*, 29:875–899, 05 2002.

[78] K. T. Clarno and M. L. Adams. Capturing the effects of unlike neighbors in single-assembly calculations. *Nucl. Sci. Eng.*, 149(2):182–196, 2005.

[79] P. Mondot and R. Sanchez. An iterative homogenization technique that preserves assembly core exchanges. *International conference on supercomputing in nuclear applications SNA'2003*, 2003. ISSN INIS-FR–2652.

[80] T. Takeda and K. K. Y. Fujita. Leakage dependent sph factor for pwr whole core transport calculation. *Int. Conf. of the Physics of Reactors Nuclear Power: A Sustainable Resource*, September 2008. doi:Casino-KursaalConferenceCenter,Interlaken,Switzerland.

[81] D. Colameco, B. Ivano, D. Beacon, and K. Ivano. Iterative transport-diffusion methodology for lwr core analysis. *SNA+MC 2013*, 41, 2014. ISSN 01104.

[82] M. Grimod, R. Sanchez, and F. Damian. A dynamic homogenization model for pebble bed reactors. *Nuclear Science and Technology*, 52:932 – 944, 2015.

[83] I. Petrovic and P. Benoist. *BN Theory: Advances and New Models for Neutron Leakage Calculation*, pages 223–282. Springer US, Boston, MA, 1997.

[84] N. Z. Cho and C. J. Park. A comparison of coarse mesh rebalance (cmr) and coarse mesh finite difference (cmfd) acceleration methods for the neutron transport calculations. *Nuclear Reactor Analysis and Particle Transport Laboratory*, NURAPT-2002-02, 2003.

[85] R. Lenain, E. Masiello, F. Damian, and R. Sanchez. Coarse-grained parallelism for full-core transport calculations. *PHYSOR 2014: The Role of Reactos Physics toward a Sunstainable Future*, 10 2014.

université PARIS-SACLAY

ÉCOLE DOCTORALE
Particules, hadrons, énergie et noyau : instrumentation, imagerie, cosmos et simulation (PHENIICS)

Titre: Une méthode d'homogénéisation dynamique pour les calculs de réacteurs nucléaires

Mots clés: Calculs Coeur, Théorie d'homogénéisation, Decomposition de domaine, HPC

Résumé: Dans les calculs de réacteurs à trois dimensions, nombreuses techniques d'homogénéisation ont été développées pour l'utilisation du schéma de calcul classique à deux étapes, basé sur les sections efficaces homogénéisées au préalable et utilisées ensuite par interpolation pour un état physique donné. D'autre part, les schémas de calcul basées principalement sur les méthode des caractéristiques, qui visent le calcul direct du réacteur sans homogénéisation, ont des performances encore limitées en raison des capacités des machines et font alors le recours à des solutions de transport simplifiées. Ce travail a pour objectif d'étudier une nouvelle approche dans laquelle l'homogénéisation dynamique est utilisée pour produire le flux neutronique de pondération sur les modèles d'assemblage tridimensionnels.

L'application de la méthode pour un calcul d'un REP en 3D est comparée aux résultats issus d'un calcul de référence numérique en transport 3D et d'un calcul classique à deux-étapes. La réalisation repose sur le calcul de haute performance et avec un haut niveau de parallélisme.

Title: A dynamic homogenization method for nuclear reactor core calculations

Keywords: Core calculation, Homogenization theory, Domain decomposition, HPC

Abstract: Three-dimensional deterministic core calculations are typically based on the classical two-step approach, where the homogenized cross sections of an assembly type are precalculated and then interpolated to the actual state in the reactor. The weighting flux used for cross-section homogenization is determined assuming the fundamental mode condition and using a critical-leakage model that does not account for the actual environment of an assembly. On the other hand, 3D direct transport calculations and the 2D/1D Fusion method, mostly based on the method of characteristics, have recently been applied showing excellent agreement with reference Monte-Carlo code, but still remaining computationally expensive for multiphysics applications and core depletion calculations. In the present work, we propose a method of Dynamic Homogenization as an alternative technique for 3D core calculations, in the framework of domain decomposition method that can be massively parallelized. It consists of an iterative process between core and assembly calculations that preserves assembly macro-exchanges. The verification tests on 2D and 3D full core problems are presented applying several homogenization and equivalence techniques, comparing against direct 3D transport calculation. For this analysis, we solved the NEA "PWR MOX/UO2 Core Benchmark" problem, which is characterized by strong radial heterogeneities due to the presence of different types of UOx and MOx assemblies at different burnups. The obtained results show the advantages of the proposed method in terms of precision with respect to two-step and performances with respect to the direct approach.

Université Paris-Saclay
Espace Technologique / Immeuble Discovery
Route de l'Orme aux Merisiers RD 128 / 91190 Saint-Aubin, France